# UNIVERSITÀ DEGLI STUDI DI TRIESTE

## XXXVII CICLO DEL DOTTORATO DI RICERCA IN

______________FISICA (PHD04)____________________________________________

__________UNIVERSITA’ DEGLI STUDI DI TRIESTE, IOM-CNR___________________

# ULTRAFAST ELECTRON AND EXCITON DYNAMICS IN TRANSITION METAL DICHALCHOGENIDES, STUDIED BY OPTICAL AND PHOTOELECTRON SPECTROSCOPIES

Settore scientifico-disciplinare: **FISICA DELLA MATERIA (FIS/03)**

DOTTORANDO
**MICHELE PERLANGELI**

COORDINATORE
**PROF. FRANCESCO LONGO**

SUPERVISORE DI TESI
**RICCARDO CUCINI**

**ANNO ACCADEMICO 2023/2024**

# Contents

**1 Introduction and theoretical background 9**
- 1.1 Optical properties in solids 9
- 1.2 Excitons in solids 12
  - 1.2.1 Tight binding excitons 12
  - 1.2.2 Weak binding excitons 13
  - 1.2.3 Intermediately bound excitons 18
  - 1.2.4 Indirect excitons transitions 18
- 1.3 A brief review of photoluminescence 19
  - 1.3.1 Photoluminescence spectroscopy 19
  - 1.3.2 Photoluminescence in semiconductors 20
  - 1.3.3 Photoluminescence Lifetime and Quantum Yield 23
- 1.4 Free Excitons, Electron-Hole Plasma and Electron-Hole Liquid in semiconductors 25
  - 1.4.1 Theoretical approach to introduce FE, EHP and EHL 25

**2 The scientific topic: Transition Metal Dichalcogenides 29**
- 2.1 General properties of 2H-TMD 29
  - 2.1.1 Defects in TMD 31
- 2.2 Excitons in TMD 35
  - 2.2.1 Spin forbidden dark excitons 36
  - 2.2.2 Indirect excitons or momentum forbidden dark excitons 36
  - 2.2.3 Biexcitons, trions, localized excitons and interlayer excitons 37
- 2.3 Exciton dynamics and photoluminescence in TMDs 38
  - 2.3.1 The intrinsic radiative lifetime and the observed radiative lifetime for excitons 39
  - 2.3.2 Non hydrogen-like excitons in TMDs 45
- 2.4 Theoretical calculations and experimental evidences of the excitonic Mott transition, and of room temperature electron hole liquid in monolayer $MoS_2$ 46
  - 2.4.1 PL dynamics for an electron-hole plasma 49
- 2.5 State of the art for the exciton physics in TMDs 49

**3 Experimental Methods 51**
- 3.1 The micro- Time Resolved PhotoLuminescence setup 51
  - 3.1.1 Advantages and disadvantages of the Gemini interferometer 53
  - 3.1.2 Effects of the non-ideality of the interferometer 54
  - 3.1.3 Photoluminescence data acquisition 56
  - 3.1.4 The time resolved PL data: how to read the 2D maps 57
  - 3.1.5 Photoluminescence data processing 59
  - 3.1.6 Effects of the IRFs on the R-L deconvolution 64
  - 3.1.7 Clarification on the quality of the experimental data 66
- 3.2 The TR-ARPES apparatus at the Sprint laboratory 67
  - 3.2.1 Introduction to Photoelectron Spectroscopy 67
  - 3.2.2 The light sources at the Sprint laboratory 67
- 3.3 The transfer system for exfoliated flakes 70

**4 Photoluminescence data analysis** **75**
4.1 Experimental methods . . . . . 75
4.2 Analysis of the errors affecting the PL spectra . . . . . 77
4.3 Energy resolution and exciton emission line-width . . . . . 79
4.4 $WS_2$, steady state photoluminescence Vs power . . . . . 80
4.5 $WS_2$, spatially-resolved steady state photoluminescence . . . . . 83
4.6 Time resolved photoluminescence data . . . . . 86
4.6.1 Initial excitation density after a pulsed excitation . . . . . 87
4.6.2 $WS_2$, time resolved photoluminescence, TR- spectra . . . . . 89
4.6.3 $WS_2$, time resolved photoluminescence, PL time dynamics . . . . . 95
4.6.4 Monolayer $MoS_2$, time resolved photoluminescence, TR- spectra . . . . . 103
4.6.5 Bulk $MoS_2$, time resolved photoluminescence . . . . . 108
4.7 Conclusions . . . . . 111

**5 Photoelectron spectroscopy data analysis** **113**
5.1 Experimental methods . . . . . 113
5.2 Static ARPES . . . . . 114
5.2.1 Surface photovoltage (SPV) . . . . . 115
5.2.2 Data processing . . . . . 117
5.3 Analysis of the valence band . . . . . 117
5.4 Analysis of the conduction band . . . . . 119
5.5 Ultrafast dynamics in conduction band around the K and $\Sigma$ points . . . . . 122
5.6 Conclusions . . . . . 125

**6 Appendix** **131**
6.1 Derivation of the explicit expression for the imaginarty part of the dielectric function $\varepsilon_2(\hbar\omega)$ . . . . . 131
6.2 Second order optical transitions in solids . . . . . 133
6.3 The NIREOS GEMINI Interferometer . . . . . 134
6.4 The Discrete Fourier Transform (D-FT) . . . . . 137
6.5 Access to the Time domain: The Time Correlated Single Photon Counting system 138
6.6 List of abbreviations and simbols used in the thesis . . . . . 141

# Abstract

In my PhD activity, I developed, tested and optimized an ad-hoc novel time resolved photoluminescence (TR-PL) experimental setup, at the Sprint and TReX Laboratory (Fermi building, Elettra Sincrotrone Trieste). This apparatus allows to record the PL spectra after an ultra-short light pulse (t=300 fs, $h\nu$=2.4 eV) excitation, and with a time resolution of $\approx$ 25 ps. Thanks to the high repetition rate (1 MHz) and to the high output power of the laser source (Coherent Monaco 1035-40-40), this experimental system constitutes the perfect tool to access the TR-PL signal of materials in both the ultra-low and ultra-high excitation regime. This study is particularly interesting in semiconducting 2D transition metal dichalcogenides (TMDs) monolayers, where the direct band gap results in a bright photoluminescence, and where a high exciton binding energy opens the possibility to investigate the exciton physics at room temperature. Excitons in TMDs can't be treated as hydrogen-like systems (weakly bound excitons) or as bound electron-hole pairs localized on single atoms or within a single unit cell (strongly bound excitons). Their intermediate behaviour between these two extreme cases poses computational difficulties for the theoretical calculations, and calls for new experimental investigations. Moreover, these tightly bound excitons in TMDs are stable at room temperature, and they dominate the light emission properties of these materials only at low or moderate excitation density, while in the high excitation density regime, the strong electron-electron exchange and correlation terms lead to a huge band-gap renormalization at high carrier density, leading to the ionization of free excitons (FE) in an electron-hole plasma (EHP) and, at even higher density, in the generation of an electron-hole liquid (EHL).

Since defects in crystals strongly affect the electronic and optical properties, including the PL efficiency, high-quality TMD monolayers with low defect concentration are desirable to perform our investigations. At this purpose, I learned the technique to mechanically exfoliate TMD monolayers from a high-quality bulk sample, to exploit the superior crystal quality and lower defect concentration, with respect to MBE or CVD grown ones, where chemical and physical defects are induced by the growth process. Since also the interactions with the substrate strongly affect the defect concentration and in general the physical properties of TMD monolayers, I learned how to use a transfer system to deposit the exfoliated flakes on a desired substrate, such as $SiO_2$ (weak interaction monolayer-substrate) or a patterned Si wafer with holes of 5 $\mu m$ diameter to obtain free-standing monolayers (no interaction with any substrate). To open the possibility to measure these exfoliated TMD flakes, which spatial size is of few microns, I implemented the micro- PL configuration in the TR-PL setup.

Finally, I combined the potentialities of the new TR-PL setup and the ability to fabricate custom TMD monolayers to perform experiments to study of the TR-PL spectrum of $WS_2$ and $MoS_2$ in the low and high excitation regime. The experimental data allow to unveil the cross-over between the FE and EHP emissions in both $WS_2$ and $MoS_2$ monolayers. In the low excitation regime, we investigated the exciton PL time dynamics in monolayer $WS_2$, accessing the exciton radiative lifetime, the rate of exciton trapping in defect states and the exciton-exciton annihilation rate. In the high excitation regime, we disentangled the FE and EHP emissions following the pulsed photo-excitation. The analysis of the EHP spectrum enables information about the band gap renormalization and the average kinetic energy of electrons and hole populating the renormalized valence and conduction bands.

Our novel experimental data allow to directly access, for the first time, the time evolution of the EHP PL emission by exfoliated $WS_2$ and $MoS_2$ monolayers (and bulk $MoS_2$), on the timescale of tens of picoseconds. This thesis constitutes a first step to perform a detailed study of the TR-PL light emission by TMD monolayers (few layers and bulk), especially at high excitation densities,

where excitons cease to dominate the light emission properties of these materials. The tight interval for the excitation density, between the formation of an EHL and the damaging of the sample, and the ultrafast time evolution of the EHP and EHL, calls for further experiments at even higher excitation densities, just below the damaging threshold, and with improved time resolution, down to the 1 ps time scale. I consider this study important since TMD monolayers seem the perfect candidates both for the study of the physics of intermediately-bound free excitons, including their phase transitions towards EHPs and EHLs at room temperature, and to gather important information about possible limitations and operating ranges of excitonic light-emitting devices.

# Introduction

Semiconducting two-dimensional transition metal dichalcogenides (TMDs), such as $MoS_2$ and $WS_2$, have attracted much scientific interest in the last two decades, due to their unique electronic and optical properties. Among these, strong light-matter interactions in the infrared to visible range and thickness-dependent properties leading to high exciton binding energy and to indirect-to-direct bandgap transition in the monolayer limit, resulting in a bright excitonic photoluminescence (PL) at room temperature. Reduced dimensionality and reduced screening of the Coulomb interactions result in a strong correlation of electrons and in a large exciton binding energy (0.3-0.8 eV). These properties make TMDs promising materials for potential applications in ultra-thin and ultra-light opto-electronic devices, such as LEDs and lasers based on the exciton emission.

However, excitons in TMDs are stable at room temperature and they dominate the light emission properties only at low or moderate excitation density. In the high excitation density regime, the strong electron-electron exchange and correlation terms lead to a huge band-gap renormalization at high carrier density, leading to the ionization of free excitons in an electron-hole plasma (EHP) and, at even higher density, in the generation of an electron-hole liquid (EHL), a quasi-incompressible fluid constituted by strongly correlated electrons and holes. This fact both poses limitations for exciton-based light emitting devices, and opens the possibility for new technological applications, such as broadband and ultra-bright lasers or LEDs.

EHPs and EHLs in TMD monolayers have been theoretically predicted and investigated by means of time resolved optical spectroscopy and steady state PL experiments. However, a study of the time resolved PL (TR-PL) spectrum of TMD monolayers after a pulsed excitation is still lacking, especially at high excitation density. This gave me the first strong motivation for the scientific work reported in this thesis.

Secondly, excitons in TMDs can't be treated as hydrogen-like systems (weakly bound excitons) or as bound electron-hole pair localized on single atoms or within a single unit cell (strongly bound excitons), as they exhibit an intermediate behaviour between these two extreme cases. This poses considerable computation difficulties for the theoretical calculations, and calls for new studies and experiments. The second motivation for the present work is the scientific interest for the study of these intermediately-bound excitons in 2D systems.

We decided to focus on exfoliated TMD monolayers thanks to their superior crystal quality and lower defect concentration, with respect to MBE or CVD grown ones. The ability to fabricate custom samples is fundamental, since it allows to obtain TMD flakes with different thicnkess, to choose the substrate, including the possibility to obtain free-standing monolayers (to remove the effects of the substrate on the photo-excited carriers), or monolayer encapsulated in hexagonal boron nitride (to protect them from athmospheric contamination), or even to build heterostructure where monolayers of different TMDs are stacked together.

In this thesis, we present novel TR-PL data for $WS_2$ and $MoS_2$ exfoliated monolayers, as a function of the excitation fluence, i.e. of the initial excitation density. We compare the measurements at low and high fluence to investigate the optical response of the system when either free excitons or the electron-hole plasma dominates, and to find the cross-over between these two regimes. The high PL quantum yield for $WS_2$ allows for an investigation of the TR-PL spectrum at very low fluences, whereas the high damaging threshold for $MoS_2$ enables a study at very high fluences. The different electronic structures, exciton binding energy and spin-orbit splitting, resulting in different spectral positions for exciton excited, make $WS_2$ and $MoS_2$ the perfect candidates to perform a 360 degree investigation. We report also original TR-PL data on bulk $MoS_2$ allowing to access important information on the indirect-band gap counterpart of the $MoS_2$ monolayer, where the enhanced Coulomb screening results in a reduction of the exciton binding energy with respect to the monolayer, yielding a dramatically different optical response with respect to the monolayer. The high damaging threshold for the bulk $MoS_2$, more than one order of magnitude above that for the monolayer, opens the possibility to study this system at very high initial excitation density, where phenomena like the band gap renormalization and the generation of electron-hole plasmas and electron-hole liquid are enhanced.

## Thesis overview

This thesis is organized in the following way:
In chapter 1, we provide the theoretical background, including the exciton theory, optical transitions in solids with and without the exciton effects, and a short review of photoluminescence.
In chapter 2, we discuss the main properties of the transition metal dichalchogenides (TMDs), such as their cystal structure and their electronic structure, including the role of defects in the electronic and optical properties. We review the properties of excitons in TMDs and we discuss the theoretical and experimental evidences of EHPs and EHLs in these materials.
In chapter 3, we provide a detailed description of the experimental methods, with particular emphasis on the TR-PL experimental setup. We present the TR-ARPES apparatus, the mechanical exfoliation technique and the transfer system for exfoliated flakes.
In chapter 4, we present the PL experimental data, providing a brief and qualitative preview of the main results.
In chapter 5, we report and analyze steady state and novel time resolved PL data for mechanically exfoliated monolayers of $WS_2$ and $MoS_2$ on $SiO_2$ substrate, and for bulk $MoS_2$.
In chapter 6, we report and analyze TR-ARPES experimental data for bulk $MoS_2$, allowing to access directly the ultrafast dynamics of the electronic and excitonic excited states, induced by a pulsed optical excitation.

# Chapter 1

# Introduction and theoretical background

In this chapter we provide a theoretical background to support all the scientific and experimental work performed in this thesis. In section 1.1 we introduce the optical properties in solids, considering only the contribution of the *free carriers*. In section 1.2 we give an introduction to the *excitons*, showing how the latter influence the optical properties in solids. In 1.3 we provide a review of the *photoluminescence* in semiconductors, describing the carrier recombination processes and showing which information can be accessed by the photoluminescence spectroscopy.

## 1.1 Optical properties in solids

In this section we summarize the optical properties of solids, in a very simplified approach where we consider a crystalline solid at T=0 K, in the adiabatic approximation (an electronic excitation happens on a much faster time scale, with respect of the atomic cores motion), semi-classical approximation (quantum mechanics for the matter, classical electromagnetic radiation fields), and the first order time dependent perturbation theory (we apply the Fermi Golden Rule).

In a crystal solid (periodic system), the energy levels of electrons can be represented as a function of their wave vector $\vec{k}$, in the so-called *band structure*, $E(\vec{k})$. At T=0 K, the highest energy band occupied by electrons is called *valence band* while the lowest unoccupied energy band is called *conduction band* [4]. In a semiconductor, these bands are well separated by an energy difference, called *band-gap*. If the maximum of the valence band and the minimum of the conduction band lie at the same value of $\vec{k}$, the band-gap is defined *direct band-gap*. Otherwise, it is defined *indirect band-gap*.

The absorption of light in solids, as well as stimulated emission are related to imaginary part of the dielectric function. This quantity is also related to all the possible transitions that can be observed in the photoluminescence spectra of solids (see section 1.3.2). The imaginary part of the dielectric function (see appendix 6.1 for its derivation) can be expressed as [6, 62]:

$$\varepsilon_2(\hbar\omega) = \frac{4\pi e^2}{\omega^2 m_e^2} \frac{2}{(2\pi)^3} \sum_{v,c} \int_{1ZB} d\vec{k} |\hat{\eta} \cdot M_{c,v}(\vec{k})|^2 \delta(E_c(\vec{k}) - E_v(\vec{k}) - \hbar\omega)) \tag{1.1}$$

where $m_e$ is the electron mass, $\omega$ and $e\hat{t}a$ are the angular frequency and the polarization of the electromagnetic field of radiation, respectively. $\vec{k}$ is the electron wave vector, $E_v(\vec{k})$ and $E_c(\vec{k})$ are the energy of the valence and conduction band calculated at $\vec{k}$, and $M_{c,v}(\vec{k})$ is the matrix element between an excited electronic state in conduction band with wave vector $\vec{k}$ and the electronic state in valence band at (almost) the same $\vec{k}$ (conservation of the wave vector). The delta accounts for the energy conservation in the optical transition, where the photon energy $\hbar\omega$ must be equal to the energy difference $E_c(\vec{k}) - E_v(\vec{k})$.

The matrix element $|\hat{\eta} \cdot M_{c,v}(\vec{k})|^2$ between a given couple of valence and conduction bands does not vary significantly with $\vec{k}$, except near special $\vec{k}_0$ vectors where it vanishes because of symmetry [6]. Neglecting these points, and taking $|\hat{\eta} \cdot M_{c,v}(\vec{k})|^2 \approx cost$, the $\varepsilon_2(\omega)$ becomes:

$$\varepsilon_2(\hbar\omega) = \frac{4\pi e^2}{\omega^2 m_e^2} |\hat{\eta} \cdot M_{c,v}|^2 \sum_{v,c} \underbrace{\int_{1ZB} \frac{2d\vec{k}}{(2\pi)^3} \delta(E_c(\vec{k}) - E_v(\vec{k}) - \hbar\omega))}_{J_{cv}(E=\hbar\omega)} \tag{1.2}$$

The imaginary part of the dielectric function is then proportional to $\omega^{-2}$ and to the quantity $J_{cv}(E = \hbar\omega)$, shown in equation 1.2. This quantity is called *joint density of states* (JDOS) and it gives the density of couples of states, one for a free electron in the conduction band and one for a free hole in the valence band, with an energy difference $E = \hbar\omega$.
By using the properties of the Dirac delta function, the JDOS can be written as

$$J_{cv}(E) = \frac{2}{(2\pi)^3} \int_{E_c(\vec{k})-E_v(\vec{k})=E} \frac{dS_{\vec{k}}}{|\vec{\nabla} E_c(\vec{k}) - \vec{\nabla} E_v(\vec{k})|} \tag{1.3}$$

where $dS_{\vec{k}}$ is the element of surface in the $\vec{k}$ space that verifies $E_c(\vec{k}) - E_v(\vec{k}) = E = \hbar\omega$. Equation 1.3 shows clearly that the $J_{cv}(E)$ is enhanced in the neighborhood of energy points such that:

$$\vec{\nabla} E_c(\vec{k}) = \vec{\nabla} E_v(\vec{k}) = \vec{0} \tag{1.4}$$

i.e. when the gradients (in $\vec{k}$) of the valence and conduction bands are both zero. More generally, the JDOS $J_{cv}(E)$ strongly increases when

$$\vec{\nabla} E_c(\vec{k}) - \vec{\nabla} E_v(\vec{k}) = 0 \tag{1.5}$$

i.e., when the conduction and valence bands are "parallel". The particular values of $E$ which verify 1.4 or 1.5 are called *critical points* or *singularities* in the joint density of states [6, 62]. We can find the analytic behaviour of $J_{cv}(E)$ near a singularity by expanding the energy difference $E_c(\vec{k}) - E_v(\vec{k})$ in Taylor series, around the critical point, up to the quadratic terms in $\vec{k} = (k_x, k_y, k_z)$:

$$E_c(\vec{k}) - E_v(\vec{k}) = E_0 + \frac{\hbar^2}{2} \left( \epsilon_x \frac{k_x^2}{m_x} + \epsilon_y \frac{k_y^2}{m_y} + \epsilon_z \frac{k_z^2}{m_z} \right) \tag{1.6}$$

where $m_x, m_y, m_z > 0$ are the *optical mass* ($\frac{1}{m_i} = \frac{1}{m_c^{(i)}} + \frac{1}{m_v^{(i)}}$, i=x,y,z. $m_c, m_v$ are the effective mass for the conduction and the valence band respectively), and where $\epsilon_x, \epsilon_y, \epsilon_z$ can be $\pm 1$.
In 3D we obtain four types of singularities, depending on the values of $\epsilon_x, \epsilon_y, \epsilon_z$:

1. $M_0$: all coefficients in the quadratic expansion are positive (minimum).
2. $M_1$ and $M_2$: two coefficients are negative and one is positive, or one coefficient is negative and two are positive (saddle point).
3. $M_3$: all coefficients are negative (maximum).

Figure 1.1 shows a schematic representation of the behaviour of the joint density of states around each type of critical points in 3D, where $A = \pi 2^{7/2} h^{-3} (m_x m_y m_z)^{1/2}$ and B is a constant which depends on the particular band structure of the material [6].
As an example, this scheme shows that at $E = E_g$ (the band gap, the absolute minimum for the energy difference $E_c(\vec{k}) - E_v(\vec{k})$), there is no absorption for $E < E_g$ and the absorption goes as $\sqrt{E - Eg}$ for $E \geq E_g$.
When going far from the critical points the term $O(E - E_0)$ becomes more relevant, and the behaviour of the JDOS deviates from that around the critical point. However, $O(E - E_0)$ vanish at least linearly as $E \to E_0$ [6].
When $|\hat{\eta} \cdot M_{c,v}(\vec{k})|^2$ vanishes (forbidden transitions) at specific $\vec{k}_0$ points, this matrix element around this point is proportional to $\vec{k} - \vec{k}_0$. The integral in equation 1.2 can be calculated explicitly, allowing to find a $\varepsilon_2(E = \hbar\omega)$ proportional to $(E - E_0)^{3/2}$ (instead of $(E - E_0)^{1/2}$) at the

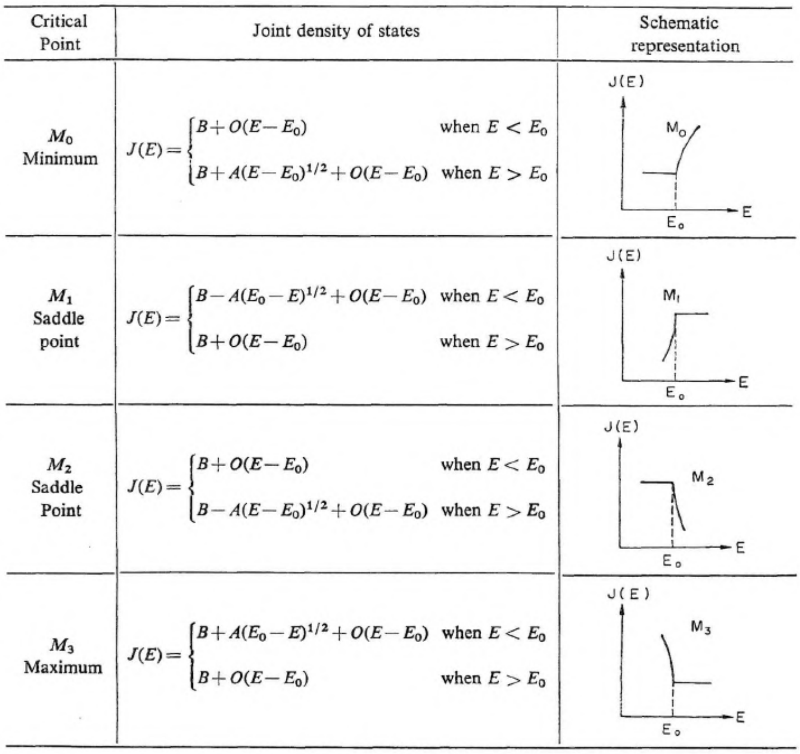

| Critical Point | Joint density of states | Schematic representation |
|---|---|---|
| $M_0$<br>Minimum | $J(E)=\begin{cases} B+O(E-E_0) & \text{when } E<E_0 \\ B+A(E-E_0)^{1/2}+O(E-E_0) & \text{when } E>E_0 \end{cases}$ | |
| $M_1$<br>Saddle point | $J(E)=\begin{cases} B-A(E_0-E)^{1/2}+O(E-E_0) & \text{when } E<E_0 \\ B+O(E-E_0) & \text{when } E>E_0 \end{cases}$ | |
| $M_2$<br>Saddle Point | $J(E)=\begin{cases} B+O(E-E_0) & \text{when } E<E_0 \\ B-A(E-E_0)^{1/2}+O(E-E_0) & \text{when } E>E_0 \end{cases}$ | |
| $M_3$<br>Maximum | $J(E)=\begin{cases} B+A(E_0-E)^{1/2}+O(E-E_0) & \text{when } E<E_0 \\ B+O(E-E_0) & \text{when } E>E_0 \end{cases}$ | |

**Figure 1.1:** *Scheme of the critical points for the JDOS in 3D. Type of critical points for the JDOS, with their analytic expressions and a schematic representation around the critical energy* $E_0$. *Figure from [6]*

absorption edge [6].
In 2D we have three types of singularities: this case is particularly interesting in this thesis, where we investigate the optical propeties of monolayers of materials like $MoS_2$ and $WS_2$. Figure 1.2 shows a schematic representation of the behaviour of the joint density of states around each type of singular points in 2D, where $A = \frac{8\pi}{c}h^{-2}(m_x m_y)^{1/2}$ and B is a constant which depends on the particular band structure of the material [6].
At $E = E_g$, the JDOS is a heavyside theta, implying that there is no absorption for $E < E_g$ and that absorption goes as a constant for $E \geq E_g$.

Weaker second order optical transitions can be observed in solids, involving for example the simultaneous absorption of two photons or the simultaneous absorption of a photon and absorption/emission of a phonon [6, 62] (see appendix 6.2).

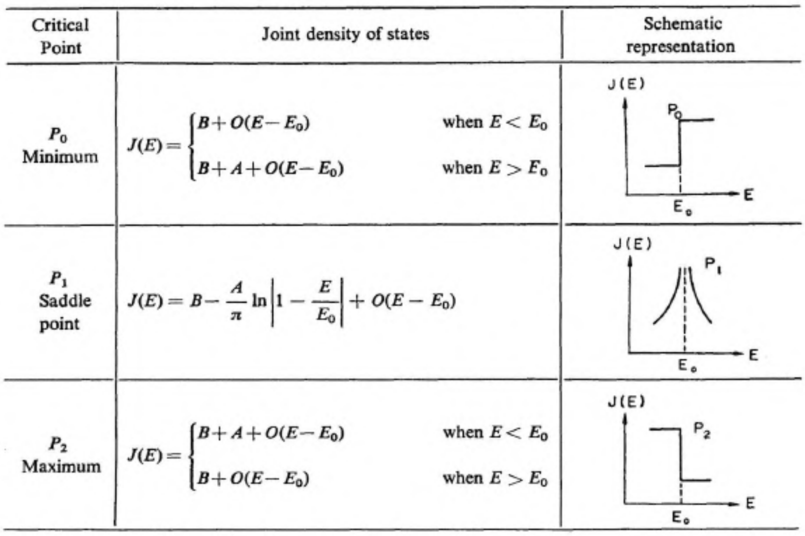

| Critical Point | Joint density of states | Schematic representation |
|---|---|---|
| $P_0$ Minimum | $J(E)=\begin{cases} B+O(E-E_0) & \text{when } E<E_0 \\ B+A+O(E-E_0) & \text{when } E>E_0 \end{cases}$ | |
| $P_1$ Saddle point | $J(E)=B-\frac{A}{\pi}\ln\left\lvert 1-\frac{E}{E_0}\right\rvert+O(E-E_0)$ | |
| $P_2$ Maximum | $J(E)=\begin{cases} B+A+O(E-E_0) & \text{when } E<E_0 \\ B+O(E-E_0) & \text{when } E>E_0 \end{cases}$ | |

**Figure 1.2:** *Scheme of the critical points for the JDOS in 2D. Type of critical points for the JDOS, with their analytic expressions and a schematic representation around the critical energy* $E_0$. *Figure from [6].*

## 1.2 Excitons in solids

The absorption of light in crystals happens for photon energies above the band gap, with a continuous absorption spectrum. However, experimentally it is possible to observe absorption peaks also below the energy band gap. In section 1.1 we discussed the absorption of light in solids considering single inter-band transitions for electrons and neglecting the Coulomb interaction between the extra electron in the conduction band and the extra hole in the valence band. This interaction is responsible for the creation of excited states in crystals, where an electron and a hole are bound together to create a quasi-particle called *exciton*. The energy $E_{EX}$ required to create an exciton in its ground state is lower than the energy band gap $E_g$, which is the energy required to create a free electron-hole pair with the minimum available energy difference. When dealing with electrons in crystals, there are two extreme approximations: the tight binding and the nearly free electron approximation. In tight binding, the electron is localized on a given atom, and the other atoms constitute only a small perturbation. In the nearly free electron approximation, the electron is delocalized in the whole crystal, moving in a weak potential. We can consider a similar approach to study excitons in crystals, giving the two extreme cases of *tightly bound excitons* and *weakly bound excitons* [6]. However, in many real cases, the situation is intermediate between these two extreme approximations. In the following sections we introduce the tight binding and weak binding excitons in solids, showing which is their contribution to the optical properties [6].

### 1.2.1 Tight binding excitons

Tight binding excitons occurs in molecular crystals or in large gap insulators [6]. In these systems, the electrons are localized on given atoms (or molecules), and it is convenient to express the Bloch functions in term of the *Wannier atomic functions* [6]:

$$\psi_{n,\vec{k}}(\vec{r}) = \frac{1}{\sqrt{N}} \sum_{\vec{\tau}_\nu} e^{i\vec{k}\cdot\vec{\tau}_\nu} a_n(\vec{r}-\vec{\tau}_\nu) \tag{1.7}$$

where $\vec{\tau}_\nu$ are vectors of the Bravais lattice.
The electronic ground state $\Psi_0$ can be written as a Slater determinant of the Wannier functions. As a trial excited state we can consider a Slater determinant where the valence band Wannier function $a_{v,\vec{\tau}_h,s_h}(\vec{r})$ is replaced by the conduction band Wannier function $a_{c,\vec{\tau}_e,s_e}(\vec{r})$, where "e" and "h" are used for electron and hole, respectively, and where $s_e = \pm 1/2$ and $s_h = \pm 1/2$ are

the eigenvalues of the spin projections along the quantization axis [6]. Since we considered a spin-independent Hamiltonian, and since these Slater determinants are eigenfunctions of the total spin in the direction of the quantization axis, with eigenvalue $\hbar(s_e - s_h)$, it is convenient to consider linear combinations of Slater determinants, to obtain eigenfunctions with defined spin multeplicity $M = 0, 1$.

A generic exciton state in tight binding can be written as

$$\Psi^{(M)}_{\vec{k}_{EX}} = \sum_{\vec{\tau}_\beta} F(\vec{\tau}_\beta) \frac{1}{\sqrt{N}} \sum_{\vec{\tau}_n} e^{i\vec{k}_{EX}\cdot\vec{\tau}_n} \Phi^{(M)}_{c\vec{\tau}_n, v\vec{\tau}_n+\vec{\tau}_\beta} \tag{1.8}$$

where $\Phi^{(M)}_{c\vec{\tau}_n, v\vec{\tau}_n+\vec{\tau}_\beta}$ is a linear combination of Slater determinants where an electron in the ground state in the unit cell $\vec{\tau}_n + \vec{\tau}_\beta$ is replaced by an electron in an excited state (conduction band) in the unit cell $\vec{\tau}_n$. M indicates the total spin multeplicity, and it can be $M = 0$ (singlet excitons) or $M = 1$ (triplet excitons). The coefficient of the expansion $F(\vec{\tau}_\beta)$ is related to the probability to find the electron and the hole in two different unit cells with distance $\vec{\tau}_\beta$. In the limit of strongly localized excitons we can write $F(\vec{\tau}_\beta) \approx \delta_{\vec{\tau}_\beta,\vec{0}}$: the electron in conduction band and the hole in the valence band belongs to the same unit cell, and equation 1.8 simpifies to:

$$\Psi^{(M)}_{\vec{k}_{EX}} = \frac{1}{\sqrt{N}} \sum_{\vec{\tau}_n} e^{i\vec{k}_{EX}\cdot\vec{\tau}_n} \Phi^{(M)}_{c\vec{\tau}_n, v\vec{\tau}_n} \tag{1.9}$$

The energy of this exciton state is given by

$$\begin{aligned} E^{(M)}(\vec{k}_{EX}) =< \Psi^{(M)}_{\vec{k}_{EX}}|H_0|\Psi^{(M)}_{\vec{k}_{EX}} > &=< \Psi_0|H_0|\Psi_0 > + < a_{c\vec{\tau}_n}|H_0|a_{c\vec{\tau}_n} > \\ &- < a_{v\vec{\tau}_n}|H_0|a_{v\vec{\tau}_n} > + \delta E_{C,X} \end{aligned} \tag{1.10}$$

It is equal to the sum of the ground state energy and the atomic excitation energy (second and third terms), plus a term $\delta E_{C,X}$ which includes the Coulomb and exchange energy between the electron constituting the exciton and electrons in different atoms, the Coulomb and exchange interactions between the electron and the hole constituting the exciton, and energy related to the probability to transfer the exciton on a nearby unit cell [6].

When an electromagnetic field is applied, the probability of transition per unit time, from the ground state $\Psi_0$ to the state where one exciton is created, $\Psi^{(M)}_{\vec{k}_{EX}}$, is given by:

$$\pi_{\Psi_0 \to \Psi^{(M)}_{\vec{k}_{EX}}} = \frac{2\pi}{\hbar} \left( \frac{eA_0}{m_e c} \right)^2 \delta \vec{k}_{EX} \delta_M |\hat{\eta} \cdot < a_c|\vec{p}|a_v > |^2 \delta(E^{(M)}_{EX} - E_0 - \hbar\omega) \tag{1.11}$$

This equation includes the conservation of the total energy, spin and momentum. The electromagnetic field of radiation induces the creation of singlet excitons (M=0), with energy $E^{(M)}_{EX} = E_0 + \hbar\omega$ and with a momentum $\vec{k}_{EX} = \vec{q} = \frac{2\pi}{\lambda}\hat{q} \approx \vec{0}$.

### 1.2.2 Weak binding excitons

Weak binding excitons occur in small gap semiconductors, where a high dielectric constant screens the Coulomb interaction between the electron and the hole constituting the exciton. In the weak binding approximation, it is convenient to use the Bloch representation for the wave function of electrons. As a trial excited state we can consider a Slater determinant $\Phi_{c\vec{k}_e s_e, v\vec{k}_h s_h}$ where the valence band Bloch function $\psi_{v,\vec{k}_h,s_h}(\vec{r})$ is replaced by the conduction band Bloch function $\psi_{c,\vec{k}_e,s_e}(\vec{r})$, where $\vec{k}_e - \vec{k}_h = \vec{k}_{EX}$ [6].

Since we considered a spin-independent Hamiltonian, and since these Slater determinants are eigenfunctions of the total spin in the direction of the quantization axis, with eigenvalue $\hbar(s_e - s_h)$, it is convenient to consider linear combinations of Slater determinants, to obtain eigenfunctions with defined spin multeplicity $M = 0, 1$.

Finally the wave function for the exciton state can be written as

$$\Psi^{(M)}_{\vec{k}_{EX}} = \sum_{\vec{k}} A(\vec{k}) \Phi^{(M)}_{c\vec{k}+\frac{1}{2}\vec{k}_{EX}, v\vec{k}-\frac{1}{2}\vec{k}_{EX}} \tag{1.12}$$

where $\Phi^{(M)}_{c\vec{k}+\frac{1}{2}\vec{k}_{EX},v\vec{k}-\frac{1}{2}\vec{k}_{EX}}$ is a linear combination of Slater determinants where the Bloch function of an electron in the valence band with wave vector $\vec{k}-\frac{1}{2}\vec{k}_{EX}$ is replaced by the wave function of an electron in the conduction band, with wave vector $\vec{k}+\frac{1}{2}\vec{k}_{EX}$, and where M is the total spin multeplicity [6]. $A(\vec{k})$ are the Fourier coefficients of the expansion of the wave function of the exciton state, on the set of Slater determinants with different wavevectors and defined spin multeplicity M.

In the weak binding limit, the function $A(\vec{k})$ is peaked in the $\vec{k}$ space and its Fourier transform, the *envelope function*

$$F(\vec{r}) = \sum_{\vec{k}} A(\vec{k}) e^{i\vec{k}\cdot\vec{r}} \tag{1.13}$$

is very extended in the real space. In the limit $\vec{k}_{EX} \to \vec{0}$, the total exciton wave function can be written as the product of the envelope function $F(\vec{r})$, which describes the relative motion of the electron and the hole, and two Bloch functions of the valence and conduction band [6].

In this approximation, considering the static dielectric constant $\varepsilon$ (the envelope function extends on a large number of units cell, hence we can consider an uniform dielectric environment between the electron and the hole), neglecting the short range electron-hole exchange interactions [6], and considering the effective mass approximation around a critical point $\vec{k}_0$ for the energy difference $E_c(\vec{k}+\frac{1}{2}\vec{k}_{EX}) - E_v(\vec{k}-\frac{1}{2}\vec{k}_{EX})$, it can be shown that $F(\vec{r})$ in equation 1.13 satisfies the *effective mass equation*:

$$\left[-\frac{\hbar^2}{2\mu_x}\frac{\partial^2}{\partial x^2} - \frac{\hbar^2}{2\mu_y}\frac{\partial^2}{\partial y^2} - \frac{\hbar^2}{2\mu_z}\frac{\partial^2}{\partial z^2} + \frac{e^2}{\varepsilon r}\right] F(\vec{r}) = (E_{EX} - E_g) F(\vec{r}) \tag{1.14}$$

where $\mu_x, \mu_y, \mu_z$ are the reduced effective mass (optical mass) in the directions x,y,z.

If we consider an isotropic crystal, where $\mu_x = \mu_y = \mu_z \equiv \mu$, equation 1.14 reduces to the Schrodinger equation for an hydrogen-like system,

$$\left[-\frac{\hbar^2}{2\mu}\nabla^2 + \frac{e^2}{\varepsilon r}\right] F(\vec{r}) = (E_{EX} - E_g) F(\vec{r}) \tag{1.15}$$

which solutions are the hydrogen-like wave functions $F_{nlm}(\vec{r})$, with energy eigenvalues

$$E^{(n)}_{EX} = E_g - \frac{Ry^*}{n^2} = E_g - \frac{\mu e^4}{2\hbar^2\varepsilon^2}\frac{1}{n^2} \quad ; \quad n = 1, 2, ... \tag{1.16}$$

where the $Ry^*$ it the *effective Rydberg*, i.e. the binding energy for an hydrogen-like system in its ground state. This is related to the *Rydberg* of the hydrogen atom ($Ry$) by the following expression:

$$Ry^* = \frac{\mu}{m_e}\frac{1}{\varepsilon_R^2} Ry \tag{1.17}$$

We define the *exciton binding energy* $E_b$ as the energy required to ionize an exciton in its ground state. This is given by the energy difference between the energy gap $E_g$ and the exciton energy in its ground state, i.e. $E_b = E^{(1)}_{EX} = Ry^*$. As an example, in GaAs, the static dielectric constant is $\varepsilon_R$=12.4, and the reduce mass is $\mu$=0.056 $m_e$ [31] (electrons-heavy holes, for example), resulting in an exciton binding energy $Ry^* \approx 5$ meV.

If we consider the case of an anysotropic crystal along one direction (say z), the reduced mass and the dielectric constant may be different in the parallel direction ($x, y$ plane) and in the orthogonal direction (z). We can denote them by $\mu_{//}, \mu_{\perp}, \varepsilon_{//}, \varepsilon_{\perp}$, and define the *anisotropy parameter* [6]:

$$\gamma = \frac{\varepsilon_{\perp}}{\varepsilon_{//}}\frac{\mu_{\perp}}{\mu_{//}} \tag{1.18}$$

When $\gamma = 1$, we recover the case of an isotropic system which solutions are the 3D hydrogen-like wave functions. When $\gamma = 0$, we are in the 2D limit, which can be analitically solved, giving (2D) hydrogen-like bound states with energy

$$E^{(n)}_{EX} = E_g - \frac{Ry^*}{(n+\frac{1}{2})^2}; n = 0, 1, 2, ... \tag{1.19}$$

For an exciton in 2D, the binding energy is $4Ry^*$, four time higher than in 3D.

### Center of mass motion and relative motion of the electron and the hole

It is useful to give an intuitive and quick picture for weakly bound hydrogen-like excitons.
For these excitons, the motion can be decomposed in the motion of the center of mass and the relative motion of the electron and the hole. The center of mass moves like a free particle of mass $M = m_c + m_v$ and wave vector $\vec{k}_{EX} = \vec{k}_e - \vec{k}_h$. The kinetic energy is given by $E_{kin} = \frac{\hbar^2 k_{EX}^2}{2M}$. The relative motion determines the internal energy of the system, and it is given by the motion of a particle of mass $\mu = (\frac{1}{m_c} + \frac{1}{m_v})^{-1}$ in a central field generated by the Coulomb attraction between the electron and the hole, screened by the dielectric constant $\varepsilon$. Similarly to the hydrogen atom, an exciton is characterized by an infinite number of bound states, and a continuum of states corresponding to the ionized exciton.
Hydrogen-like excitons can be depicted in a two particle diagram, where the total energy of the exciton is represented versus the total wave vector of the exciton $\vec{k}_{EX}$.

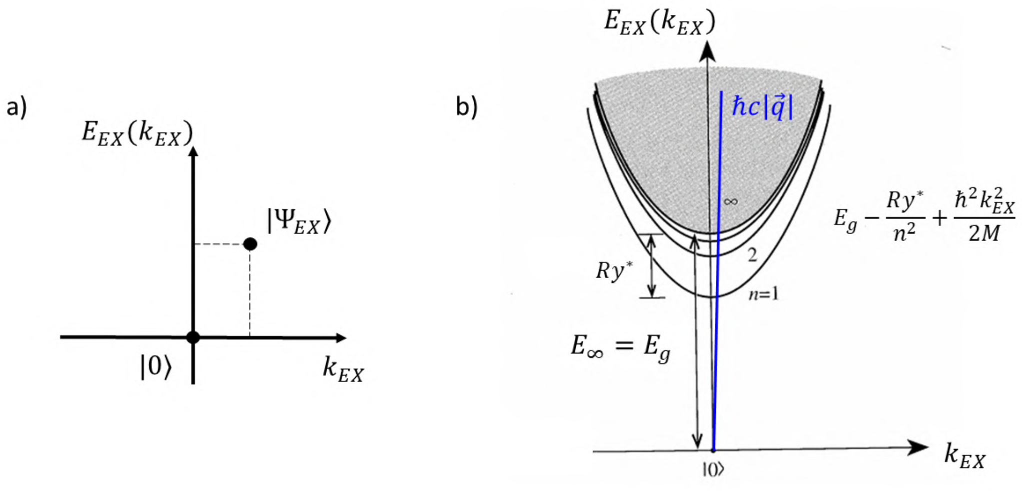

**Figure 1.3:** *a) Representation of the ground state of the crystal and the state with one exciton, in a two particle picture. Here $\vec{k}_{EX} = \vec{k}_e - \vec{k}_h$ is the total wave vector of the exciton and $E_{EX}(k_{EX})$ is the total energy, given by the sum of the kinetic energy ($E_{kin}$) and the internal energy ( $E_{EX}^{(n)}$ ) contributions. b) Energy dispersion for an exciton ($k_{EX} = |\vec{k}_e - \vec{k}_h|$), given by a bundle of discrete parables for the bound states, and a continuum for the ionized states. The energy dispersion of a photon is drawn in the same graph, showing that only excitons with a small kinetic energy can be resonantly created by an optical excitation.*

The origin of the diagram corresponds to the ground state, without excitons. All the possible excited states are represented by the graphs of the functions describing the exciton total energy:

$$E_{EX}(\vec{k}_{EX}) = E_{kin}(\vec{k}_{EX}) + E_{EX}^{(n)} = \frac{\hbar^2 k_{EX}^2}{2M} + E_g - \frac{Ry^*}{n^2} \qquad , \qquad n = 1, 2, ... \tag{1.20}$$

This expression corresponds to a bundle of infinite parables, with vertex in the point $(\vec{0}, E_g - \frac{Ry^*}{n^2})$. The exciton ground state is represented by the lowest parable with n=1. An exciton can be created from the ground state, by providing simultaneously a momentum $\vec{k}_{EX}$ and an energy $E_{EX}(\vec{k}_{EX})$. In an optical excitation, this condition can be achieved within the *light cone*, i.e. at the intersection between the photon dispersion $E(q) = \hbar c|\vec{q}|$ and one of the parables described by equation 1.20.
This implies that only excitons with $\vec{k}_{EX} \approx \vec{0}$ can be created due to the absorption of a photon. Similarly, only excitons with $\vec{k}_{EX} \approx \vec{0}$ can decay radiatively by emitting photons. However, since excitons are the excited states with lowest energy in crystals, the creation of an exciton can follow the scattering and relaxation of photo-excited free carriers.

Since excitons are bosons, the occupation number of thermalized excitons can be described by the Bose-Einstein distribution:

$$n(\mu, T) = \frac{1}{e^{\frac{E-\mu}{k_B T}} - 1} \tag{1.21}$$

**Optical properties with exciton effects in a two band model semiconductor, in the weak binding approximation**

For interband transitions of free carriers, considering only a couple of valance and conduction bands, around a critical point of the $M_0$ type, and at $\vec{k} = \vec{0}$, the imaginary part of the dielectric function, $\varepsilon_{2F}$ is given by equation 6.11 [6]. For first class transitions, we can set $\hat{\eta} \cdot M_{cv}(\vec{k}) = \hat{\eta} \cdot M_{cv}(\vec{0}) = cost$, and integrate over the first Brillouin zone. We obtain

$$\begin{aligned} &\varepsilon_{2F}(\hbar\omega) = 0 && \text{for } \hbar\omega < E_g \qquad (1.22) \\ &\varepsilon_{2F}(\hbar\omega) = \frac{4\pi^2 e^2}{m_e^2 \omega^2} |\hat{\eta} \cdot M_{cv}(\vec{0})|^2 \frac{1}{2\pi} \left( \frac{2\mu}{\hbar^2} \right)^2 (\hbar\omega - E_g)^{1/2} && \text{for } \hbar\omega > E_g \end{aligned}$$

Without exciton effects, there is no absorption below the band gap $E_g$, while the absorption above $E_g$ is proportional to $\frac{1}{\omega^2}(\hbar\omega - E_g)^{1/2}$.
By including exciton effects (in the weak binding approximation), it is possible to show [6] that the transition rate of equation 6.8, i.e.

$$\pi_{|v,\vec{k}>\to|c,\vec{k}'>} = \frac{2\pi}{\hbar} \left( \frac{|e|A_0}{m_e c} \right)^2 |\hat{\eta} \cdot M_{cv}(\vec{k})|^2 \delta(E_c(\vec{k}') - E_v(\vec{k}) - \hbar\omega)$$

becomes:

$$\pi_{\Psi_0 \to \Psi^{(M)}_{\vec{k}_{EX}}} = \frac{2\pi}{\hbar} \left( \frac{|e|A_0}{m_e c} \right)^2 \left| \sum_{\vec{k}} A(\vec{k}) \hat{\eta} \cdot M_{cv}(\vec{k}) \right|^2 \delta(E_{EX} - E_0 - \hbar\omega) \tag{1.23}$$

where $A(\vec{k})$ is the (anti) Fourier Transform of the envelope function. For first class optical transitions, where the matrix element can be considered constant around the critical point we can set $M_{cv}(\vec{k}) = M_{cv}(\vec{0})\ \forall \vec{k}$. By using the definition of the envelope function, we get $F(\vec{0}) \equiv \sum_{\vec{k}} A(\vec{k})$. Hence, finally we obtain:

$$\pi_{\Psi_0 \to \Psi^{(M)}_{\vec{k}_{EX}}} = \frac{2\pi}{\hbar} \left( \frac{|e|A_0}{m_e c} \right)^2 |\hat{\eta} \cdot M_{cv}(\vec{0})|^2 |F(\vec{0})|^2 \delta(E_{EX} - E_0 - \hbar\omega) \tag{1.24}$$

where there is the "extra term" involving the envelope function, and where the energy Dirac delta connects the ground state energy with the energy of a state with one exciton. This differences enable the absorption below the bandgap, at energies $E_g - \frac{Ry^*}{n^2}$, only for s states of the exciton, and with an intensity of the absorption lines which decrease as $1/n^3$ (resulting in a finite absorption coefficient at $E = \hbar\omega \approx E_g$).
Above the band gap, the imaginary part of the dielectric function becomes is modified by a factor

$$|F_{s00}(\vec{0})|^2 = \frac{\pi x e^{\pi x}}{sin_h(\pi x)} \qquad , \qquad x = \left[ \frac{Ry^*}{\hbar\omega - E_g} \right]^{1/2} \tag{1.25}$$

The imaginary part of the dielectric function, with exciton effects, results:

$$\varepsilon_2(\hbar\omega) = \varepsilon_{2F}(\hbar\omega) \frac{\pi x e^{\pi x}}{sin_h(\pi x)} \tag{1.26}$$

It is interesting to study this expression in the limits for $x << 1$ and $x >> 1$. We get:

$$\begin{aligned} &\varepsilon_2(\omega) \approx \varepsilon_{2F} \qquad \text{if } x << 1 \iff \hbar\omega - E_g >> Ry^* \qquad (1.27) \\ &\varepsilon_2(\hbar\omega) = \varepsilon_{2F} 2\pi x \propto \frac{1}{\omega^2}(Ry^*)^{1/2} \qquad \text{if } x >> 1 \iff \hbar\omega - E_g << Ry^* \end{aligned}$$

Figure 1.4 a) shows the absorption coefficient in 3D, including exciton effects. Below the bandgap, absorption happens for $\hbar\omega = E_g - \frac{Ry^*}{n^2}$ with the intensity of the absorption line decreasing as $1/n^3$, and with a constant finite value in the limit $lim_{n\to+\infty}$. The absorption coefficient above bandgap is given by equation 1.26. The absorption coefficient for free carriers (dashed line), proportional to $\sqrt{\hbar\omega - E_g}$ is also shown.

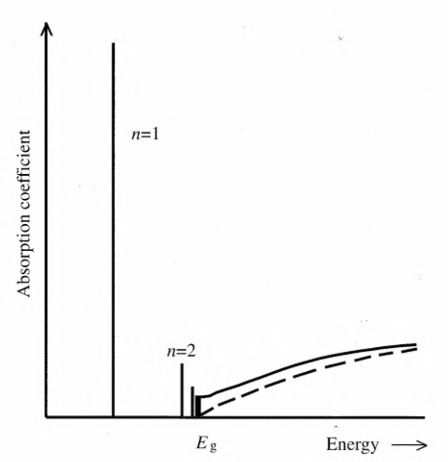

**Figure 1.4:** *a) Dashed line: absorption coefficient of a 3D solid, in the two band model, without exciton effects. There is no absorption for $E < E_g$, while the absorption cofficient is proportional to $\sqrt{E - E_g}$ above the band gap. Continous lines: absorption coefficient with exciton effects, showing infinite discrete lines for $E < E_g$, with intensity decreasing as $1/n^3$. Above bandgap, the absorption coefficient is nearly constant for $E \approx E_g$, and nearly proportional to $\sqrt{E - E_g}$ for $E >> E_g$. Figure from [86]*

### 1.2.3 Intermediately bound excitons

In the previous subsections, we introduced the case of tight binding and weak binding excitons. However, in many real systems, the excitons don't belong to these two extreme cases. For example, the lowest exciton states in semiconductors and excitons in insulators exhibit an intermediate behavior. In this case, the wave function of an exciton can be always written as in equation 1.12, but in this case, the coefficient function $A(\vec{k})$ is not strongly peaked in the $\vec{k}$ space, which means that we should consider all the expansion over $\vec{k}$, and we can't describe the exciton state by using the envelope function. In other words, the Fourier transform of the function $A(\vec{k})$, i.e. the envelope function is not very extended in the real space, implying that the use of the static dielectric constant, to evaluate the effect of the screening between the electron and the hole, is no longer a good approximation.

### 1.2.4 Indirect excitons transitions

At $T \neq 0K$ we should take into account the interaction between the excitons and the lattice oscillations. This interaction gives rise to a spatially modulated dielectric function, to a broadening of the exciton emission line, and it enables optical transitions where an *indirect exciton*, i.e. an exciton with $\vec{k}_{EX} \neq \vec{0}$, can be created by the simultaneous absorption of a photon and absorption/emission of a phonon [6].

To introduce the indirect exciton transitions we can consider the weak binding approximation and a two-band model, where the valence band maximum and the conduction band minimum are located in different $\vec{k}$ points in the first Brillouin zone. Let's consider a situation where the maximum of the valence band is located ad $\vec{k} = \vec{0}$, while the conduction band minimum is located at $\vec{k} = \vec{q}_0$. By expanding the energy bands arount their maximum/minimum, at the second order, we obtain:

$$E_c(\vec{k}_e) = E_g + \frac{\hbar^2}{2m_c}(\vec{k}_e - \vec{q}_0)^2 \tag{1.28}$$

$$E_v(\vec{k}_h) = -\frac{\hbar^2}{2m_v^*}k_h^2$$

The effective mass equation, 1.15 becomes

$$\left[\frac{\hbar^2}{2\mu} - \frac{e^2}{\varepsilon r}\right] F(\vec{r}) = (E_{EX} - E_g - \frac{\hbar^2}{2M}\left(\vec{k}_{EX} - \vec{q}_0)^2\right) F(\vec{r}) \tag{1.29}$$

We obtain again an hydrogen-like Schrodinger equation, which energy eigenvalues are dependent on the wavevector of the conduction band minimum $\vec{q}_0$ and on the parameter $\vec{k}_{EX}$:

$$E_{EX}(\vec{k}_{EX}) = E_g - \frac{Ry^*}{n^2} + \frac{\hbar^2}{2M}(\vec{k}_{EX} - \vec{q}_0)^2 \tag{1.30}$$

For $\vec{k}_{EX} = \vec{q}_0$ the exciton energy is given by the energies eigenvalues for an hydrogen-like system. When $\vec{k}_{EX} \neq \vec{q}_0$, the exciton energy can be obtained by adding the kinetic energy $\frac{\hbar^2}{2M}(\vec{k}_{EX} - \vec{q}_0)^2$ to the hydrogen-like energy eigenvalues.

It is possible to create an indirect exciton, with a second order transition with a photon and a phonon. The conservation of energy and momentum, in a transition where a photon and a phonon are absorbed to create an indirect exciton, with energy $E_{EX}$ and momentum $\vec{k}_{EX} = \vec{q}_0$ can be written as:

$$E_{EX}(\vec{k}_{EX}) = E_0 + \hbar\omega + \hbar\Omega \tag{1.31}$$

$$\vec{k}_{EX} = \vec{q}_0 \approx \vec{q}_p$$

where $\hbar\omega$ is the energy of the photon, $\hbar\Omega$ is the energy of the phonon, and $\vec{q}_p$ is the wavevector of the phonon.

## 1.3 A brief review of photoluminescence

*Luminescence* is the spontaneous emission of light by a system (atoms, molecules, solids, etc) in an excited electronic state. Unlike absorption and stimulated emission, spontaneous emission occurs without the intervention of an electromagnetic field of radiation. To formulate the theory of the spontaneous emission it is necessary to abandon the semiclassical approximation and to quantize also the electromagnetic field (in addition to the matter), writing the vector potential in terms of creation and destruction operators. The quantized electromagnetic field has a ground state, which is called *vacuum state* or *zero photon state*. The interaction between this state and an excited electronic state (for example the $2p$ state of the hydrogen atom) can lead to the de-excitation of the latter towards the ground state (example $1s$ state of the hydrogen atom) with the creation of a photon. Since the process is not stimulated by an electromagnetic field of radiation, the time scale for spontaneous emission or luminescence (100 fs to s) is much higher than the time scale rate of absorption or stimulated emission (even for low intensities of the electromagnetic field of radiation) being the latter proportional to the incident photon flux. On the other hand, the selection rules (for the permitted optical transitions) for absorption and stimulated emission remain valid also for spontaneous emission [23]. If the excitation of the system is due to the absorption of light, the spontaneous emission of light is called *photoluminescence* (PL).

Luminescence can be divided into two categories, *fluorescence* and *phosphorescence*, depending on the nature of the excited states. Fluorescence is the spontaneous emission of light from *singlet excited states*, in which the electron in the excited orbital and the electron in the ground state orbital have opposite spin. In this case, the radiative decay of excited electrons occurs on the nanosecond time scale. On the other hand, phosphorescence is the emission of light from *triplet excited states*, in which the electron in the excited orbital has the same spin projection as the electron in the ground state orbital. In this case, the transitions towards the ground state are prohibited (it requires a spin flip), and the emission rate is slow (from $10^3$ to $10^{-1}$ photons per second), i.e. the lifetime of the excited states ranges from milliseconds to a few tens of seconds. Usually phosphorescence is not seen at room temperature, because there may be other faster de-excitation processes (non-radiative recombinations) competing with the spontaneous emission of light.

In solids, the electron wavevector conservation plays a crucial role in optical transitions. In direct band gap semiconductors, photoluminescence occurs with first order optical transitions (in time dependent perturbation theory), yielding a high radiative recombination rate. In indirect band gap semiconductors photoluminescence is due to second order optical transitions, for example with a phonon and a photon, resulting in a low radiative recombination rate.

### 1.3.1 Photoluminescence spectroscopy

PL from materials can be measured by means of *photoluminescence spectroscopy*. In this approach, the sample is *photo-excited* by a light source and the PL light is collected and revealed by a light detector. The most commonly used excitation source in a PL experiment is a laser, which is powerful, collimated, coherent, and quasi monochromatic. The excitation laser can be in continuous wave (CW) or pulsed, resulting in two different kind of excitations of the material. The CW laser emits light continuously, as a sinusoidal and quasi monochromatic electromagnetic wave, the material is continuously excited, with a constant generation term for excited electrons, as electrons in the excited states relax towards the ground state. The system reachs a dynamic equilibrium between photo-excitation and relaxation, where the *excitation density*, i.e. the number of excited electron-hole pairs per unit volume, remains almost constant in time.

A pulsed laser emits light pulses with time duration $\tau_P$ and a repetition rate $\nu_{REP}$. In this case the sample is excited by the light pulse which constitute a generation term which lasts for a short time: when the laser pulse fades, the generation term is set to zero, and the system relaxes towards the ground state, until the subsequent light pulse comes to re-excite the sample. After a pulsed excitation, the PL light is emitted as the system relaxes towards its ground state, while the density of the excited electron-hole pairs decreases in time.

In the simplest PL experiment, we can excite the sample with a laser, collect the PL light with a lens and focus it on a photo-diode, to measure the intensity. However, in PL spectroscopy we are usually interested in the photon energy distribution of the PL light. This information give access to the energy of the electronic excited states with respect to the electronic states of the system in the ground state. The simplest approach to measure the spectrum of the PL light is the use of a monochromator and a photodiode. The latter records the PL intensity while scanning the wavelength with the monochromator. Another possibility is to use an interferometer (see chapter 3).

Beside the spectral information, it is possible to measure the time dynamics of the PL light, in a *time-resolved photoluminescence* experiment. In this experiment, a pulsed laser is used to excite the sample, while a single photon avalanche diode and a fast acquisition board are used together to achieve the time resolution, in the so-called *time correlated single photon counting* approach (see chapter 3).

Moreover, it is possible to perform two kind of spatially resolved PL experiments:

1. PL spatial profile: the PL spectrum (or simply the integrated PL intensity) is measured as a function of the position on the sample with respect to the (center) position of the excitation laser, which is kept fixed.

2. PL imaging: the integrated PL intensity by all the emitting area is measured, as the position of the excitation source is moved along the surface of the sample.

Spatially resolved photoluminescence allows to get information about the diffusion length of the photo-excited carriers, the spatial structure of the sample and its homogeneity.

### 1.3.2 Photoluminescence in semiconductors

The electronic properties of a semiconductor are fully characterized by its band structure. At T=0 K, the valence band of the semiconductor is full, while the conduction band is empty: there are no free electrons and the material is insulating. In semiconductors at finite temperature T>0, two kind of carriers exist: electrons and holes (left by electrons in chemical bonds). As the temperature increases, more and more thermal electrons occupy the conduction bands, leaving an equal number of holes in the valence band. The absorption of light (photo-excitation), described (in 3D) by equations 1.22 and 1.26, promotes electrons in the conduction band and holes in the valence band. If the photon energy of the excitation light is above the bandgap of the semiconductor, the excited electrons in the conduction band have an excess energy with respect to the conduction band minimum. The imaginary part of the dielectric function (equations 1.22 and 1.26) determines all the possible transitions that can be observed in photoluminescence, i.e. the radiative recombination of electron-hole pairs. However, electron-electron scattering (fs time scale) and electron-phonon scattering (ps time scale) give rise to a quasi-thermal distribution for electrons, where the latter occupy the lowest available energy states on the bottom of the conduction band. The occupation of the conduction band by quasi-thermal electrons and of the valence band by quasi-thermal holes, can be described by their Fermi Dirac distribution, with a quasi-temperature and chemical potentials for electrons and holes, $\mu_e$ and $\mu_h$ [59]. The recombination of these thermalized carriers is responsible for the strong emission peaks that can be observed in the photoluminescence spectra. The lower emission photon energy in the PL spectrum is related to the band gap. The PL intensity and the temporal response of the PL emission are related to the details of the band structure, such as direct or indirect bandgap, and the relative energy difference between the absolute minimum/maximum of the CB/VB and other local minima/maxima.

Beside free carriers, in a semiconductor there are many-particle states, such as excitons, biexcitons, and exciton molecules, electron-hole plasmas (EHPs) and electron-hole liquids (EHLs) [23, 69]. An insight on this argument will be provided in section 1.4

A real semiconductor is characterized by the presence of impurities in the crystal lattice. An impurity can be a chemical defect, such as a substitutional atom in the crystal structure that can act as a donor, acceptor, or as a neutral impurity. Beside chemical defects, there are physical defects like vacancies, interstitial, grain boundaries and other imperfections in the crystal structure. Impurities implies the presence of other electronic states within the band structure of the semiconductor.

The introduction of new energy levels in the band structure of the semiconductor enables new possible optical transitions, both in the absorption and in the photoluminescence. Figure 1.5 a) shows a scheme of the band structure of a direct band gap semiconductor along with the main radiative recombination pathways. Among these, radiative interband recombination of free carriers across the bandgap, hot carriers (carrier with an energy difference above the bandgap), donor to valence band (D-VB) and conduction band to acceptor (CB-A) recombinations are shown.

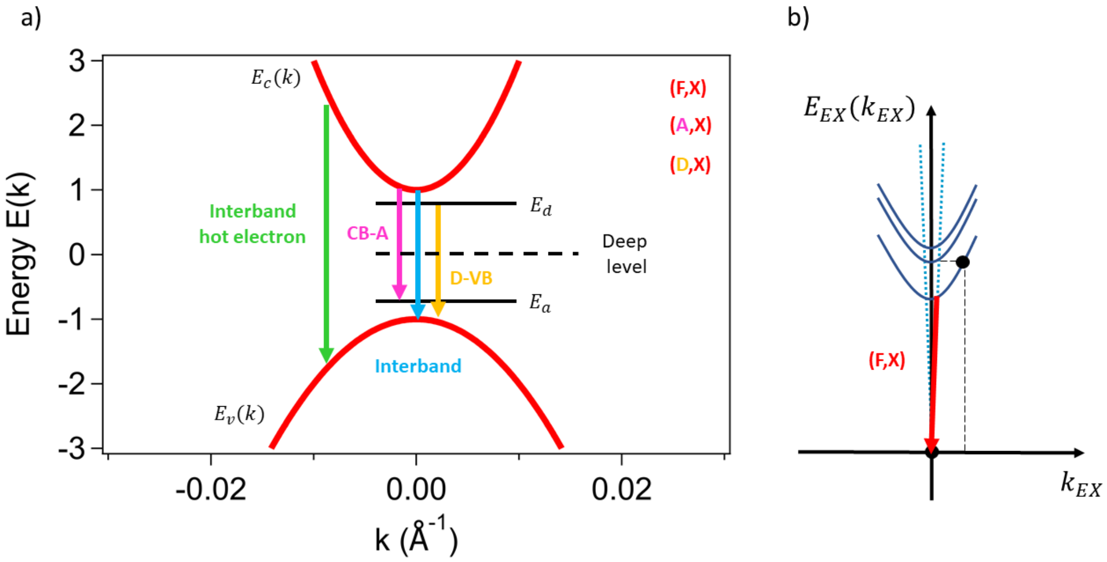

**Figure 1.5:** *a) Scheme of the band structure of a direct band gap seminconductor, including impurities (acceptors, donors and deep impurity levels). Many carrier recombination processes are shown. Radiative: band to band, hot electrons, conduction band to acceptor (CB-A), donor to valence band (VB-D). b)Two particle picture to describe the exciton transitions. The energy* $E_{EX}$ *of direct excitons is represented as a function of the exciton wavevector* $\vec{k}_{EX}$*. Beside the free excitons transition (F,X), there are excitons bound to acceptors (A,X) and excitons bound to donors (D,X).*

Figure 1.5 b) shows a separate scheme, in the two particle picture, where the exciton energy levels are represented. The radiative recombination of a free exciton (F,X) is represented. Beside this, excitons bound to donors (D,X) or to acceptors (A,X) can decay radiatively. Non-radiative *Shockley Read Hole* recombination (capture of free carriers in defect states), and non-radiative *Auger* recombination (one electron and hole recombine, giving their energy and momentum difference to another electron) are also relevant processes.

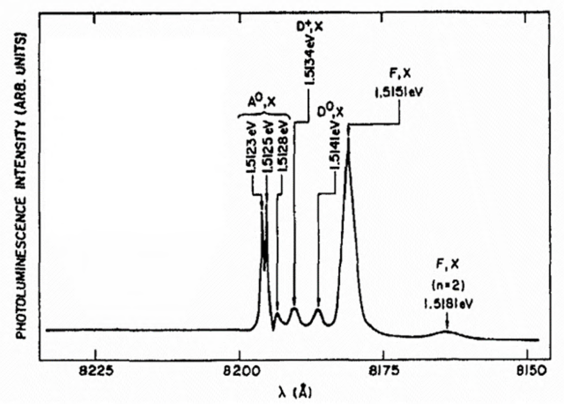

**Figure 1.6:** *Low temperature (5 K) photoluminescence spectrum of undoped GaAs MBE-grown at 670 °C, where excitons bound to acceptors (A,X), excitons bound to positively charged donors (D+,X), and free excitons (F,X) transitions are visible. Figure from [23].*

Figure 1.6 shows a low temperature (5 K) photoluminescence spectrum of undoped GaAs, where different transitions are visible: excitons bound to acceptors (A,X), excitons bound to positively charged donors (D+,X), and free excitons (F,X) in the ground state and in the excited state with n=2 (hydrogen-like model applies for GaAs).

The photoluminescence spectrum depends on the lattice temperature, on the carrier density (see 1.4), on the defect concentration. The lattice temperature affects the electronic bandgap, and thus it determines the low energy edge of the PL spectrum. The temperature dependence on the bandgap can be fitted with the following equation:

$$A + \frac{BT^2}{C+T} \tag{1.32}$$

where A, B and C are constants characteristic of the material.

In most semiconductors, such as III-V semiconductors (GaAs, Si, GaP), the exciton binding energy is of the order of 5-10 meV. Therefore, the temperature plays an important role, since these excitons can ionize well below the room temperature (thermal energy $\approx 25$ meV). Moreover, the temperature affects also the linewidth of the exciton emissions, with a linear dependence of the latter with the temperature, at low temperature [54]. Figure 1.7 a) and b) report the temperature dependent PL spectra of a GaAs/AlGaAs heterostructure [23] showing the effect of the temperature on the bandgap and on the PL exciton emission. At low temperature (2-4 K) the PL spectrum exhibit a peak at 1.51 eV, associated to free excitons, and a shoulder about 10 meV below, associated to excitons bound to neutral donors. As the temperature increses the two peaks can't be resolved and the spectrum broadens due to the exciton-phonon interactions. At T=40 K the emission peak in the spectrum is red-shiftd with respect to the spectrum at 4 K, due to the change of the bandgap with temperature. The shape of the spectrum is almost symmetric, with a sharp emission line. At temperature T>60 K, the peak of the PL spectrum shifts towards lower photon energy (temperature dependent bandgap), and it becomes more and more asymmetric: the low energy edge of the PL spectrum is always determined by the bandgap, and by the contribution of localized states inside the electronic bandgap induced by defects or disorder (Urbach tail). On the other hand, at high energy side, the PL spectrum decreases as the quasi-Maxwell Boltzmann distribution for photo-excited electrons. This is valid for free carrier emission and in the low excitation regime (non-degeneracy regime: $E - \mu_e >> k_B T$). In this case, the temperature can be extracted by fitting the high energy tail of the PL spectra.

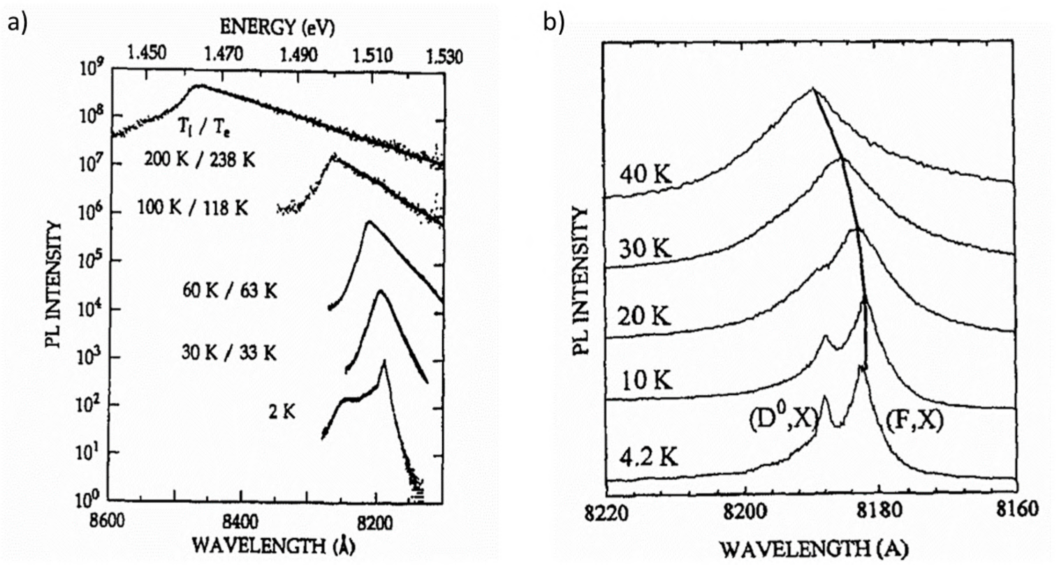

**Figure 1.7:** *a, b) Temperature dependent PL spectra for GaAs/AlGaAs heterostructure. Spectra are shown with an offset. In panel a) the PL intensity is represented in log scale. Figure from [23].*

### 1.3.3 Photoluminescence Lifetime and Quantum Yield

In this section we introduce two important concepts: the photoluminescence *lifetime* and the *Quantum Yield* (QY).

In general, the lifetime $\tau^{\alpha}$ is defined as the time at which the a physical quantity $Q$ is decreased by a factor $\alpha$ with respect to its value at the instant $t = t_0$.

$$Q(t = t_0 + \tau_{PL}^{\alpha}) = \frac{Q(t = t_0)}{\alpha} \tag{1.33}$$

The QY is defined as the ratio between the number of PL photons emitted and the total number of photon absorbed by the photo-excited system (i.e. the number of electrons generated by the photo excitation), in a defined time interval:

$$QY = \frac{N_{ph-emitted}}{N_{ph-absorbed}} \tag{1.34}$$

To introduce in an easy way the lifetime and the QY we consider the simplest situation where we have a 2 level system, with $N_1$ electrons in the lowest energy level (1) and $N_2$ electrons in the highest energy level (2). Electrons can decay from level 2 to level 1, radiatively with a rate $A_R$ and non-radiatively with a rate $A_{NR}$. The total decay rate is $A_{21} = A_R + A_{NR}$. For this system, in absence of a generation term for electrons in the energy level (2), the following differential equation holds for the number of electrons in the excited state:

$$\frac{dN_2(t)}{dt} = -A_{21} N_2(t) \tag{1.35}$$

where the initial condition can be written as $N_2(t_0) = N_2^{(0)}$. The solution for this differential equation is a single exponential:

$$N_2(t) = N_2^{(0)} e^{-A_{21}(t-t_0)} \tag{1.36}$$

Here, the overall lifetime can be defined as $\tau_{21} = \frac{1}{A_{21}}$, and it is the time at which the number of electrons in the level 2 is decreased by a factor $1/e$ with respect to its initial value:

$$N_2(\tau_{21}) = \frac{N_2^{(0)}}{e} \tag{1.37}$$

The number of emitted photons per unit time is equal to the absolute value of the radiative part of the time derivative of the number of electrons in the level 2. Hence the PL intensity is proportional to this quantity:

$$I_{PL} = \left.\frac{dN_2(t)}{dt}\right|_R = \tilde{k}A_R N_2(t) = \tilde{k}A_R N_2^{(0)} e^{-A_{21}(t-t_0)} = I_0 e^{-A_{21}(t-t_0)} = I_0 e^{-\frac{t-t_0}{\tau}} \tag{1.38}$$

where $\tilde{k}$ is a proportionality constant (expressed in $W/m^2$). In this case the PL lifetime is the same as the lifetime for the number of electrons in the level 2. Moreover, although only the radiative decay channel contributes to the PL intensity, both radiative and non-radiative channels contributes to the PL lifetime.

By defining the radiative and non-radiative lifetime as $\tau_R = 1/A_R$ and the $\tau_{NR} = 1/A_{NR}$, the overall PL lifetime can be written as

$$\frac{1}{\tau_{21}} = \frac{1}{\tau_R} + \frac{1}{\tau_{NR}} \tag{1.39}$$

In our simple 2 level system, the QY is given by the number of electrons that decay radiatively from 2 to 1, divided by the total number of electron that decay from 2 to 1, and then it is given by the ratio between the radiative decay rate and the total decay rate:

$$QY = \frac{A_R}{A_{21}} = \frac{\tau_{21}}{\tau_R} \tag{1.40}$$

If $\tau_{21} \approx \tau_R$, the radiative channel is dominant with respect to the non-radiative channel, and the QY approach the unity. If $\tau_{21} << \tau_R$ it means that $A_{21} >> A_R$, and in this case the non-radiative channel is dominant, and the QY goes to zero. In this simple 2 level system, by measuring the PL lifetime and the QY we can access to the radiative and non-radiative lifetime for the photo-excited population.

In the recombination model for a semiconductor, the situation is more complex, since the total recombination rate is given by:

$$R = An + Bnp + Cn^2p \tag{1.41}$$

where A is the Shockley-Read-Hall recobination rate (free carrier trapping in defect states), B is the radiative recombination rate for free carriers, and C is the Auger recombination rate. Here n and p are the density of electrons and holes in the material, respectively. If the material is an intrinsic semiconductor, or when the excitation density is much higher than the density of doping atoms (donor or acceptors), we can assume n=p. The QY is again given by the ratio between the radiative recombination rate and the overall recombination rate:

$$QY = \frac{Bnp}{An + Bnp + Cn^2p} \approx \frac{Bn^2}{An + Bn^2 + Cn^3} = \frac{Bn}{A + Bn + Cn^2} \tag{1.42}$$

The QY is a function of the electron density. Assuming that the A, B and C ratio are independent on the electron density, the maximum for the QY can be calculated by imposing the first derivative of the QY with respect to the density equal to zero. The result is particularly simple: $n_{MAX-QY} = \sqrt{A/2C}$.

In semiconductors, the temperature affects the QY efficiency, since the defect assisted Shockley Read Hall recombination increases as the temperature increases.

## 1.4 Free Excitons, Electron-Hole Plasma and Electron-Hole Liquid in semiconductors

When a semiconductor is photoexcited electrons and holes are generated. At low excitation density, electrons and holes can pair to form non-interacting excitons, called *free excitons* (FE). The PL line-shape of free excitons exhibits a sharp peak at a photon energy given by the difference between the bandgap of the material and the exciton binding energy. As the excitation density increases, trions, biexcitons and other exciton complexes can form. When the excitation density is further increased to a critical value called the *Mott density*, $n_M$, FEs give rise to a gas of ionized excitons, an *electron-hole plasma* (EHP). This transition results from the screening of the Coulomb interaction between electrons and holes due to the high carrier density, which reduces the exciton binding energy and leads to the dissociation. The presence of a high density of ionized excitons (i.e free electrons and holes) induces a band gap renormalization (BGR). This gives rise to a red-shift in the PL emission peak, and in a broadening of the spectrum, due to the population of the renormalized conduction band by free electrons, and of the renormalized valence band by free holes. The maximum kinetic energy of free electrons and holes in the conduction and valence band can be described by the *quasi Fermi energy* for electrons $E_{F,e}$ and holes $E_{F,h}$. The width of the PL spectrum, in an EHP regime is approximately given by $E_{F,e} + E_{F,h} + 2k_BT$. At very high excitation densities, above a *critical density* $n_c$ which minimizes the free energy per e-h pair, and below a critical temperature $T_c$ the electron-hole plasma can give rise to an ensemble of strongly correlated free electrons and holes, an *electron-hole liquid* (EHL). The PL spectrum for the EHL exhibit the same features of the PL spectrum for an EHP, with a red-shift due to the BGR and a width given by the sum of the kinetic energy of free electrons and holes, plus the thermal energy. However, the EHL exhibit features similar to a classical liquid, such as the incompressibility: when an EHL is formed in a semiconductor, a further increase in the excitation power density does not result in an increase of the electron-hole density, which remains constant, but it gives rise to an expansion of the electron-hole liquid. For this reason, the peak position and the line-shape of the PL in a EHL remain unchanged as the excitation power is further increased.

### 1.4.1 Theoretical approach to introduce FE, EHP and EHL

To formalize the phase transitions of FE, EHP and EHL we can consider the diagram in figure 1.8 a), where the average free energy per free e-h pair is represented as a function of the e-h density. The free energy per e-h pair is the average energy required to create an electron-hole pair. At T=0 K and at zero density, this energy is the energy gap:

$$E_{e-h}(0) = E_g \tag{1.43}$$

The average energy required to create an exciton in its ground state is:

$$E_{EX}(0) = E_g - E_b \tag{1.44}$$

At finite density $n$ the average free energy per electron-hole pair can be written as the sum of the exchange and correlation potentials and the average kinetic energy per electron-hole pair:

$$E_{e-h}(n) = E_g - \mu_x(n) - \mu_c(n) + \frac{1}{2}(E_{F,e}(n) + E_{F_h}(n)) \equiv \overbrace{E_g - BGR(n)}^{E'_g} + \bar{K}(n) \tag{1.45}$$

where $\mu_x$ and $\mu_c$ are the exchange and correlation potentials per pair, which sum is the band gap renormalization $BGR$, and $E_{F,e}, E_{F,h}$ are the quasi Fermi energy for electrons and holes, which average gives the average kinetic energy $\bar{K}$. The average energy to create an exciton is given by:

$$E_{EX}(n) = E'_g(n) - E'_b(n) = E_g - BGR(n) - E'_b(n) \tag{1.46}$$

Experimentally, the energy of the exciton optical transition does not vary significantly with density. Thus, we can assume that $E_{EX}(n) = E_{EX}(0)$, resulting in

$$E_g - E_b = E_g - BGR(n) - E'_b(n) \iff E'_b(n) = E_b - BGR(n) \tag{1.47}$$

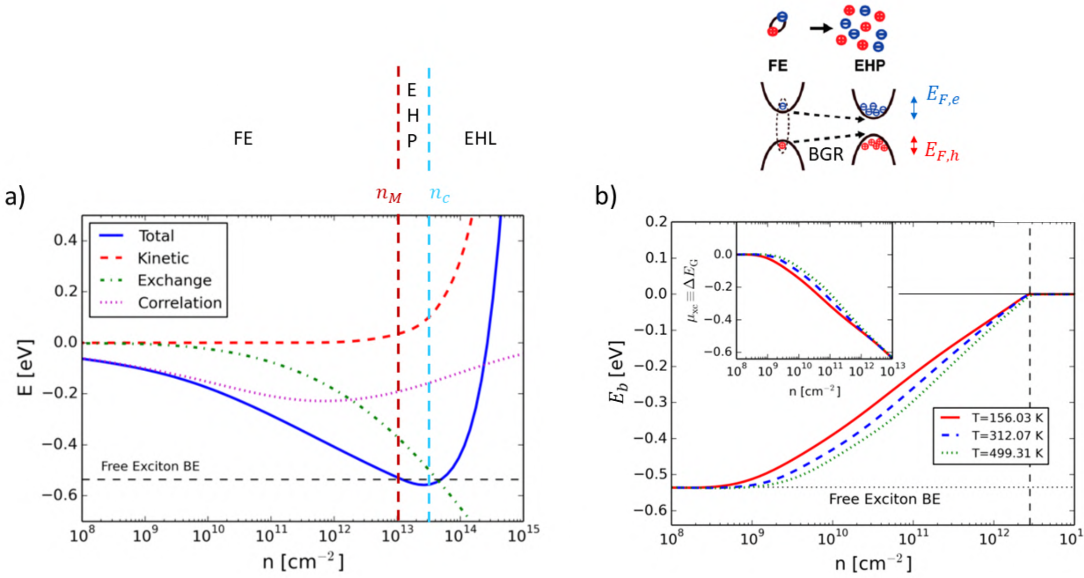

**Figure 1.8:** *Calculations for monolayer* $MoS_2$ *[69] a) Average free energy (net of* $E_g$*) per e-h pair,* $E_{e-h}$ *versus the e-h density. The contributions of the exchange and correlation terms and that of the kinetic energy are also shown. The energy to create a free exciton,* $E_{EX}$ *is plotted, and it is constant. The Mott density is the density such that* $E_{e-h}(n) = E_{EX}(n)$*. For* $n > n_M$*, free excitons ionize in an electron-hole plasma (EHP). The density* $n_c$ *which minimize the average free energy electron-hole pair, is a critical density at which the EHP condense in an electron-hole liquid (EHL), if the temperature is below a critical temperature* $T_c$*. The density regions correpsonding to FE, EHP and EHL are shown above. b) Free exciton binding energy* $E_b'$ *and BGR as a function of the e-h density. Figure adapted from [69, 91]*

Figure 1.8 b) shows the calculated exciton binding energy $E_b'$ and the $BGR$ (inset) as a function of density, at three values of temperature. The value of density at which $E_b' = 0$ does not depend on the temperature.

Figure 1.8 a) reports $E_{e-h}(n)$, and $E_{EX}$ (net of the energy gap $E_g$). This curve gives the following information:

1. When the density is such that $E_{EX} < E_{e-h}(n)$, the excitons are the stable configuration. This happens below a density value called the Mott density, $n_M$.

2. When $E_{EX} > E_{e-h}(n)$, excitons tend to ionize and to give rise to the electron-hole plasma, which is the stable configuration.

3. The Mott density is the density that satisfies

$$E_{EX} = E_{e-h}(n) \iff E_g - BGR(n) - E_b'(n) = E_g - BGR(n) + \bar{K}(n) \tag{1.48}$$

yielding

$$E_b'(n) = -\bar{K}(n) \tag{1.49}$$

This "negative binding energy" means that, to give rise to an electron-hole plasma, excitons need not only to have zero binding energy, but also an additional energy equal to the average kinetic energy of free electrons and holes in the EHP, at that density.

4. In the canonic ensemble, the pressure is given by the derivative of total the free energy $A(N, V, T)$ with respect to the volume, with constant temperature and number of particles:

$$P = -\left(\frac{\partial A}{\partial V}\right)\bigg|_{N,T} = -\left(\frac{\partial A}{\partial n}\frac{\partial n}{\partial V}\right)\bigg|_{N,T} = \frac{n}{V}\left(\frac{\partial A}{\partial n}\right)\bigg|_{N,T} \tag{1.50}$$

The derivative of the average free energy per electron-hole pair, $E_{e-h}(n) = \frac{A(N,V,T)}{N}$, with respect to the density is then related to the pressure of the EHP, according to

$$P = n^2 \left( \frac{\partial E_{e-h}(n)}{\partial n} \right) \Bigg|_{N,T} \tag{1.51}$$

When the $n < n_c$, the pressure is negative, and the EHP tends to increase its density, by contracting in droplets of density $n_c$. When $n > n_c$, the pressure is positive, and the EHP tends to decrease its density, by expanding [15]. This behavior is typical for incompressible liquids, which tends to recover its constant density value via expansion. For this reason, an EHP at density $n \geq n_c$ is called electron-hole liquid. EHPs or EHLs in semiconductors are created via photo-excitation. When trying to create an EHL at density $n > n_c$, the EHL expands, keeping the denisity value at $n = n_c$.

5. The e-h recombination is important to determine the density of the EHP, as it is in competition with the effect of the pressure. If the lifetime of carrier is long, an EHP can contract into droplets to form an EHL. This happens in high quality indirect band gap semiconductors, such as Silicon or Germanium at low temperature, where the PL lifetime is of the order of 1-10 $\mu s$.

We point out that the theoretical calculations reported in figure 1.8 for monolayer $MoS_2$ give an approximated result, since they have been performed by using an empiric potential, the effective mass and the envelope function approximation. As we discussed in section 1.2, these assumptions don't hold for excitons with high (or intermediate) binding energy.

# Chapter 2

# The scientific topic: Transition Metal Dichalcogenides

Since the first mechanical exfoliation of graphene, in 2004, two dimensional materials (2D materials) have attracted research interest for physics, chemistry and material science. Among these materials, Transition Metal Dichalcogenides (TMDs) are interesting because of their semiconducting properties, strong light-matter interactions in the near infrared and visible range and tightly bounded excitons which dominate the optical properties of TMDs even at room temperature. The indirect-to-direct band gap transition in the monolayer limit resulting in an efficient photoluminescence [76], and the breaking of inversion symmetry in the monolayer, giving rise to two different valleys in the first Brilloun zone, with different interactions with left and right circularly polarized light, make these ultra-thin materials suitable for potential opto-electronic and valleytronic applications [54].

## 2.1 General properties of 2H-TMD

TMDs are layered materials of the type $MX_2$, where M is a transition metal (Mo, W) and X is a chalchogen (S, Se, Te). A single layer of TMD is made of one layer of transition metal atoms sandwiched between two layers of chalcogen atoms. Bonds between atoms within a single layer are mainly covalent, while different layers are hold together by Van Der Walls forces. Because of the Van Der Walls nature of the bonds between different layers, it is possible to separate them by mechanical exfoliation, to obtain quasi 2D samples, down to the monolayer limit. This is particularly interesting because the properties of these materials depend strongly on the number of layers.

The TMD's crystal lattice may be either hexagonal (2H) or monoclinic (1T'). The hexagonal structure 2H is interesting because of its semiconducting properties, with an energy band-gap in the near infrared to visible spectral range (1.6 eV for monolayer $MoTe_2$ to 2.5 eV for monolayer $WS_2$). One of most interesting properties in a 2H TMD is the indirect-to-direct bandgap transition in the monolayer limit, which leads to strong photoluminescence from TMD monolayers.

Figure 2.1 a) shows the crystal structure of a 2H-$MoS_2$ monolayer. Figure 2.1 b) displays the crystal structure of the bulk $MoS_2$, which lattice parameters are a=3.1 Å(distance between two transition metal atoms in the same atomic plane), and c=12.3 Å(twice the interlayer distance). Note that the unit cell of the bulk $MoS_2$ extends on two monolayers [17]. The first Brillouin zone is hexagonal (top view), as shown in figure 2.1 c). The high symmetry points $\Gamma, K, M$ and the high symmetry line $\Sigma$ are represented. Figure 2.1 d) shows the calculated band structure for bulk and monolayer $MoS_2$ [90], projected along the high symmetry directions. The bulk has an indirect bandgap from $\Gamma$ to $\Sigma$, while the monolayer has a direct band gap at the K point. The large spin-orbit coupling in TMD leads to the splitting of both the valence and conduction bands, with a splitting energy of about 200-400 meV and 20-40 meV respectively. As an example, in $MoS_2$ the spin orbit splitting of the valence band is of about 170 meV in the bulk and 150 meV in the monolayer.

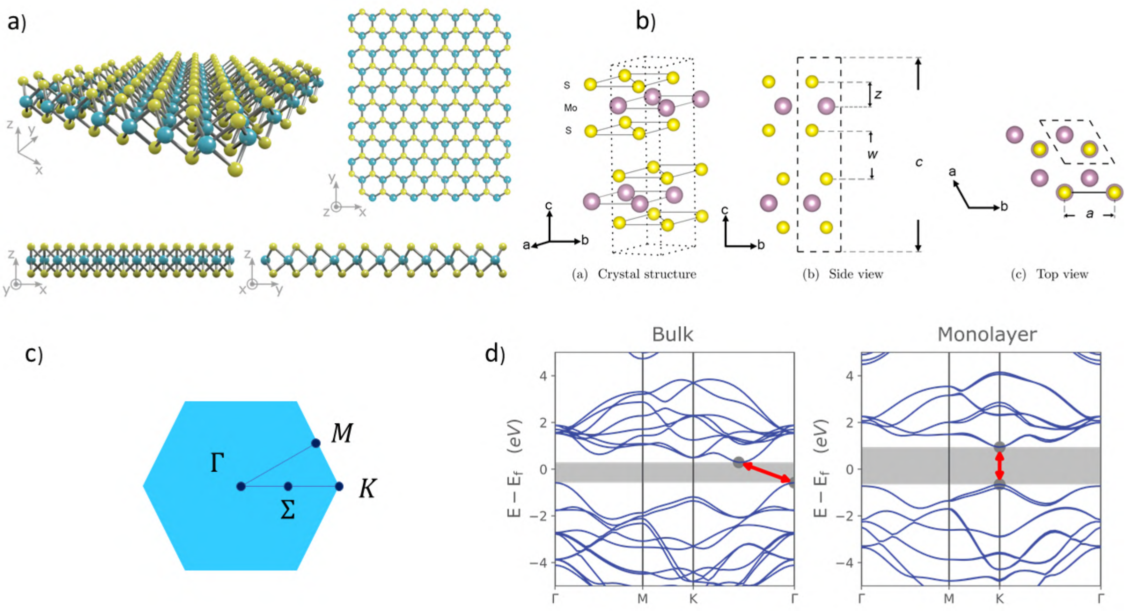

**Figure 2.1:** *a) crystal structure of a 2H-$MoS_2$ (and of a 2H-TMD). The 3D view is shown, beside the view from x, y and z directions. Figure from [90]. b) Crystal structure for the bulk $MoS_2$, with 3D view, side view and top view. The lattice parameters are a=3.16 Å, z=1.59 Å, w=2.96 Åand c=12.4 Å. Figure from [17] c) Sketch of the top view of the first brillouin zone of 2H-$MoS_2$, with the high symmetry points $\Gamma, \Sigma, K, M$. d) Calculated band structure of bulk and monolayer $MoS_2$, projected along the high symmetry directions. The band-gap is drawn as a red arrow, and it is indirect for the bulk, direct for the monolayer. Figure from [90].*

The monolayer of a TMD lacks spatial inversion symmetry, giving rise to two different valleys, K and K', at the vertices of the hexagonal first Brillouin zone. Light absorption in the K and K' valleys is induced respectively by left circularly polarized light and right circularly polarized light. Figure 2.2 shows some details of the band structure of the bulk $MoS_2$, exploiting the results of an angle resolved photo-electron spectroscopy (ARPES) experiment, using synchrotron light (APE beamline). Figure 2.2 a) shows the top view of the first Brillouin zone of bulk $MoS_2$, together with the experimental energy surface 200 meV below the valence band maximum. The energy bands at Γ and K points are clearly visible. Figure 2.2 b) displays other constant energy surfaces around the K point, showing how the valence band spreads and splits going below the valence band maximum. Figure 2.2 c) shows the experimental photoemission intensity versus the electron binding energy (with respect to the valence band maximum), along the $\Gamma K$ direction, for the bulk $MoS_2$, allowing to detect and quantify a spin-orbit splitting of $\approx$ 170 meV. The experimental valence band at the $K$ point is in good agreement with the tight binding band structure calculated for a monolayer $MoS_2$, shown in figure 2.2 d).

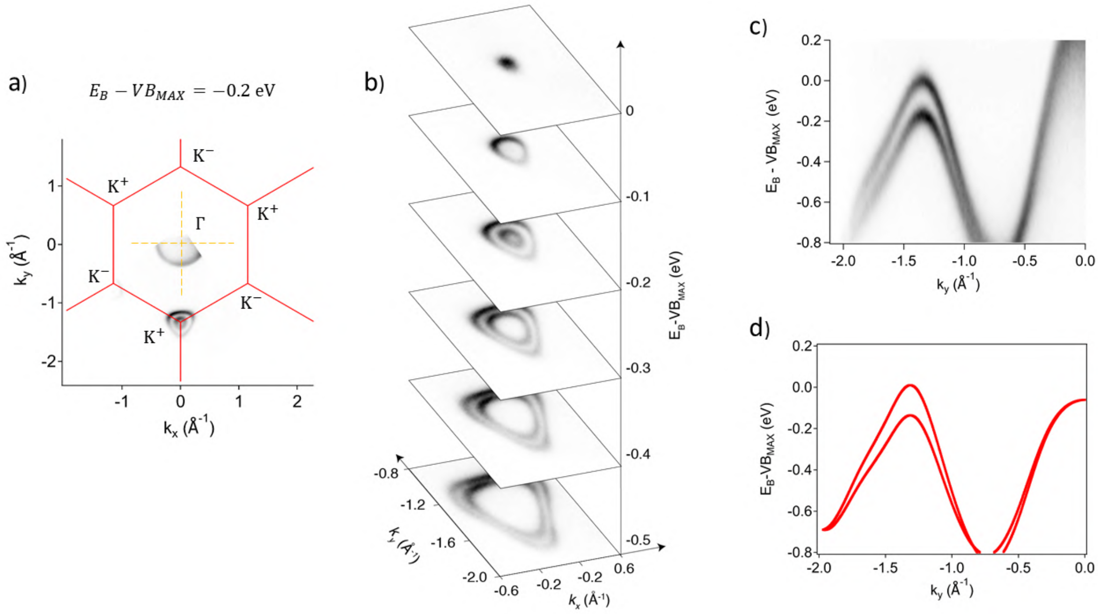

**Figure 2.2:** *a) Sketch of the top view of the first brillouin zone of 2H-MoS$_2$, togheter with the experimental constant energy surface for electrons in bulk MoS$_2$, result of a static ARPES measurement performed at the APE beamline (Elettra Sincrotrone Trieste) b) Extended view which shows six constant energy surfaces for electrons in bulk MoS$_2$. c) Experimental photoemission intensity along the direction $\Gamma - K$. d) Calculated band structure of monolayer MoS$_2$, along the direction $\Gamma - K$, obtained with the tight binding method.*

### 2.1.1 Defects in TMD

In real exfoliated TMD monolayers, intrinsic structural defects play an important role in limiting the mechanical, transport and optical properties, as evidenced by electrical transport and PL measurements [65, 51]. TEM investigations have been used to detect atomic defects in MoS$_2$ monolayers, revealing an high concentration of sulphur vacancies. Beside this, interstitial defects, dopant impurities, dislocations and grain boundaries have been observed [28, 95, 45, 97, 79, 55]. Since TEM measurements damage and introduce new point defects in the sample, STM measurements have been performed to investigate the native defect structure in high quality mechanicaly exfoliated MoS$_2$ monolayers on Au(111) [80]. These measurements were performed at room temperature and ambient pressure of nitrogen. The samples were mechanically exfoliated using the sonification technique (in contrast to TMD exfoliated monolayers with the scotch tape, that we have investigated in our experiments). Figure 2.3 shows an atomic resolution STM image (20 nm × 20 nm) of the exfoliated monolayer MoS$_2$ on Au(111)[80]. The image allows to identify the hexagonal lattice with a periodicity of $0.32 \pm 0.01$ nm, corresponding to the top sulphur layer. The brighter features are associated to adsorbed molecules, while the dark triangular holes are atomic scale discontinuities. Line profiles along the perfect atomic structure and along the triangular holes (figure 2.3 b) show that the discontinuities are centered on a lattice site of the top sulphur layer, indicating the vacancy of sulphur atoms. The concentration of defects found in these measurements is not uniform accross all the sample surface, and range from $5 \cdot 10^{12}\ cm^{-2}$ to $5 \cdot 10^{13}\ cm^{-2}$.
This defects density is many order of magnitude higher than that in classical semiconductors (Si, Ge or GaAs) [71], and of the same order of magnitude of the excitation density in our TR-PL experiments in the high excitation regime, thus giving an important contribution to our experimental results (see chapter 4).
The contribution of chemical defects on the carrier lifetimes and PL efficiency (QY) have been investigated for exfoliated monolayers WS$_2$. Liu *et al* [46] investigated three particular types of defects: sulphur vacancies ($V_S$), substitution of one sulphur atom by an oxygen atom ($O_S$) and substitution of two sulphur atoms with one oxygen atom ($O_{2S}$). They intentionally exposed an exfoliated monolayer to an oxygen plasma, to induce the subsequent formation of the three types

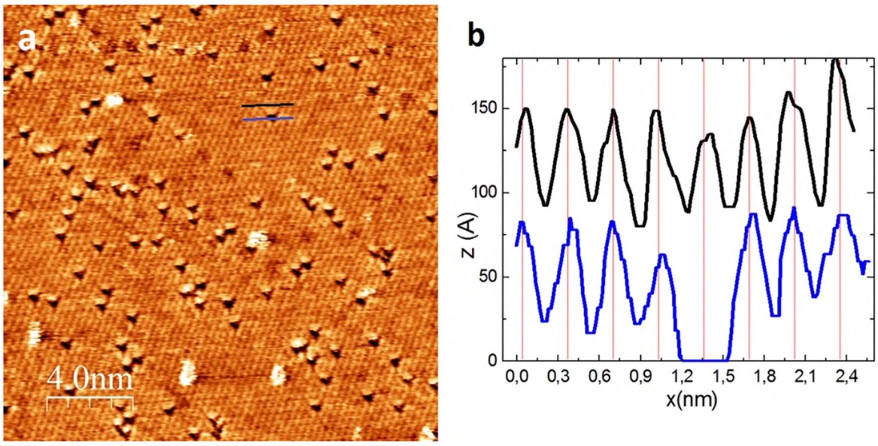

**Figure 2.3:** *a) Atomic resolution STM image of exfoliated monolayer* $MoS_2$ *on Au(111) substrate. The STM image* ($V_{bias}$=50 mV, $I_t$=2 nA) *clearly resolves individual point defects (dark triangles) and adsorbed molecules (white spots). b) Tunneling current profiles along the perfect crystal structure and along a point defect, showing that the defect is located at the same position of a missing atom. Figure from [80]*

of defects, and they performed steady state PL and TR-PL experiments to investigate the role of these defects on the PL lifetime and QY.

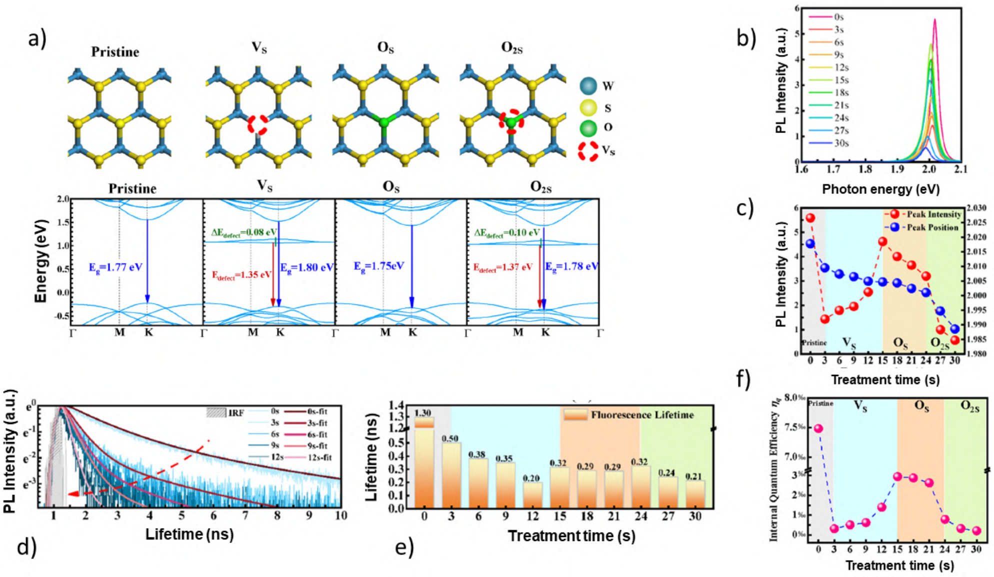

**Figure 2.4:** *a) Top view of the crystal structure of* $WS_2$*, without defects, and with three kind of defects: sulphur vacancy* ($V_S$)*, one sulphur atoms substituted by one oxygen atom* ($O_S$) *and two sulphur atoms substituted by one oxygen atom* ($O_2S$)*. The calculated band structure with the three types of defects is shown below. b) PL spectra of the* $WS_2$ *monolayer measured for different treatment times of the monolayer with an oxygen plasma, inducing the subsequent formation of the three kind of defects. c) Integrated PL intensity and peak position versus the treatment time. d) PL time dynamics at different exposition times, fitted by bi-exponential functions. e) PL lifetime versus the treatment time. f) PL quantum yield versus the treatment time. [46]*

Figure 2.4 a) shows a scheme of the top view crystal structure of a $WS_2$ monolayer, without defects, and with $V_S$, $O_S$ and $O_{2S}$ defects. The calculated band structure, projected along the $\Gamma - K$

direction is also represented, showing the presence of energy levels within the bandgap for the crystal with $V_S$ and $O_{2S}$ defects types, while the iso-electronic $O_S$ defect induces modifications in the electronic band structure without introducing electronic states in the bandgap. Figure 2.4 b) shows the PL spectra for $WS_2$ monolayer versus the time of exposition of the plasma oxygen. The corresponding integrated PL intensity and position of the emission peak are plotted in figure 2.4 c), where the oxygen plasma exposition time axis is divided in intervals where a specific type of defect dominates the response of the monolayer: the PL intensity decreases in the $V_S$ defect regime, and increases again in the $O_S$ regime, due to the iso-electornic character of this type of defect. In the $O_{2S}$ regime, the PL intensity decreases again. Figure 2.4 d) reports the PL time dynamics for treatments time up to 12 s. The PL lifetime extracted by the fit of the PL time dynamics is reported in figure 2.4 e), showing a decrease of more than one order of magnitude from pristine $WS_2$ to $WS_2$ with $V_S$ defects type. The PL quantum yield is reported in figure 2.4 f). The QY of pristine $WS_2$ is about the 0.75 %, it decreases by more than one order of magnitude when $V_S$ defects dominate, it increases again to about 0.3 % when $O_S$ defects dominate, and it decreases below the 0.1 % in the $O_{2S}$ defect regime [46].

The influence of the density of defects on the PL quantum yield of TMD monolayers is reported in steady state and time resolved pholuminescence measurements on monolayer $MoS_2$ "as exfoliated" and chemically treated with an organic super acids (TFSI) [2], showing an enhance in the PL quantum yield in the treated monolayer from the 0.6% to 95 %, beside an increase in the PL lifetime of more than two orders of magnitude. This is due to the passivation of the defects states, leading to a dynamic equilibrium between only the exciton formation and radiative exciton decay, under CW excitation at low excitation intensity leading to the near unity QY. At high excitation intensity, resulting in high exciton density, the QY decreases because other non-radiative recombination channels contribute, such as the exciton-exciton annihilation (EEA).

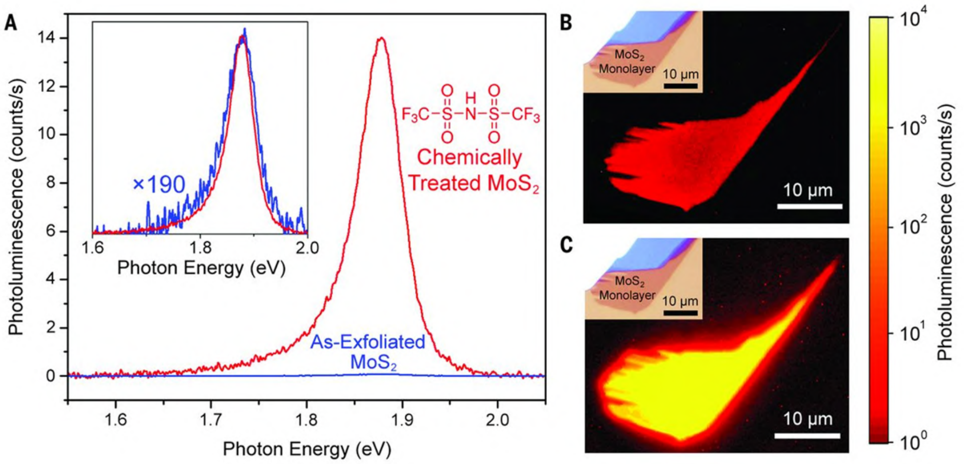

**Figure 2.5:** *A) Photoluminescence spectrum of "as exfoliated" and chemically treated $MoS_2$ monolayer, showing an increase in the PL intensity of a factor 200. B,C) Optical image of the and PL intensity map of the $MoS_2$ monolayer. After the chemical treatment, the PL intensity increases uniformly along all the flake. Figure from [2].*

Since the passivation of the defect states due to treatment with TFSI is not stable after exposure to air, water, or other commonly used solvents, the encapsulation of the treated monolayer in a 200 nm thick transparent polymer (CYTOP) was successfully employed [41], achieving near unity QY and stable TMD monolayers. The spectral features of the excitonic emission are preserved after the encapsulation and the super acid treatment (except for a slight reduction in the emission of the low energy tail).

### The superior quality of exfoliated monolayers

Defects in crystals strongly affect the electronic and optical properties, including the PL efficiency and lifetime. For this reason, high quality samples are desirable to investigate the intrinsic properties of materials. In particular, regarding TMD, exfoliated samples represent the best chance to obtain monolayers (and in general thin flakes) with a high crystal quality. Exfoliated TMDs often exhibit a better crystal quality with respect to molecular beam epitaxy (MBE) or chemical vapor deposition (CVD) grown ones. The superior quality is due to the intrinsic quality of bulk crystals, which can be grown in a controlled way, resulting in a high-purity and low defect concentration. Exfoliated monolayers are directly taken from the inner part of a bulk sample, maintaining the intrinsic high quality. The growth of a monolayer on a substrate is affected by the quality and by the contamination of the surface of the substrate itself. Exfoliated monolayers are characterized by an uniform thickness on a distance scale of tens of microns, while CVD or MBE grown monolayer may be affected by local fluctuation of thickness. Finally, exfoliated monolayers can be transferred on weakly interacting substrates (or even suspended on patterned substrate with holes), where they can adhere without significant lattice mismatch issues, while the growth of a single layer with CVD or MBE techniques is affected by the nucleation of the first atom groups on the substrate, that can introduce the presence of different domains, strain or lattice mismatch, resulting in a lower crystal quality [25, 85].

However, exfoliated TMD monolayers are also characterized by a significant defect density. In particular, TMD monolayers on $SiO_2$ substrate are affected by the surface defects and charged bulk defects of the $SiO_2$ substrate, and by adsorbed molecules (water, $CO_2$, ecc). Freestanding monolayers are not affected by the defects of the substrate surface, but on the other hand they present two surfaces that can be contaminated by adsorbed molecules. Nowadays, the best possibility to solve the problem of surface defects and atmospheric contamination of monolayers is to exfoliate them in protected environment, such as in glovebox (in an Argon atmosphere), and to encapsulate them with hexagonal boron nitride (h-BN) [10].

In summary, in TMD monolayers, the defect concentration can be as high as $10^{13}\ cm^{-2}$, which is comparable or even higher with respect to the density of free excitons in the low or intermediate excitation regime. Thus, defects mediated non-radiative recombination strongly affect the lifetime of photo-excited carriers and the PL dynamics, as will be discussed in detail in the data analysis for TR-PL and TR-ARPES, in chapter 4 and in chapter 5, respectively.

## 2.2 Excitons in TMD

The 2D character and the weak dielectric screening leads to enhanced Coulomb interactions in 2D TMD, resulting in a high exciton binding energy (0.3-1.0 eV) [26]. Since this binding energy is much larger than $k_B T$ at room temperature, excitons dominate the optical properties in these materials, allowing to investigate the exciton physics at room temperature and above, without the constraint of cryogenic temperature, necessary to have non-ionized excitons in conventional III-V semiconductors, such as GaAs. This property also opens the possibility of potential new applications for highly efficient exciton-based opto-electronic devices.

The optical spectra of TMDs are characterized by two peaks, corresponding to the so-called A and B excitons, arising the spin-orbit splitting of the valence band, which is of about 200 meV for the molybdenum-based TMD, and 400 meV in the tungsten-based TMDs. The splitting of the conduction band is of few tens of meV, leading to a conduction band which is nearly spin-degenerate at room temperature. On the other hand, at low temperature the conduction band splitting plays an important rule.

The exciton binding energy $E_b$ is defined as the energy necessary to ionize an exciton in its ground state into a free electron-hole pair. We recall that the energy of the optical transition for the exciton in its ground state $E_{EX}$ is related to the (renormalized) free-particle bandgap $E_g$ and to the exciton binding energy $E_b$, according to:

$$E_{EX} = E_g - E_b$$

There are different approaches to determine the exciton binding energy, such as using the scanning tunneling spectroscopy to obtain $E_g$ and absorption or PL measurements to get $E_{EX}$. Another possibility is to measure the contrast of reflectance, which reveals the positions of the s-like excitonic states, up to 5s, allowing an extrapolation of $E_g$. Moreover, it is possible to investigate the exciton excited states by probing the internal exciton optical transitions (example 1s-2p), in a "two-photon" (visible + infrared) absorption experiment [50].

Recent studies have shown that it is possible to tune the emission photon energy for the excitons $E_{EX}$, by tuning the exciton binding energy or the free particle bandgap of TMD monolayers. The exciton binding energy can be tuned by engineering the dielectric environment (i.e. the substrate), while the free particle bandgap can be tuned by applying a tensile strain [27, 36].

The absorption coefficient of TMDs at the excitonic resonance is very high. In $MoS_2$, its value at 1.9 eV (A exciton resonance) is 20 times higher than the absorption coefficient of GaAs at 1.45 eV (just above the band gap) [66]. A $MoS_2$ monolayer absorbs more than the 2% of the incident light at the A and B exciton resonances (1.87 eV and 2.02 eV) and even more above the band gap (in the range [2.5, 3.6] eV). This strong white light absorption by TMD monolayers promotes them as suitable for potential applications in ultra-thin solar cells [20].

The linewidth of exciton resonances is determined by the dephasing time of excitons (the average life-time of the exciton in a coherent superposition of its quantum states, before losing the phase relation, due to interactions with the environment), which depends on the radiative and non-radiative scattering channels [54]. At low temperature, the radiative lifetime of excitons constitute the main decay channel for the exciton polarization, resulting in an intrinsic linewidth of the exciton resonance [10]. In $WSe_2/Al_2O_3$ the intrinsic radiative lifetime of excitons is of about 200 fs, corresponding to a linewidth of 3 meV. For $WS_2$ encapsulated in h-BN a linewidth of 1.7 meV has been reported [1]. In the weak excitation regime (exciton-exciton interactions are negligible), as the temperature is increased, the broadening of the emission line width is mainly induced by the scattering between excitons and acoustic phonons. This results into a linear increase of the exciton linewidth with temperature, below T=100 K. Above this temperature, optical phonons contribute, resulting in a super linear temperature dependence of the exciton linewidth [54]. Defects and exciton-exciton interactions also strongly contribute to inhomogeneous broadening [21, 9]. The linewidth of the exciton emission lines at room temperature is of about 30-40 meV .

The strong spin-orbit splitting and the electronic band structure properties give rise to the presence of both *bright* and *dark* excitons. Bright excitons can radiatively decay by emitting photons, with a first order optical transition (see section 1.2, equation 1.23). There are two conditions that must be satisfied to have a bright exciton: 1) The electron and hole constituting the exciton must have the same spin. 2) Both the energy and momentum must be conserved. Hence, the energy of the emitted photon must be equal to the exciton energy: $h\nu = E_{EX}$, and the exciton wavevector $\vec{k}_{EX}$ must be equal to the wavevector of the light $\vec{q} = \frac{h\nu}{\hbar c} \approx \vec{0}$ (where $\hbar$ is the Planck constant divided by $2\pi$ and $c$ is the speed of the light). If one of these two condition is not verified, the exciton is called to be 'dark', because it requires a second order optical transition (in time dependent perturbation theory), to emit light conserving the energy, the spin and the momentum simultaneously.

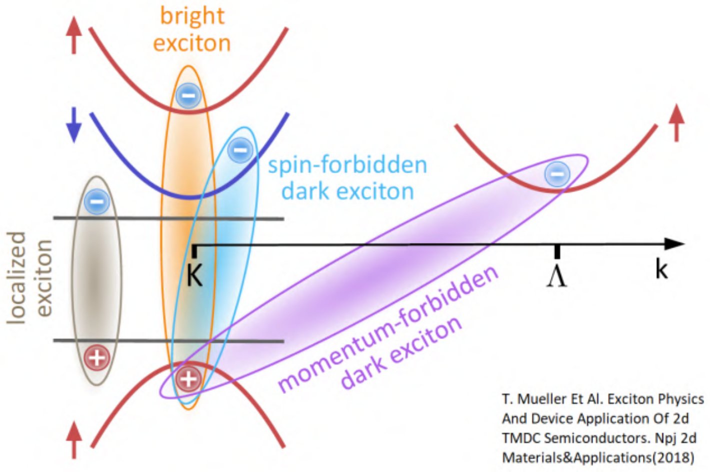

T. Mueller Et Al. Exciton Physics And Device Application Of 2d TMDC Semiconductors. Npj 2d Materials&Applications(2018)

**Figure 2.6:** *Sketch of the band structure at K and Λ points for a TMD. The red and blue bands are respectively the spin up and the spin down bands. Different exciton types are represented: the KK bright excitons (orange), the KK spin forbidden dark excitons (light blue), the KQ momentum forbidden dark excitons (violet), and a localized exciton (gray) [54].*

### 2.2.1 Spin forbidden dark excitons

If the spin of the electron and hole constituting the exciton is opposite, the excitonic complex is called *spin forbidden dark exciton*. Interestingly, the spin-orbit interaction has an opposite sign for molybdenum- and tungsten-based TMD. Hence, in the molybdenum-based TMD the bright excitons are the lowest energy states, while in tungsten- based TMD, the spin forbidden dark excitons are favored. This results in a high PL quantum yield for $MoS_2$ and low PL quantum yield for $WS_2$ at low temperature. As the temperature increases, the PL quantum yield for $WS_2$ increases, since more and more excitons occupy the energetically higher bright states.

Recent experiments demonstrate the possibility to "brighten" these spin forbidden dark excitons, by applying strong in-plane magnetic fields which can couple to the spin of the charge carriers (Zeeman effect) [53].

### 2.2.2 Indirect excitons or momentum forbidden dark excitons

When the wavevector of the exciton differs significantly from zero, the exciton is called indirect exciton or *momentum forbidden dark exciton*. In a very simplified approach, where we consider hydrogen-like excitons in TMDs, we can describe the bright excitons as constituted by an electron and a hole both at the K point in the first Brillouin zone. For this reason the brigh excitons are also called the KK excitons. However, in tungsten-based TMD, the absolute minimum of the conduction band is located at the Λ valley. Hence the lowest energy states (in our simplified hydrogen-like approach) are indirect excitons with an electron at the Λ valley and a hole in the K valley, yielding a majority of these $K\Lambda$ momentum forbidden dark excitons. In monolayer $WSe_2$. these states have an energy about 80 meV lower than the KK bright excitons [94].

Since the dark excitons cannot decay radiatively (at the first order), their life-time can be much longer than that of bright excitons. For this reason they can constitute a reservoir of potential

light emitter.
Phonons can assist the radiative recombination of momentum forbidden dark excitons. Moreover, it is possible to activate these dark excitons is the presence of high dipole moment molecules on the monolayer. These molecules can disturb the translational symmetry of the TMD lattice, softening the crystal momentum conservation constraint, leading to brightening of the $K\Lambda$ exciton. Figure 2.7 c) shows an example of the brightening of $K\Lambda$ dark excitons, via coupling with merocyanine molecules [19].

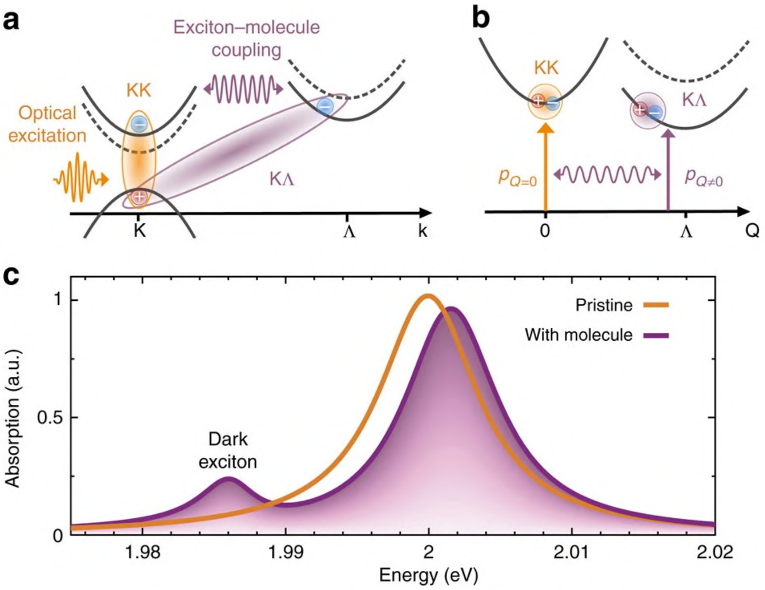

**Figure 2.7:** *a) Scheme of the electronic dispersion of TMDs around the K and Γ valleys. b) Scheme of KK and $K\Lambda$ excitons in the two particles picture. c) Absorption spectrum of the monolayer $WS_2$. The absorption spectrum of the pristine monolayer exhibit a single peak at ≈ 2.002 eV. In presence of high dipole moment merocyanine molecules, a second peak, ascribed to the absorption by $K\Lambda$ excitons, appears at ≈ 1.986 eV [19].*

### 2.2.3 Biexcitons, trions, localized excitons and interlayer excitons

Beside (neutral) free excitons, localized excitons, interlayer excitons, charged excitons (trions) and biexcitons are relevant in these materials.
*Localized excitons* are constituted by an electron and a hole trapped in local potential wells due to the presence of an impurity, defects or external fields in the crystal stucture. At low temperature, the emission from localized excitons can be detected as narrow peaks (below 120 $\mu eV$ in free standing WSe2 monolayers) below the KK bright exciton, while as the temperature increases the thermal energy is sufficient to ionize these excitons. The localized excitons often appear at the edges of the TMD samples, where the density of impurity is increased [78].
*Interlayer excitons* appear in Van der Waals heterostructures when two monolayers of different TMD are put in contact. Interlayer excitons are constituted by an electron and a hole located in two different TMD layers [67].
*Trions* are positively or negatively charged excitons, constituted by two electrons and a hole or by one electron and two holes.
*Biexcitons* are systems constituted by two excitons, bound togheter. The energy to create a biexciton is lower than the energy required to create two free excitons.

## 2.3 Exciton dynamics and photoluminescence in TMDs

In this section we describe the dynamics of photo-excited excitons in TMDs. The three main steps in this dynamics are the optical excitation, the exciton formation, the exciton thermalization and the exciton decay. The optical excitation can be either resonant or above bandgap.

In resonant excitation, the photon energy of the excitation light is close to the energy of the transition of the exciton (i.e. $E_{EX} = E_g - E_b$). The excitons are immediatly created in their ground state. These excitons are called *coherent excitons*, or polarized excitons. The exciton-phonon scattering give rise to the so-called polarization-to-polulation transfer, leading to the formation of incoherent excitons on a sub-ps time scale. As an example, a resonant excitation with left circularly polarized light creates polarized coherent bright excitons in the K valley. This polarization decays on the ps time scale, due to an efficient inter-valley coupling between excitons via exchange interaction [8]. Another important mechanism to take into account is the dark-bright exciton scattering, suggesting that the spectral position of bright and dark states plays an important role in the decay of the valley polarization [5].

In above bandgap excitation, the photon energy of the excitation light is higher than $E_{EX}$. In this case the light creates either excitons in excited states (for $E_{EX} < h\nu < E_g$), or free electrons and holes (for $h\nu > E_g$ ) which subsequently relax towards the conduction/valence band minimum/maximum via carrier-carrier and carrier-phonon scattering, on the sub ps to ps time scale. Finally carriers further lower their energy giving rise to a thermalized exciton distribution. This happens through a cascade of newly formed excitons from excited higher exciton excited states towards the ground state, via the Rydberg-like series of bright and dark excitonic states (we always use the simplify hydrogen-like picture to provide a quick and intuitive picture of the much more complicated real exciton physics in this materials). At this point, only a small part of the incoherent excitons located within the light cone (with a vanishing momentum) can decay radiatively and contribute to PL. The PL quantum yield depends on the temperature, on whether the exciton lower energy states are bright or dark, on the exciton density and on the density of defects in the crystal structure. In the low excitation limit, excitons are so far from each other that their interaction is negligible. Hence they can decay either radiatively or non-radiatively via defect assisted recombination paths. The differential equation for the exciton density can be written as follows:

$$\frac{dn(t)}{dt} = -A_R n(t) - A_{NR} n(t) \tag{2.1}$$

where $A_R$ is the radiative recombination rate, while $A_{NR}$ is the non-radiative rate at which excitons are trapped in defect states. The radiative and non-radiative lifetimes $\tau_R$ and $\tau_{NR}$ are define as the reciprocal of the respective rates. Here we focused on the decay of the exciton density after a pulsed excitation, hence the equation 2.1 does not include a generation term, that must be taken into account for a continous wave excitation. The solution of this differential equation is:

$$n(t) = n_0 e^{-(A_R + A_{NR})(t-t_0)} \tag{2.2}$$

where $n_0 = n(t_0)$ is the initial exciton density. The PL intensity is proportional to the radiative part of the time derivative of the density of excitons in the material. In this case:

$$I(t) \propto A_R n(t) = cost \cdot A_R n_0 e^{-(A_R + A_{NR})(t-t_0)} \tag{2.3}$$

It is possible to relate the observed lifetime $\tau = \frac{1}{A_R + A_{NR}}$ to the radiative and non-radiative lifetime by using the definition of the quantum yield:

$$\tau_R = \frac{\tau}{QY} \tag{2.4}$$

We highlight that equation 2.1 holds when the radiative and non radiative recombination time are kept as constants, i.e. neglecting possible effects such as a time dependent temperature, affecting the radiative lifetime, or the time dependent density resulting in a potential saturation of the defect states, affecting the non-radiative lifetime.

In the medium excitation regime, exciton-exciton interactions become important, and as the exciton density increases the Auger exciton-exciton annihilation becomes the dominant recombination

channel. In this process, two exciton interacts, leading to the decay of the first exciton, while the second exciton is ionized in a hot free electron-hole pair.
In the medium excitation regime, the differential equation for the density can be written as:

$$\frac{dn}{dt} = -Bn(t) - Cn(t)^2 \tag{2.5}$$

where $B = A_R + A_{NR}$ and $C$ is the exciton-exciton annihilation rate. The solution of this differential equation is:

$$n(t) = \frac{B}{C} \frac{1}{(e^{B(t-t_0)}[1 + \frac{B}{Cn_0}] - 1)} \tag{2.6}$$

The PL intensity is given by

$$I(t) = cost \cdot A_R n(t) = cost \cdot A_R \frac{B}{C} \frac{1}{(e^{B(t-t_0)}[1 + \frac{B}{Cn_0}] - 1)} \tag{2.7}$$

In the high excitation regime, excitons can dissociate in free electrons and holes, and equation 2.5 is no longer correct to describe the system.

### 2.3.1 The intrinsic radiative lifetime and the observed radiative lifetime for excitons

The intrinsic radiative lifetime $\tau^0_{RAD}$ is the lifetime for the radiative decay of coherent excitons, photo-excited resonantly, and it can be considered when the exciton-phonon and exciton-exciton interaction time is much longer than $\tau^0_{RAD}$, i.e. at low temperature and low exciton density. In this condition, the radiative lifetime can be obtained by the homogeneous linewidth of the exciton emission line, $\gamma_h$, using the energy-time uncertainty relation:

$$\tau^0_{RAD} = \frac{\hbar}{\gamma_h} \tag{2.8}$$

For a Lorentzian emission line, the following relation holds:

$$\tau^0_{RAD}[ps] = \frac{0.658}{\gamma_h[meV]} \tag{2.9}$$

where $\gamma_h$ is the FWHM of the Lorentzian function.
The intrinsic radiative lifetime for Wannier-Mott (weak binding) excitons in 2D semicondutcors can be written as:

$$\tau^0_{RAD} = \frac{\hbar\varepsilon}{2q} \left(\frac{E_{EX}}{e\hbar v}\right)^2 (a_B^{2D})^2 \tag{2.10}$$

where

1. $\varepsilon$ is the static dielectric constant.
2. c is the speed of light.
3. $E_{EX}$ is the energy of the exciton optical transition.
4. $q = \frac{h\nu}{\hbar c} = \frac{E_{EX}}{\hbar c}$ is the wave vector for emission of light.
5. $a_B^{2D} = \frac{\varepsilon\hbar^2}{4\mu e^2}$ is the Bohr radius for the exciton in 2D.
6. $\mu$ is the reduced mass for the excitons, defined as $\frac{1}{\mu} = \frac{1}{m_c} + \frac{1}{m_v}$. $m_c$ and $m_v$ are the effective mass for electrons and holes, respectively, at the K (or K') valley.
7. $v$ is the *Kane velocity*, related to the inter-band matrix element of the electron momentum. In a simplified two band model this quantity is given by $v = \sqrt{E_g/(2m_e)}$

For monolayer $MoSe_2$, the calculated intrinsic radiative lifetime is $\tau_{RAD}^{0-theory} = 300$ fs [57, 83], while the experimental value obtained with TR-PL, at low temperature and low excitation density, is about $\tau_{RAD}^{0-exp} = 1.8 \pm 0.2$ ps [68]. The difference between the calculated and experimental lifetime may be due to the fact that the calculations have considered Wannier Mott excitons in the weak binding limit, which is not valid for excitons in TMD. It is important to highlight that even ay low temperature and low excitation density, the real intrinsic line-width cannot be directly measured, since it is impossible to get rid of any contribution to inhomogeneous broadening. The only possibility is to try to extrapolate this value at zero temperature, zero exciton density and zero density of defects in the material.

When the exciton-phonon interaction time become comparable with the intrinsic radiative lifetime, we should consider a thermalized exciton population, with a an effective radiative lifetime given by:

$$\tau_{RAD}^{eff} = \frac{3}{2}\frac{k_B T}{E_0}\tau_{RAD}^{0} \tag{2.11}$$

This lifetime depends on the thermal energy $k_B T$ and on the maximum kinetic energy of excitons within the light cone, $E_0^{MAX} = \frac{\hbar^2 q^2}{2M}$, where $M = m_c + m_v$. Equation 2.11 holds when $k_B T >> \gamma_h$ and $k_B T >> E_0$.

By using equations 2.10 and 2.11, an effective radiative lifetime at room temperature of $\approx 500$ ps have been calculated for monolayer $MoS_2$ [57]. For monolayer $MoSe_2$, an effective radiative lifetime of $\approx 900$ ps have been calculated at room temperature [57]. A similar value has been observed experimentally for $WS_2$, by means of TR-PL measurements at room temperature [93]. However, in high quality mechanically exfoliated samples the effective radiative lifetime at room temperature is about 2 ns, more than 2 times the predicted value. This happens for our TR-PL experimental data on monolayer $WS_2$ on $SiO_2$, as we will discuss in detail in chapter 4. Moreover, in chemically treated monolayers, with low defect concentration and near unity QY, the measured radiative lifetime can be about 10-20 ns [24, 2], 20 to 40 times higher than the values predicted using equation 2.11.

To explain this discrepancy, a model has been proposed for chemically treated monolayer $MoS_2$, where the apparent long dynamics is ascribed to the slow detrapping of excitons from defect states with a very low recombination rate towards the ground state [24]. In this work, temperature-dependent steady state PL measurements, at low excitation power, have been performed on chemically treated monolayer $MoS_2$, showing a significant PL emission by defect states at low temperature, and a negligible contribution by free excitons. As the temperature increases, the free exciton contribution becomes more and more pronunced, while the defect contribution decreases, and it becomes negligible at room temperature (see figure 2.8 a) and b) ).

Power-dependent steady state PL measurements at fixed temperature (77 K) have shown a dominant defect contribution to the PL at low excitation power, and a free exciton contribution that becomes more significant as the excitation power increases (see figure 2.8 c) ) [24].

These data suggests a high occupation of defect states by trapped excitons and a negligible density of free excitons at low temperature, resulting in a PL spectrum dominated by defects. But when the temperature increases, yielding a higher population the free excitons, their contribution to the PL becomes dominant. Moreover, at 77 K and low power, there is an high occupation of defect states by trapped excitons, and a negligible density of free excitons, and the PL spectrum is dominated by defects. As the power increases, the exciton generation rate is so high that the trap states are saturated, giving rise to a non-negligible density of free excitons, and in a dominant emission by the latter.

This data allow to conclude that the radiative recombination rate of free excitons is much higher than the recombination rate of trapped excitons. To confirm this, temperature-dependent TR-PL dynamics integrated in energy in the range 1.5-1.8 eV (defect emission energy band) have been acquired.

Figure 2.9 reports these dynamics, showing a slow decay with a lifetime of 4 $\mu s$ at T=77 K. As the temperature increses, a faster component is detectable in the time dynamics, which can be associated to the detrapping of excitons from defect states, followed by radiative recombination of the newly formed free excitons. As the temperature increases, this recombination channel becomes more and more privileged. To unveil which are the spectral and time contributions, TR-PL maps have been acquired at 77 K and at room temperature (293 K). Figure 2.10 b) shows the TR-PL

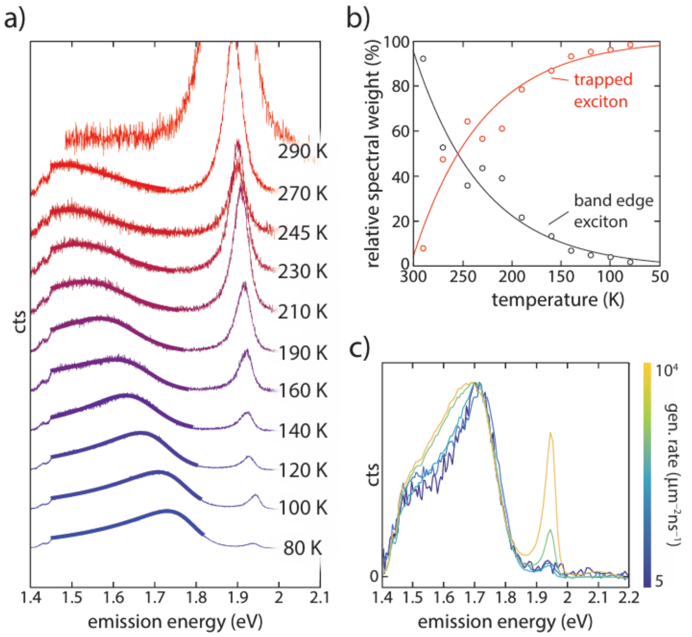

**Figure 2.8:** *PL data for chemically treated monolayer $MoS_2$ a) Temperature-dependent steady state PL spectra. Excitons trapped in defect states give rise to the broadband emission in the range 1.5-1.8 eV, which dominates the spectrum at low temperature. The sharp emission line at 1.95 eV is due to the decay of free excitons. At low temperature, this emission is barely detectable, while as the temperature increses, this feature becomes dominant. b) PL intensity, integrated in the free exciton and trapped excitons spectral ranges, as a function of the temperature. At low temperature trapped excitons dominate, at high temperature free excitons dominates. The crossover is at about 250 K. c) Power-dependent steady state PL spectra at 77 K. At low excitation power, the defects emission dominates. As the excitation power increases, the contribution of free excitons becomes relevant, due to the saturation of the defect states at high generation rates for excitons. Figure from [24]*

map acquired at 77 K, where a sharp emission at 1.95 eV with short lifetime and a broadband emission in the range 1.65-1.85 eV with a long lifetime are detectable. In this experiment, the energy per pulse and the repetition rate (76 MHz) of the excitation laser are such that the defect states are almost always saturated when a new excitation pulse arrives on the sample. This results in the short dynamics at the time zero, reflecting the true radiative lifetime of free excitons at low temperature. Figure 2.10 c) reports the PL time dynamics at 1.95 eV, and its fit with a single exponential, giving a lifetime of about 150 ps (at 77 K). Extrapolating this value at room temperature, a radiative lifetime of 580 ps can be obtained.

The TR-PL map represented in figure 2.10 a) is completely different, showing an emission at ≈ 1.9 eV, with a lifetime on the ns time scale, while the PL emission by defects is no more detectable. All this data allow to conclude that the apparent long exciton lifetime at room temperature is determined by the de-trapping of excitons from defect states, which constitute a resevour for free excitons. Since the radiative lifetime of free excitons is much shorted than the radiative lifetime of trapped excitons, when the thermal energy is sufficient to enable the de-trap of excitons, the faster radiative channel dominates the recombination towards the ground state.

This model can be described by two coupled differential equations, which describe the time evolution of the density of free excitons, $n_X$ and trapped excitons, $n_{XT}$:

$$\frac{dn_X}{dt} = R_{gen} - k_{RAD} \cdot n_X - k_{TRAP} \cdot \left(1 - \frac{n_{XT}}{N_0}\right) + k_{DETRAP} \cdot n_{XT} \tag{2.12}$$

$$\frac{dn_{XT}}{dt} = -k_{RAD}^{TRAPPED} \cdot n_{XT} - k_{DETRAP} \cdot n_{XT} + k_{TRAP} \cdot \left(1 - \frac{n_{XT}}{N_0}\right)$$

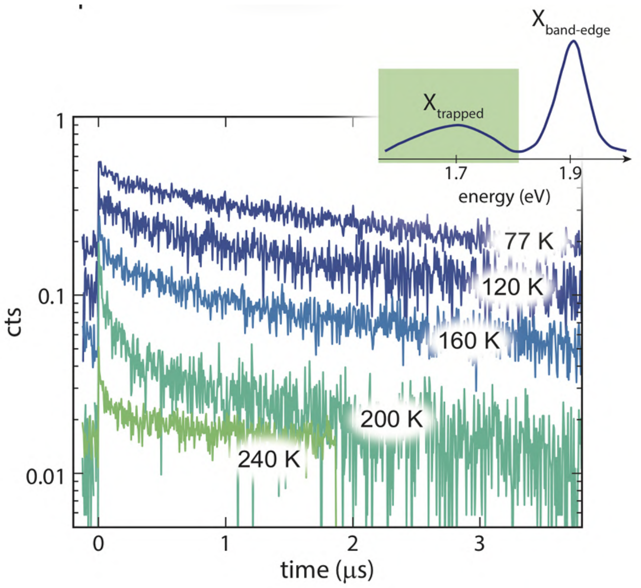

**Figure 2.9:** *TR-PL of chemically treated monolayer* $MoS_2$*. PL dynamics integrated in 1.5-1.8 eV, versus temperature. At low temperature, T=77 K, the dynamics can be fitted with an exponential decay with* $\tau_{RAD}^{TRAPPED} \approx 4\mu s$*. At 77 K the de-trapping is not relevant in affecting the PL time dynamics of this states. As the temperature increases, a faster component appears at early times, due to the de-trapping of excitons and subsequent radiative recombination of free excitons. Figure from [24].*

where $R_{gen}$ is the rate of generation of excitons, $k_{RAD}$ is the radiative recombination rate for free excitons, $k_{TRAP}$ is the rate at which excitons are trapped in defect states, $k_{DETRAP}$ is the rate at which excitons de-trap from defect states, and $k_{RAD}^{TRAPPED}$ is the radiative recombination rate for trapped excitons (of the order of 4 $\mu s$). $N_0$ is the saturation density, corresponding to the density of defect states. When the number of free excitons approaches $N_0$, defects are saturated, and the contribution of capture of free excitons $k_{TRAP} \cdot (1 - \frac{n_{XT}}{N_0})$ vanishes. The de-trap rate is related to the trap rate, by the relation:

$$k_{DETRAP} = k_{TRAP} e^{-\frac{\Delta E}{k_B T}} \tag{2.13}$$

where $\Delta E$ is the energy difference between the free exciton transition and the trapped exciton transition, and $k_B T$ is the available thermal energy. Of course there is not only one single energy level for traps, but a continuous band with a density of states. Hence, also the de-trap rate depends on the depth of the defect level, and only in first approximation it can be calculated by considering a fixed value for the energy of the defect states. This model have been used to fit the exciton TR-PL dynamics at room temperature for chemically treated $MoS_2$: by using a $k_{RAD}^{TRAPPED} = 4\mu s$, obtained by the fit of the dynamics at 77 K, Goodman *et al* [24] obtained $k_{TRAP} = 3 \cdot 10^{11} s^{-1}$ and a saturation density of $N_0 = 4 \cdot 10^6 cm^{-2}$.
It is important to highlight that this model is valid only for a chemically treated TMD, with a QY that approaches the unity, since it neglects the non-radiative recombinations due to the trapping of free excitons in defects where they fast decay non-radiatively towards the ground state. In "as-exfoliated" monolayer, this contribution is often dominant, resulting in a QY of 0.1 % for $MoS_2$ and 5-6 % in $WS_2$. The contribution of "slow defects" giving rise to the apparent long lifetime, is less relevant in these systems. However, for high quality as-exfoliated monolayers, the de-trap of excitons from this states can be important. As we will discuss in the data analysis for $WS_2$ in chapter 4, the photo-excited free exciton density rapidly decreases due to the capture in fast defect states, while the remaining free excitons follow a dynamics which can be efficiently described by the dynamic model discussed in this section. While analysing TR-PL time dynamics, the generation rate is zero after the pulsed excitation. The initial conditions for the coupled differential equations

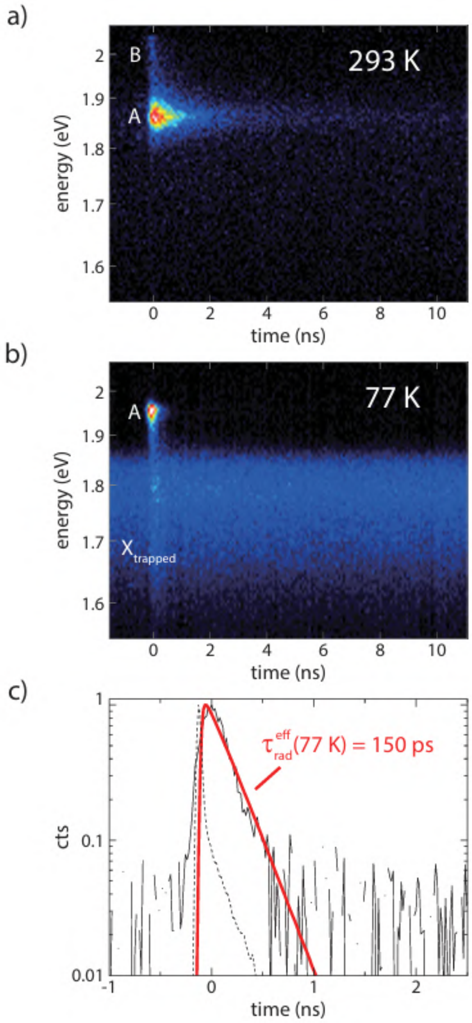

**Figure 2.10:** *TR-PL measurements for chemically treated monolayer* $MoS_2$*. a) TR-PL intensity map at room temperature shows the emission of free excitons (A and B). A slow dynamics on the ns time scale is detectable, due to the de-trapping of excitons from "slow" defect states. b) TR-PL intensity map at 77 K. The fast dynamcs at 1.95 eV is associated to the radiative recombination of free excitons immediately after the pulsed photo-excitation: since the defect states are saturated, the initial free exciton density decay via radiative recombination with* $\tau_{RAD}^{eff}$*. The almost constant signal in the range 1.5-1.85 eV is associated to the radiative recombination of excitons trapped in defect states. c) PL time dynamics at 77 K integrated in the range 1.9-2.0 eV, along with the instrument response function (IRF) of the system. The fit of this dynamics, with a single exponential convoluted with the IRF, gives an effective radiative lifetime of* $\approx 150$ *ps. Figure from [24].*

are the following:

$$n_X(0) = n_0 \tag{2.14}$$

$$n_{XT}(0) = 0 \tag{2.15}$$

i.e. the initial free exciton density is equal to the injected excitation density, while the initial trapped excitons density is zero.

Finally, it's important to note that this model neglects the role of spin-forbidden and momentum-forbidden dark excitons, which can also contribute, resulting in a modified apparent lifetime for the bright free excitons. This model will be resumed in chapter 4, when we analyze the energy integrated TR-PL data for monolayer $WS_2$.

### 2.3.2 Non hydrogen-like excitons in TMDs

Excitons in TMDs can't be treated as hydrogen-like systems (weak binding excitons) or as bound electron-hole pairs localized on single atoms or within a single unit cell (tight binding excitons). Their intermediate behaviour between these two extreme cases poses computational difficulties for the theoretical calculations [89].
As discussed in section 1.2, for hydrogen-like excitons in 2D the binding energy is 4 times larger with respect to hydrogen-like excitons in 3D (see equations 1.16 and 1.19) Moreover, in 2D the dielectric screening is reduced since the electric field lines between the electron and hole constituting the exciton extends outside the crystal (see fig 2.11 a) ) [13]. This results in an increasing of the exciton binding energy with respect to a weak binding hydrogen-like system. A scheme of the absorption spectrum of bulk and monolayer TMD is shown in figure 2.11 b), reflecting an increase in both the free particle bandgap and the exciton binding energy for the monolayer [13].
For intermediately bound excitons, there is an appreciable change in the disposition of the exciton energy levels with respect to the Rydberg-like series, especially for the ground state and for low quantum number states. The correct theoretical approach to treat these systems is very complicated and it is briefly described in section 1.2 of chapter 1. However, a possible simplified approach to use the weak binding 2D model to describe excitons in TMD consists in considering an effective dielectric constant dependent on the quantum number n of the hydrogen-like system [13]. Figure 2.11 c) reports the transition energies (up to the 5s) for excitons in $WS_2$ monolayers, obtained experimentally by reflectance contrast measurements (blue points). The theoretical energies, calculated by using the effective dielectric constant, are represented as red triangles. The continuous line represents the fit of the experimental points with an hydrogen-like model in 2D, showing that the result of the fitting is good for energies corresponding to high quantum numbers, while it fails for 1s and 2s states. The inset shows in figure 2.11 c) the value of the effective dielectric constant, as a function of the quantum number, showing that this value approach the unity for a quantum number n>3 [13].

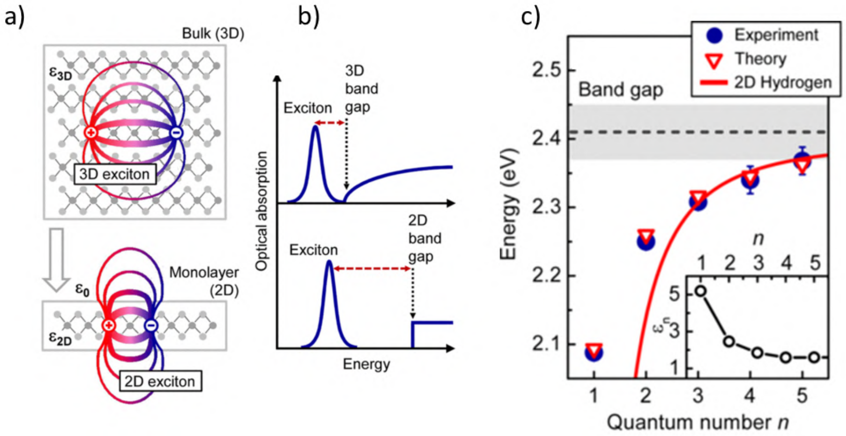

**Figure 2.11:** *a) Representation of an exciton in a bulk (3D) and monolayer (2D) TMD. b) Scheme of the absorption spectrum of bulk and monolayer TMD. c) Exciton transition energies for monolayer $WS_2$, obtained experimentally (reflectance contrast, blue points) and theoretically (effective dielectric constant, red triangles). The experimental data are fitted with a 2D hydrogen-like model. Inset of figure c) Effective dielectric constant plotted versus the hydrogen-like quantum number n. Figure adapted from [13].*

## 2.4 Theoretical calculations and experimental evidences of the excitonic Mott transition, and of room temperature electron hole liquid in monolayer $MoS_2$

In the high excitation regime, free excitons (FE) can dissociate and generate an electron-hole plasma (EHP), and at even higher densities to an electron hole liquid (EHL). Both theoretical [69] and experimental works [91, 92] have reported the possibility of the formation of a room temperature EHL in free standing monolayer $MoS_2$, under CW excitation.
Rustagi *et al* [69] have calculated the theoretical phase diagram for the photo-induced phase transitions from FE to an EHP and to an EHL. Figure 2.12 a) shows the e-h chemical potential versus the density, at different temperatures. The dashed lines represent the Maxwell construction, where a constant chemical potential value intersects the calculated chemical potential at fixed temperature, to obtain two equivalent delimited areas (the asymmetry appears because the density axis is plotted in log scale). The density value that delimit the two equivalent area regions determine the interval of coexistence of two phases in a first order transition. In our system, the two phases are FE/EHP (depending on the ionization ratio for excitons) and EHL. At T=312 K, close to room temperature, the density interval for the cohexistence of these two phases is $\approx [10^8, 3 \cdot 10^{13}] cm^{-2}$. At the critical temperature, $T_c$, the coexistence interval reduces to one single point, a critical density $n_c$. For temperatures $T > T_c$, the derivative of the chemical potential with respect to the density is always positive, and it is impossible to form a EHL. There is an empirical relation between the critical temperature for the EHL, $T_c$ and the exciton binding energy $E_b$, given by:

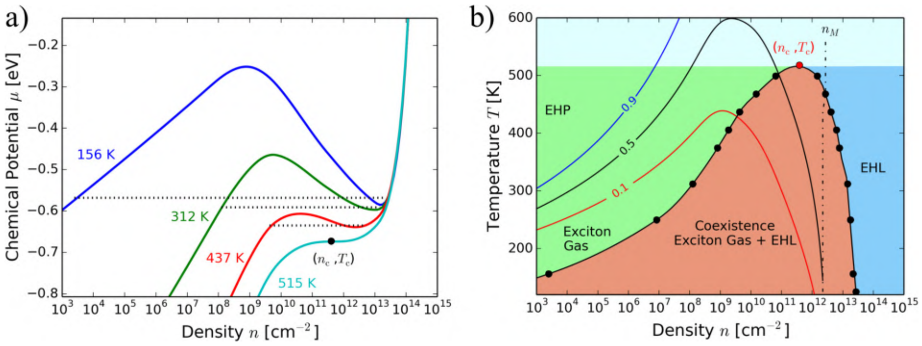

**Figure 2.12:** *a) Calculated chemical potential as a function of the number density of e-h pairs, in a freestanding monolayer* $MoS_2$*, for different temperatures. The dashed lines represent the equal area Maxwell constructions, to determine the density interval of coexistence of FE/EHP and EHL. b) Phase diagram for e-h pairs versus density and temperature, calculated by using the chemical potential curves like that in panel a). The diagram is divided in regions of density and temperature that favores the formation of FE/EHP (green), of EHL (light blue), the coexistence of FE/EHP and EHL (orange), and of a hot EHP (light blue). The curves reported in the diagram are lines of constant ionization ratio for FE/EHP, with values 0.1, 0.5 and 0.9. Figure from [69].*

$$k_B T_c \approx 0.1 E_b \tag{2.16}$$

In $MoS_2$, $E_b \approx 0.5$ eV, resulting in a critical temperature of $\approx 600$ K.
Figure 2.12 b) reports a 2D map phase diagram, versus the e-h density and temperature. To obtain this diagram, several chemical potential curves at different temperatures are used to compute the coexistence region for FE/EHP and EHL. The green area corresponds to density and temperature values that result in the formation of FE or EHP. The orange area corresponds to the coexistence of FE/EHP and EHL, while the blue area corresponds to the EHL. The light blue area, above the critical temperature, corresponds to FE/EHP. The ratio between the number of FE and the number of e-h pair in the EHP is given by the Saha ionization equation, which describe the equilibrium:

$$\frac{\alpha}{1-\alpha} = \frac{g_e g_h}{g_{EX}} \frac{1}{n\lambda_T^2} e^{-\frac{E_b'(n)}{k_B T}} \tag{2.17}$$

where $\alpha = n_e/n_{EX}$ is the ionization ratio, $n_e$ is the density of the EHP and $n_{EX}$ the density of excitons. $E_b'(n)$ is the binding energy of excitons at density n (which depends on the band gap renormalization). $g_e = 4$ is the degeneracy for electrons (spin and valley), $g_h = 2$ is the degeneracy for holes (valley) and $g_{EX} = 2$ is the degeneracy of excitons (valley). $\lambda_T = \frac{h}{\sqrt{2\pi M_{e-h}^o k_B T}}$ is the thermal de Broglie wavelength of the e-h pair. Figure 2.12 b) reports also the curves at constant ionization ratio 0.1, 0.5 and 0.9. Above the Mott density, the ionization ratio is always equal to 1. In this work, Rustagi *et al* [69] have found a critical temperature of 515 K and a corresponding critical density of $3.8 \cdot 10^{11} cm^{-2}$. At room temperature, they found a critical density of $3 \cdot 10^{13} cm^{-2}$ for the EHL.

Yu *at* al [91] report experimental evidences of a room temperature electron hole liquid in free-standing monolayer MoS$_2$, by means of steady state PL experiments.

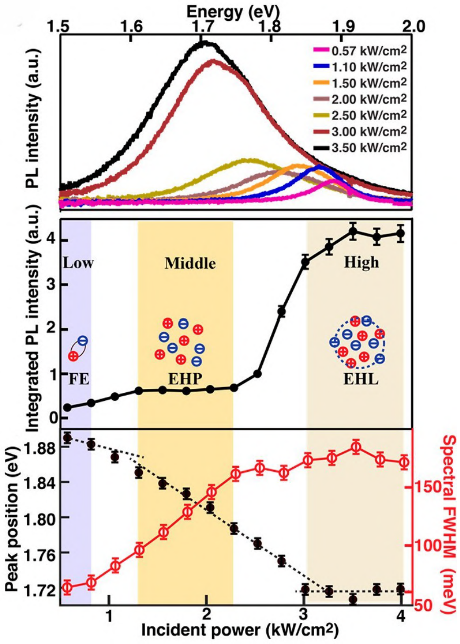

**Figure 2.13:** *Freestanding 1L-MoS$_2$. PL spectra (high), integrated PL intensity (middle), peak position and spectral FWHM (low) versus the CW laser excitation intensity. At low intensity, the PL spectrum exhibits the FE emission. As the intensity increases, the PL emission line red-shifts and broadens. For intensities higher than 3 kW/cm$^2$, the spectrum position and width don't vary. This is the typical behavior of an EHL. Figure from [91].*

Figure 2.13 reports the steady state PL spectra at several CW excitation intensity, ranging from 0.5 $kW/cm^2$ to 3.5 $kW/cm^2$. At low intensity, the PL spectrum is characterized by the sharp FE emission line at 1.9 eV. As the excitation intensity increases, the PL spectrum red-shifts and broadens, due to the bandgap renormalization and to the kinetic energy of free carriers of the EHP (the effect of temperature introduces a red-shift of $\approx$ 40 meV and broadening of $\approx$ 35 meV). At high excitation intensity, redshift and broadening saturate, resulting in a PL spectrum which is independent on further increases in the excitation intensity, typic for an EHL. The peak position and the spectral FWHM of the PL spectrum is reported in the low part of figure 2.13. This figure reports also the integrated PL intensity versus the excitation power. In the FE regime, the PL integrated intensity linearly increases, while in the EHP regime the PL integrated intensity is almost constant. At the edge of the EHP to EHL transition, the integrated PL intensity increases of about a factor 4, when the excitation intensity is increased of only the 20%. This is ascribed to the strong correlation of electrons and holes in the EHL, resulting in a higher PL efficiency [48, 64]. In this work, Yu *et al* used a CW laser at 532 nm with a spot size of $\approx 35\mu m$ as excitation source, finding a threshold intensity of $\approx 1.5 kW/cm^2$ for the FE to EHP transition and a threshold intensity of $\approx 3 kW/cm^2$ for the EHP to EHL transition. They ascribe the possibility of the formation of a room temperature EHL to high exciton binding energy and to the long carrier lifetime in free-standing monolayers. However, other experiments [2] have shown that the carrier lifetime in freestanding TMD monolayers (even in chemically treated ones) is not long enough to allow the formation of a EHL, or to easily reach a sufficient density to enable the FE to EHP transition. In [7], Bataller *et al* tried to explain the results reported in [91], by considering the thermal expansion of the crystal lattice in freestanding monolayer $MoS_2$, which results in a direct-to-indirect bandgap transition, extending the carrier lifetime by more than two orders of magnitude.

In 2023, Yu at al have performed steady state PL experiments [92] on freestanding monolayer $MoS_2$, by using a CW laser at 532 nm, with a spot size of about 1 $\mu m$, much smaller than the spot used in their previous similar work [91]. The intensity dependent PL spectra allow to identify the FE-EHP and EHP-EHL phase transitions, with intensity thresholds much higher with respect to that found in [91]. They ascribe this difference to the effect of the smaller spot size of the excitation laser, resulting in different spatial temperature profiles and in a different transport behavior of photo-carriers. Figure 2.14 shows the PL spectra measured in [92, 49] at three excitation intensities (panels a, b and c), at the center of the photo-excited area (top graphs) and few microns far away from the center of the photo-excited area (bottom graphs).

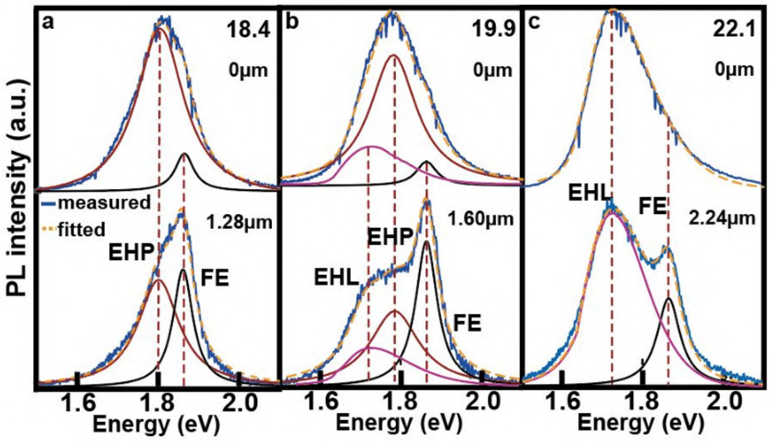

**Figure 2.14:** *PL spectra of freestanding monolayer $MoS_2$, photoexcited with a CW laser at 532 nm with a spot size of 1 $\mu m$. PL spectra at three excitation intensities (18.4, 19.9 and 22.1 $kW/cm^2$), measured at the center of the excited area (top graphs) and 1.28, 1.60 and 2.24 $\mu m$ away from the center (low graphs). The spectra are fitted including the contribution of FE, EHP and EHL. From [49], supplementary information of [92].*

At 18.4 $kW/cm^2$, the PL spectra can be fitted with two peaks, corresponding to the FE and EHP emission. Away from the center of the photo-excited area, the contribution of FE is more pronunced, due to the lower density with respect to the center. At 19.9 $kW/cm^2$, a third peak is needed to fit the PL spectra at the center and away from the center of photo-excitation. At this intensity, we have a cohexistence of FE, EHP and EHL, within the emitting area, which is characterize by a non-constant profile of density (and temperature). At 22.1 $kW/cm^2$, the spectra can be fitted with two peaks, corresponding to EHL (center of the photo-excited area) and FE (away from the photo-excited area). In this work, Yu *et al* obtain the density of the EHL at room temperature in three ways: they obtain $4 \cdot 10^{13}$ $cm^{-2}$ by fitting the PL spectra, $3.7 \cdot 10^{13}$ $cm^{-2}$ by the analysis of the bandgap renormalization, and a $4.56 \cdot 10^{13} cm^{-2}$ by theoretical calculation with a thermodinamic model to minimize the free energy per e-h pair [92].

Other experiments [75] have demonstrated a gradual Mott transition for free excitons in $WSe_2$ monolayers. They observed a PL emission line which is almost independent on the CW excitation intensity, while in the pulsed excitation regime they observed a broadening of the emission line towards lower photon energy, with a threshold fluence of $\approx 1$ $mJ/cm^2$, with an optical excitation $\approx 70$ meV below the A exciton energy $E_{EX}$ (optical bandgap).

### 2.4.1 PL dynamics for an electron-hole plasma

In the EHP regime, the recombination processes are completely different with respect to the free excitons. The equation for the e-h density writes as follows:

$$\frac{dn}{dt} = -Dn - Fn^2 - Ln^3 \tag{2.18}$$

where $D = A_{NR}$ is the non-radiative (Shockley-Read-Hall) recombination rate, related to the trapping of e-h in defect states, F is the radiative recombination rate for the EHP, and L is the non-radiative Augere recombination rate. The PL intensity is given by the radiative part of the time derivative of the carrier density:

$$I(t) = cost \cdot Fn^2(t) \tag{2.19}$$

In this case, the solution of the differential equation for the density is not trivial. However, it is possible to solve numerically equation 2.18, and to insert the solution in the equation 2.19, and to use the latter as a fit function.

## 2.5 State of the art for the exciton physics in TMDs

In TMD monolayers, strongly bound excitons dominate the optical response at room temperature and above, allowing for the investigation of the exciton physics and making these materials promising for the realization of exciton-based opto-electronic devices [54]. Theoretical calculations and experiments have been performed to determine the exciton binding energy, yielding a value in the range 0.3-0.8 eV for monolayer $WS_2$ [26, 13, 96] and 0.5-1.0 eV for monolayer $MoS_2$ [42, 91]. Bulk TMDs also exhibit a high exciton binding energy, as compared with traditional III-V semiconductors, due to their 2D character. As an example, the exciton binding energy in bulk $MoS_2$ is about 80-100 meV [37, 70], a high value compared with the exciton binding energy in silicon or GaAs.
The dependence of the exciton binding energy on the number of layers in TMD [37], as well as the effects of the substrate and of the strain have been widely investigated [40, 27, 36]. Since 2010, TR- photoluminescence, optical and photoelectron spectroscopy experiments have been performed to investigate the exciton dynamics on the sub-picosecond to nanosecond time scale, allowing to obtain the radiative and non-radiative recombination of free excitons, as well as exciton-exciton annihilation rate [57, 93, 63]. Power dependent steady state PL experiments have been performed on monoleyers $MoS_2$, showing a red-shift and broadening of the exciton emission line when the excitation power increases, signalling the transition from free excitons (FE), to an electron hole plasma (EHP) and finally to an electron hole liquid (EHL) [91, 92, 49]. However a complete study of the time evolution of the PL spectrum, in TMD monolayers, after a pulsed excitation is still lacking, expecially at high excitation density. The aim of the experimental work performed and reported thesis is to move the first steps in this direction, by investigating the TR-PL spectra of exfoliated monolayers $WS_2$ and $MoS_2$, as a function of the excitation fluence. Our preliminary results allow to observe a broadband emission with the features of an EHP at high fluence and immediately after the pulsed excitation (see the data analysis in chapter 4). However the time resolution of our TR-PL experimental system (described in chapter 3), is not sufficient to fully record the time evolution of the EHP, calling for further TR-PL measurement with a time resolution of $\approx$ 1 ps, for example using a streak camera.
The fluence range to observe the transition from free excitons to EHP spans on about one order of magnitude. On the other hand, the fluence range to observe the EHP to EHL transition is tight, and very close to the damaging threshold for TMD monolayers. For this reason, it is challenging to observe an EHL emission in time resolved photoluminescence.

# Chapter 3

# Experimental Methods

Most of the experimental work reported in this thesis have been performed at the Sprint Laboratory, a structure which is located at the Fermi building, at Elettra Sincrotrone Trieste. Sprint is a laser laboratory for ultrafast spectroscopies, among which time resolved angle resolved photoelectron spectroscopy (TR-ARPES), transient grating (TG), time resolved PL and time resolved RAMAN.
In the first section we introduce the micro- photoluminescence experimental setup, which allows to measure both the steady state (SS-) and the time resolved (TR-) PL by samples with a spatial size of few micron. We provide many details about the most important instruments used in this apparatus: the Interferometer (Gemini - NIREOS), the single photon detector (SPAD - MPD) and the fast acquisition board for the time resolution (TimeHarp260P - PicoQuant).
In the second section we provide a general overview on the Sprint laboratory, describing the pulsed light sources available, including the OPA setup to generate light in the visible range with tunable wavelength, and the High Harmonic Generation setup to produce light the extreme ultraviolet (EUV) regime. Finally we introduce the Photoelectron Spectroscopy (PES), and we present the experimental chamber for TR-ARPES.
In the third section we describe the mechanical exfoliation technique, and the transfer system for exfoliated flakes.

## 3.1 The micro- Time Resolved PhotoLuminescence setup

The micro- time resolved Photoluminescence (TR-PL) experimental setup is a new apparatus, built in the 2020 during my Master thesis in the TReX group, at the Sprint and TReX laboratory. Figure 3.1 shows the TR-PL experimental setup at the before and after the upgrades implemented during my PhD. Today, the last version of the micro- TR-PL setup is the result of the collaboration between the TReX group (Elettra Sincrotrone Trieste) and the Sprint group (IOM-CNR, NFFA project). During my PhD work, we have made many improvements to the first basic version of the TR-PL experimental setup, by adding the possibility to measure samples with a size of few $\mu m$, thus allowing to measure for example a selected exfoliated flake of a TMD. The new micro-PL setup allows also to measure the steady state photoluminescence (SS-PL), when a CW laser (instead of the pulsed laser) is used to excite the sample. In this configuration, the SPAD detector acts as a photon counter. A removable mirror, with a magnetic support, allows to easily switch from the TR- to the SS- configurations. It is also possible to perform spatial PL measurements, by using a CCD camera as a detector, placed immediately after the Gemini interferometer.
One of the most important limitations of this micro TR-PL experimental is that it allows to perform measurements only at room temperature. As a next step in the development, a cryostat could be implemented.

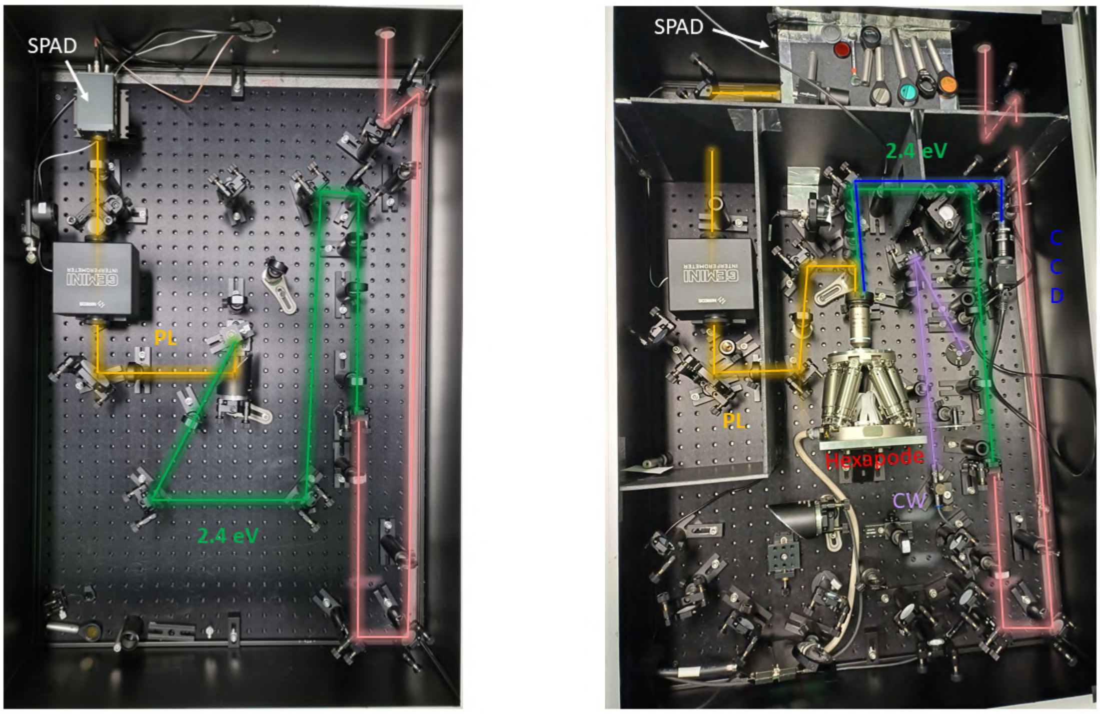

**Figure 3.1:** *TR-PL experimental setup in the summer 2021 (left), and in spring 2024 (right).*

Figure 3.2 shows a sketch of the setup for micro-PL spectroscopy. The excitation source for TR-PL experiments is a femtosecond laser (Coherent Monaco 1035-40-40), producing pulses with an energy of 40 $\mu J$ and a duration of 300 fs (FWHM), with tunable repetition rate (maximum 50 MHz), and with emission at $\lambda_0$ =1034 nm (1.20 eV). The second-harmonics at $\lambda_0/2$ =517 nm (2.40 eV) is generated in a BBO crystal and used as excitation light. A microscope objective (Magnification Ma=40X, Working Distance WD=0.6 mm, Numerical Aperture NA=0.65) is used to focus the excitation light to a 3 $\mu$m diameter spot (FWHM) on the sample. The emitted PL is collected in back-scattering geometry by the same microscope objective. A beam splitter 50%-50% allows to exploit this geometry and to drive the PL light to an interferometer (GEMINI, Nireos. See appendix 6.3) and finally to a single photon avalanche photodiode (SPAD, Micro Photon Devices. See appendix 6.5). A notch filter at 514 nm (14 nm width) is used to block the reflected and scattered laser light, which is collected by the microscope objective together with the PL. The sample is mounted on a precision piezo-electric manipulator (Hexapode, PI), which allows to move it along the optical axis of the objective (z) and in the orthogonal plane (x,y), and to rotate it around each axis. A CCD camera looks directly inside the microscope objective, showing the image of the surface of the sample, with a 40X magnification. A white light acts as an illuminator for the microscope objective, allowing to see the magnified image of the surface of the sample. This micro-PL system allows to select a specific region of the sample to measure, with an accuracy of less than 1 micron, as the minimum reproducible movement of the Hexapode manipulator is of 500 nm (more details on the Hexapode data sheet [32]).

Access to the time-domain of the PL signal is achieved via TCSPC (Time-Correlated Single Photon Counting), using a fast acquisition board (TimeHarp 260P), which receives in input two electric signals: a reference signal (sync) for the excitation laser, provided by a fast photodiode which measures the intensity of a small fraction of the excitation beam, and a signal from the SPAD detector (input), when a single photon is detected.

The spectral domain is accessed via a discrete Fourier-Transform (FT) approach [61, 60] (see appendix 6.4), using a Nireos GEMINI interferometer. In a TR-PL measurement, the Gemini Interferometer and the TCSPC system are used together to obtain PL maps versus time after excitation and emission photon energy.

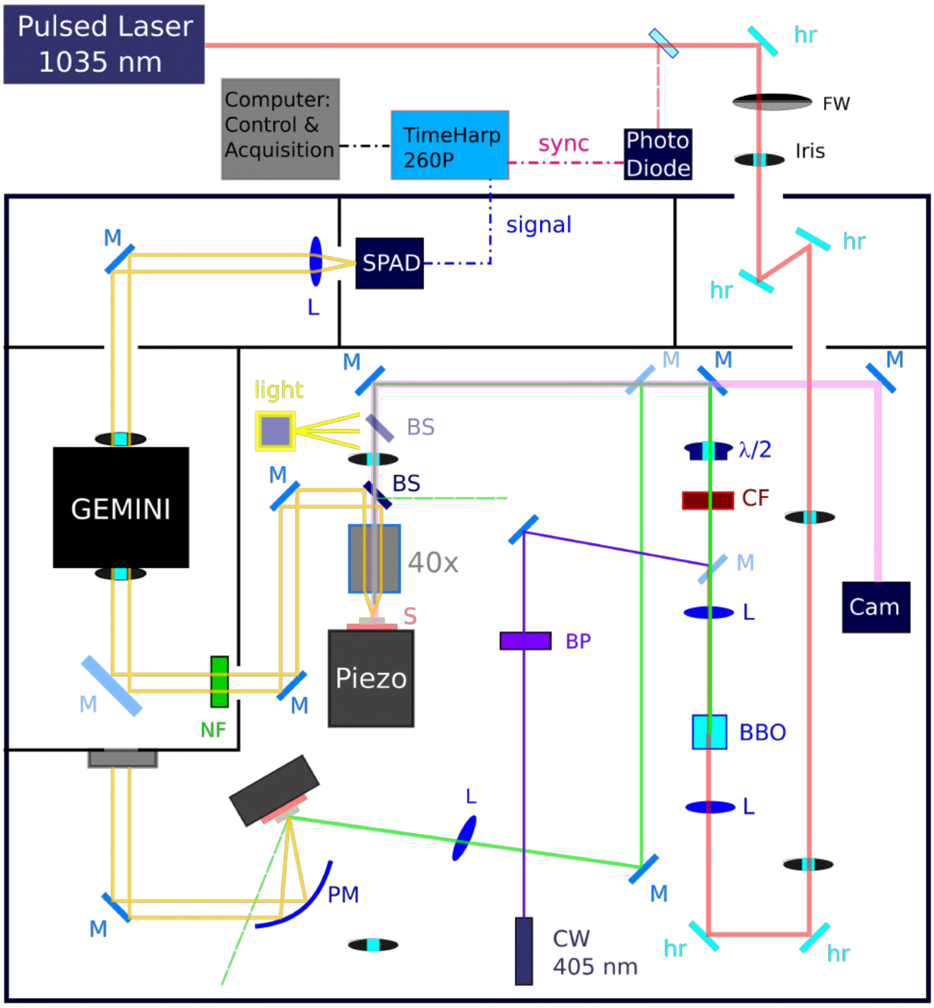

**Figure 3.2:** *Sketch of the experimental setup for steady state and time resolved photoluminescence. A femtosecond laser (coherent Monaco 1035-40-40) is frequency doubled ($h\nu = 2.40$ eV) and focused on the sample by a 40x microscope objective, for excitation. The emitted PL is collected in backscattering and driven to an interferometer (Nireos GEMINI) and then to a single photon avalanche photodiode (SPAD), connected to an acquisition board (TimeHarp 260P). The labels of the optical elements have the following meaning: L=lens; hr=800 nm dielectric mirror; Iris=pinhole iris; M=Ag metallic mirror; CF=colored filter; $\lambda/2$=halfwave plate; BS=beam splitter; 40x=microscope objective with 40x magnification; Piezo=precision manipulator Hexapode, PI; NF=notch filter at 514 nm ; GEMINI: interferometer GEMINI (NIREOS); SPAD=single photon avalanche photo diode (MPD); CW 405 nm=continous wave laser at 405 nm; BP=bandpass filter at 405 nm, with bandwidth ±1nm.*

### 3.1.1 Advantages and disadvantages of the Gemini interferometer

An interferometer has advantages and disadvantages with respect with a monochromator. The main advantages is that it can provide quickly spectral information on a broad spectral range. The interferometric approach is suitable to measure broadband spectra, and to keep an eye on what happens on the whole visible range. Moreover, this approach allows to maximize the number of photons at the detector, since all the light crosses the interferometer: the output signal is maximum in the interference maxima. The monochromator never transmit all the incoming light, even when the entrance and exit slit are completely open. Hence, the interferometer allows to easily detect and align low photon flux PL signal on the detector, especially when the light spectrum is broadband.

On the other hand, the approach with a monochromator is preferable when a high spectral resolution is required to measure sharp emission lines, in a well known spectral range. Moreover, the monochromator gives immediately access to the spectrum of the light, avoiding the Fourier transform operation.

The Gemini interferometer has several advantages with respect to a more common Michelson interferometer. The latter is subject to uncorrelated vibrations of the two mirrors, introducing an unknown casual error in the position of the movable mirror (the x axis of the interferogram). Moreover, it is difficult to align a light beam in the interferometer with an accuracy at the $\mu rad$. Beside this, it is important to take into account the reflectivity of the mirrors in the explored spectral range (or use mirrors with a constant reflectivity in that range). The Gemini interferometer has a common straight path, avoiding uncorrelated and different perturbations for the two replicas, and yielding an easy alignment. Finally the Gemini interferometer is effective in the wide spectral range where it is almost transparent, [250, 3500] nm, which includes the whole visible range. On the other hand, the calibration from pseudo-frequency to optical frequency is necessary.

The *gear ratio* of an interferometer is defined as the

$$G_{ratio} = \frac{\Delta l}{\Delta \tilde{l}} \tag{3.1}$$

where $\Delta l$ is the error on the position of the translator of the movable mirror (Michelson) or the wedge of the birefringent prism (Gemini), and $\Delta \tilde{l}$ is the error introduced on the optical path by the positioning error $\Delta l$. For a Michelson interferometer, an error $\Delta l$ on the position of the movable mirror introduces an error on the optical path equals to $\Delta \tilde{l} = 2\Delta l$, resulting in $G_{ratio} = 2$. For the Gemini interferometer, and error on the position of the wedge of the birefringent prism introduces an error $\Delta \tilde{l} = \Delta l sin\alpha \Delta n(\nu)$, resulting in $G_{ratio} \approx 50$. Hence, the error introduced by a positioning error on the optical path is about two order of magnitude lower for the Gemini interferometer.

### 3.1.2 Effects of the non-ideality of the interferometer

The appendix 6.3 reports the working principle of the Gemini inteferometer in an ideal condition, without taking into account the non-ideality of the optical (polarizers and birefringent prisms) or mechanical elements, i.e. the precision manipulator to translate the wedge of the second birefringent prism. To analyze the features of the spectra it is important to understand the impact of the possible non-ideality of the instruments on the experimentally measured spectrum of the light. To characterize the Gemini interferometer, we measured the spectrum of sources with a well known emission. As an example, we report data acquired for a laser pointer with emission at 635 nm, using an interferometer step of 0.005 mm, in the range $[0, 7]$ mm (1400 total points). Figure 3.3 reports the experimental interferogram (green dots) and a pure sine function (red dots) with the same spatial frequency of the nominal frequency of the laser pointer, in the range $[0, 1]$ mm. The right axis reports the difference between the two functions, highlighting the non-ideality of the acquired interferogram.

Figure 3.4 a) reports the FT (magnitude) of the interferogram (green curve) and the FT of the sine function (red curve). These exhibit a peak at k=33.5 $mm^{-1}$, which corresponds with the emission wavelength of the laser pointer.

However, the FT of the experimental interferogram exhibits additional peaks of lower intensity, shown in detail in figure 3.4 b). There are peaks symmetric with respect to the main peak (1 and 1', 2 and 2'), and other additional peaks (3, 4, 5).

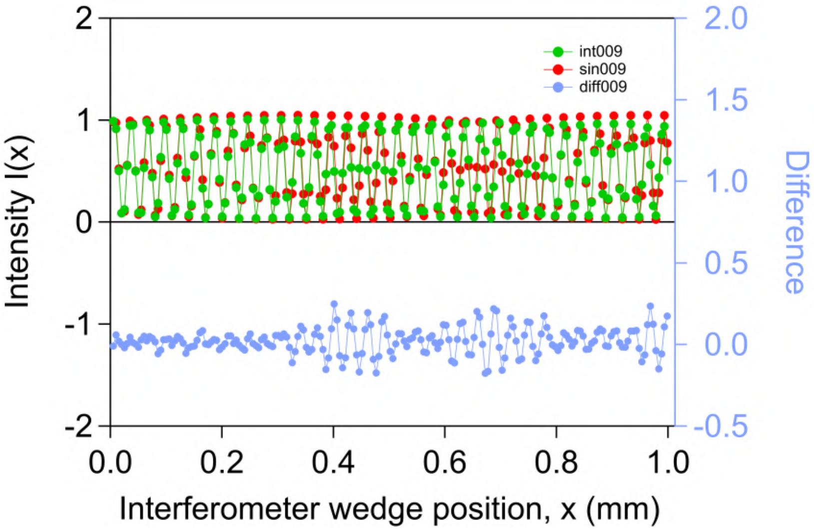

**Figure 3.3:** *Red dots) Interferogram measured with the Gemini interferometer for a laser with emission at 635 nm. The data was acquired in the range* $[0, 7]$ *mm with a step of* $0.005$ *mm. In the figure we show the* $[0, 1]$ *mm. Green dots) pure sine function, calculated at the same interferometer wedge positions of the interferogram. Light blue dots) Difference between the sine points and the interferogram points.*

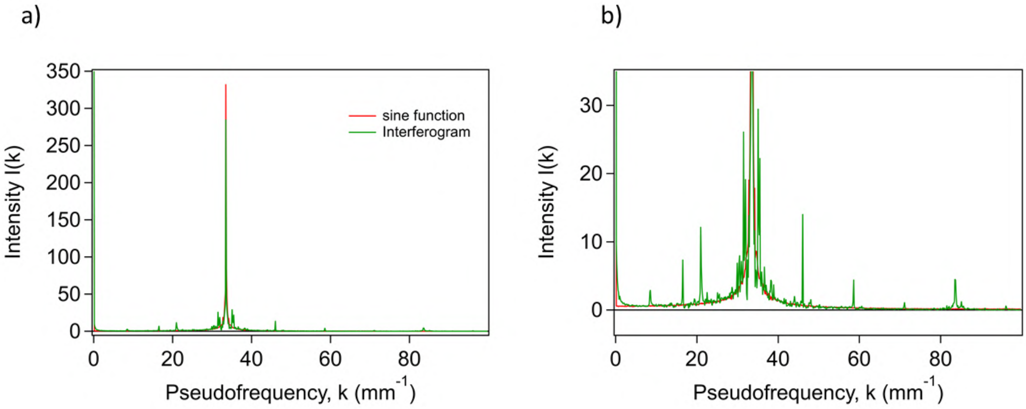

**Figure 3.4:** *a) Magnitude of the Discrete Fourier transform of the sine point series and of the experimental interferogram acquired with the Gemini interferometer for a laser pointer at 635 nm. The spatial pseudo-frequency range is [0, 100]* mm$^{-1}$ *(701 points). A sharp peak at the k=33.5* mm$^{-1}$ *is clearly detectable. b) Zoom of the graph shown in panel a), for low intensity values. Additional peaks are clearly detectable for the FT of the experimental interferogram.*

### The time instrument response function (IRF)

The instrument response function (IRF) of the TCSPC system is the time histogram obtained when measuring a light pulse with duration much shorter than the time response of our system ($\approx$ 50 ps). We measured the IRF by using the $300 fs$ pulsed laser, Monaco-1035-40-40. Figure 3.5 reports seven IRFs measured independenty and subsequently, with the GEMINI Interferometer in a fixed position, corresponding to a maximum of the interference. The red dotted curve is the IRF measured by the TR-PL map acquired for the pulsed laser, and energy integrated in the interval [2.3, 2.5] eV. The latter was acquired few months before, with a sligthly different configuration of the TR-PL setup (different positions for optical filters, different alignment of the excitation laser and of the collection optics). The main sistematic difference between this IRF and the seven IRFs is the shoulder just before the time zero.

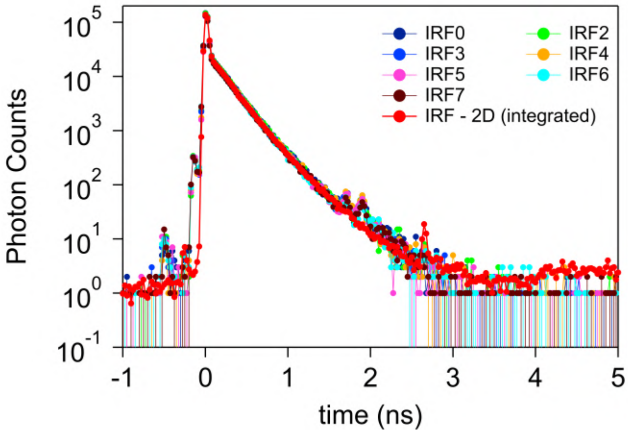

**Figure 3.5:** *IRF of the TCSPC system, in the interval* $[-1, 5]ns$*, acquired subsequently for seven times, in the same configuration for the TR-PL experimental setup. Red dots: IRF measured in a different configuration optical filters and excitation laser alignment.*

To evaluate the error on the IRF we normalized the seven IRFs to unit area, we compute the average and the standard deviation at each time. The left axis of figure 3.6 a) reports the average photon counts $\mu_{PC}$ at each time, with an error bar corresponding to ± a standard deviaton $\sigma_{PC}$. The right axis reports the ratio $\sigma_{PC}/\mu_{PC}$ at each time, allowing to estimate the relative error. Figure 3.6 b) shows a zoom around the time zero for $\mu_{PC}$ (left axis) and $\sigma_{PC}/\mu_{PC}$ (right axis).

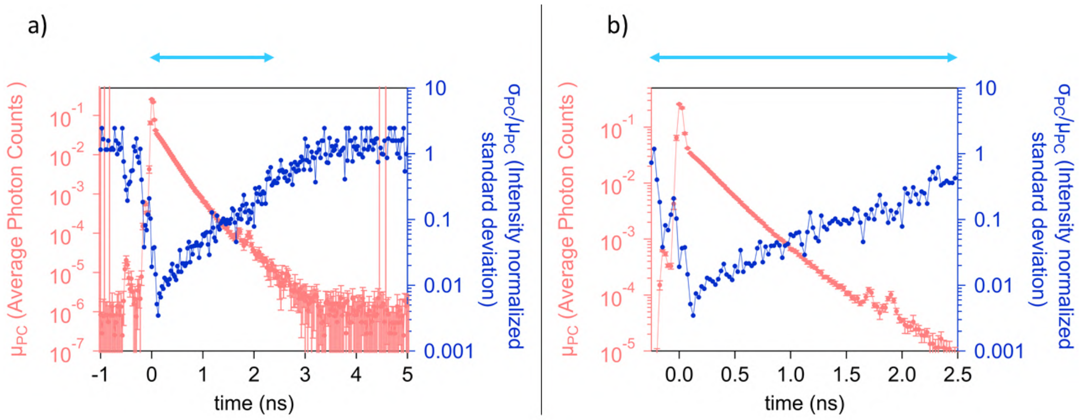

**Figure 3.6:** *a) Average of the seven IRFs reported in figure 3.5 (left axis), and ratio between the standard deviation and the average (right axis). b) Zoom in the time interval* $[-0.25, 2.5]ns$*, highlighted by the light blue arrow.*

On the raising edge (50 ps before the peak), the relative error is about 20%, and it is one order of magnitude lower on the peak (t=0 ps). Its minimum value, ≈ 0.3 %, is found at $t = 150$ ps. For $t > 150$ ps, the relative errors increases as the time increases. The features just before the time zero and at about 1.7 ns and and 1.9 ns are sistematic, since they are reproduced in the average IRF. This may be due to multiple reflections or scattering of the laser light, producing secondary pulses, more than two order of magnitude weaker than the main pulse.

### 3.1.3 Photoluminescence data acquisition

In this subsection we briefly explain how the PL data are acquired, both in a SS- and TR- measurements. All the instruments in the experimental setup are connected to a computer, and controlled by a common macro created with the software LabView.

In a SS-PL measurement the sample is continuously excited by a CW laser. We use the SPAD to count the total number of detected photons per second as we scan the wedge position of the interferometer. The parameters that can be set by the user are the range of the scan for the wedge position of the interferometer, the step between two subsequent wedge positions, and the integration time for the SPAD. The interferometer position is set to a selected initial value, the PL counts at the SPAD are recorded at this position, then the interferometer position is moved by one step, the PL counts are recorded again, and this procedure is iterated for the all scan range of the interferometer. The output raw data is a single interferogram, which after applying the Fourier transform gives the spectrum of the light.

In a TR-PL measurement, the sample is photoexcited by a pulsed laser. In this kind of measurement, we use the TCSPC system to acquire time histograms while we scan the wedge position of the interferometer. Here the user can set also the time range (length of the histogram) and the width of the bins of the histogram. The interferometer position is set to a selected initial value, a time histogram is obtained with the TCSPC system, then the interferometer position is moved by one step, another time histogram is recorded, and this procedure is iterated for the all scan range of the interferometer. The output raw data is a 2D map, the *TR- interferogram* map, where time histograms at different fixed wedge positions are attached together. A profile at a fixed time for the histogram is an interferogram at that time and its Fourier transform gives the spectrum of the light at that time. After the Fourier transform of each interferogram at each time, the final result is a 2D map, the *TR- spectra* map , which represents the PL intensity (arbitrary units) versus time after excitation and versus emission photon energy.

In a SS-PL with space resolution for the PL emission, we use a CCD as a detector to acquire images of the PL emitted by the surface of the sample. As scanning the wedge position of the interferometer the image changes due to interference. If the spectrum of the PL light is not uniform along the whole image, there are different contributions to the interferogram. Hence, by selecting different regions of interest and by integrating the signal there, it is possible to obtain different interferograms and then a spatially resolved spectrum of the PL light.

This approach has an advantage with respect to the standard SS-PL measurement with the SPAD, where all the PL signal is focused on a single pixel detector, especially when the excitation laser spot is small compared to the dimension of the region from which the PL signal is collected. The density profile of the excitation laser as well as the diffusion of excited carriers play a crucial role in the spatial resolved spectrum. On the other hand, the CCD camera is not as sensitive as the SPAD, allowing thus to measure only signal which intensity is high enough. Moreover, it is not possible to achieve the time resolution with the CCD camera, since it records a time integrated signal that can not be used as an input of the TimeHarp260 P acquisition board, and correlated to the reference signal of the excitation laser (sync).

### 3.1.4 The time resolved PL data: how to read the 2D maps

Figure 3.7 reports an example of experimental raw data for TR-PL: an *TR- interferogram map* acquired with the TR-PL experimental system, using the Gemini interferometer and the TCSCP approach simultaneously. The color map represents the PL photon counts versus time after excitation and versus the position of the wedge of the interferometer. Horizontal profiles in this maps are PL time histograms acquired at a fixed position of the interferometer: two examples are shown in the low panel of the figure 3.7. In a TR-PL measurement, this map is obtained by rows, by the acquisition of N time histograms at fixed positions of the interferometer. Vertical profiles in this map, available when the data acquisition is finished, are interferograms at a fixed time with respect to the time of photo-excitation. The right panel in figure 3.7 reports two interferograms at the time zero and at $t = 150$ ps.

The TR- interferogram maps are processed with an automatic software which performs the discrete Fourier transform of the interferograms at each time, giving access to the TR- spectrum.

Figure 3.8 represents the *TR- spectra map*, where the PL intensity (arbitrary units) is represented in color scale versus time after excitation and emission photon energy. Horizontal profiles in this maps are PL time dynamics at a fixed photon energy. Two examples of time dynamics, at 1.6 eV and 1.95 eV, are reported in the low panel of the figure 3.8. Vertical profiles in this map are PL spectra at a fixed time after the photo-excitation. The right panel in figure 3.7 reports two spectra, at the time zero and at $t = 150$ ps, given by the Fourier transform of the two interferograms shown

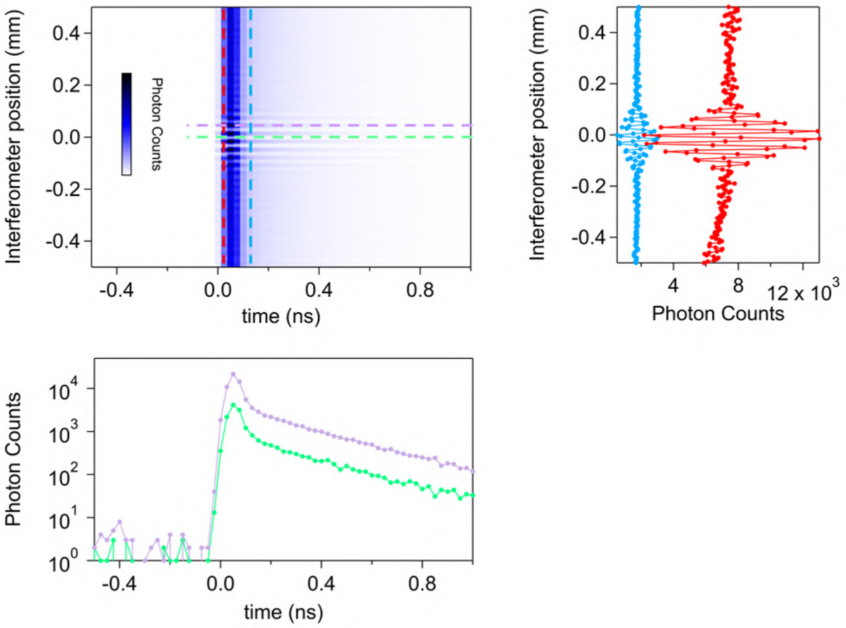

**Figure 3.7:** *TR- interferogram map, representing the PL photon counts versus time after photo-excitation and versus the interferometer wedge position. Low) Horizontal profiles at $l = 0$ mm and $l = 0.025$ mm, representing time histograms at fixed interferometer wedge positions. Right) Vertical profiles at t=0 ps and t=150 ps, representing interferograms at fixed times after photo-excitation.*

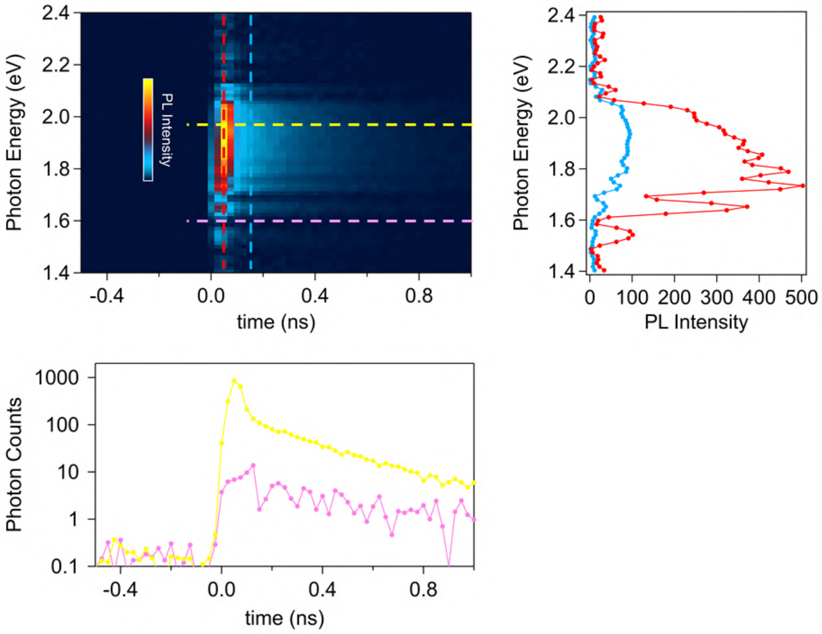

**Figure 3.8:** *TR- spectra map, representing the PL intensity (in color scale) versus time after photo-excitation and versus the emission photon energy. Low) Horizontal profiles at $h\nu = 1.6$ eV and $h\nu = 1.95$ eV, representing time dynamics at fixed emission photon energies. Right) Vertical profiles at t=0 ps and t=150 ps, representing spectra at fixed times after photo-excitation.*

in figure 3.7.
The TR- spectra maps are deconvoluted by the time instrument response function (IRF), by using the Richardson-Lucy method, discussed in section 3.1.5. As an example, we report the deconvoluted map, corresponding to the TR- spectra map shown in figure 3.8 a).

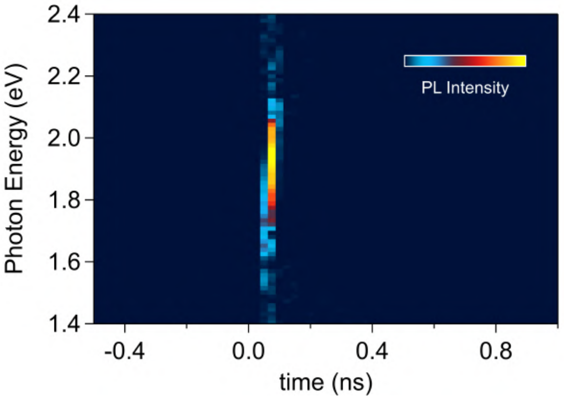

**Figure 3.9:** *TR- spectra map, obtained by the deconvolution by the instrument response function (Richardson-Lucy method) of the map reported in figure 3.8 a).*

The deconvoluted map gives access to the PL spectrum with a time step of 25 ps, the minimum bin size of the time histogram acquired with the TCSPC system (see chapter 3). However, it's important to highlight that each spectrum at time $t^*$ in the deconvoluted map is not an istantanous PL spectrum, but it is an average of the PL spectra in a time interval of width 25 ps, centered at $t^*$.

### 3.1.5 Photoluminescence data processing

In this subsection we provide an insight into the processing of the experimental raw data. In particular, we introduce the two different methods that we used for the deconvolution of the measured time dynamics by the instrument response function of the TCSPC system: the Fourier transform deconvolution and he Richardson-Lucy deconvolution.

**Fourier transform deconvolution**

This approach exploits the deconvolution theorem, which states that the Fourier transform of the convolution of two functions is given by the product of the Fourier transform of the two functions, i.e.

$$FT[f * g] = FT[f] \cdot FT[g] \tag{3.2}$$

In our measurements, f*g represents the measured signal ($S_m$), f is the instrument response function (IRF), and g is the true signal (S) that we want to obtain. Hence, we simply revert the equation 3.2, and obtain:

$$FT[S] = \frac{FT[S_m]}{FT[IRF]} \tag{3.3}$$

Finally, to obtain the true signal we perform the anti-Fourier transform:

$$S = FT^{-1}\left[\frac{FT[S_m]}{FT[IRF]}\right] \tag{3.4}$$

In figure 3.10 a) and c) we show two examples of the convolution of mathematics functions, performed analytically with the software Igor Pro. Red curves are exponential functions with short and long life-time respectively. The black curves are the IRF of our TCSPC system, and the blue curves are the convolution of the exponential functions and the IRF. This graphs show that the convolution with the IRF strongly modifies the original function. Figure 3.10 b) and d) show the original exponential functions and the deconvolution of the convoluted blue curves of figures 3.10 a) and c) respectively, performed with our deconvolution macro.
We decided to perform this test to check our deconvolution macro, and how well the original mathematical functions are reproduced after a convolution and deconvolution process. The result is good, but looking more in detail, we can see that the deconvolution adds oscillations with respect

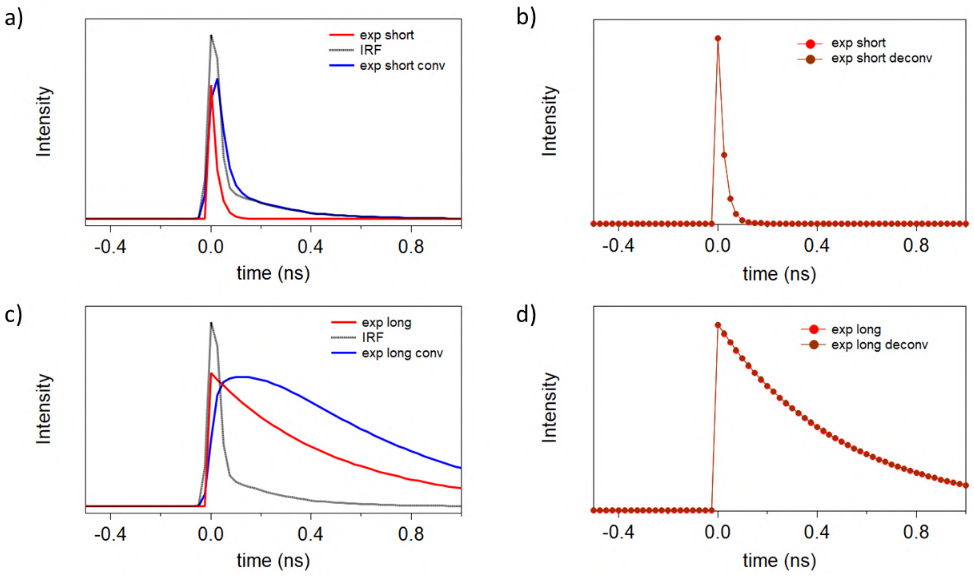

**Figure 3.10:** *a), c) Exponential functions with short and long life-time respectively (red curves), IRF of the TCSPC system (black curves) and their analytic convolution (blue curves). b), d) Exponential functions with short and long life-time respectively (red curves), and the deconvolutions of the analytic convolutions shown in panels a) an c).*

to the analytical functions. Figure 3.11 shows the exponential function with the short life-time compared with the deconvolution of the same exponential function convoluted with the IRF of the TCSPC system. This graph highlights the oscillations introduced by the convolution and deconvolution procedures.

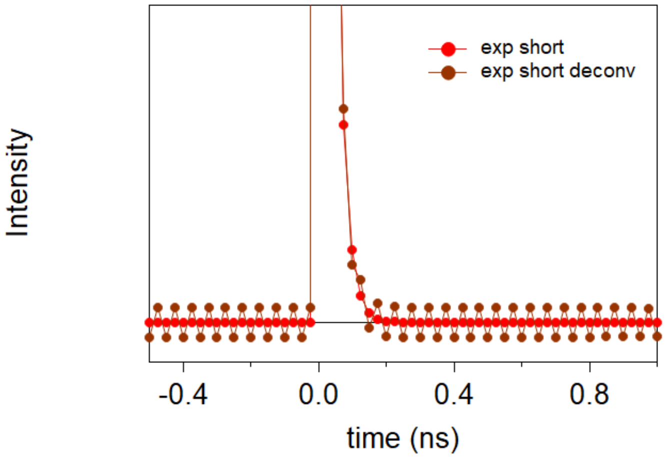

**Figure 3.11:** *Exponential function with the short life-time (red), and deconvolution of the same function convoluted with the IRF of the TCSPC system. The latter exhibits oscillations introduced by the Fourier transform deconvolution.*

Moreover, by adding random noise to the convoluted functions before using the deconvolution macro, the result get worse, as shown in figure 3.12. We added noise with an uniform distribution in the range [-0.05, 0.05] (green curve) and [-0.1, 0.1] (orange curve), where the intensity at the peak is $\approx 3.25$. The deconvolution of these dynamics exhibits oscillations that become more and more relevant, as the noise level is increased. Moreover, the noise in our measurements could be proportional to the intensity of the signal, introducing a higher (in absolute value) noise around the peak.

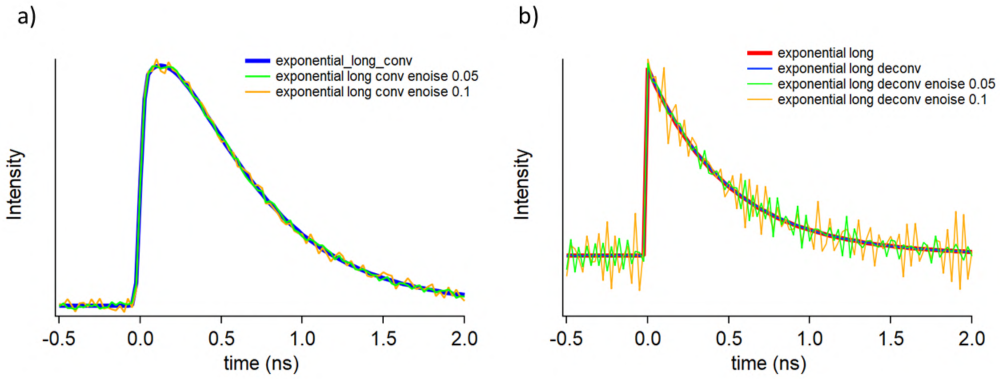

**Figure 3.12:** *a) Convolution between an exponential function and the IRF without noise (blue curve), and with two different leveles of random noise. b) Exponential function (red thick curve ) and the deconvolutions of the convoluted function without and with different random noise level shown in panels a).*

Since the PL maps are constituted by several time dynamics for each emission photon energy, an automatized Fourier transform deconvolution has been developed to process the whole PL maps energy vs time. In figure 3.13 a) and c) we show the "as measured" PL maps for a monolayer WS2, at two different fluences. Figure 3.13 b) and d) show the deconvoluted maps, using our macro with the Fourier transform approach.

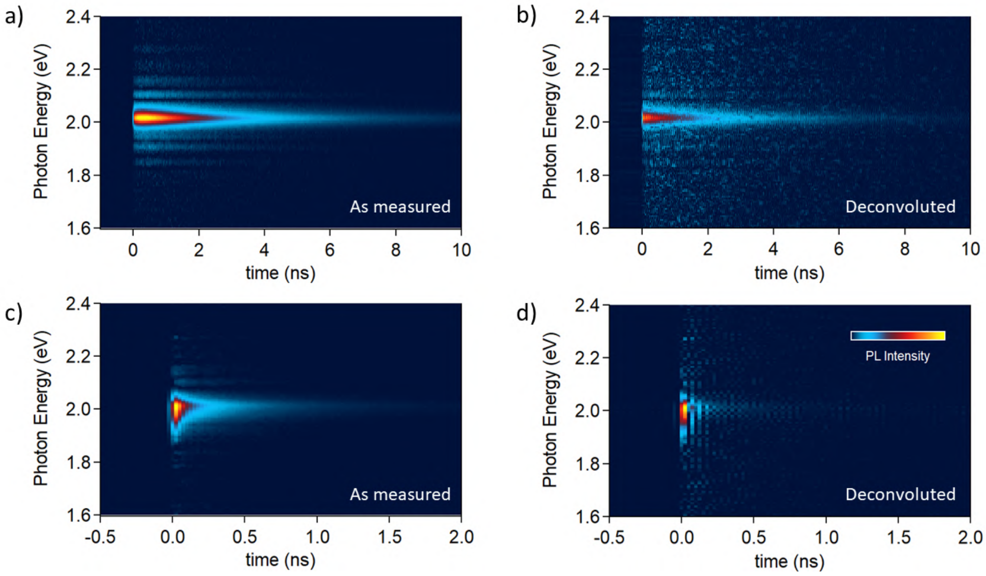

**Figure 3.13:** *a) , c) "As measured" PL maps for a monolayer WS2. b), d) Deconvolution of PL maps shown in panels a) and c) respectively.*

### Richardson-Lucy deconvolution

The Fourier transform approach for the deconvolution introduces oscillations and noise in the real time dynamics. For this reason we tried another approach: the Richardson-Lucy deconvolution. This is an iterative procedure where each point of the signal at the iteration N+1 is calculated from the same point signal at the iteration N, according to the following equation:

$$S_j^{(N+1)} = S_j^{(N)} \cdot \sum_{i=-R}^{R} \frac{Sm_i}{c_i} \cdot IRF_{i-j} \tag{3.5}$$

where $S$ is the deconvoluted true signal that we want to obtain, $Sm$ is the measured signal (true signal convoluted with the IRF), and $c_i$ is a coefficient calculated as

$$c_i = \sum_{i=-R'}^{R'} IRF_{i-j} \cdot S_j^{(N)} \tag{3.6}$$

The values of R and R' for the indexes i and j are chosen to include all the values such that the "scalar products" ( $< S_m, IRF >$ and $< IRF|S >$) differs are significantly from zero. The result of the Richardson-Lucy deconvolution is probabilistic, and it depends on the number of iterations, $N$. If the procedure converges, for $N > \bar{N}$ the result of the Richadson Lucy deconvolution converges to the maximum likelihood.

Figure 3.14 a) and b) shows the deconvolution of two measured PL time dynamics with the Fourier transform (FT) and Richardson Lucy (R-L) methods. The result is similar, showing the same trend for the data. However, the Fourier transform methods clearly introduces strong oscillations in the intensity of the signal, up to one order of magnitude for subsequent points. The R-L deconvolution also introduces noise with respect to the measured data, but the result of is much better, especially at times close to the time zero $t_0$.

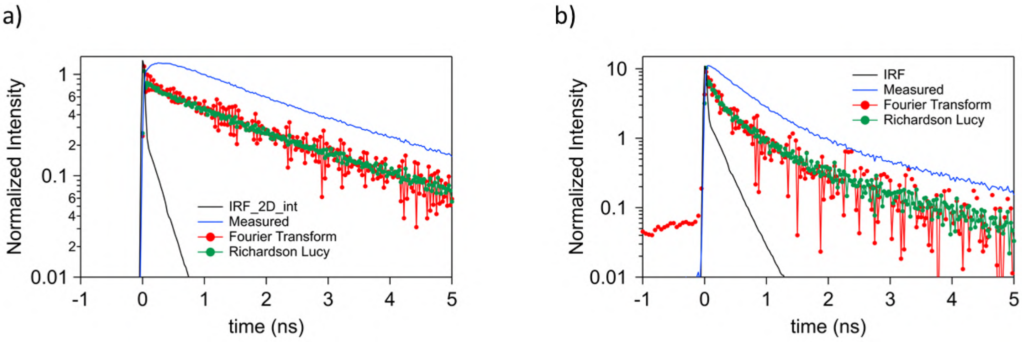

**Figure 3.14:** *Measured PL time dynamics (blue), IRF (black), and comparison between Fourier transform (red) and Richardson Lucy (green) deconvolutions.*

The FT deconvolution method is effective to reveal the "real" dynamics of the experimental data at long times, and it has the advantage that it require much less time for the computation with respect to the R-L method, allowing to deconvolve TR-PL maps (1000 time values x 150 photon energy values) in few hours. On the other hand, the Fourier trasform deconvolution does not give a good result for the spectra at times close to $t_0$. Figure 3.15 shows an example of TR- spectra at four subsequent time delays, obtained after the deconvolution of the whole PL map, with the two approaches. While at t=25 ps and t=50 ps the results are similar, the spectra at 0 ps and 75 ps obtained with the FT method are not clear, as they exhibit a negative intensity in the spectral range of interest, due to the oscillations introduced by the FT. In contrast, the result of the R-L deconvolution is good at every time around $t_0$. On the other hand, the deconvolution of a whole map with the R-L method requires a much longer computation time with respect to the FT method.

Figure 3.16 shows an example of two TR-PL maps (monolayer $MoS_2$ at high fluence, in chapter 4 we will encounter again these TR- spectra), deconvoluted with the two methods, in the time interval [-0.5, 1.0] ns. The R-L deconvolution is the more accurate approach for both the time evolution of the spectrum and the time dynamics. The R-L approach is particularly effective when the TR-PL maps exhibit a short dynamics with a significant time evolution of the spectrum. Hence, we used this method to deconvolve the TR-PL maps to analyse the time evolution of the spectra in

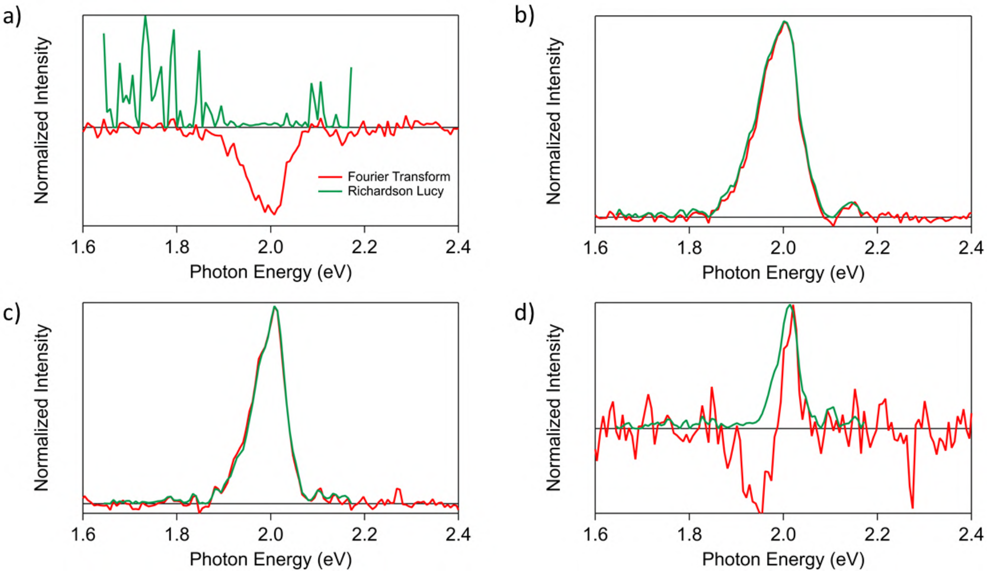

**Figure 3.15:** *PL spectra at four subsequent times (step 25 ps), obtained by the deconvolution of the PL map with the Fourier transform method (red) and Richardson Lucy method (green).*

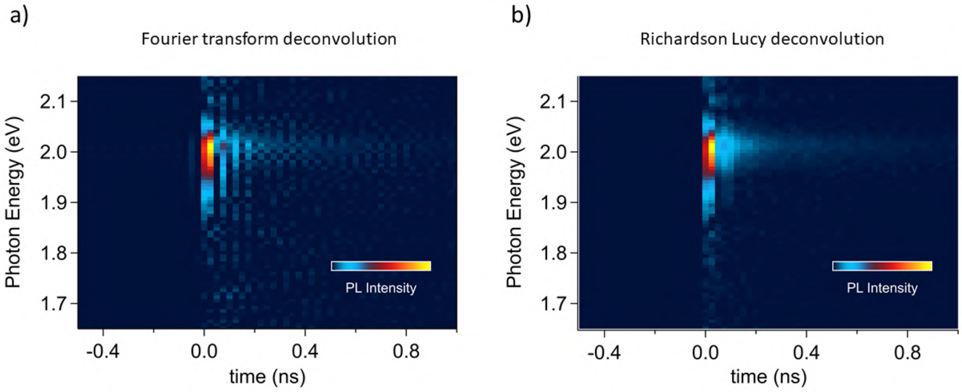

**Figure 3.16:** *TR-PL maps, deconvoluted with FT and R-L.*

a small time interval around $t_0$. We also used this approach to deconvolve every energy-integrated PL dynamics, in the full time range (it does not require too much time to deconvolve one single time dynamics with R-L). Instead, we used the FT approach to deconvolve TR-PL maps that exhibits a long dynamics and a poor time evolution of the spectrum around $t_0$. Finally it is useful to compare the results obtained with two different methods, to have a confirm on the results of the deconvolutions.

### 3.1.6 Effects of the IRFs on the R-L deconvolution

We computed the R-L deconvolutions of a selected PL time dynamics using the seven different IRFs reported in figure 3.5, to evaluate the fluctuations of each point. The average of these seven deconvoluted dynamics, and their normalized standard deviations (i.e.the standard deviation on each time divided by the average intensity at that time) are shown in figure 3.17.

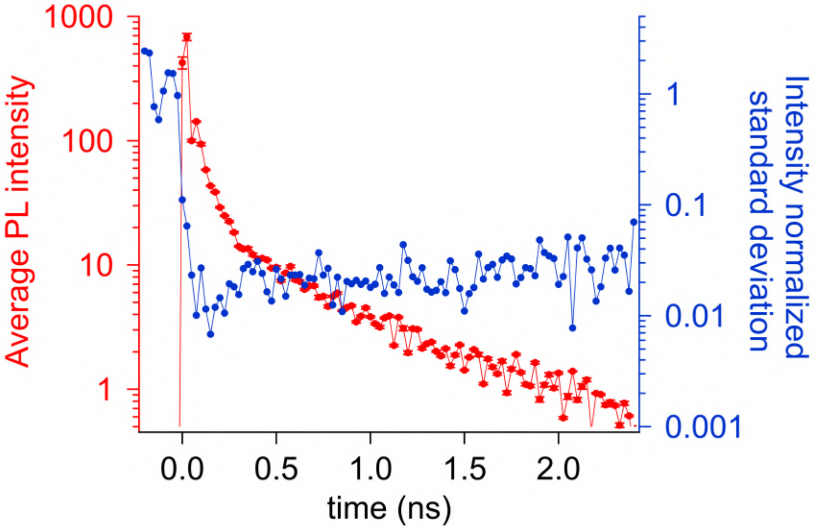

**Figure 3.17:** *Average of the deconvolutions of the same PL time dynamics, performed with the seven different IRF, acquired subsequently in the same experimental conditions, and reported in figure 3.5 (left axis). Normalized standard deviation on each point of the deconvoluted time dynamics (right axis).*

Before the time zero, the relative error is about the 100%, while for $t \geq t_0$ the error decreases below the 10%. For $t \geq 100$ ps, the relative error is about the 1-2 %.
On the other hand, it's important to point out that when anything is modified in the TR-PL setup (optics, optical filters, excitation beam alignment), it is fundamental to acquire the new IRF to perform the deconvolution. Figure 3.18 shows how the result of the deconvolution vary significantly using the IRF acquired in the same condition of the TR-PL measurement, and another IRF acquired in different conditions (without an optical filter, ND 1.0).
In figure 3.18 a) and b) the two IRFs are shown in a wide and tight time range. The latter exhibits a small difference around $t_0$, where the points of the IRF1 are "in advance" with respect to the IRF2. Figure 3.18 c) and d) reports the difference between the TR-PL map deconvoluted with the IRF1 and with the IRF 2, where the blue color is related to a positive difference, the red color is related to a negative difference. This implies that before $t_0$, the difference is negative (raise edge: IRF1>IRF2), while after $t_0$ the difference is positive (IRF2>IRF1). Figure3.19 shows the spectra at $t = 0, 25, 50, 100$ ps, deconvoluted with the two IRFs, and their difference.
These data allows to conclude that using a IRF1 in advance with respect to an other IRF2, the deconvoluted spectra with IRF1 appears to be in advance with respect to that deconvoluted with the IRF2.
This analysis allows to conclude that the IRF is critical to determine the result of the deconvolution, and it hihglights the necessity to always use the correct IRF to obtain a the correct result. To ensure this, when anything is changed in the TR-PL setup, the new IRF should be measured and associated to the experimental data acquired in that precise configuration.

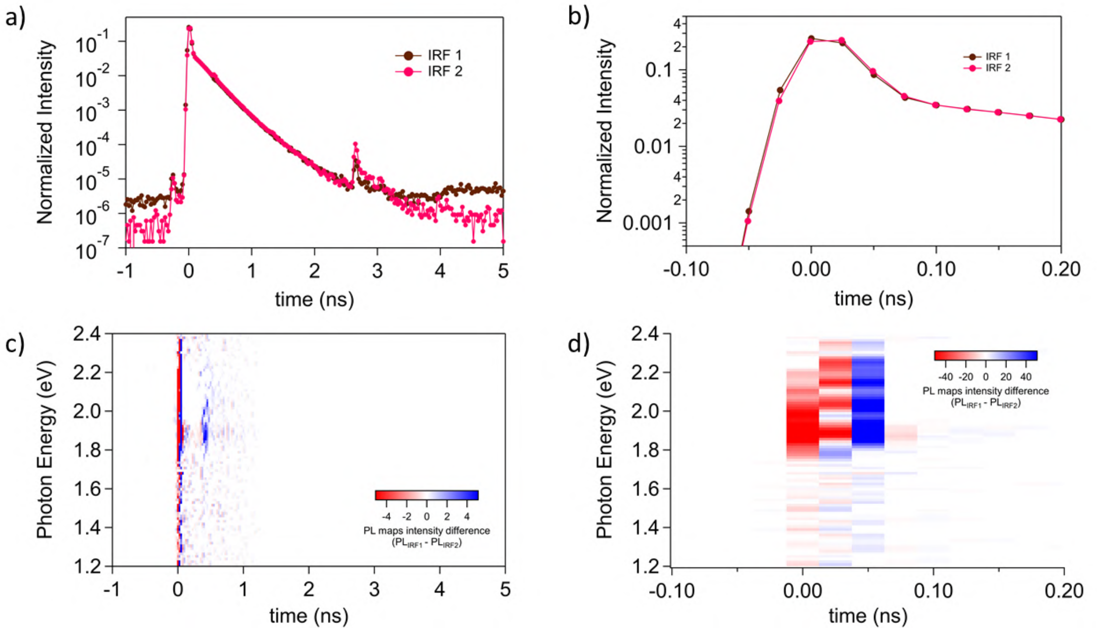

**Figure 3.18:** *a, b) IRF measured with two different dispositions of the optical elements in the TR-PL experimental setup. c) Difference map, between the deconvoluted map obtained by using the same raw data and the two different IRF shown in panels a and b. d) Zoom around the time zero of the difference map shown in panel c.*

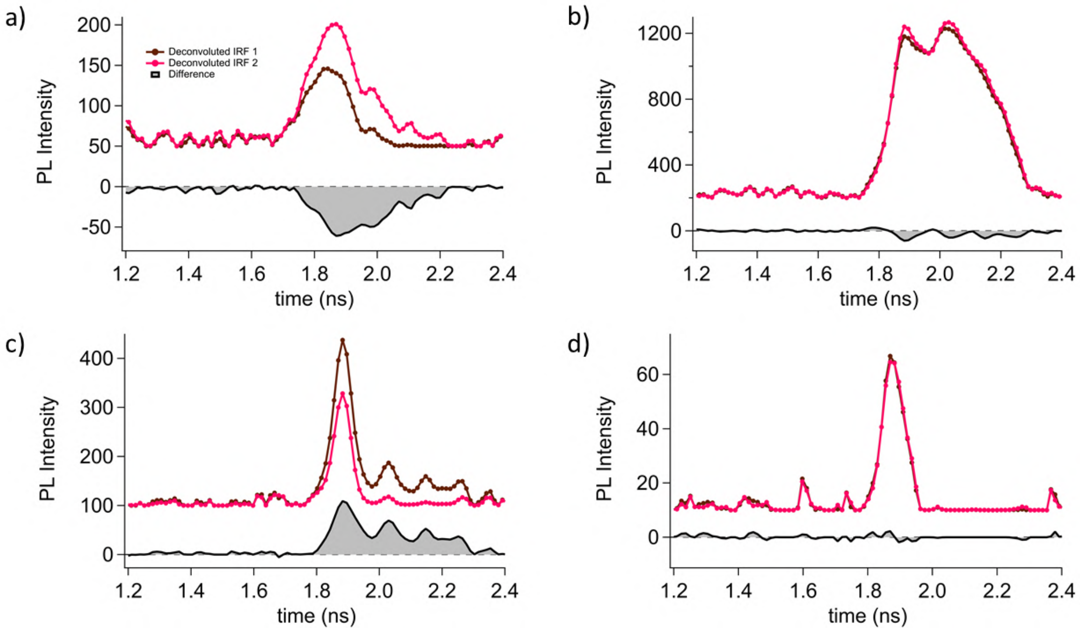

**Figure 3.19:** *TR- spectra at t=0 ps, 25 ps, 50 ps and 100 ps, extracted by the TR- spectra map deconvoluted with the two different IRF, shown in figure 3.18 a) and b).*

### 3.1.7 Clarification on the quality of the experimental data

As we show in sections 3.1.3, 3.1.4 and 3.1.5, the final TR-spectra maps are obtained after a two mathematic operations: the discrete Fourier transform of the interferograms at each time delay and the deconvolution of the time dynamics by the time IRF, at each emission photon energy. In particular, the latter introduces noise in the original experimental data. Hence, we highlight that the quality of the data may be improved by the optimization of the data processing, for example by finding the exact number of iterations for the Richardson-Lucy deconvolution to converge (additional iterations introduce noise).

Moreover, the non-ideality of the Gemini interferometer, discussed in section 3.1.2, introduces additional systematic features and peaks in the PL spectra.

To remove these features it would be possible to try to perform another deconvolution by the spectral IRF, which can be obtained by measuring the spectrum of a monochromatic source, with the same spectral resolution (interferometer scan range) used for the experimental data. However, this operation again would introduce additional noise to the PL spectra.

In the future, our aim is to optimize the data quality, and to keep under control every non-physical effect introduced by this new TR-PL experimental system.

## 3.2 The TR-ARPES apparatus at the Sprint laboratory

The Sprint laboratory is a facility which has been projected and developed within the NFFA Trieste project, and it is situated at the Fermi experimental hall, at Elettra Sincrotrone Trieste. The Sprint beamline allows to perform time resolved angle resolved photoelectron spectroscopy (TR-ARPES) experiments in the ultrafast time domain, using pulsed and coherent ultrashort light sources with tunable wavelength, in the IR to EUV spectral range.

### 3.2.1 Introduction to Photoelectron Spectroscopy

Photoelectron Spectroscopy (PES) is a surface sensitive experimental technique based on the photoelectric effect. A light source is used to trigger the emission of electrons by the sample, with a kinetic energy which is given by

$$E_k = h\nu - E_B - \Phi \tag{3.7}$$

where $h\nu$ is the photon energy of the light, $E_B$ is the binding energy of the photo-emitted electron with respect to the Fermi energy, and $\Phi$ is the work function, i.e. the energy required to extract from the material an electron at the Fermi level with zero kinetic energy. This *photon in-electron out* technique gives access almost directly to the occupied electronic states in matter. The Angle Resolved Photoelectron Spectroscopy (ARPES), opens the possibility to measure simultaneously the kinetic energy and the angle of emission of the photo-emitted electron. When measuring a crystal, the angle of emission gives access to the crystal momentum of the electron along the plane of the surface:

$$k_{//} = \sqrt{\frac{2m_e}{\hbar^2}}\sqrt{E_k} sin\theta \tag{3.8}$$

The knowledge of the $k_{//}$ and $E_k$ gives access to the electronic band structure of the material up to the Fermi level, while the unoccupied states are not accessible in a stationary ARPES measurement. The pump-probe approach allows to access also these unoccupied states, and to investigate their dynamics, in the so called Time Resolved ARPES (TR-ARPES). We use two ultra-short light pulses: the first pulse is named *pump*, and it is used to excite the sample in an out-of-equilibrium condition. The second pulse is named *probe*, and it is used to measure the out-of-equilibrium property of interest. By varying the time delay between the pump and the probe, it is possible to access the ultra-fast time dynamics of the investigated properties.

In the pump-probe TR-ARPES, the pump pulse in the infrared to visible range is used to transiently populate excited electronic states within the band structure of the material, while the probe pulse, in the UV to EUV range, is used to trigger the photoemission of electrons.

### 3.2.2 The light sources at the Sprint laboratory

The main light sources at the Sprint Laboratory are two twin table-top femtosecond lasers (Pharos master and Pharos slave, Yb:KGV), producing 300 fs (FWHM) pulses with $400\mu J$ energy per pulse and with emission at $\lambda_0$ =1030 nm (1.20 eV). The maximum repetition rate that preserves the energy per pulse is 50 kHz, and it be reduced by using a divider (pulse picker). On the other side, the repetition rate can be increased from 50 KHz up to 1 MHz (x20), with a proportional reduction (/20) of the energy per pulse.

The two Pharos laser's outputs are driven to different optical setups to manipulate and tune the light to use in every experiment, for both the pump and probe beams.

The first of these is the optical parametric amplifier (OPA) setup, where the ORPHEUS-F OPA (Light Conversion) is used to achieve a tunable pump beam in the spectral range $[640, 2550]$ nm ([0.48, 1.94] eV). If a higher photon energy is required, we use a nonlinear crystal to double-frequency the OPA light, allowing to extend the spectral range down to 320 nm (3.87 eV). The ORPHEUS-F OPA is also equipped with a pulse compressor, allowing to obtain pulses between 30 and 50 fs, depending by the selected wavelength.

Finally at the Sprint laboratory we use the Pharos laser to produce extreme ultraviolet (EUV) light, by means of *High Harmonics Generation* (HHG). This is a non-linear process where an ultra intense light beam is focused on a target (gas, plasma), giving rise to the generation of high odd harmonics.

Figure 3.20 shows a scheme of the experimental setup for the TR-ARPES. The pump pulse is produced by the Pharos master and driven to the ORPHEUS-F OPA and to a pulse compressor, to tune the wavelength and to compress the pulse duration down to the transfor limited value. Then the pump pulse passes through a delay line and finally it is focused on a spot of about 300 $\mu m$ on the sample. If needed, we use a telescope and a BBO crystal to double frequency the pump pulse. The probe pulse is produced by the Pharos slave, which is locked in phase with the Pharos master. We drive its second harmonics at 2.4 eV to the HHG *generation chamber*, where a Argon gas jet is generated with the use of a nozzle to produce a small region with a pressure of 3 to 6 bars. By focusing the laser beam on this region, if the intensity is sufficiently high, the Argon gas leaf generates the high (odd) harmonics of 2.4 eV (up to the $13^{th}$), with a pulse duration down to 100 fs. In the generation chamber the Argon pressure is so high only next to the nozzle, while it decreases rapidly with the distance, down to $10^{-4}$ mbar. This is important to allow the propagation of the just generated EUV light towards the monochromator chamber (pressure $10^{-7}$ mbar), where a grating allows to select the harmonics to send to the experimental chamber, and to use as probe. Finally, the EUV probe beam is focused on the sample on a spot of about 100 $\mu m$, with spatial overlap with respect to the pulse beam.

The experimental chamber for ARPES at the Sprint laboratory is equipped with an hemispherical electron energy analyzer (Scienta SES 2002). The energy resolution of the analyzer is determined by the width of this slit. At the Sprint laboratory, the analyzer slit width is tunable (in the vertical direction) down to 200 $\mu m$, corresponding to an energy resolution of 10 meV. The sample is mounted on a precision manipulator, which allows to move it by software. We can translate it along x,y,z directions and rotate around the z axis (vertical). Recently we implemented the possibility to rotate (tilt) the sample also along the horizontal axis parallel to the surface of the sample, allowing to vary the "fixed" angle $\vartheta_y$ in a measurement. The analyzer can operate in fixed mode or swept mode for the kinetic energy. In the fixed mode, we set the pass energy and we select a fixed kinetic energy window centered at $E_k^{(0)}$ and with a width of 0.9 eV. An system of electrostatic grids and lenses allows to manipulate the photoemitted electrons to set $E_k^{(0)} = E_p$. In

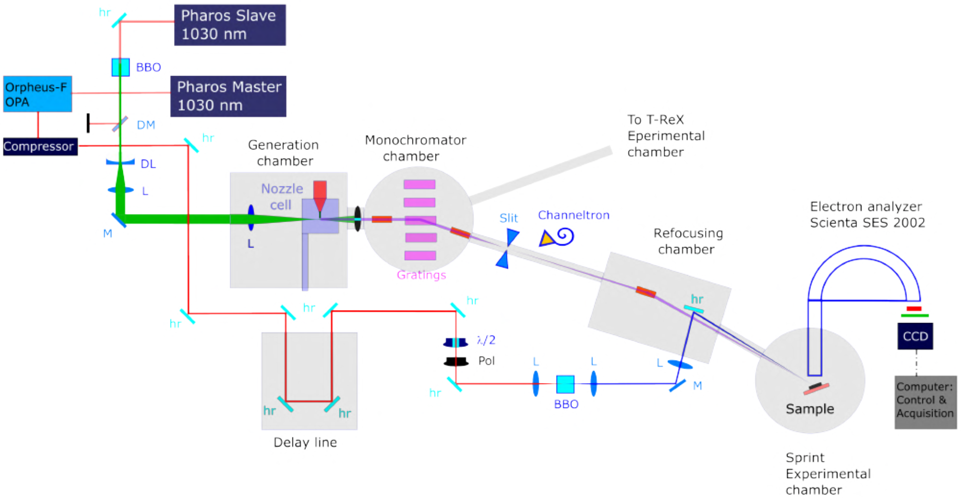

**Figure 3.20:** *Scheme of the TR-ARPES experimental setup, at the Sprint laboratory. Pump: the femtosecond lasers Pharos master is driven to an OPA and a pulse compressor, it crosses a delay line and it is finally focused on the sample (if higher photon energy is needed, the second harmonic is generated in a BBO crystal). Probe: the SHG of the femtosecond lasers Pharos master is driven to a generation chamber and focused on a Argon gas nozzle for the high harmonic generation; the desired harmonic is selected with a grating and finaly focused on the sample. The labels of the optical elements have the following meaning: L=lens; hr=800 nm dielectric mirror; Iris=pinhole iris; M=Ag metallic mirror; DM=dielectric mirror with high reflectivity at 1030 nm ; λ/2=halfwave plate; Pol=linear polarizer; BBO=non linear crystal for second harmonic generation.*

the swept mode, we perform a scan in kinetic energy, by varying the voltage of electrostatic grids and lenses.

A micro channel plate (MCP) detector is placed at the exit of the electron analyzer. This device is a 2D array of electron multipliers, capable to detect single electrons with spatial resolution. When a single electron is detected, the amplified signal of the MCP is able to excite a phosphorous screen (watched by a CCD camera) in a specific position $(E_k, \vartheta_x)$, related to the kinetic energy and the angle of the photoelectron.

Beside the experimental chamber, at the Sprint lab there is a preparation and characterization chamber. Here we can clean and prepare the surface of the samples via sputtering with Ar+ iones and annealing with irradiation, electronic bombardment or current flow. LEED and Augere systems are available to check the surface of the samples, both from a structural and chemical point. Finally we can perform *in situ* growth of new surface structures by means of evaporators (examples gold or tin), or via exposion of gas (example oxygen or etylene) in the preparation chamber.

## 3.3 The transfer system for exfoliated flakes

In this section we describe the exfoliation technique and the transfer system that we used to prepare the samples for the PL measurements. We exfoliated monolayers of $WS_2$ and $MoS_2$ from a bulk crystal (HQ graphene), using a scotch tape of polyethilene (PE) film coated with a pressure sensitive acrylic-based adhesive (NITTO).
In the exfoliation procedure, depicted in figure 3.21 we use a piece of tape on the bulk Van Der Waals crystal, to remove some layers from the surface. We iterate this procedure about 3-4 times, until we see by eye a thin layer of TMD powder on the tape. Finally we place this tape on a PDMS polymer, to deposit part of the exfoliated material.

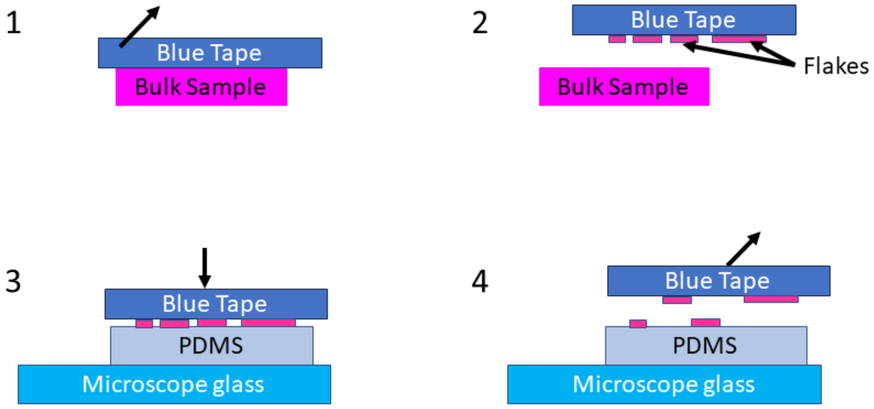

**Figure 3.21:** *Schematic representation of the exfoliation of TMD flakes from a bulk crystal (1 and 2), and deposition on a PDMS polymer sticked on a microsope glass (3 and 4).*

Figure 3.22 shows an example of exfoliation of $MoS_2$. A photo of the bulk sample is shown in panel a), while panel b) shows a photo of every step of the exfoliation procedure, from the bulk sample to flakes on the PDMS. Panel c) shows a zoom on the first, second and third exfoliation, and of the PDMS. Panel d) shows the 5x magnified optical image of the PDMS with $MoS_2$ flakes.
By looking at the PDMS with the optical microscope, we can see several flakes of TMD, of different shape, roughness and thickness, depending on how the flake breaks away in the exfoliation procedure. Since the reflection and transmission of light by the flake is related to its thickness, proportional to the number of layers, it is possible to identify thin flakes by eye, and even to distinguish a monolayer from a bilayer.
Figure 3.23 b) shows an optical image (with 20x magnification ) of the surface of a PDMS polymer with a flake of $WSe_2$, where it is possible to identify a bulk, a few layer, a bilayer and a monolayer. We should point out that the identification by eye is not 100% reliable, and that characterization techniques, like PL, raman or STM, are needed to identify the exact number of layers. Figure 3.23 b) reports the steady state PL spectra for the monolayer, bilayer and bulk $WSe_2$ of the flake shown in the image of panel b). By the comparison with PL spectra found in literature [77] we can associate the mearured spectra to that of a monolayer and bilayer. As expected, the spectra for the bulk differs from that of the trilayer reported in [77], with a shift at lower photon energy, in agreement with the reduction of the indirect band gap as the number of layers increases.
After identifying, through microscope inspection, a monolayer or few-layer candidate, it is possible to transfer it on a selected substrate, such as SiO2, diamond, or even on a patterned surface of Si, with holes of 5-10 micron diameter, to obtain a freestanding flake.
We use a transfer system which scheme is depicted in figure 3.24. There are two stages which can be separately translated along x, y, z directions and rotated around the z axis by an angle $\theta$. Moreover it is possible to translate all the system along x and y directions.
The substrate is placed on the stage 2, with the surface facing upwards. The PDMS with TMD flakes on its surface, facing downwards, is sticked on a microscope glass which is fixed on the stage 1. The substrate and the PDMS must ba placed approximately at the same x,y coordinated, and

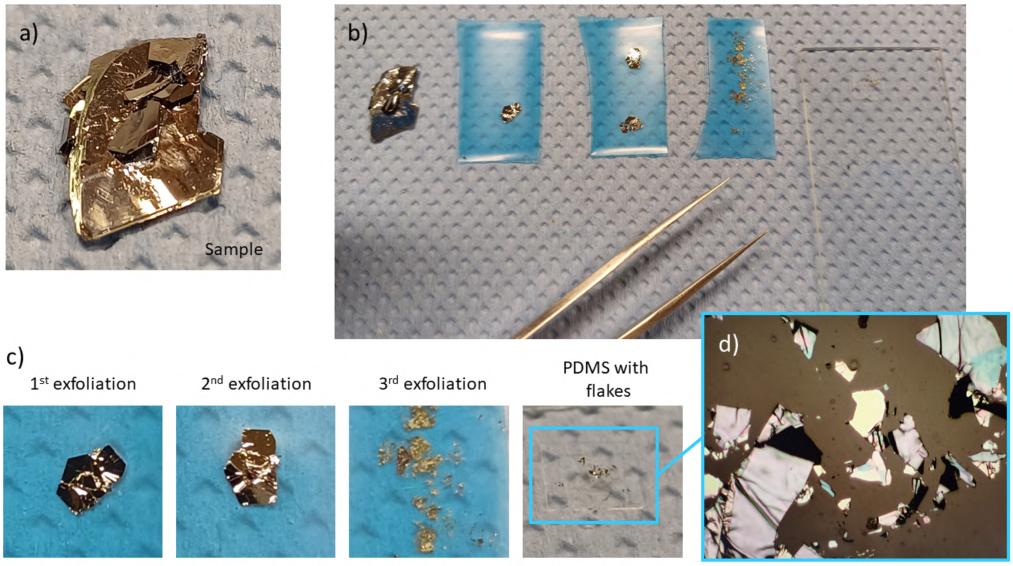

**Figure 3.22:** *a) Sample of* $MoS_2$*, by HQ-graphene[30]. b) exfoliation sequence: from the bulk sample to TMD powder on the PDMS polymer. c) Zoom of the exfoliated materials, in the first, second and third exfoliation iteration, and finally PDMS with TMD powder. d) Optical image with 5x magnification of the surface of the PDMS with TMD flakes.*

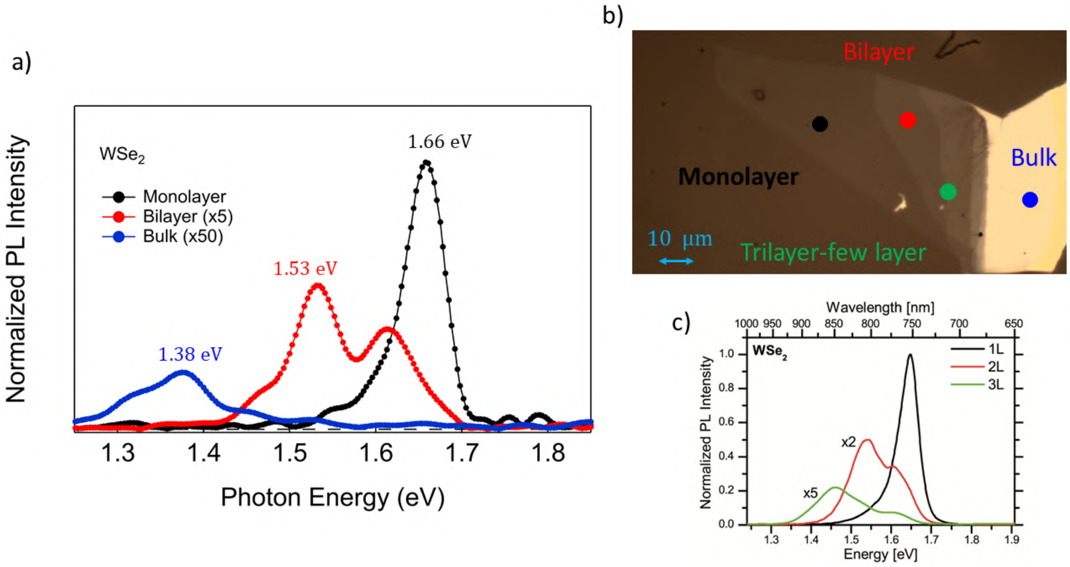

**Figure 3.23:** *a) Measured PL spectra for the monolayer, bilayer, few layer and bulk. b) Optical image (20x) of a WSe2 flake exfoliated on PDMS. Bulk, few layer, bilayer and monolayer WSe2 are visible by eye. c) PL spectra for monolayer, bilayer and trilayer, measured in [77].*

face each other, making it possible to bring them into contact by means of a traslation of the stage 2 along z. The initial z coordinate of the surface of the substrate should be few millimiters lower than that of the surface of the PDMS. The image collected by the miscoscope objective should be focused on the plane of the PDMS surface, showing the focused image flake to transfer, while the image of the substrate is initially defocused. While slowly raising the z coordinate of the stage 2, the substrate gets closer to the PDMS, and its image appears more and more focused. Now it is possible to translate the stage 2 along x,y to select the exact region for the transfer. The spatial selectivity is particularly important, for example, when we want to transfer a monolayer on

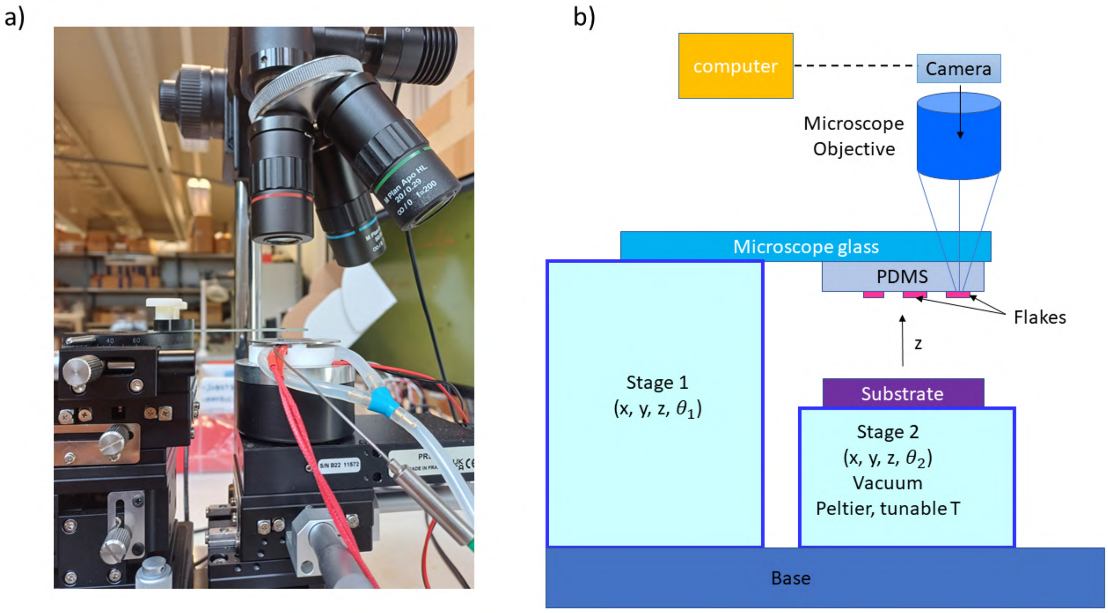

**Figure 3.24:** *a) Photograph of the transfer system, corresponding to the scheme shown beside, in the panel b).*

a patterned substrate and suspend the monolayer on a hole.
When the x,y position of the stage 2 are set, this stage can be raised until the two surfaces make contact. In the microscope image, it is possible to see a "bubble" advancing on the surface, indicating which regions of the substrate and PDMS are touching each other. When these regions include the TMD flake to transfer, we can lower again the z coordinate of the stage 2, and slowly separate the substrate and the PDMS (we see the bubble retreating). When the substrate is far enough from the focal plane (PDMS surface), if the transfer is successfull, the image of the transfered flake should be defocused. At this point we can unmount the microscope glass, and focus the image on the surface of the substrate, to check the result of the transfer.
The microscope objective is optically connected to a CCD camera equipped with a mini computer. This allows to visualize the optical images on a monitor and to save them on a USB drive. Figure 3.25 shows the optical image of a $WS_2$ flake on PDMS at two different steps of the transfer (a and b), and the final result of the the transfer on a $SiO_2$ substrate (c). Only a small and fragmented part of the monolayer is successfully transfer. Figure 3.25 d) shows an example of a bilayer $WS_2$ transferred on a patterned Silicon substrate with a 5 $\mu m$ hole. The bilayer is intact and part of it is suspended and freestanding on the hole.
By using this transfer system, it is possible to stack together two or more flakes by iterating the transfer procedure, to obtain an heterostructure. As an example, we can obtain a monolayer encapsulated in hexagonal boron nitride (h-BN). Another possibility to obtain an heterostructure is stacking together two monolayers of different TMD, such as $MoS_2$ and $WS_2$, to investigate the properties of these composed materials.

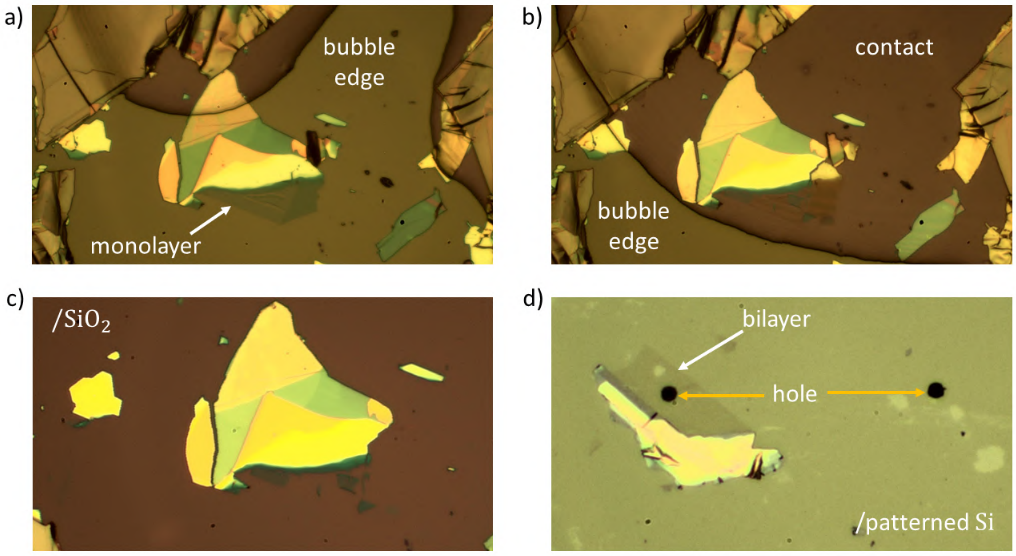

**Figure 3.25:** *a), b), c) Three steps of the transfer of a flake including a monolayer* $WS_2$ *from the PDMS to a* $SiO_2$ *substrate. a) PDMS and* $SiO_2$ *are partially in contact where a dark "bubble" is visible, on the top. The monolayer does not touch the* $SiO_2$ *substrate. b) The "bubble" edge is now in the lower part of the image. The monolayer and the substrate are in contact. c) Flake transferred on the* $SiO_2$ *substrate, partially successfull: the monolayer is broken, and only few fragmented parts are transferred. d) Bilayer* $WS_2$ *successfully transferred on a patterned Si substrate. Two holes of 5* $\mu m$ *diameter are clearly visible, and part of the bilayer is suspended on one of them.*

# Chapter 4

# Photoluminescence data analysis

In this chapter we report and analyze the photoluminescence experimental data. All measurement are performed at room temperature and athmospheric pressure. We performed steady state and time resolved PL experiments on exfoliated monolayers $WS_2$ and $MoS_2$, transferred on $SiO_2$ substrate.

We acquired steady state PL data to characterize the samples (number of layers, quantum efficiency), and to study the dependence of the spectrum on the CW excitation intensity. Moreover, we performed spatially resolved steady state PL measurements, to evaluate the contribution to the PL spectrum, arising from the different regions of the photo-excited area.

We performed time resolved PL measurements to study the time evolution of the PL spectrum, especially at high excitation fluence, where a high initial excitation density can induce a transition from free excitons to an electron-hole plasma. With these measurements we aim to detect this transition. The comparison between two materials, $WS_2$ and $MoS_2$, with a different quantum yield, exciton binding energy and the spin-orbit splitting, allows to obtain complementary information.

We measured the TR-PL of bulk $MoS_2$ to study the PL dynamics in the indirect bandgap counterpart of the monolayer $MoS_2$. Moreover, while measuring the bulk, it is possible to use very high excitation fluence, up to 10 $mJ/cm^2$ (while monolayer starts damaging below 1 $mJ/cm^2$), allowing to investigate this system in an extreme excited condition.

## 4.1 Experimental methods

A CW laser at 405 nm (photon energy 3.05 eV) is used as excitation source for the steady state PL measurements, while the second harmonic of a femtosecond pulsed laser at 515 nm (2.4 eV) is used for the time resolved PL experiments. The excitation lasers are focused on the sample with a microscope objective (Olympus 40x), while the PL is collected in backscattering with the same microscope objective. The spectral detection is performed with an interferometer (Gemini, NIREOS), while the time resolution is achieve via time correlated single photon counting (TCSPC), by using a single photon avalanche photodiode (SPAD) and a fast acquisition board (PicoQuant, Timeharp260P). A precision piezo manipulator (hexapode) can be used to move the sample with an accuracy of $\approx 1\ \mu m$, allowing to select the position on the sample to measure. $WS_2$ and $MoS_2$ single crystals (HQ-graphene [30]) were mechanically exfoliated in air to obtain monolayers and few layers flakes. The latter were transferred on $SiO_2$ substrate and characterized with steady state PL measurements at low intensity. Figure 4.1 a) shows the optical image of an exfoliated flake $MoS_2$ on PDMS (magnification 20x). The high-contrast parts of the flake are thick bulk crystals, while the faded parts are thin crystals. In this image, a monolayer and bilayer can be identified. The spatial size of the monolayer is about $50\ \mu m \times 20\ \mu m$. Figure 4.1 b) shows the optical image of the same flake, transferred on a $SiO_2$ substrate, showing that the monolayer appear slightly fragmented and damaged on a "macroscopic" scale. Figure 4.1 c) shows a zoom of the monolayer, spatially oriented as mounted on the sample holder of the PL experimental setup (rotated by $\approx$ -120° with respect to the previous image). This image can be directly compared with the PL image shown in figure 4.1 d), where the PL intensity is represented in color-scale versus the position on the sample (in $\mu m$). This map is obtained by acquiring the integrated PL intensity with the

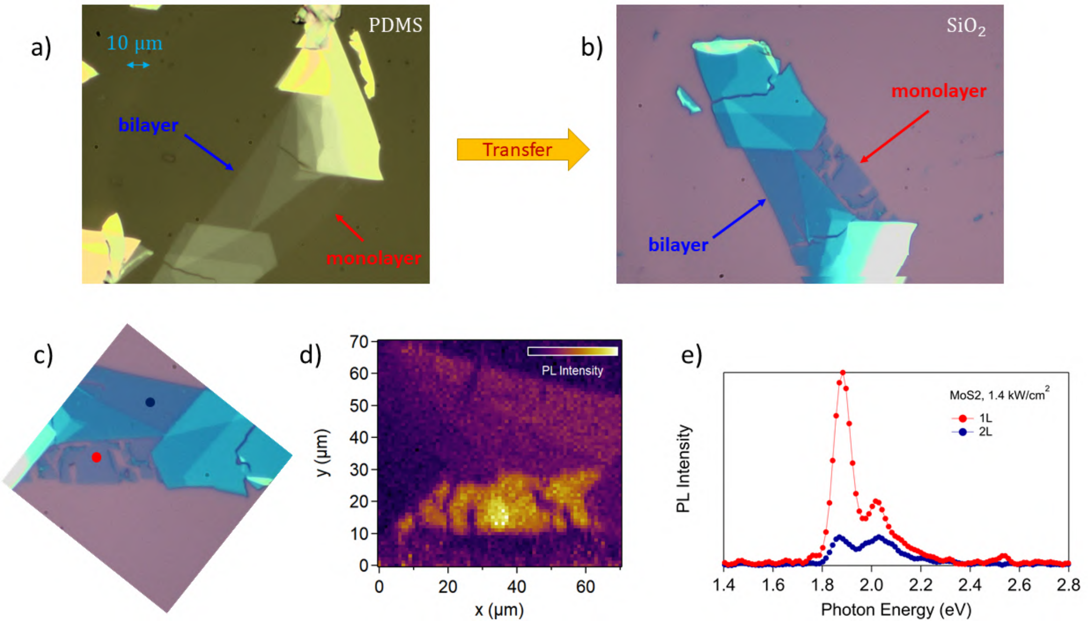

**Figure 4.1:** *a) Optical image (magnification 20x) of $MoS_2$ flake exfoliated on PDMS. A monolayer and a bilayer can be identified. b) Optical image of the same $MoS_2$ flake, after the transfer on a $SiO_2$ substrate. The monolayer and bilayer are still detectable. c) Zoom of the monolayer ad the bilayer from the image shown in panel b. The image have been rotated for a direct comparison with the PL map shown in panel d. d) PL map of the TMD flake, where the integrated PL intensity is plotted in colorscale as a function of the position in $\mu m$. The bright feature corresponds to the monolayer $MoS_2$. e) Steady state PL spectra acquired on the monolayer and bilayer $MoS_2$, in the positions marked on the optical image of panel c.*

SPAD while scanning the position of the sample with the Hexapode manipulator(1 pixel=1 $\mu m$ × 1 $\mu m$). The PL image shows an high intensity in the area corresponding to the monolayer, and an appreciable intensity from the bilayer. The monolayer exhibits regions where it is locally homogeneous extending for about 5 of $\mu m$. Figure 4.1 e) shows the steady state PL spectra for the monolayer and bilayer $MoS_2$, with a good agreement with previous experimental data reported in literiture [47, 22], allowing us to characterize the number of layers of the exfoliated flakes.

## 4.2 Analysis of the errors affecting the PL spectra

It's important to evaluate the error on the intensity of the spectral points. Since the number of photons detected per unit time follows the Poisson statistics, we associate an expectation value equal to the number of photon counts, and an error (standard deviation) equal to the square root of the photon counts, on each point of the interferograms:

$$C_i = C_i^{(0)} \pm \sqrt{C_i^{(0)}} \tag{4.1}$$

where $C_i^{(0)}$ is the experimental number of counts of the interferogram. The Poisson statistics determine a range delimited by two interferograms given by

$$\begin{aligned} C_{low} &= C_0 - \sqrt{C_0} \\ C_{high} &= C_0 + \sqrt{C_0} \end{aligned} \tag{4.2}$$

The two spectra obtained by the Fourier transform of $C_{low}$ and $C_{high}$ can determine the range for the spectrum obtained by the Fourier transform of the measured interferogram. Since the Fourier transform is linear, the error propagates according to the following equations:

$$FT(C_{low}) = FT(C_0 - \sqrt{C_0}) = FT(C_0) - FT(\sqrt{C_0}) \tag{4.3}$$

$$FT(C_{high}) = FT(C_0 - \sqrt{C_0}) = FT(C_0) + FT(\sqrt{C_0}) \tag{4.4}$$

We compute this operation on two interferograms for monolayer MoS$_2$, to evaluate this contribution to the error on the PL spectra.

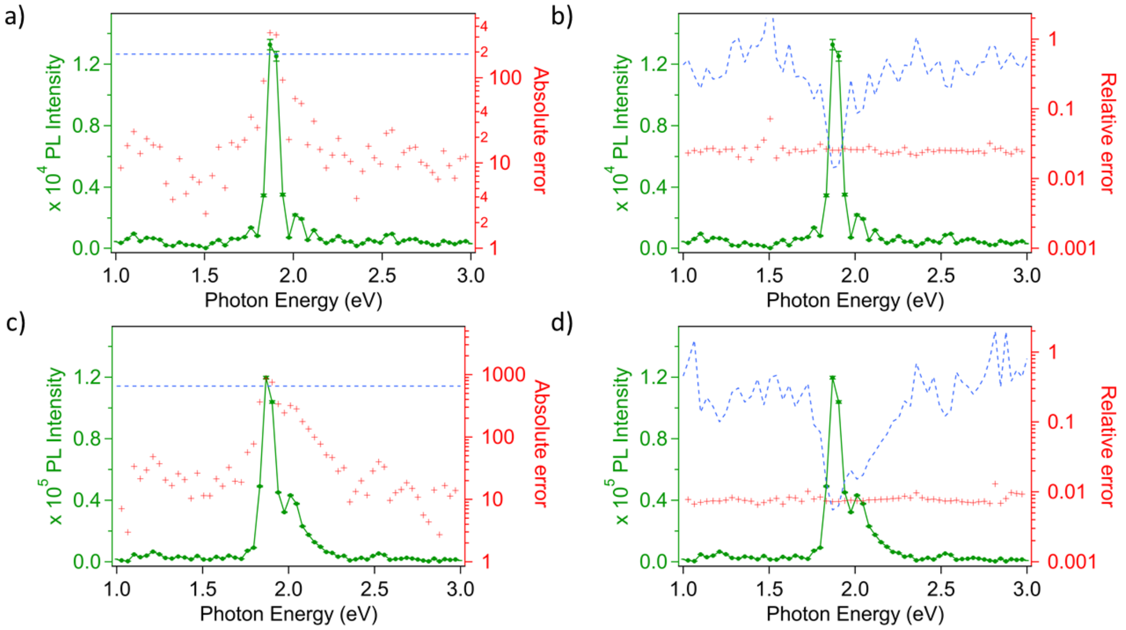

**Figure 4.2:** *PL spectra of monolayer MoS$_2$ on SiO$_2$ at two excitation powers, where each point is plotted along with the error bars (left axis). The right axis reports the absolute and relative errors on each experimental point, calculated with two methods: propagation through Fourier transform of the Poissonian error on each point of the interferogram (red cross), and standard deviation of the intensity of the spectrum far away from the emission peak (blue dashed line). Low power spectrum in panels a) and b), high power spectrum in panels c) and d). Absolute error in panels a) and c), relative error in panels b) and d).*

Figures 4.2 a) and c) reports the PL spectra (left axis) at two different excitation intensity (0.042 $kW/cm^2$ and 1.4 $kW/cm^2$). The absolute Poisson errors are plotted in log scale (right axis). The absolute Poisson error exhibits a trend which is similar to the PL spectrum, as expected, since it is calculated by the FT of an "interferogram" given by the square root of the photon-counts interferogram. The dash line is a constan error, equal to the standard deviation of the intensity of the spectral points on the tails, far away from the emission peak. Figures 4.2 b) and d) shows the same PL spectra (lef axis), along with the relative error (absolute error divided by the intensity of the spectrum). The Poisson relative error is almost constant, around the 3 % for the spectrum at low intensity, and below the 1 % for the spectrum at high intensity. The relative error associated to the constant error (fluctuation of the spectrum on the tails), is around 100 % where there is not signal, and it decreases down to the 1 % on the emission peak. These data suggest that the Poisson error underestimates the error on the experimental points. Another method to evaluate the error on the spectral experimental points consists in measuring N interferograms, subsequently, getting the spectra through Fourier transform, and then calculating the average and standard deviation on each spectral point, photon energy by photon energy. Figure 4.3 a) reports five spectra for $WS_2$ at low excitation intensity $(1 < W/cm^2)$. Figure 4.3 b) reports the average spectrum, which points are calculated as the average of the five spectral points belonging to the five spectra reported in panel a. The error bars are given by ± the standard deviation on the five spectral points.

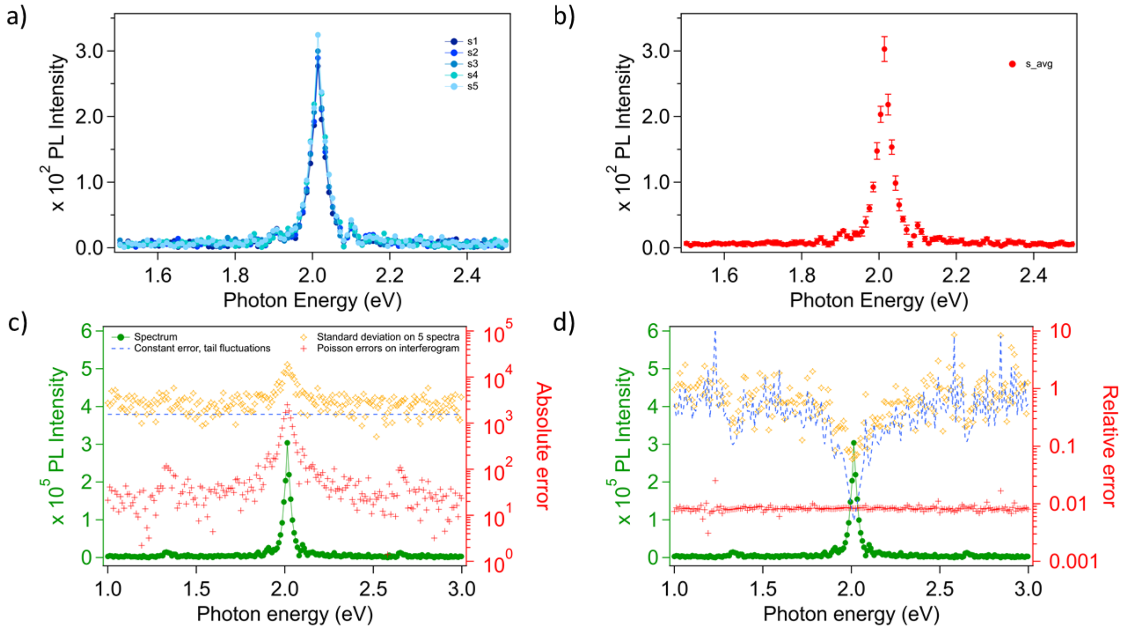

**Figure 4.3:** *a) Steady state PL spectra for* $WS_2$ *monolayer, acquired subsequently. b) Average of the five spectra shown in panel a, with error bars given by the standard deviation of each point. c) Average steady state PL spectrum (left axis), along with the absolute errors (right axis) calculated with three methods: propagation through Fourier transform of the Poissonian error on each point of the interferogram (red cross), standard deviation of the intensity of the spectrum far away from the emission peak (blue dashed line), standard deviation of the intensity on each experimental point, for the five spectra shown in panel a (yellow dots). d) Same as panel c, with relative error on the right axis.*

Figure 4.3 c) and d) reports the average PL spectrum (left axis), along with the absolute and relative errors (right axis), respectively. The error calculated via the standard deviation of the 5 spectral points are represented as orange dots. The relative error is about the 10 % around the peak, and about 100 % on the tails. This error is compared with the Poisson error computed on the avarage interferogram of the 5 measurements (red points), and with the constant error, obtained by computing the standard deviation of the intensity of the average spectrum, on the tails.

Ideally, computing the average and the standard deviation, on each point, for different spectra is the best way to compute the error on PL spectra. However, it requires to acquire the interferogram many times, and it is based on the assumption that the experimental conditions and the sample don't vary in time, between the subsequent measurement (reasonable for measurements at very low intensity).

## 4.3 Energy resolution and exciton emission line-width

We evaluated the effect of the resolution on the PL spectra. We acquired an interferogram for monolayer $WS_2$ at low excitation intensity ($1\ W/cm^2$ <), in the interferometer range [-0.5,5.0] mm. We perform the Fourier transform of this interferogram on the full range, and on reduced ranges (we "cut" the interferogram). Figure 4.4 a) reports the spectra obtained by the Fourier transform of the interferogram on different ranges (shown in the legend). For a scan range <1 mm, the peak is constituted by few spectral points, resulting in an apparent broad spectrum. As the scan range increases, above 1 mm, the peak of the spectrum converges to its real shape (neglecting possible fine structures). Figure 4.4 c) reports the energy step as a function of the interferomter scan range, for selected values of the scan ranges. We fitted this point with a power function:

$$f(l) = A + Bl^p \tag{4.5}$$

We obtained p=-1.011 ± 0.003, as expected by equations 3.8 and 3.9.

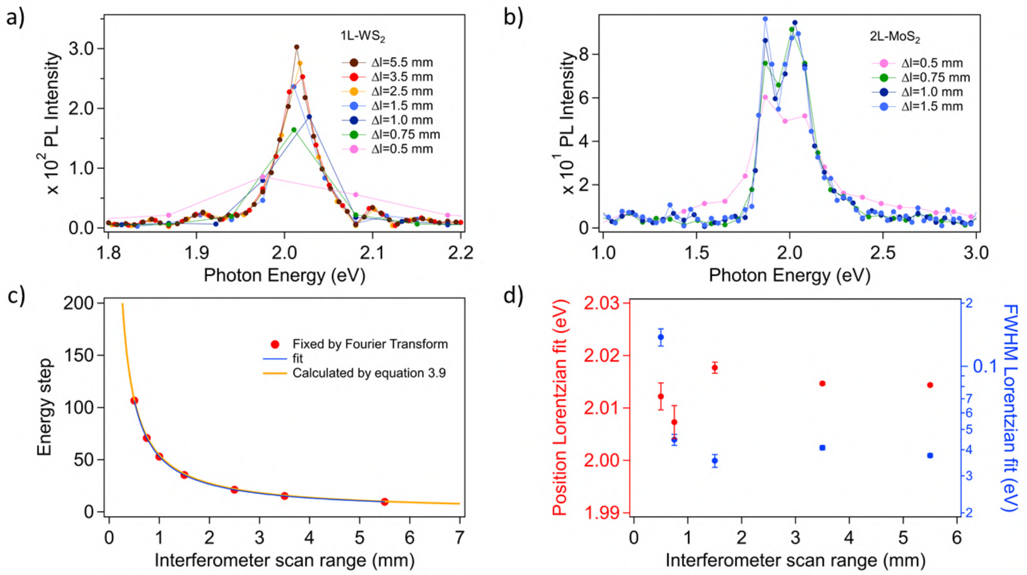

**Figure 4.4:** *Steady state PL spectra for monolayer $WS_2$, obtained by Fourier transform of the acquired interferogram on different scan ranges, shown in the legend. b) Steady state PL spectra for bilayer $MoS_2$, obtained by Fourier transform of the acquired interferogram on different scan ranges, shown in the legend. c) Energy step of the spectra, as a function of the interferometer scan range. Energy steps fixed by the Fourier transform for the spectra shown in panel a (red dots), fit of these points with a power function (blue line), spectral resolution of the Gemini interferometer, as calculated with the equation 3.8-3.9, reported on the theoretical manual of the instrument. d) Fit parameters for the spectra shown in panel a (Lorentzian function). The peak position (left axis) and the FWHM (right axis), are plotted versus the interferometer scan range.*

Figure 4.4 c) reports also the energy step as calculated with equation 3.9, taken from the theoretical manual of the Gemini interferometer [29]. This curve match the experimental points and their fit. Figure 4.4 d) reports the position of the peak and the FWHM for spectra reported in the panel a, as extracted by a Lorenzian fit, at different scan ranges. The peak position does not vary with the scan range, while the FWHM strongly decreases as the scan range increases from 0.5 mm to 1.5 mm, and is almost constant for l>1.5 mm.

Figure 4.4 b) reports the PL spectra for a bilayer $MoS_2$, obtained by Fourier transform of the acquired interferogram for different scan ranges. The bilayer $MoS_2$ exhibits two peaks with energy difference ≈ 150 meV. At low resolution (l=0.5 mm) the two peaks are not resolved. As the resolution increases above l=0.75 mm, we can resolve the two peaks: we need at least 3-4 spectral points between the to two close peaks, to resolve them.

## 4.4 $WS_2$, steady state photoluminescence Vs power

We performed steady state PL measurements on 1L-$WS_2$ on $SiO_2$. Figure 4.5 a) shows the raw interferogram acquired for monolayer $MoS_2$ on $SiO_2$, at low excitation intensity. The PL spectrum, obtained by the Fourier transform of this interferogram, is shown in figure 4.5 b) We point out that in the following we represent the PL spectra as "lines and points" only to help the visualization of the PL spectra.

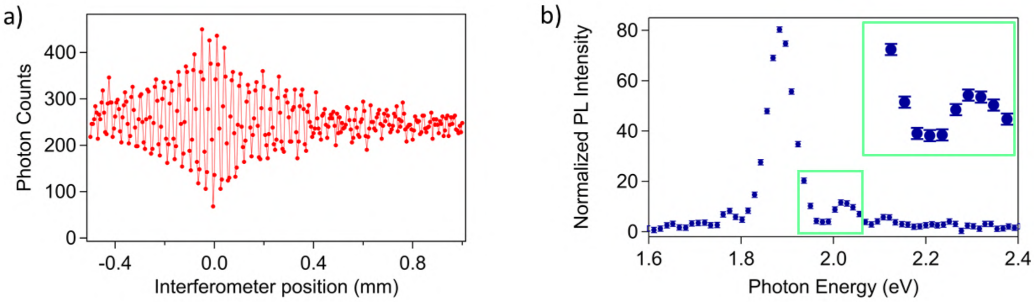

**Figure 4.5:** *Steady state PL measurement on 1L-$MoS_2/SiO_2$ at low excitation intensity (42 $W/cm^2$). a) Raw interferogram, showing the photon counts versus the interferometer position. b) Spectrum obtained by the Fourier transform of the interferogram shown in panel a. The experimental points are shown with the error bars. The inset displays a zoom on the highlighted region, to show the experimental points with their error bars.*

We performed power-dependent steady state PL measurements on monolayer $WS_2$ on $SiO_2$, to characterize the sample and to get information on the lattice heating, on the PL quantum yield and on the diffusion of photo-excited carriers.
The incident excitation powers are reported in the table 4.1.

| Measurement | Incident Power ( $\mu W$ ) | Relative error | Absolute Error ( $\mu W$ ) |
|---|---|---|---|
| 1 | 0.043 | 0.5 | 0.0215 |
| 2 | 0.850 | 0.25 | 0.21 |
| 3 | 2.940 | 0.1 | 0.3 |
| 4 | 9.8 | 0.05 | 0.5 |
| 5 | 44.5 | 0.05 | 2.2 |
| 6 | 98 | 0.05 | 4.9 |

**Table 4.1:** *Incident excitation power, along with relative and absolute error, for the power-dependent steady state PL measurements.*

Figure 4.6 a) reports the normalized PL spectra for $WS_2$, at the different excitation power, shown in the legend along with the multiplication factor, to normalize the spectra at the emission peak. Figure 4.6 b) shows the non-normalized spectra in log scale. At low power the emission line shows no significant change as the excitation incident power increases, there is only an increase in the integrated intensity. At power P>10 $\mu W$ the spectrum exhibits a red-shift and broadening. To obtain quantitative values for the shift and the broadening, we fitted the spectra with a Lorentzian function:

$$f(E) = bkg + \frac{f_0}{(E - E_0)^2 + (FWHM/2)^2} \tag{4.6}$$

where $bkg$ is the background intensity, $f_0$ is related to the maximum intensity of the emission peak, $E_0$ is the peak position, and FWHM is the full width at half maximum. At low intensity the peak of the spectrum is at $2.023 \pm 0.001$ eV and a FWHM of $0.040 \pm 0.001$ eV. Figure 4.6 c) reports the shift of the peak $\Delta E = E_0' - E_0$ (left axis, red dots) and the peak FWHM (right axis, blue dots) versus the excitation power. This shows that the peak significantly red-shift and broadens for an excitation incident power P>10 $\mu W$. At the maximum excitation incident power ($\approx 100$ $\mu W$), the peak is redshifted by $\Delta E = -0.014 \pm 0.001$ eV, and with a FWHM of $0.051 \pm 0.002$ eV (broadening of ≈ 11 meV with respect to the peak at low intensity).

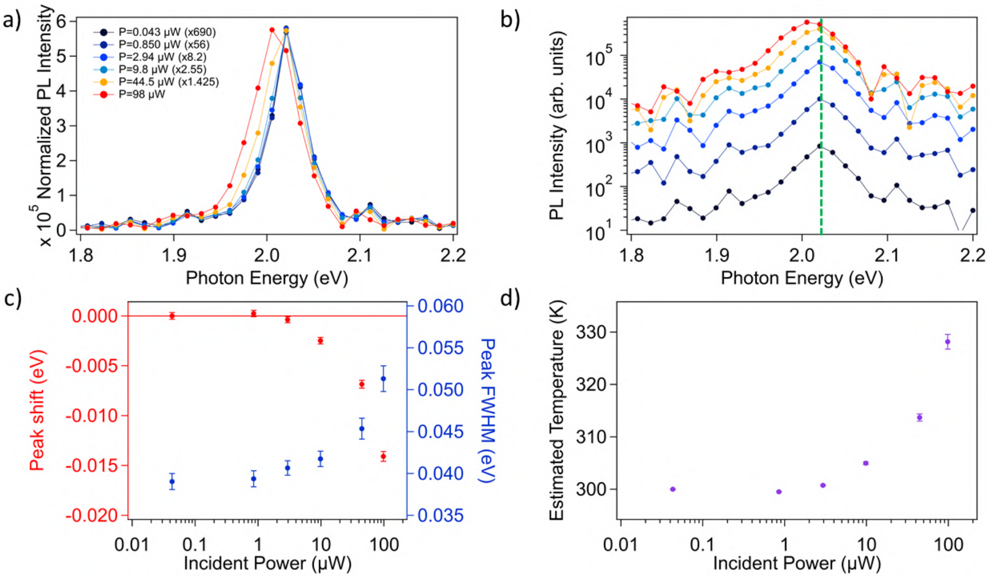

**Figure 4.6:** *a) Power dependent steady state PL spectra for monolayer $WS_2$. The intensity is normalized to the emission peak. b) Non normalized steady state PL spectra for monolayer $WS_2$, in log scale. c) Parameters of the Lorentzian fit for the power dependent spectra: peak shift (left axis, red dots) and peak FWHM (right axis, blue dots) versus the incident excitation power. d) Estimated tamperature versus the incident power, calculated by using the peak shift, and the energy gap dependence on the temperature for monolayer $WS_2$ [56].*

We associate the peak shift to an increase of the temperature of the sample, under CW irradiation. In semiconductors, the change in temperature induces a change in the free particle bandgap, which for $WS_2$ is about $\Delta E_g^{(T)} = 0.0005$ eV/K [56]. We can estimate the temperature of the sample by using this value, as

$$T = 300K + \frac{\Delta E}{\Delta E_g^{(T)}} \tag{4.7}$$

Figure 4.6 d) shows the estimated temperature versus the incident excitation power, along with the error bars, assuming an error of the 50% on $\Delta E_g^{(T)}$. The effect of the temperature is not sufficient to explain the broadening of the emission line [12]. The latter can be associated to exciton-exciton interactions, or to an increase in the contribution of the trion (charged exciton) at high excitation power [3].

We integrated each PL spectra, to obtain the integrated PL intensity (in arbitrary units). The latter is plotted versus the incident excitation power, in figure 4.7 a). We normalized the integrated PL intensity by dividing it by the incident excitation power:

$$\tilde{QY}(P) = \frac{I_{PL}(P)}{P} \tag{4.8}$$

This quantity, $\tilde{QY}$ can be named *relative* $QY$, since it is proportional to the PL quantum yield (QY), and it gives the information about the relative radiative efficiency, as a function of the excitation power. The relative QY is plotted in figure 4.7 b), with error bars calculated by using the propagation of errors formula, the absolute errors on the incident excitation power of table 4.1, and an error on the integrated PL intensity given by its square root (Poisson statistics). The relative QY exhibits an initial increase and a decrease for power P>3 $\mu W$. We associate the first increase of the relative QY to a partial saturation of defects states, resulting in an increase of the radiative efficiency. We associate the decrease of the relative QY to the exciton-exciton annihilation, which becomes dominant above a threshold density. A decreasing in the PL QY in monolayer $MoS_2$ has been reported in [84].

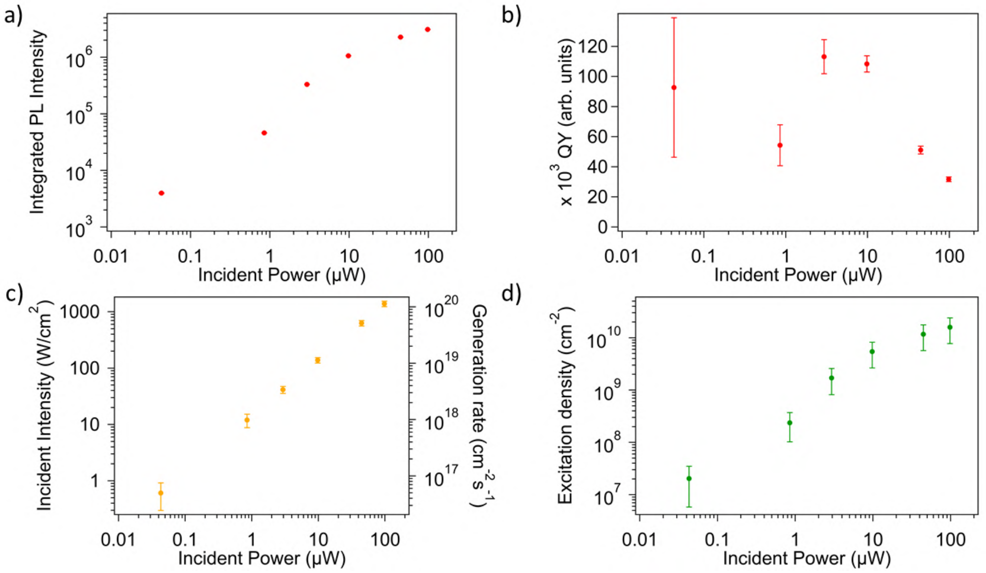

**Figure 4.7:** *Analysis of the power dependent steady state PL spectra for monolayer $WS_2$. a) Integrated PL intensity versus the incident excitation power b) Integrated PL intensity, divided by the incident excitation power. c) Calculated incident intensity versus the incident power. d) Calculated excitation density (number of e-h pair per unit area), versus the incident excitation power.*

We estemated the excitation density n as a function of the incident excitation power, under the CW excitation. We first calculated the incident laser intensity, defined as:

$$I_{exc}(P) = \frac{P}{A} \tag{4.9}$$

where A is the photo-excited area, that in first approximation is given by the circle with diameter the FWHM of the Gaussian profile of the excitation laser( $d_{spot} \approx 3\ \mu m$ ). The numeric value for the excitation intensity can be obtained by the following equation:

$$I_{exc}[W/cm^2] = 10^{-6} \frac{P[\mu W]}{\pi \cdot \left(\frac{d_{spot}[cm]}{2}\right)^2} \tag{4.10}$$

We used the laser intensity to compute the *generation rate* for electron-hole pairs, i.e. the number of electron-hole pairs created per unit area and per unit time by the excitation laser:

$$G(I_{exc}) = \frac{\gamma I_{exc}}{h\nu} \tag{4.11}$$

where $\gamma = 0.04$ is the fraction of the excitation intensity absorbed by the monolayer. We calculated this value of $\gamma$ by considering a reflectivity of $\approx 50\%$, and an absorption coefficient of $\approx 8.7 \cdot 10^5$ cm$^{-1}$ [66]. Figure 4.7 c) shows a plot of the incident intensity (left axis) and the generation rate (right axis), as a function of the incident excitation power.

The excitation density, as a function of the excitation power, can be estimated as follows. The differential equation for the density in the photo-excited area, in a general case and considering excitons, can be written as:

$$\frac{\partial n(\vec{r},t)}{\partial t} = G(t) + D \cdot \nabla^2 n(\vec{r},t) - \frac{n(\vec{r},t)}{\tau} - Cn^2(\vec{r},t) \tag{4.12}$$

where G(t) is a time dependent generation rate, D is the diffusion coefficient (we assume constant), $\tau$ is the lifetime for radiative and non-radiative monomolecular recombinations of excitons (proportional to the density) and C is coefficient for non-radiative bimolecular recombinations (proportional to the density squared), due to the exciton-exciton annihilation. This equation can be solved numerically, however we can easily obtain an approximate value, by using the following assumptions:

1. We neglect the spatial diffusion of excitons (this approximation will be discussed in the subsequent section).
2. We consider a spatially uniform density in the photo-excited area (no dependence of the density on the position $\vec{r}$).
3. We consider a constant generation rate G(t)=G. This assumption is reasonable when exciting with a CW laser, assuming that its output power is stable in time.
4. We consider the system in a steady state (the time derivative of the density with respect to the time can be set to zero), yielding a constant equilibrium density.

By using these assumption, equation 4.12 simplifies to:

$$G - \frac{n}{\tau} - Cn^2 = 0 \rightarrow Cn^2 + \frac{n}{\tau} - G = 0 \tag{4.13}$$

This is a second order equation in n, which solution is given by

$$n = \frac{-\frac{1}{\tau} \pm \sqrt{\frac{1}{\tau^2} + 4GC}}{2C} \tag{4.14}$$

We consider only the positive solution, since the density is positive. We use the power dependent generation rate calculated with equation 4.11, a lifetime $\tau \approx 500$ ps, and an exciton-exciton annihilation rate C=0.5 $cm^2 s^{-1}$ [93]. We obtain the power-dependent equilibrium density, under CW excitation, represented in figure 4.7 d). The error is calculated by using the propagation of errors, by considering the error calculated on the generation rate (and shown in figure 4.7 a), and an error of 50% on $\tau$ and on the exciton-exciton annihilation coefficient C. We point out that this is an over estimate of the density, since we considered a lifetime of 500 ps, which is an upper limit, especially when the defect density is high [84, 82].

## 4.5 $WS_2$, spatially-resolved steady state photoluminescence

We acquired the optical image of the spot of the excitation laser on the sample, since this information is fundamental to calculate size of the photo-excited area. We used the CCD camera which looks directly inside the microscope objective showing the image of the surface of the sample. First, we needed to get the calibration from pixel to distance in $\mu m$. To do this, we acquired the image of a patterned Silicon substrate, with holes of 5 $\mu m$ diameter and relative distance 100 $\mu m$. Figure 4.8 a) shows the image of the surface of this patterned sample, with 40x magnification, where the black spots are the holes in the substrate. We acquired horizontal and vertical profiles in this image, to map the coordinates of the two holes. The profiles, shown in figure 4.8 b), exhibit negative peaks, corresponding to the holes. We consider the center of these peaks to obtain the coordinates of the two points, in pixels: $\vec{v}_1 = (1073, 722)$ and $\vec{v}_2 = (943, 1245)$.
Since we know that the distance between the two holes is 100 $\mu m$, we used the Pythagorean theorem to calculate get this distance in pixels. Finally, we obtained:

$$1\,pixel = 0.185\,\mu m \tag{4.15}$$

Figure 4.9 a) shows the optical image of the excitation laser (top) and of the PL light emitted by the $WS_2$ monolayer (bottom). We acquired the latter by inserting an optical filter between the sample and the CCD, to block the straight light of the excitation laser.
Figure 4.9 b) reports horizontal and vertical profiles extracted from the images in panel a). The x and y axis are expressed in $\mu m$ (we used equation 4.15 for the calibration). We also acquired the images of the PL light with lower excitation power, to compare the spatial profiles. Figure 4.10 a) and c) reports the horizontal and vertical PL profiles acquired at low excitation power (0.8 $\mu W$), while panels b) and d) reports the profiles at high excitation power (3 $\mu W$).
We fitted the profiles with a Gaussian function, to analyze the spatial shape of the light for the laser and the PL. The FWHM of the light spots are reported in table 4.2.

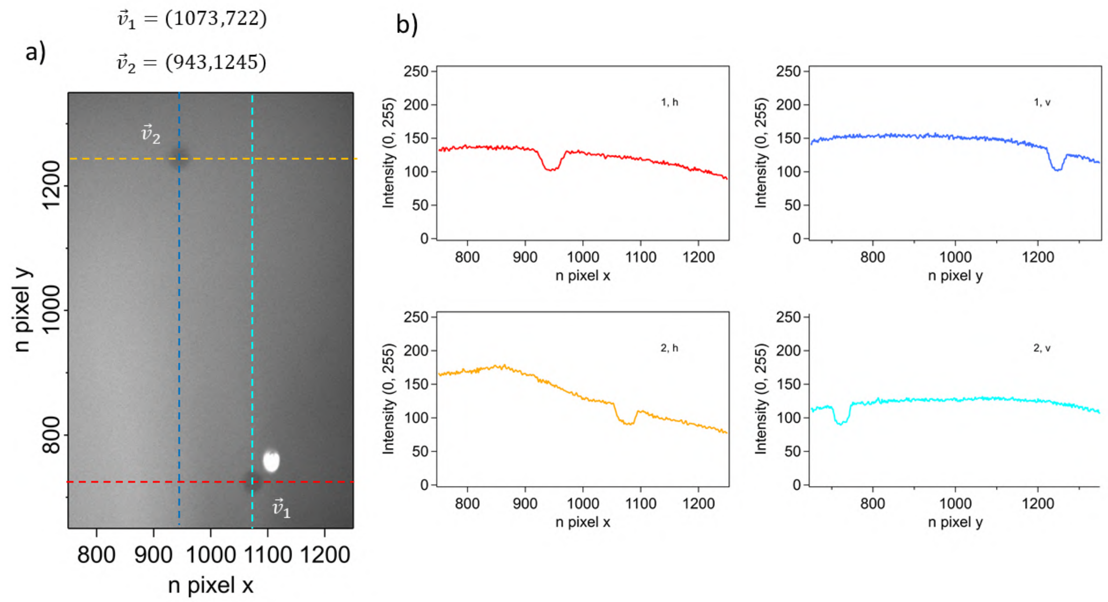

**Figure 4.8:** *a) Optical image of a patterned Silicon substrate with holes of 5 $\mu m$ diameter, and a mutual distance of 100 $\mu m$. This image have been acquired with a CCD camera, and it is used to calibrate the pixel-distance. b) Horizontal and vertical profiles along the two holes, allowing to get the coordinates of the center of each hole, in pixel.*

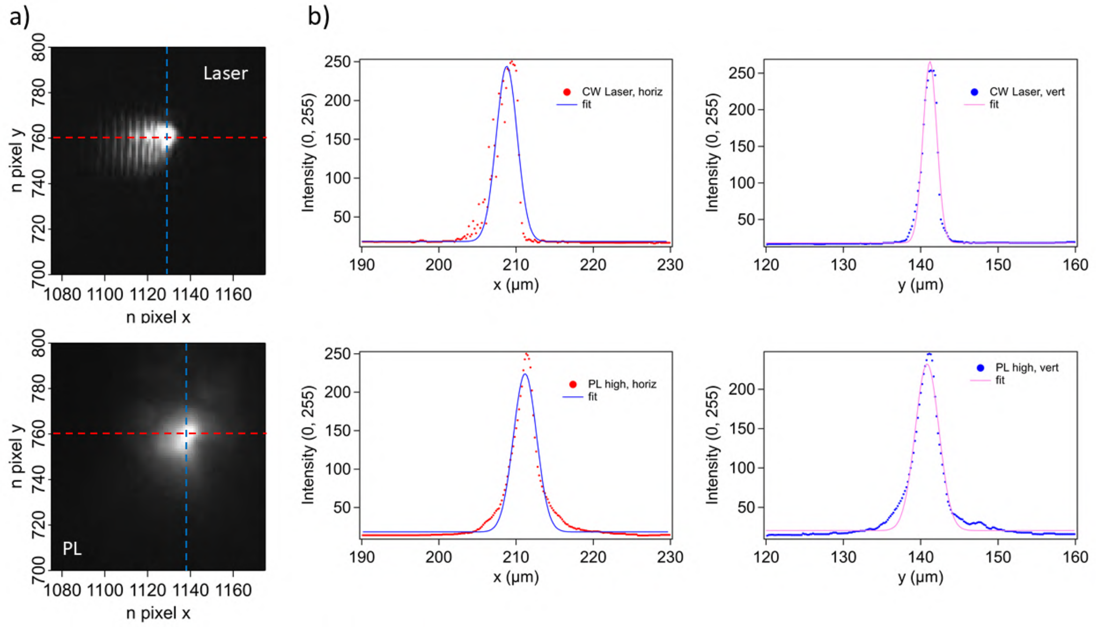

**Figure 4.9:** *a) Spot of the excitation laser (top) and spot of the PL emitted by a $WS_2$ monolayer (bottom), as acquired by the CCD camera. b) Horizontal and vertical profiles of the laser spot (top) and of the PL spot (bottom), along with the fits (Gaussian).*

These data show that the PL spatial profile is larger than the excitation laser, suggesting that the diffusion of excitons is not negligible. The FWHM of the low power PL emission along the vertical direction is about 1 $\mu m$ larger than the FWHM of the excitation laser along the same direction, an increase of $\approx 50\%$. However, by increasing the excitation power by more than a factor 3, the FWHM increases from 3.2 $\mu m$ to 3.6 $\mu m$.

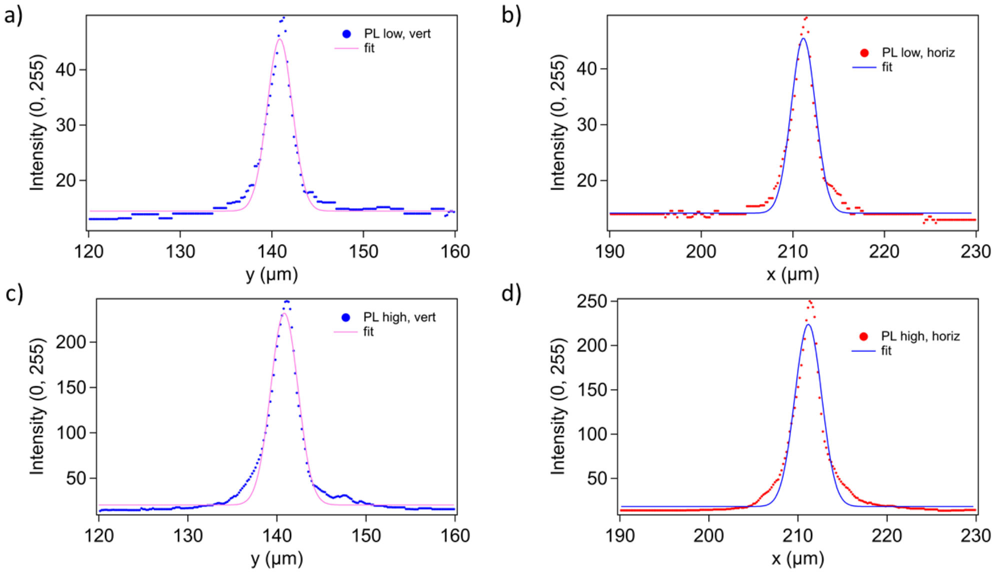

**Figure 4.10:** *Vertical and horizontal profiles of the PL spot on the* $WS_2$ *monolayer, at low excitation power (panels a, b) and high excitation power (panels c, d).*

| Light source | FWHM of the spot ( $\mu m$ ) |
|---|---|
| Laser, horizontal | $3.197 \pm 0.09$ |
| Laser, vertical | $2.101 \pm 0.03$ |
| PL, horizontal (3 $\mu W$) | $3.55 \pm 0.06$ |
| PL, vertical (3 $\mu W$) | $3.617 \pm 0.05$ |
| PL, horizontal (0.8 $\mu W$) | $3.128 \pm 0.05$ |
| PL, vertical (0.8 $\mu W$) | $3.242 \pm 0.05$ |

**Table 4.2:** *FWHM of the spatial profiles along the* $x$ *and* $y$ *directions, for the excitation laser and for the PL light, at two excitation powers.*

Since the density profile of the PL light is not spatially uniform, and since in most of the PL experiments (in particular for TR-PL) we use the SPAD as a detector, where all the PL light is focused on a single pixel, it is important to evaluate the contribution to the PL spectrum arising from different regions of the photo-excited area. At this purpose, we measured the steady state PL spectrum for the exfoliated monolayer WS2 on SiO2, at high excitation power (100 $\mu W$), at different positions with respect to the center of the photo-excited area. To perform these measurements we used a CCD camera detector and we integrated the PL signal on three different regions of interest on the sample: the center of the photo-excited area (2x2 pixel), and two outer regions. Figure 4.11 shows the normalized and non-normalized steady state PL spectra, arising from the different regions, along with a scheme of the regions of interest.

These data show that at the center of the photo-excited region the spectrum presents one peak at 2.015 eV that we associate to the A free exciton emission, and a shoulder at 1.975 eV that can be associated to trions [3]. As going far from the center, the emission line becomes more and more sharp, as the relative intensity of the shoulder at 1.975 eV decreases. This effect can be explained by the higher density at the center of the photoexcited region, yielding in a higher probability to ionize part of the free excitons in an EHP. The presence of free carriers may favor the formation of charged excitons. The effect of the excitation density on the trion peak has already been observed in power dependent PL experiments on monolayer $WS_2$, as shown in figure 4.12 [87].

By looking at the non-normalized spectra (figure 4.11), it's clear that the PL intensity arising for the center is much lower than the intensity integrated in the outer region. Hence, the contribution of the high-density spectrum arising from the center is weak when we integrate the intensity on all the emission spot. This effect must be taken into account when analyzing all the PL data acquired with the SPAD detector.

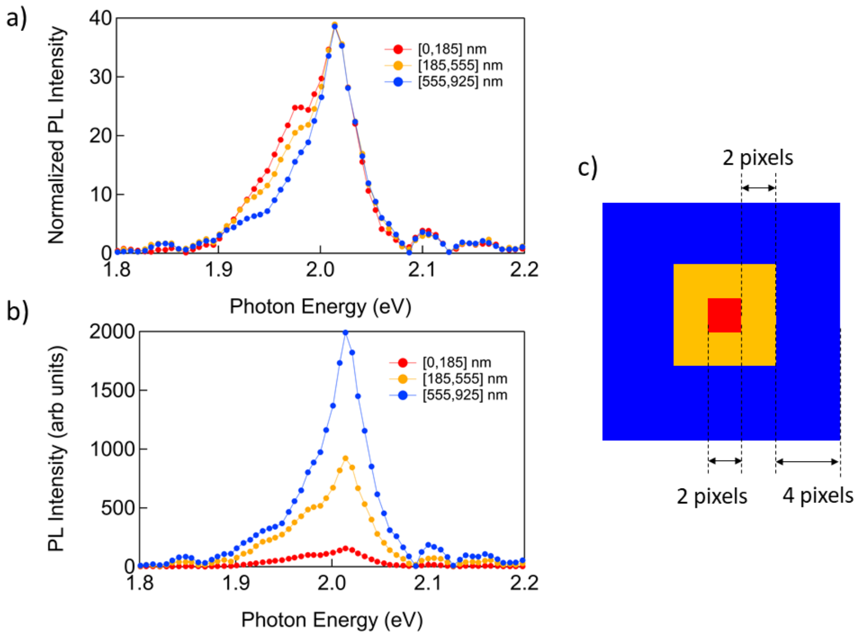

**Figure 4.11:** *Steady state photoluminescence spectra for exfoliated monolayer WS2 on SiO2, emitted by three different regions on the sample: the center of the photoexcited area (red curve), and two concentric outer regions (orange and blue curves). a) Normalized PL spectra. b) Non Normalized PL spectra. c) Regions of interest, where the PL light is collected, depicted with the same color code of the PL spectra plotted in the panels a and b.*

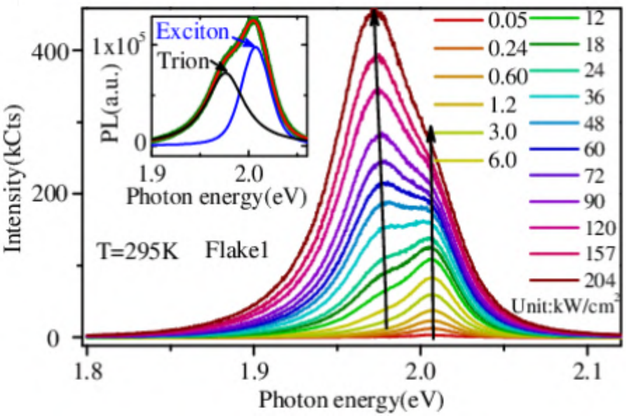

**Figure 4.12:** *Power dependent PL spectra for monolayer $WS_2$, at room temperature. Figure from [87].*

## 4.6 Time resolved photoluminescence data

We performed time resolved PL measurements on exfoliated monolayers $WS_2$ and $MoS_2$ on $SiO_2$, and on bulk $MoS_2$. The aim of these measurements is to study the time evolution of the PL spectrum after an ultrashort pulsed excitation, especially at high excitation fluence, corresponding to an initial high excitation density, where free excitons can ionize in an electron-hole plasma (see chapter 1, section 1.4.1). We compare the measurements at low and high fluence to investigate the optical response of the system when either excitons or the electron-hole plasma dominates, and to find the cross-over between these two behaviors. The comparison between two different materials allows to understand how the electronic structure and the exciton binding energy affect the optical properties in these systems. $WS_2$ and $MoS_2$ are perfect candidates for this kind of investigation, because they exhibit a different spin-orbit splitting, resulting in different spectral positions for exciton excited states, a different damaging threshold (higher for $MoS_2$), and a different PL quantum yield (higher for the $WS_2$ at room temperature). The latter properties allow to easily measure the TR-PL at very low excitation densities for $WS_2$ (range $7 \cdot 10^8$ - $2.5 \cdot 10^{12}$ $cm^{-2}$ ), and to explore high excitation densities for $MoS_2$ (range $2 \cdot 10^{11}$ - $2 \cdot 10^{13}$ $cm^{-2}$ ). The experimental data on bulk $MoS_2$ allow to access important information on the counterpart of the $MoS_2$ monolayer, where the quasi-2D (instead of 2D) character, the indirect bandgap and an the enhanced Coulomb screening (see chapter 2, section 2.3.2), leading in a reduction of the exciton binding energy with respect to the monolayer, result in a dramatically different optical response with respect to the monolayer. Moreover, the bulk sample allows to perform PL measurements at extreme excitation fluences, more than one order of magnitude above the damaging threshold for the monolayer, allowing to investigate the system at very high initial excitation density, where phenomena like the band gap renormalization and the generation of electron-hole plasmas and electron-hole liquid are enhanced.

### 4.6.1 Initial excitation density after a pulsed excitation

The excitation density is defined as the density of photo-excited electrons and holes per unit volume (or per unit area, if we consider a TMD monolayer). The excitation density strongly affects the properties of photo-excited carriers, and hence the PL emission line. For this reason it is useful to estimate the initial excitation density, after a pulsed excitation. The excitation fluence of a pulsed source is defined as the energy per pulse divided by the area of the photo-excited region:

$$\phi = \frac{E_{pulse}}{A} \tag{4.16}$$

where the energy per pulse can be calculated by dividing the power of the excitation pulsed laser by its repetition rate:

$$E_{pulse}[\mu J] = \frac{P[\mu W]}{\nu_{rep}[s^{-1}]} \tag{4.17}$$

Only a fraction of this energy is absorbed by the sample:

$$E_{pulse}^{(abs)} = (1 - R) \cdot \delta E_{pulse} \tag{4.18}$$

where R is the reflectivity of the material and $\delta$ is the fraction of the transmitted energy per pulse absorbed in the sample. These quantities are dependent on the excitation photon energy ($E_{exc} = h\nu$). The fraction $\delta$ can be calculated by using the absorption coefficient and the thickness of the sample. We use the Beer-Lambert formula for the attenuation of the light in the matter:

$$I(\tilde{z}) = I_0 e^{-\alpha(h\nu)\tilde{z}} \tag{4.19}$$

where $I_0$ is the intensity of the light transmitted in the material, and $I(\tilde{z})$ is the intensity at depth $\tilde{z}$ in the material. The ratio $I(\tilde{z})/I_0$ gives the relative intensity of the light transmitted for $z > \tilde{z}$. Hence, the intensity absorbed for $0 < z < \tilde{z}$ is given by $1 - I(\tilde{z})/I_0$. If we consider a TMD monolayer with thickness $\tilde{t}$ (the thicnkess of a monolayer is $\approx$ 1 nm), the fraction of the absorbed energy per pulse can be calculated as:

$$\delta = 1 - \frac{I(\tilde{t})}{I_0} = 1 - \frac{I_0 e^{-\alpha(h\nu)\tilde{t}}}{I_0} = 1 - e^{-\alpha(h\nu)\tilde{t}} \tag{4.20}$$

Finally, to obtain an estimation of the initial excitation density, we divide the absorbed energy per pulse by the photon energy of the excitation laser (we do the assumption that any absorbed photon gives rise to an electron-hole pair), and by the area of the photo-excited region:

$$n = \frac{E_{pulse}^{(abs)}}{h\nu} = \frac{\frac{P}{\nu_{rep}}(1 - R)\delta}{Ah\nu} = \frac{\frac{P}{\nu_{rep}}(1 - R)(1 - e^{-\alpha(h\nu)\tilde{t}})}{Ah\nu} \tag{4.21}$$

For our time resolved PL measurements, we photo-excited the sample with a pulsed laser with repetition rate 1 MHz, with photon energy $h\nu \approx 2.4$ eV. The reflectivity of $WS_2$ and $MoS_2$ are 0.42 and 0.43 respectively [66]. The absorption coefficients at $h\nu = 2.4$ eV are respectively $2.9 \cdot 10^5$

$cm^{-1}$ and $2.8 \cdot 10^5$ $cm^{-1}$ [66]. We measured a laser spot size diameter of $d_{spot} \approx 3$ $\mu m$ at FWHM, resulting in an area of

$$A = \pi \left( \frac{d_{spot}}{2} \right)^2 = \pi 1.5^2 10^{-8} cm^2 \approx 7 \cdot 10^{-7} cm^2 \tag{4.22}$$

To estimate the initial excitation density, we assumed that all the light pulse is absorbed within the area given by equation 4.22, and we made the assumption that the initial excitation density is constant in this photo-excited area.

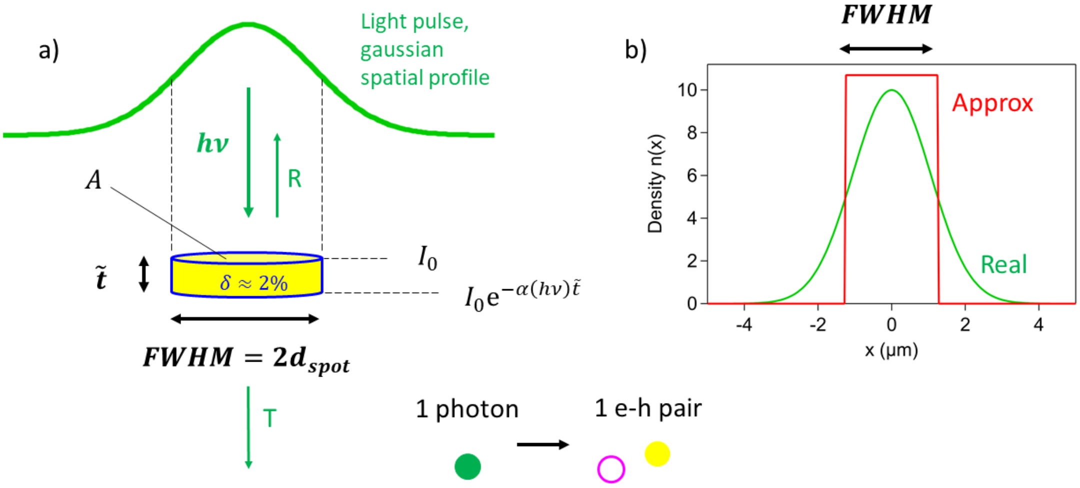

**Figure 4.13:** *a) Scheme of the photo-excitation of a TMD monolayer: a fraction $\delta$ of the excitation laser (Gaussian transverse intensity profile), related to the reflectivity, to the absorption coefficient and to the thickness of the monolayer, is absorbed within a region that in first approximation can be considered as a circle with diameter the FWHM of the laser profile. b) Real and approximated density profile (in 1D) after a pulsed excitation.*

Figure 4.13 shows a scheme of the photo-excitation of a TMD monolayer. The incoming pulsed laser, with transverse gaussian spatial profile is partially reflected and partially transmitted by the surface of the monolayer. A fraction $\delta$ of the transmitted part is absorbed within the monolayer. The approximated photo-excited area is represented as a cylinder with height the thickness of the monolayer, and base diameter equal to the FWHM of the laser profile. The real and approximated density profiles (the integrals are normalized) are represented in panel b). With this approximation we over-estimate the density at the center of the photo-excited area, and we neglect the contribution of the Gaussian tails.

Figure 4.14 a) and b) reports the excitation fluences and the estimated initial excitation densities, as a function of the incident power of the excitation pulsed laser, for the seven measurements that we performed on the $WS_2$ monolayer.

We calculated the errors on the fluence and on the excitation density by considering the errors on the measured excitation power, an error of the 10% on the photo-excited area and on the reflectivity, and an error of the 20% on the absorption coefficient.

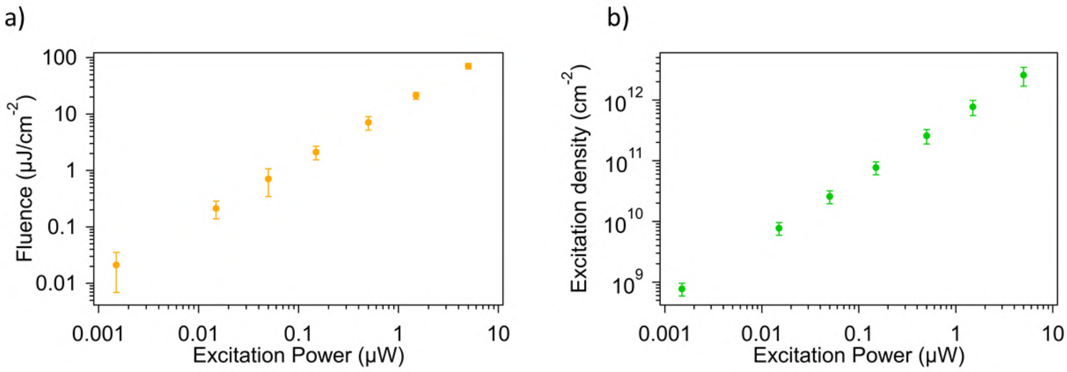

**Figure 4.14:** *a) Calculated fluence and (initial) excitation density as a function of the excitation power of the pulsed laser (at 1 MHz repetition rate). b) Calculated excitation density for monolayer $WS_2$ on $SiO_2$, as a function of the excitation power of the pulsed laser. The excitation density for monolayer $MoS_2$ is similar, and it differs only because of the different absorption coefficient.*

### 4.6.2 $WS_2$, time resolved photoluminescence, TR- spectra

We performed TR-PL measurements on 1L-$WS_2$ on $SiO_2$ substrate, at 7 excitation fluences (corresponding different initial excitation density), reported in table 4.3.

| Measurement | Fluence $\mu J/cm^2$ | Initial excitation density $(cm^{-2})$ |
|---|---|---|
| 001 | 0.02 | $8 \cdot 10^8$ |
| 002 | 0.2 | $8 \cdot 10^9$ |
| 003 | 0.7 | $2.5 \cdot 10^{10}$ |
| 004 | 2 | $8 \cdot 10^{10}$ |
| 005 | 7 | $2.5 \cdot 10^{11}$ |
| 006 | 20 | $8 \cdot 10^{11}$ |
| 007 | 70 | $2.5 \cdot 10^{12}$ |

**Table 4.3:** *Measurements on 1L-$WS_2$ on $SiO_2$, reporting the fluence and the initial excitation density*

The initial excitation density can be estimated by the initial excitation fluence, by considering the reflectivity of the material, the absorption coefficient and the thickness (shown in detail in chapter 5).

Figure 4.15 a) and c) reports the TR- interferogram maps for the measurements 001 and 007 reported in table 4.3, at the lowest and highest fluences. The corresponding interferograms at the time t=0 ps, are reported in the panels b) and d) respectively.

Figure 4.16 reports the TR- spectra maps for the measurements 001, 002, 003, and 007. These maps are obtained by the Fourier transform of the TR- interferogram maps. Figure 4.17 shows the TR- spectra maps for the measurements 001, 002, 003, and 007, deconvoluted by the time IRF, and represented in the interval $[-1, 2]$ ns $\times[1.7, 2.15]$ eV.

At low fluence, the TR-PL spectra map shows a sharp emission line at 2.0 eV, with a long lifetime, corresponding to the A exciton emission. As the fluence increases, the PL lifetime decreases. At the highest fluence, the spectra around the time zero exhibit a broadening towards lower photon energy. The "horizontal bands" far from the emission peak are related to the non-ideality of the Gemini interferomter, which introduces additional non-physical peaks in the PL spectra (see section 3.1.2). Figure 4.18 shows time resolved spectra for monolayer $WS_2$ on $SiO_2$, extracted from the TR- spectra maps (shown in figure 4.16), at t=-25 ps, at the time zero, at 25 ps, 50 ps, and 100 ps, at four excitation fluences, corresponding to the measurements 001, 005, 006 and 007 reported in table 4.3. The fluences are reported on the top right of each graph. The spectra are normalized to the emission peak, to highlight the differences in the spectral shape.

At low fluence, the emission line is peaked at 2.015 eV with a FWHM of ≈ 45 meV, and shows no

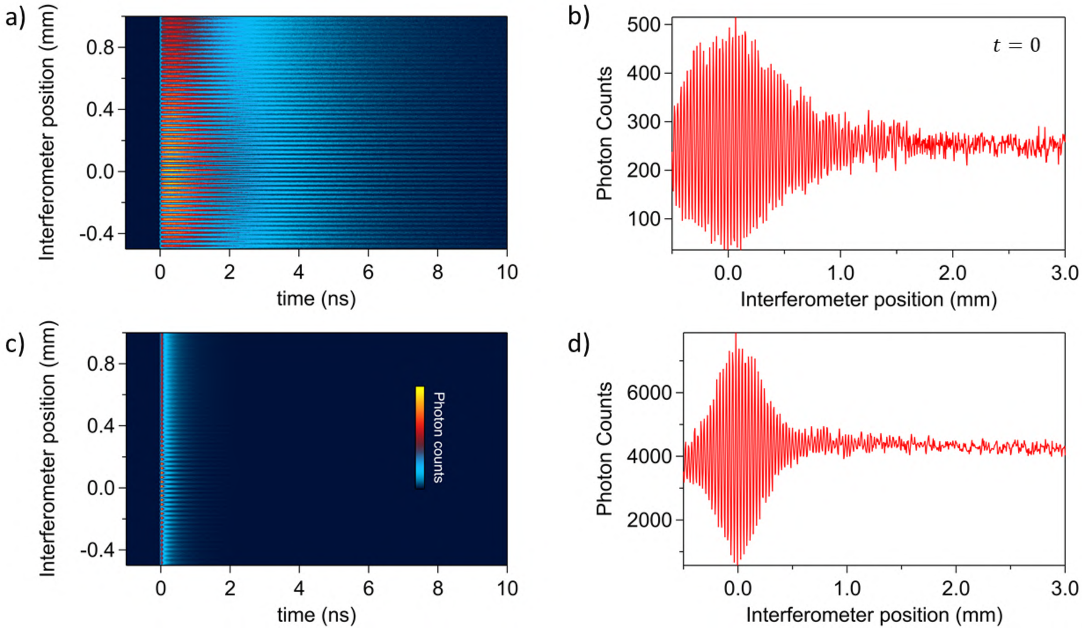

**Figure 4.15:** *Experimental TR-PL data for 1L-$WS_2$ on $SiO_2$. a, c) TR- interferogram maps at the lowest and highest fluences: $\phi = 20\ nJ/cm^2$ and $\phi = 70\ \mu J/cm^2$. b, d) Interferograms at the time $t = 0$ ps, extracted respectively from the maps a) and c).*

significant time dependence. As the fluence increases, the spectrum broadens around the time zero. The onset of this broadening is observed at $\approx 7\ \mu J/cm^2$, corresponding to an initial excitation density of $\approx 2.5 \cdot 10^{11}\ cm^{-2}$.

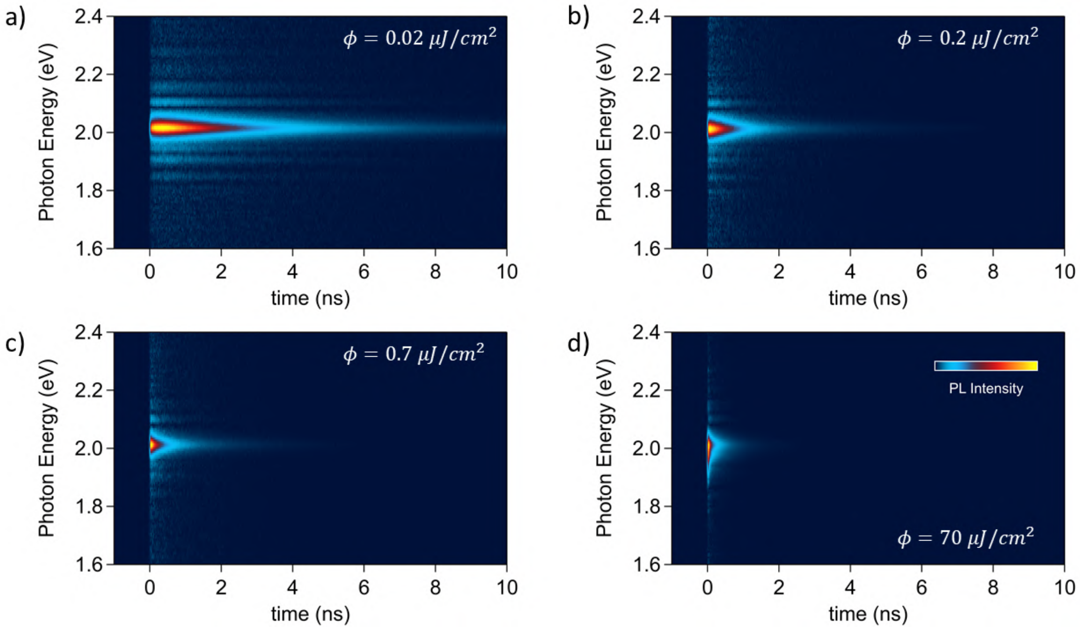

**Figure 4.16:** *1L-WS$_2$ on SiO$_2$: TR- spectra maps 001, 002, 003 and 007. Original maps, non deconvoluted by the IRF.*

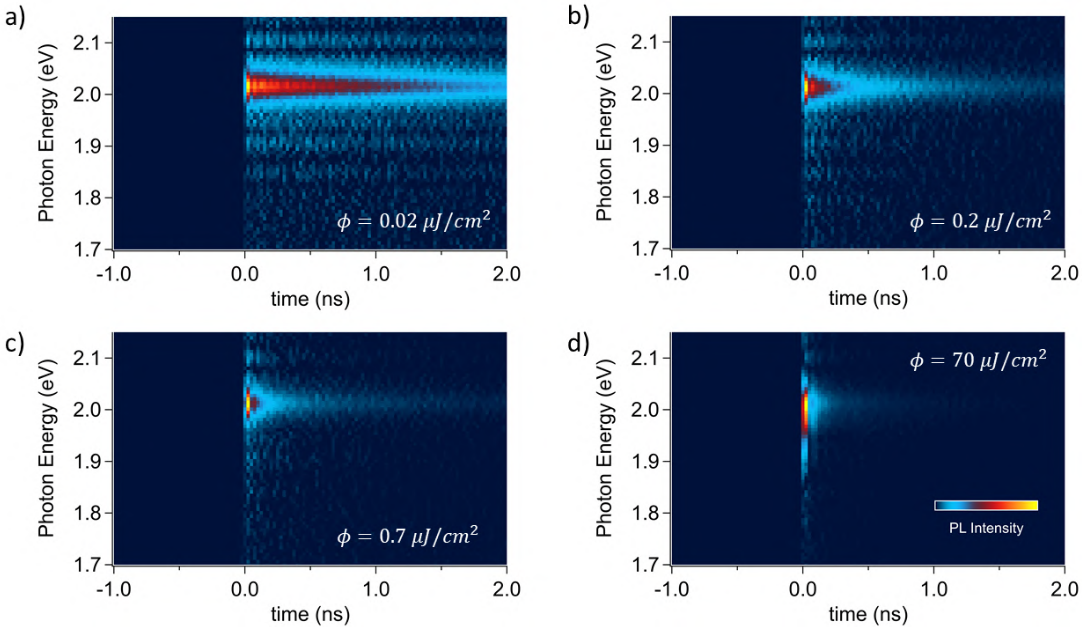

**Figure 4.17:** *1L-WS$_2$ on SiO$_2$: TR- spectra maps 001, 002, 003 and 007, deconvoluted by the time IRF(Richardson-Lucy): a) 0.02 $\mu J/cm^2$ b) 0.2 $\mu J/cm^2$ c) 0.7 $\mu J/cm^2$ d) 70 $\mu J/cm^2$.*

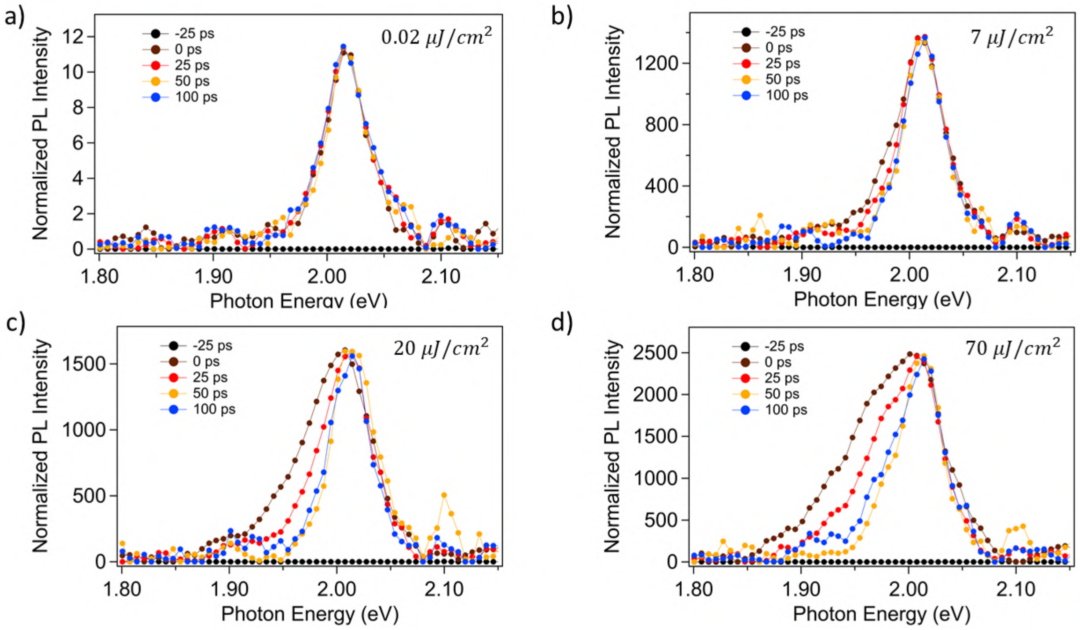

**Figure 4.18:** *Monolayer $WS_2$ on $SiO_2$. TR- spectra at t=-25, 0, 25, 50 and 100 ps, at four excitation fluences, reported in each graph.*

### $WS_2$, analysis of the spectrum at the time zero

The analysis of the PL spectrum at the time zero provides direct information on the effects of the initial carrier density. Figures 4.19 a) and b) show PL spectra at the time zero at each excitation fluence, normalized to the emission peak and to the integration time respectively. For fluences $\phi < 2\ \mu J/cm^2$, the PL spectrum shows not appreciable variation, while at higher fluences, the emission line significantly broadens towards lower photon energy.

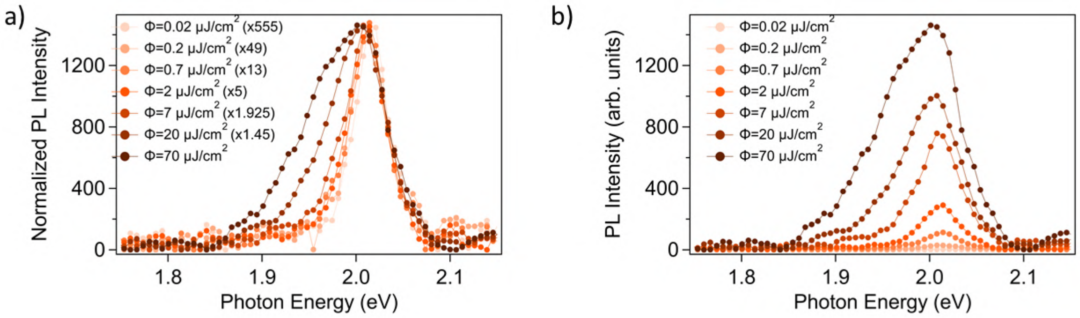

**Figure 4.19:** *PL spectra of monolayer $WS_2$ at the time t=0 ps, at each excitation fluence. a) Spectra normalized to the peak. b) Spectra normalized to the integration time.*

We performed a multipeak fitting to distinguish possible different spectral component in the PL spectrum. In first approximation, we decide to use two Gaussian peaks. However, we should point out the contributions to these PL spectra are much more complex, for the following reasons:

1. The PL spectra are integrated in 25 ps. Since the carrier density strongly decreases in few ps after excitation [14], the observed PL spectrum in our data is the sum of a continuum of PL spectra arising from different excitation density, as the latter decreases.

2. The spatial profile of the excitation density is not uniform, yielding in the presence of a continuum of density-dependent spectral contribution to the observed PL spectrum.

3. The shape of the emission spectrum for an electron-hole plasma in a 2D semiconductor is not Gaussian. To describe its emission line, in first approximation we should multiply the JDOS in 2D (see chapter 1, section 1.1, figure 1.2), including the effect of the density (/time) dependent band gap renormalization, by the quasi Fermi-Dirac distribution for electrons and holes, and convolute the result with the spectral resolution.

Hence, the following analysis is only semi-quantitative, giving information on the spatial and temporal average of the different, approximated, spectral contributions. However, it allows to extract parameters such as the position, the width and the area (integral) of the emission peaks necessary to fit the PL spectra. Figure 4.20 shows the multipeak fitting for the PL spectra at the time zero, at the three higher excitation fluences: 70, 20 and 7 $\mu J/cm^2$. At the highest fluence, $\phi$=70 $\mu J/cm^2$ (initial excitation density $\approx 2.5 \cdot 10^{12}$ $cm^{-2}$), the PL spectrum can be fitted with two Gaussian peaks, with spectral positions $1.971 \pm 0.006$ eV and $2.011 \pm 0.002$ eV respectively. The area of the peak at lower photon energy (peak 0) is about seven times higher than the area if the peak at higher photon energy (peak 1). The FWHM of the two peaks are $0.105 \pm 0.006$ eV and $0.060 \pm 0.006$ eV respectively. At $\phi$=20 $\mu J/cm^2$ (initial excitation density $\approx 8 \cdot 10^{11}$ $cm^{-2}$), the spectral positions and the FWHM of the peaks don't vary significantly (within the error bars). On the other hand, the area of the peak0 decreases by a factor about 3 with respect to the higher excitation density, while the area of the peak 1 is almost unchanged. This suggest that the contribution of the peak 0 is strongly dependent on the initial excitation density. At $\phi$=7 $\mu J/cm^2$ (initial excitation density $\approx 2.5 \cdot 10^{11}$ $cm^{-2}$), the spectrum can be fitted with one single Gaussian peak (peak 1), with spectral position $2.009 \pm 0.001$ eV and FWHM $0.058 \pm 0.002$ eV (almost unchanged with respect to the highest fluences). We fitted the PL spectra at each of the lowest fluences with a single Gaussian peak (not shown here), and we extracted the position, the FWHM and the peak area. These parameters are reported in figure 4.20 d), e) and f) respectively, as a function of the excitation fluence (bottom axis) and of the initial excitation density (top axis), calculated by using the equation 4.21. The energy position of the peak 1 slowly increases as the fluence decreases, up to a value of $2.017 \pm 0.001$ eV at the lowest excitation fluence. The FWHM of the peak 1 decreases as the fluence decreases, down to a value of $0.044 \pm 0.001$, approaching the value that we obtained in the steady state PL measurement at low excitation intensity for the CW

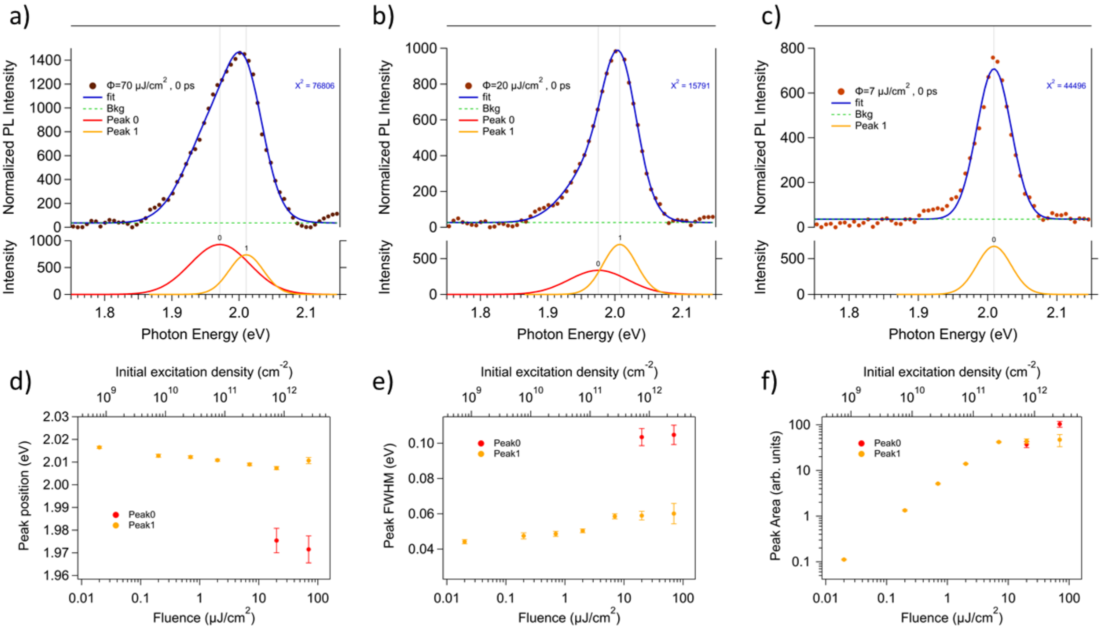

**Figure 4.20:** *TR-PL of monolayer $WS_2/SiO_2$. Spectra at the time zero. a,b,c) Multipeak fitting with two Gaussian functions (peak0 and peak1), shown only for the three highest excitation fluences (see legends on each graph). d,e,f) Fit parameters as a function of the fluence (bottom axis) and of the initial excitation density (top axis): peak position, peak FWHM and peak area.*

laser.
We associate the peak 0, resulting in the broadening of the emission line towards lower photon energy, to the presence of an electron-hole plasma (EHP) at high excitation density. We associate the peak 1 to the free exciton (FE) emission. The threshold density for the ionization of free excitons (FE) is found to be between $2.5 \cdot 10^{11}\ cm^{-2}$ and $2.5 \cdot 10^{12}\ cm^{-2}$. A similar threshold for the formation of the EHP have already been reported [14]. Above this density value, we observed a damaging of the $WS_2$ monolayer.

### $WS_2$, analysis of the time resolved spectrum at the highest excitation density

The analysis of the time resolved PL spectra at the highest excitation fluence, $\phi$=70 $\mu J/cm^2$ (excitation density $\approx 2.5 \cdot 10^{12}\ cm^{-2}$), provides information on the effects of the time evolution of the system, as the density of photo-excited carriers decreases. The multipeak fitting of the PL spectra at different times after excitation allows to capture the time evolution of the different contributions to the PL spectra. We performed a multipeak fitting with two Gaussian peaks, at five significant time delays: 0 ps, 25 ps, 50 ps, 100 ps, and 200 ps. Figure 4.21 a), b) and c) reports the multipeak fitting for the first three spectra. At 0 ps, the spectrum can be fitted with two

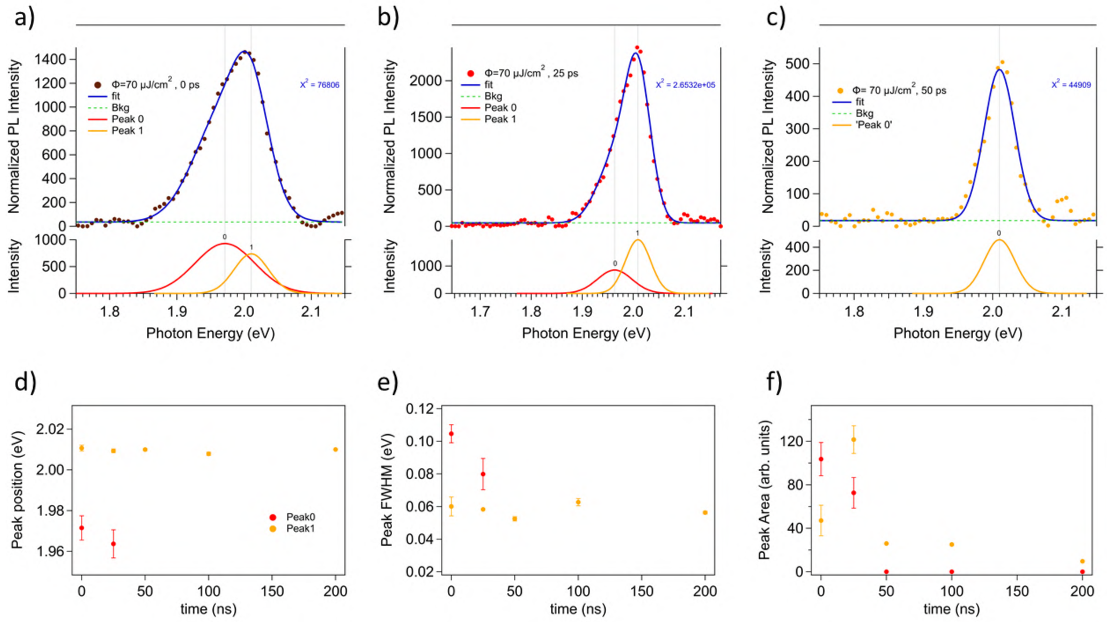

**Figure 4.21:** *TR-PL of monolayer $WS_2/SiO_2$. TR- spectra at the highest excitation fluence ($\phi$=70 $\mu J/cm^2$) a,b,c) Multipeak fitting with two Gaussian functions (peak0 and peak1), shown only for the first three times: 0 ps, 25 ps and 50 ps. d,e,f) Fit parameters as a function of the time after excitation: peak position, peak FWHM and peak area.*

Gaussian peaks with spectral positions $1.971 \pm 0.006$ eV and $2.011 \pm 0.002$ eV, and FWHM of the two peaks are $0.105 \pm 0.006$ eV and $0.060 \pm 0.006$ eV, respectively. These peaks are associated to the EHP emission and to the FE emission, respetively. The peak at lower photon energy, associated to the EHP emission, constitutes the main contribution to this spectrum. At 25 ps the positions and FWHM of the peaks are almost unchanged with respect to the time zero. Instead, the ratio between the peak area is reversed. The FE dominates the PL spectrum at 25 ps. At 50 ps, and at the subsequent time delays, the PL spectrum can be fitted with a single Gaussian peak. The fit parameters are reported in figure 4.21 d,e,f). The peak positions show no significant variation in time, within the error bars. The FE emission line does not vary with the carrier density, since the bandgap renormalization and the reduction of the FE binding energy are similar (see chapter 1). We expected the peak 0 to blue-shift as the time increases, because of the reduction of the bandgap renormalization as the carrier density decreaes. Instead, we observe a red-shift of this peak, but this is not significant within the error bar. However, this behavior calls for further investigation.

The FWHM of the exciton emission line remains almost unchanged in time, with a value of $\approx 60$ meV. The FWHM of the EHP emission significantly decreaes from 0 ps to 25 ps, as well as the area of the related peak. The area of the exciton peak exhibits an initial increase (from 0 ps to 25 ps), and then a monotonic decrease towards zero, due to the exciton radiative and non-radiative recombination. The initial increase of the integrated FE emission can be associated to the binding of the free electrons and holes in the EHP to form FEs.

#### Effect of the temperature on the TR-PL spectra

As discussed in chapter 1 and in the section 4.4, the temperature plays an important role on the position of the peaks of the PL spectra, due to the temperature induced change in the free particle bandgap $E_g$. We evaluated the lattice heating induced by the absorption of the laser pulse, by using the equation:

$$Q = mc_T\Delta T \iff \Delta T = \frac{Q}{mc_T} \tag{4.23}$$

where $\Delta T$ is the temperature variation, Q is the heat absorbed by the sample due to the absorption of the light pulse, and $c_T$ is the specific heat. m is the mass of the photo-excited area, given by the product of the mass density in 3D and the photo-excited volume. Since the QY of the $WS_2$ is lower than the 5%, we can assume that the absorbed heat Q is equal to the absorbed energy per pulse. We estimate the order of magnitude of $\Delta T$ by using the density of $WS_2$, $\rho = 7.5\ kg/m^3$ and the specific heat of $WSe_2$ [33], $c_T = 226\ J/kg\cdot K$ (the numeric value for $WS_2$ and $MoS_2$ can't be found in literature, and we assume that the value for $WSe_2$ is of the same order of magnitude). The, absorbed energy per pulse is given by

$$E^{abs}_{pulse} = \frac{P}{\nu_{rep}}(1-R)(1-e^{\alpha(h\nu)\tilde{t}}) \tag{4.24}$$

where we used the same notation of equation 4.21. By combining equation 4.23 and 4.24, with $Q = E^{abs}_{pulse}$ and $m = 5.3\cdot 10^{-17}$ kg, we obtain the following espression for the increase in temperature in $WS_2$ monolayer, as a function of the excitation power in $\mu W$ of the pulsed laser (at 1 MHz repetition rate):

$$\Delta T[K] \approx 1.2\cdot P[\mu W] \tag{4.25}$$

At the maximum excitation power, $P=5\ \mu W$, corresponding to a fluence of 70 $\mu J/cm^2$, the increase in the lattice temperature in the monolayer $WS_2$ is $\Delta T \approx 6$ K (similar to the value reported in [38]), resulting in a shift of the PL emission peak of $\approx 3$ meV [56]. Since the energy difference between the spectral positions of the peak0 and peak1 at the time zero, in the previous analysis is greater than 30 meV, we can neglect the contribution of the laser-induced lattice heating. Moreover, the estimated increase in the lattice temperature by using this approach is valid only when most of the excess energy of the photo-excited carriers is transferred to the crystal lattice, while at the time zero (within 25 ps) carriers are not yet thermalized.

### 4.6.3 $WS_2$, time resolved photoluminescence, PL time dynamics

The analysis of the energy integrated PL time dynamics provides direct information on the radiative and non-radiative carrier recombination pathways. We integrated the TR-PL maps, in the range [1.7, 2.2] eV, and we normalized the intensity by the acquisition time. Figure 4.22 shows the energy integrated and normalized time dynamics at three excitation fluences. At the lowest fluence, 0.02 $\mu J/cm^2$, the PL intensity exhibits a decay which slope is almost constant (in log scale). As the fluence increases by one order of magnitude, a fast component in the decay appears at times $t<2$ ns. As the fluence increases, the fast component becomes more and more pronounced, as the slope in the first 100 ps increases. On the other hand, at long time delays we observe an overlap of the three time dynamics, reflecting the behavior of the system when the excitation density drops below a threshold value.

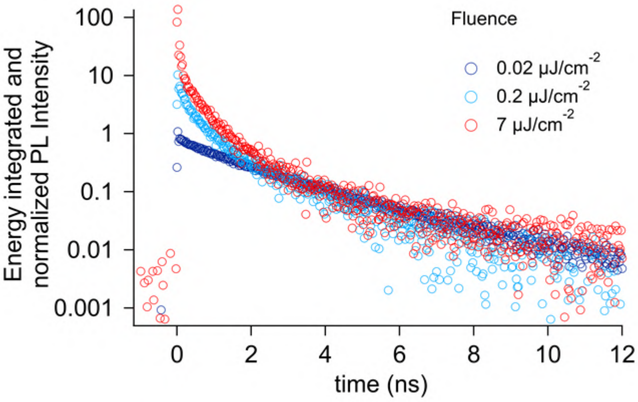

**Figure 4.22:** *Energy integrated TR-PL time dynamics, for monolayer $WS_2/SiO_2$, at three fluences.*

### A first approach: three-exponential fitting

We fitted the PL dynamics with a function given by the sum of three exponentials, to access the lifetimes associated to the different components of the decay. The fit function is given by:

$$I_{PL}(t) = I_1 exp^{-\frac{t-t_0}{\tau_1}} + I_2 exp^{-\frac{t-t_0}{\tau_2}} + I_3 exp^{-\frac{t-t_0}{\tau_3}} \tag{4.26}$$

where $I_1, I_2, I_3$ are the intensities of the different components, and $\tau_1, \tau_2, \tau_3$ are the time constants. We fitted the experimental data in the range [0.075, 11] ns, where the time zero is $t_0 = 0.075$ ns. We were not able to start the fit at earlier times (such as t=0.025 ns), because the PL dynamics exhibits another faster component in the first 50 ps, as it can be seen by looking at figure 4.22 a). The experimental data and fits are shown in figure 4.23, for four excitation fluences.

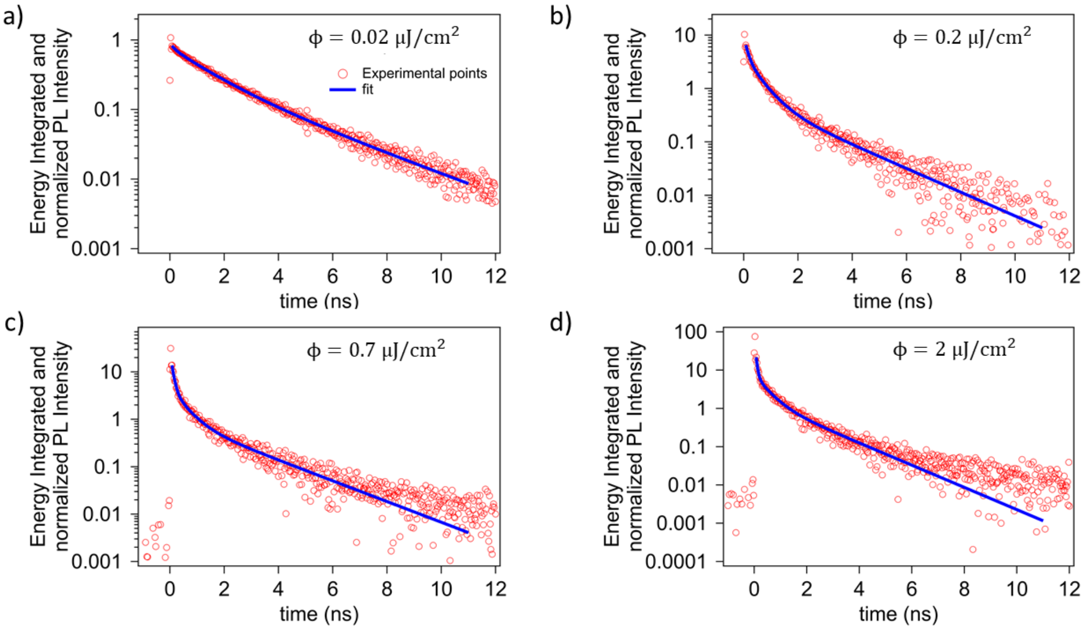

**Figure 4.23:** *Energy integrated TR-PL time dynamics, for monolayer $WS_2/SiO_2$, at four fluences, indicated on each graph. The experimental data are plotted along with the fits, performed with a function given by the sum of three exponentials.*

The result of the fit is good, especially at the lowest excitation fluences, while as the fluence increases above 0.7 $\mu J/cm^2$ the dynamics at long times can't be reproduced accurately. The fit parameters are reported in figure 4.24 versus the excitation fluence. The PL intensity decay

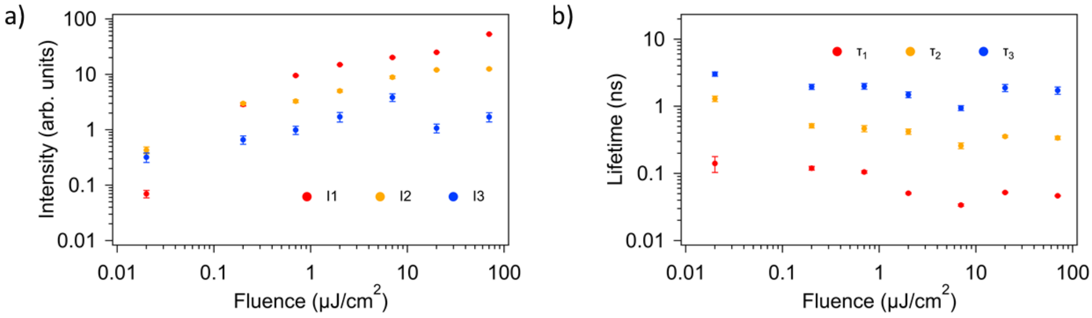

**Figure 4.24:** *Parameters of the "three-exponential" fits, plotted versus the excitation fluence. a) Intensity of the three exponential functions ($I_1, I_2, I_2$ of equation, 4.26). b) Time constants of the three exponential functions ($\tau_1, \tau_2, \tau_3$ in equation 4.26).*

exhibits three time constants, in the range 40-150 ps, 0.25-1.3 ns and 0.94-3.03 ns respectively. At low fluence, the PL intensity corresponding to the faster dynamics, $I_1$, is about 1/5 and 1/6 of the intensity of the slower components, $I_2$ and $I_3$. As the fluence increases, the relative intensity associated to the faster component increases, and it becomes dominant for a fluence $\phi >0.2\ \mu J/cm^2$. At the two highest fluences, the PL intensity associated to the slower component shows a fast decrease, while the intensity of the faster component still increases. The fitted lifetimes $\tau_1, \tau_2, \tau_3$ exhibit a decreasing trend for fluences $\phi <20\ \mu J/cm^2$, while their value slightly increases above this fluence. This can be associated to a different excitation regime, with a threshold fluence $\approx 20\ \mu J/cm^2$, as confirmed also by the analysis of the TR- spectra. Although the dynamics of the EHP can't be investigated, since there are only two experimental points, for times t=0 ps and t=25 ps (while now we fitted the dynamics for t>75 ps), the different physics of the system seems to affect the PL time dynamics.

Although the fitting with three exponentials provides some information on the PL time dynamics, this approach doesn't give access to important physical constant of the investigated system, such as the radiative and non radiative lifetime of carriers.

### Fit function by solving the analytic solution of the differential equation for the exciton density

At low excitation density (fluence $\phi < 20\ \mu J/cm^2$), most of the carriers are excitons. In this excitation regime, we are interested in extract the exciton radiative lifetime and the exciton-exciton annihilation coefficient. Hence, we tried a second approach, exploiting the solution of the differential equation 2.5, for the free exciton density, which includes the radiative and non-radiative recombination of excitons and the exciton-exciton annihilation (see chapter 2). The solution of this equation is given by equation 2.6. Let us recall the differential equation 2.5

$$\frac{dn(t)}{dt} = -Bn(t) - Cn^2(t) \tag{4.27}$$

and its solution:

$$n(t) = \frac{B}{C} \frac{1}{(e^{B(t-t_0)}[1 + \frac{B}{Cn_0}] - 1)} \tag{4.28}$$

where C is the exciton-exciton annihilation rate, and B is the sum of the radiative and non-radiative recombination rate for free excitons. $t_0$ is the initial time, and $n_0 = n(t_0)$ is the initial exciton density, which is given by the initial excitation density. The PL intensity is given by the radiative part of the time derivative of the exciton density (see chapter 2). The non-radiative recombination rate in TMD monolayers, due to the capture of free excitons in defect states, have been observed to be on the order of few picosecond [14, 72]. Hence, in our TR-PL data we don't have the time resolution to capture this dynamics. For this reason, we can use an approximate approach, where we consider $B \equiv B'$ as an effective radiative recombination rate, and an initial exciton density which is lower than the initial excitation density. We set this value to one half of the calculated initial excitation density. In this approximation, we can write the following expression for the PL intensity:

$$I_{PL}(t) = KB'n(t) \tag{4.29}$$

where K is a constant to reproduce the arbitrary units, and where the radiative recombination rate $A_R$ of equation 2.7 is replaced by the effective radiative recombination rate B'. The PL intensity of equation 4.29 can be written explicitely, by using the solution of equation 4.28, with B=B', and $n_0 \rightarrow n'_0 = n_0/2$.

$$I_{PL}(t) = KB'\frac{B'}{C}\frac{1}{(e^{B'(t-t_0)}[1+\frac{B'}{Cn'_0}]-1)} \tag{4.30}$$

The PL intensity at the time zero is given by

$$I_{PL}(0) = KB'n'_0 \equiv I_0 \tag{4.31}$$

It is useful to rewrite 4.30 in terms of the initial intensity, instead of the initial density, allowing to fix the initial value of $I_0$ in the fit procedure. The final fit function is given by

$$I(t) = \frac{B'^2}{\tilde{C}}\frac{1}{(e^{B'(t-t_0)}[1+\frac{B'^2}{\tilde{C}I_0}]-1)} \tag{4.32}$$

$$C = K\tilde{C}; K = \frac{I_0}{B'n'_0}$$

We used this function to fit the PL dynamics at four excitation fluences, ranging from 0.2 $\mu J/cm^2$ to 7 $\mu J/cm^2$. We fixed the value of B' at 0.4 $ns^{-1}$, which allows to fit the time dynamics at long time delays, and use $\tilde{C}$ as the only free parameter. The results for the exciton-exciton annihilation coefficient are reported in figure 4.25. We obtained an exciton-exciton annihilation coefficient in the range 1-4 $cm^2s^{-1}$, which is more than one order of magnitude higher than the rate found in [74] (transient absorption, CVD $WS_2$ monolayers), and two to ten times higher than the rate found in [93] (TR-PL, exfoliated $WS_2$ monolayers). However, we should point out that our result is dependent on the guess on the initial excitation density. The lower is the value of the initial density $n'_0$, the higher is the value for the fitted exciton-exciton annihilation coefficient. This fact calls for further investigation on the carrier dynamics and recombination on the ultrafast time scale, to unveil the decay of the exciton density within the first 25 ps.

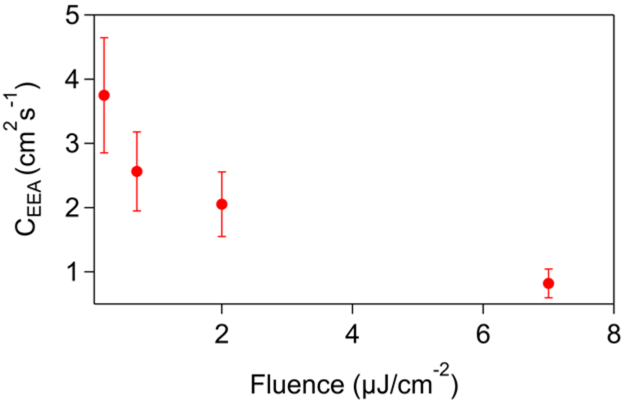

**Figure 4.25:** *Exciton-exciton annihilation rate versus the excitation fluence. These data are extracted by the fitting of the energy integrated PL time dynamics with the analytic solution of the differential equation for the exciton density.*

### Dynamic model for the TR-PL in TMD

By using the analytic solution of the differential equation, we are able to estimate the exciton-exciton annihilation coefficient, using an effective radiative recombination rate for free excitons.

However in this model, we can't access the real radiative lifetime for free excitons. Moreover, we don't take into account the possible fast trapping of free excitons in defect states, which is a key mechanism in exciton dynamics and recombination, as reported by many experimental works [24]. We exploited the model described in [24], which is explained in detail in chapter 2, section 2.3. In this model, that there are two kinds of defects are considered in the $WS_2$ monolayer:

1. "Fast" defects, where a consistent part of the photo-excited excitons (or free carriers) are captured on the ps time scale. The rate of recombination from these defect states towards the ground state is very high.
2. "Slow" defects, where the photo-excited excitons are trapped, and which recombination rate towards the ground states is slow (on the $\mu s$ time scale) [24]. Excitons can de-trap from the trap states, if the energy difference between the free exciton and the trapped exciton is $\approx k_B T$.

Fast and slow defects have a random spatial distribution, as well as the photo-excited excitons. The latter can be created in regions where the crystal is perfect, in regions where there is a fast defect, or in a region where there is a slow defect. Hence, part of the free excitons recombine in fast defects on the ps time scale, part of the carriers are captured in slow defects, where they can either decay slowly towards the ground state or de-trap to give rise again to free excitons. Part of the carriers can be created in regions where the crystal is perfect, and subsequently recombine radiatively, or diffuse and be captured either in slow or fast defects. The density of defects plays a crucial role, especially for slow defects, where the recombination rate of trapped excitons towards the ground state is low. These defect can be saturated, resulting in a quenching of their contribution to the capture of free excitons. Our model takes into account these processes.

To help the reader, we rewrite here the coupled differential equations 2.12 describing the time evolution of the density of free excitons, $n_X(t)$ and trapped excitons, $n_{XT}(t)$, where we added the exciton-exciton annihilation contribution.

$$\begin{aligned}\frac{dn_X}{dt} &= -k_{RAD}\cdot n_X - Cn_X^2 - k_{TRAP}\cdot\left(1-\frac{n_{XT}}{N_0}\right) + k_{DETRAP}\cdot n_{XT} \\ \frac{dn_{XT}}{dt} &= -k_{RAD}^{TRAPPED}\cdot n_{XT} - k_{DETRAP}\cdot n_{XT} + k_{TRAP}\cdot\left(1-\frac{n_{XT}}{N_0}\right)\end{aligned} \tag{4.33}$$

We remind that $k_{RAD}$ is the radiative recombination rate for free excitons, $k_{TRAP}$ is the rate at which excitons are trapped in "slow" defect states, $k_{DETRAP}$ is the rate at which excitons de-trap from defect states, and $k_{RAD}^{TRAPPED}$ is the radiative recombination rate for trapped excitons (of the order of 1 $\mu s$). $N_0$ is the saturation density for the slow defects. The de-trap rate is related to the trap rate, by the relation:

$$k_{DETRAP} = k_{TRAP}e^{-\frac{\Delta E}{k_B T}} \tag{4.34}$$

where $\Delta E$ is the energy difference between the free exciton transition and the trapped exciton transition, and $k_B T$ is the available thermal energy. We solved numerically the coupled differential equations 4.33.

$$\begin{aligned}n_X(t_{i+1}) &= n_X(t_i) + \delta t\cdot\big(-k_{RAD}\cdot n_X(t_i) - Cn_X(t_i)^2 - k_{TRAP}\cdot(1-\frac{n_{XT}(t_i)}{N_0}) \\ &\quad + k_{DETRAP}\cdot n_{XT}(t_i)\big) \\ n_{XT}(t_{i+1}) &= n_{XT}(t_i) + \delta t\cdot\big(k_{RAD}^{TRAPPED}\cdot n_{XT}(t_i) - k_{DETRAP}\cdot n_{XT}(t_i) \\ &\quad + k_{TRAP}\cdot(1-\frac{n_{XT}(t_i)}{N_0})\big)\end{aligned} \tag{4.35}$$

where, we used a step $\delta t = 100fs$. The PL intensity is proportional to the radiative part of the time derivative of the free exciton density, i.e.

$$I_{PL}(t_i) = K\cdot k_{RAD}n_X(t_i) \tag{4.36}$$

The proportionality constant K gives the ratio between the PL intensity in arbitrary units and the number of emitted photons, in the unit time. We used 4.36 as a fit function for our data, where

$n_X(t)$ is calculated step by step by using the numeric solution show in in equation 4.35. In the fitting procedure, we kept fixed the energy difference between the free exciton and the trapped exciton levels, the radiative recombination rate for trapped excitons, the saturation density of slow defects, the proportionality constant K and the temperature. The fixed values of these parameters are reported in table 4.4:

| $\Delta E$ (meV) | $k_{RAD}^{TRAPPED}$ $(ns^{-1})$ | $N_0$ $(cm^{-2})$ | T (K) | K |
|---|---|---|---|---|
| 10 | $10^{-4}$ | $2 \cdot 10^8$ | 300 | $4 \cdot 10^{-9}$ |

**Table 4.4:** *Values for the fixed parameters in the fitting procedure.*

The free parameters of the fit are the radiative recombination rate for free excitons ($k_R$), the exciton-exciton annihilation rate ($C$), the trap rate for free excitons ($k_{TRAP}$) and the initial excitation density ( $n_X(t_0)$). The latter is strongly correlated with the proportionality constant K. Hence, in the fitting procedure, we set the value of K, in the fitting of the dynamics at the lowest fluence, such that the fitted initial exciton density is about one half with respect to the calculated excitation density. In every other fitting procedure, we kept K fixed to the same value. Table 4.5 reports the free fitting parameters, and their values, for four excitation fluences $\phi$.

| $\phi$ $(\mu J/cm^2)$ | $k_{RAD}$ $(ns^{-1})$ | C $(cm^2 s^{-1})$ | $k_{TRAP}$ $(ns^{-1})$ | $n_X(t_0)$ $(cm^{-2})$ | $n_0$ $(cm^{-2})$ |
|---|---|---|---|---|---|
| 0.02 | $0.58 \pm 0.01$ | $1(*)$ | $14.89 \pm 0.52$ | $5.25 \cdot 10^8 \pm 6 \cdot 10^6$ | $7.7 \cdot 10^8$ |
| 0.2 | $0.78 \pm 0.04$ | $2.39 \pm 0.13$ | $15.45 \pm 1.09$ | $3.02 \cdot 10^9 \pm 1.6 \cdot 10^8$ | $7.7 \cdot 10^9$ |
| 0.7 | $0.61 \pm 0.05$ | $1.45 \pm 0.11$ | $8.06 \pm 3.07$ | $1.29 \cdot 10^{10} \pm 1.1 \cdot 10^9$ | $2.6 \cdot 10^{10}$ |
| 2 | $1.16 \pm 0.07$ | $1.69 \pm 0.09$ | $5.42 \pm 5.02$ | $1.63 \cdot 10^{10} \pm 9 \cdot 10^8$ | $7.7 \cdot 10^{10}$ |

**Table 4.5:** *Values for the free parameters, obtained by the fitting procedure. Note: the exciton-exciton annihilation rate for the lowest fluence was kept fixed at 1 $cm^2 s^{-1}$.*

The experimental data and the fits are shown in figure 4.26, for the four excitation fluences. This fitting procedure allows to capture the dynamics for $t \geq 25$ ps. For the time dynamics at the lowest fluence, shown in panel a) of figure 4.26, the fit well reproduces the time dynamics for t<5 ns,

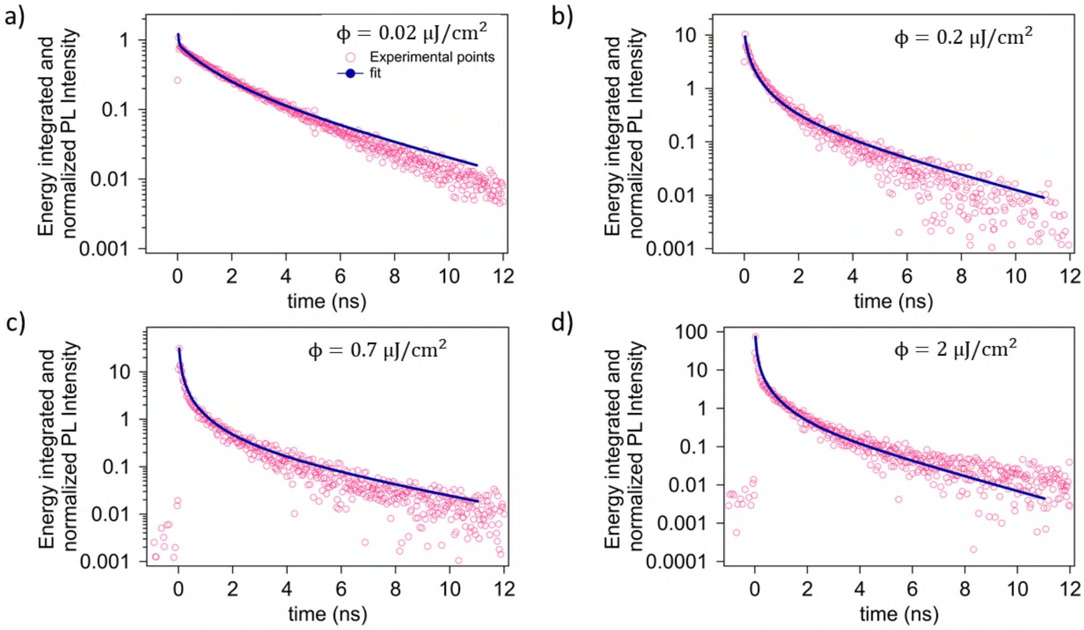

**Figure 4.26:** *Energy integrated TR-PL time dynamics, for monolayer WS$_2$/SiO$_2$, at four fluences, indicated on each graph. The experimental data are plotted along with the fits, performed with the fit function 4.36, exploiting the dynamic model described in the main text.*

even in the first two-three experimental point, where the three-exponential approach is not able to unveil the first fast decay, that according to this model is due to the initial fast capture of free excitons in slow defect states, until the latter are saturated. However, the dynamics at $t > 5$ ns, is not perfecly reproduced. At 0.2 $\mu J/cm^2$, 0.7 $\mu J/cm^2$ and 2 $\mu J/cm^2$, the fit reproduces both the fast dynamics at short time, and the slow dynamics at long times. We associate the initial fast dynamics to the exciton-exciton annihilation. This contribution dominates when the "slow" defect states are saturated, and when the density of free exciton which is sufficiently high to make the exciton-exciton annihilation the main recombination process. As the density decreases, the contribution of the exciton-exciton annihilation decreases, and the radiative exciton recombination is favored, until the "slow" defect states are saturated. When a dynamic equilibrium is set between the trapping and de-trapping of free excitons, the free excitons that de-trap from defect states and subsequently recombine radiatively result in an "apparent" long PL lifetime. The fit parameters are reported in figure 4.27. We plot the radiative lifetime for free excitons ($\tau_{RAD} = 1/k_{RAD}$) and the time constant for the trapping of free excitons ($\tau_{TRAP} = 1/k_{TRAP}$) instead of the radiative recombination rate and the trapping rate. The radiative lifetime for free excitons, shown in panel a) of figure 4.27, ranges from 0.86 ns to 1.72 ns, which can be compared with the value found by Yuan et al [93], of 0.856 ns. The time constant for the trapping of free excitons in the slow defect states is found to be in the range 65-185 ps (see figure 4.27 c), with an error that increases as the excitation fluence increases. This can be related to the fact that, at high initial excitation densities, the defect states are immediately saturated, yielding in a time dynamics which is dominated by free excitons in a large time interval (except in a very short initial time window where part of the excitons are quicky trapped to saturate the defect states). The exciton-exciton annihilation rate, shown in figure 4.27 b), ranges from 1.4 to 2.4 $cm^2s^{-1}$, of the same order of magnitude of the coefficients found in the previous section, and 2 to 10 times higher with respect to previous results [24, 93]. We associate this discrepancy to their over estimate of the initial excitation density, while we take into account the fast drop of the exciton density due to the fast non-radiative decay of excitons within few ps, which we observed in the pump-probe photoemission data, and that have been observed in other TR- reflectivity experiments [72, 14, 63]. The value for the exciton-exciton annihilation rate at the lowest excitation fluence should not be considered, since it was kept fixed to 1 $cm^2s^{-1}$ in the fitting procedure: at the lowest fluence, the exciton-exciton annihilation almost

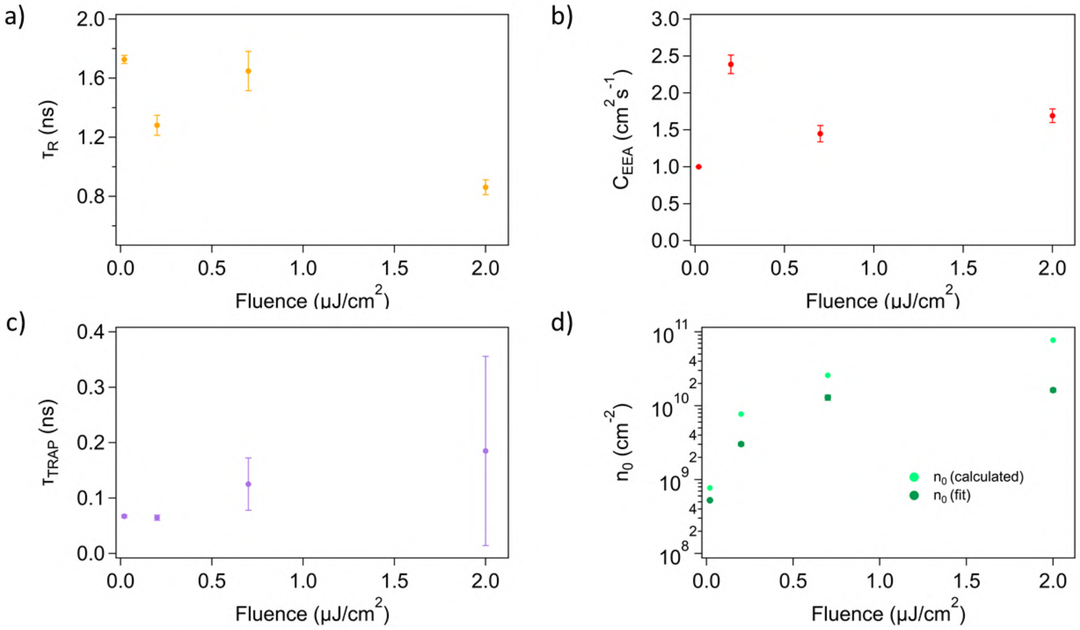

**Figure 4.27:** *Fit parameters extracted by the dynamic model described in this section. Each parameter os plotted versus the excitation fluence. a) Exciton radiative lifetime. b) Exciton-exciton annihilation rate. c) Time constant for the trapping of excitons in defects states. d) Initial exciton density: fitted (dark green) and calculated (light green).*

does not contribute to the exciton recombination, and the value of this coefficient is almost non-relevant in the fitting procedure. The fitted value of the excitation density is shown in figure 4.27 d).

### 4.6.4 Monolayer $MoS_2$, time resolved photoluminescence, TR- spectra

We first characterized the $MoS_2$ monolayer with steady state PL. Figure 4.28 a) shows the PL spectra monolayer $MoS_2$ on $Si_O2$ at three excitation intensities. As the intensity increases, the B exciton emission becomes more pronunced. A similar behaviour have been observed in [39], on CVD grown monolayer $MoS_2$ on $SiO_2$.

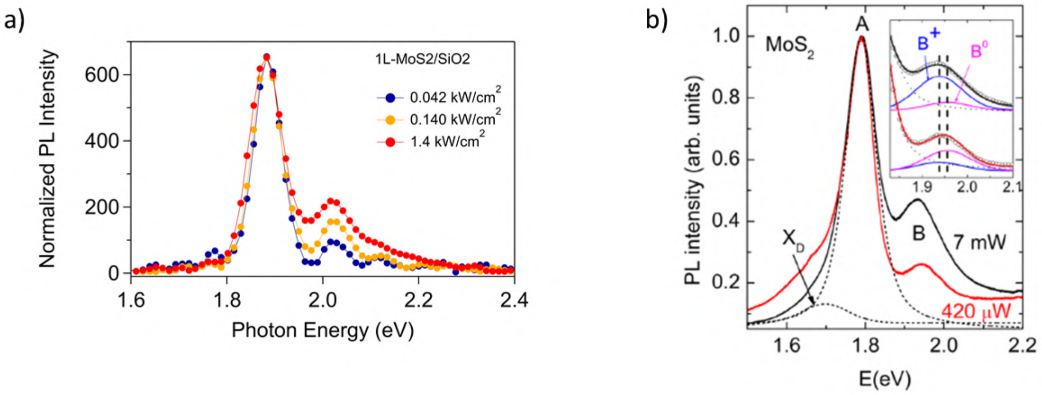

**Figure 4.28:** *Steady state PL for 1L-$MoS_2/SiO_2$ versus excitation intensity. a) Original experimental data. b) Data taken from the literiture [39].*

We performed TR-PL measurements on 1L-$MoS_2$ on $SiO_2$ substrate, at 5 excitation fluences, reported in table 4.6.

| Measurement | Fluence $\mu J/cm^2$ | Initial excitation density $(cm^{-2})$ |
|---|---|---|
| 001 | 6 | $2 \cdot 10^{11}$ |
| 002 | 20 | $8 \cdot 10^{11}$ |
| 003 | 70 | $3 \cdot 10^{12}$ |
| 004 | 200 | $8 \cdot 10^{12}$ |
| 005 | 600 | $2 \cdot 10^{13}$ |

**Table 4.6:** *Measurements on 1L-$MoS_2$ on $SiO_2$, reporting the fluence and the initial excitation density*

Figure 4.29 a) and c) reports the TR- interferogram maps for the measurements 001 and 003 reported in table 4.6. The corresponding interferograms at the time t=0 ps, are reported in the panels b) and d) respectively. Figure 4.30 reports the TR- spectra maps for the measurements 001, 002, 003, and 007, obtained by the Fourier transform of the TR- interferogram maps. Figure 4.31 reports the TR- spectra maps for the measurements 001, 003, 004, and 005, deconvoluted by the time IRF, and represented in the interval $[-1, 2]$ ns $\times [1.6, 2.4]$ eV . At the lowest fluence, 6 $\mu J/cm^2$, the A and B exciton peaks are detectable at 1.9 eV and 2.05 eV. The latter is detectable only at times close to t=0 ps. As the excitation fluence increases, the PL lifetime decreases, and the spectrum at short times broadens towards higher photon energy.

Figure 4.32 shows time resolved spectra for monolayer $MoS_2$ on $SiO_2$, extracted from the TR-spectra maps (shown in figure 4.31), at the time zero, at 25 ps, 50 ps, and 100 ps, at four excitation fluences, corresponding to the measurements 002, 003, 004 and 005 reported in table 4.6. The fluences are reported on each graph. The spectra are normalized to the emission peak, to highlight the differences in the spectral shape. At each fluence, the spectrum at the time t=0 ps is red-shifted with respect to the subsequent spectra, and it broadens as the fluence increases. At t=25 ps and at low fluence (20 $\mu J/cm^2$), the PL spectrum at t=25 ps shows a main peak at 1.88 eV (FWHM of ≈ 65 meV), corresponding to the A exciton, and a second peak with lower intensity at 2.03 eV, corresponding to the B exciton. The latter becomes more pronounced as the fluence increases. The broadening and redshift of the spectrum at the time zero, as well as the enhance in the intensity of the B exciton emission (and of the tail towards high emission photon energies) at t=25 ps exhibit a threshold between 20 $\mu J/cm^2$ and 70 $\mu J/cm^2$, similarly to what we observed for $WS_2$.

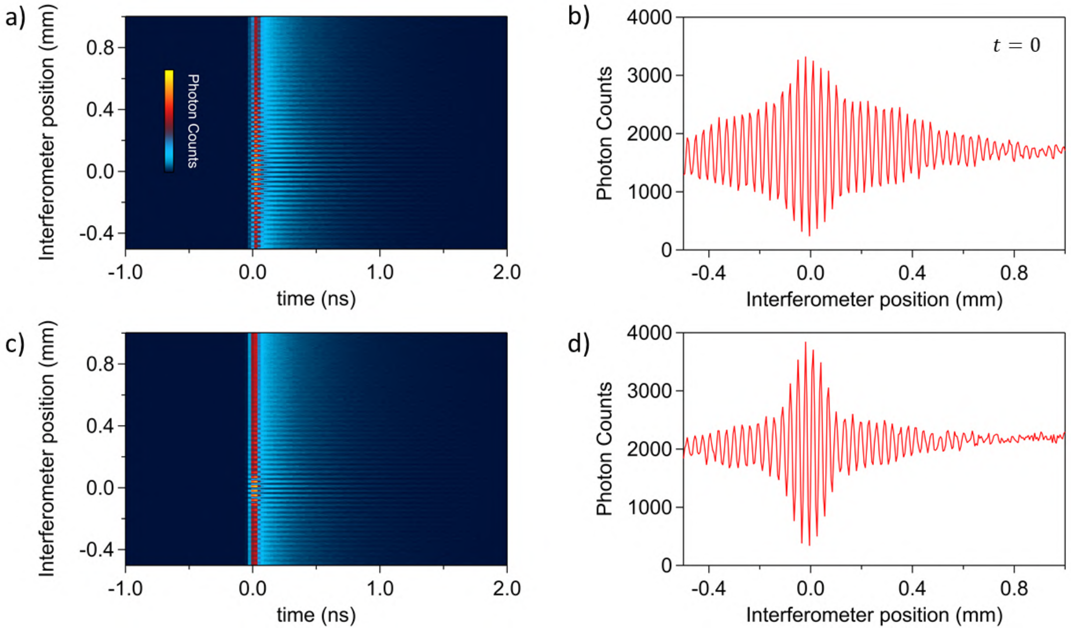

**Figure 4.29:** *Experimental TR-PL data for 1L-$MoS_2$ on $Si_O2$. a, c) TR- interferogram maps at the lowest and highest fluences: $\phi = 6\ \mu J/cm^2$ and $\phi = 70\ \mu J/cm^2$. b, d) Interferogram at the time $t = 0$ ps, extracted respectively from the maps a) and c).*

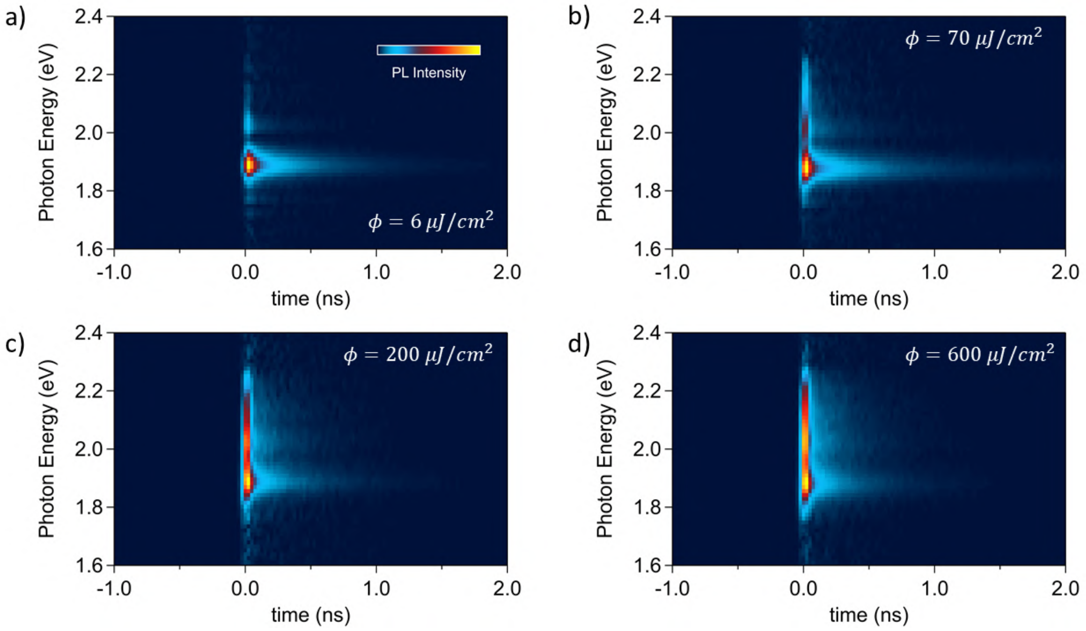

**Figure 4.30:** *1L-$MoS_2$ on $SiO_2$: TR- spectra maps 001, 003, 004 and 005. Original maps, non deconvoluted by the IRF.*

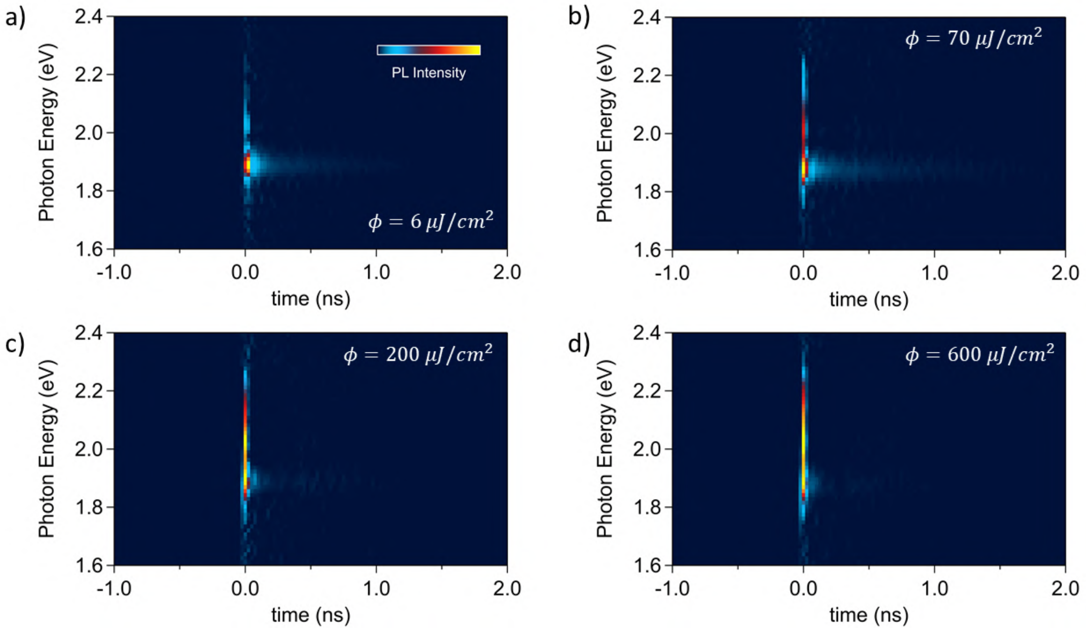

**Figure 4.31:** *1L-MoS$_2$ on SiO$_2$: TR- spectra maps 001, 003, 004 and 005, at four excitation fluences, deconvoluted by the IRF (Richardson-Lucy): a) 6 $\mu J/cm^2$ b) 70 $\mu J/cm^2$ c) 200$\mu J/cm^2$ d) 600 $\mu J/cm^2$.*

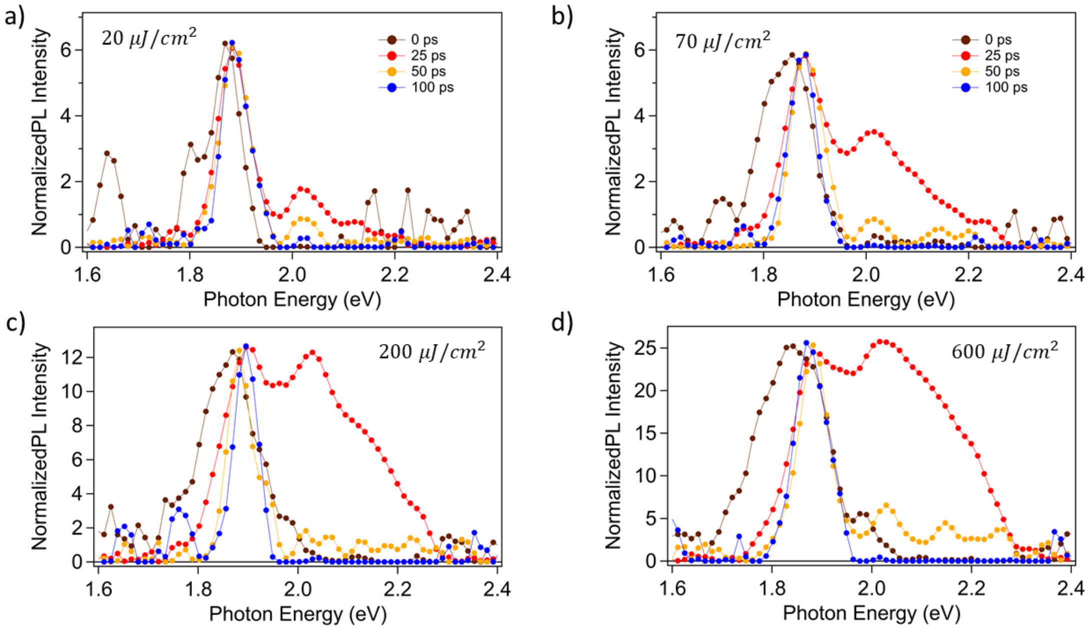

**Figure 4.32:** *Monolayer MoS$_2$ on SiO$_2$. TR- spectra at t=0, 25, 50 and 100 ps, at four excitation fluences, reported in each graph.*

### Monolayer MoS$_2$, TR-PL, analysis of the spectrum around the time zero

The analysis of the PL spectrum around the time zero provides information on the effects of the initial carrier density. Figure 4.33 a) and b) shows the spectra at t=0 ps and at t=25 ps respectively, at the highest fluence (600 $\mu J/cm^2$), compared with the free exciton emission spectrum (lowest fluence, spectrum at t=100 ps). The spectrum at the time zero shows a red-shift of ≈ 60 meV with respect to the free exciton emission line, and a FWHM around 170 meV. Shift and broadening of the PL spectrum can be due to the effect of the temperature (exciton-phonon interactions) which results in a change in the free particle bandgap. In monolayer MoS$_2$ this effect leads to a red-

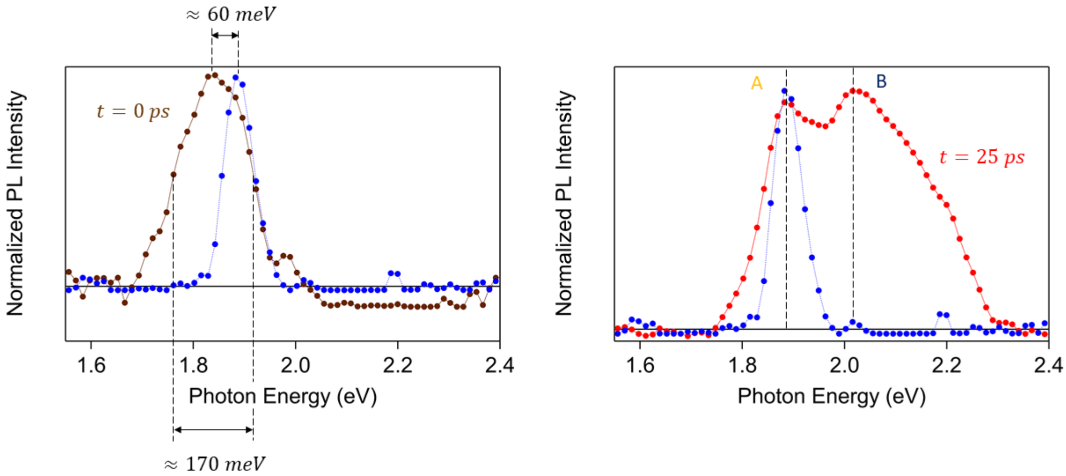

**Figure 4.33:** *TR-PL spectra of monolayer $MoS_2$, at the highest fluence, at t=0 ps (right, brown spectrum) and t=25 ps (left, red spectrum). Each of these spectra is plotted along with the PL spectrum of the A exciton, taken from the measurement at the lowest fluence and at t=100 ps.*

shift of -0.4 meV/K and a broadening of 0.04 meV/K [12]. By using equation 4.25 we estimated a raise in the lattice temperature around 50 K (a similar increase of the temperature, at this fluence has been reported in [44]) at the highest excitation fluence, leading to -20 meV red-shift and 2 meV broadening. Another effect to take into account is the exciton-exciton interactions, which in monolayer $MoS_2$ leads to an exciton density dependent blue-shift of $10^{-12}$ $meV cm^2$ and a broadening of $10^{-12}$ $meV cm^2$ [12]. At the highest excitation fluence, 600 $\mu J/cm^2$, the calculated initial excitation density is of the order of $2 \cdot 10^{13}$ $cm^{-2}$, yielding an exciton-exciton induced blue-shift of +20 meV and a broadening of about 20 meV. The resulting overall shift of the emission peak due to the joint effect of temperature and exciton-exciton interactions is then negligible, while total line broadening due to these two effects is around 25 meV, and does not explain what we observe, with a shift and broadening greater than 50 meV and 100 meV respectively. To explain our data, we should include the effect of the high exciton density, which leads to the band gap renormalization for the free-carriers, due to the exchange and correlation terms in the energy per e-h pair, and to a proportional reduction of the exciton binding energy, induced by the increased screening due to the high exciton density. As the initial excitation density approaches the Mott density, free excitons dissociate to give rise to an electron-hole plasma (EHP), as discussed in section 1.4. The BGR leads to a redshift of the PL emission at photon energies below the free exciton transition, $E < E_{EX}$, as the e-h kinetic energy, related to the occupation of the renormalized valence band and conduction band by the free electrons and holes in the EHP, is responsible for the broadening of the emission line. In monolayer $MoS_2$, the e-h kinetic energy, above the Mott density, is approximately given by $10^{-11} meV\ cm^2$. For an e-h density of $2 \cdot 10^{13}$ $cm^{-2}$, the kinetic energy per e-h pair is about 200 meV, a value similar to the FWHM of the PL spectrum at the time zero. We tried to perform measurements at higher fluence of about 1.2 $mJ/cm^2$, but we irreversibly damaged the sample. In the future it would be worth to perform new measurements, increasing the fluence between 600 $\mu J/cm^2$ and 1.2 $mJ/cm^2$, to try to observe a denser EHP or even the EHL.

At t=25 ps, the spectrum is broadband and it contains the emission peaks of the A and B excitons. This spectrum is dramatically different with respect to the spectrum at the time zero, signalling an ultrafast evolution of the EHP along with a fast formation of A and B excitons. The TR-PL spectra acquired with our experimental system are given by the average of PL spectra emitted within in 25 ps around the nominal time (example: the spectrum at 25 ps is the average in the interval [12.5, 37.5] ps). Hence, when the time evolution of the system is fast, many contributions may appear in the TR- spectrum, making it challenging to disentangle them. However, we explain the broadband spectrum at t=25 ps as due to the sum of the PL spectra of an EHP (first part of the time interval) and of hot excitons (second part of the interval). Auger recombination of the EHP as well as exciton-exciton annihilation can provide enough energy to ionize the excitons to give rise to hot free e-h pair. The PL light emitted as these e-h pairs thermalize towards the lowest available excited states can explain the broadband spectrum, with a pronounced B exciton emission and a tail towards higher lower photon energy. Importantly, we observe this broadband spectrum only at t=25 ps, while at t=50 ps the A exciton represents the dominant feature in the PL spectrum, as can be seen in fig 4.32 d). This can be related to the fact that exciton-exciton annihilation (EEA) and Auger recombinations are processes favored at high excitation density, leading to a fast decrease of the excitation density itself.

Figure 4.34 a) and b) show the PL spectra, normalized to the acquisition time, at the t=0 ps and at t=25 ps, at each excitation fluence. The latter shows how the fluence (i.e. the initial carrier density) affects the shape and the width of the PL spectrum at t=25 ps, due to the density dependent effects of Auger and EEA. We fitted the spectra at the time t=0 ps with a Gaussian function, to extract the peak position, the peak FWHM and the peak area. The fitting and the extracted parameters are reported in figure 4.35.

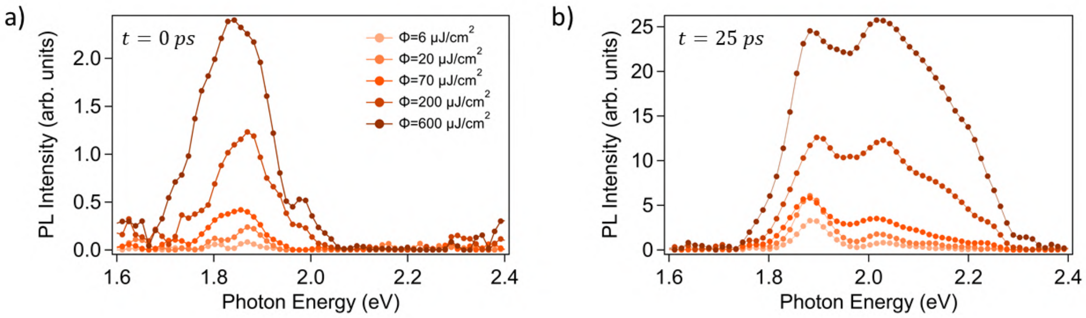

**Figure 4.34:** *PL spectra of monolayer* $MoS_2$*, normalized to the integration time, at each excitation fluence. a) Spectra at the time t=0 ps. b) Spectra at the time t=25 ps.*

The peak position obtained by the Gaussian fitting is reported in figure 4.35 d). The points are scattered on the plot, and it barely allows to notice a red shift of the peak position as the fluence increases. In particular, the fourth point shows a singular behavior. We associate this to an artifact introduced by the TCSPC system and by the deconvolution procedure, due to the fact that, between then third and fourth measurement we removed a neutral density filter used to attenuate the excitation laser, thus, modifying the optical path of the latter, and hence the time between the reference signal and the photo-excitation. We used the same IRF to deconvolute all the spectra, while the latter should be measured at each slight modification of the optics in the TR-PL setup. To correctly compare the data for the fluences 001, 002, 003 with the fluences 004 and 005 we should repeat these measurements.

Figure 4.35 e) reports the FWHM of the Gaussian fit. As the fluence increases, the peak FWHM increases from about 80 meV to 160 meV. This data show that the spectrum significantly broadens when the excitation density is higher than $2 \cdot 10^{12} cm^{-2}$, which is close to the predicted Mott density for $MoS_2$, $\approx 3 \cdot 10^{12}\ cm^{-2}$ [69]. The FWHM extracted from the lowest fluence is around 115 meV, showing a singular behavior, that we associate to the high noise level for the corrisponding PL spectrum. Figure 4.35 f) reports the area of the Gaussian fit functions, showing a linear increase with the excitation fluence.

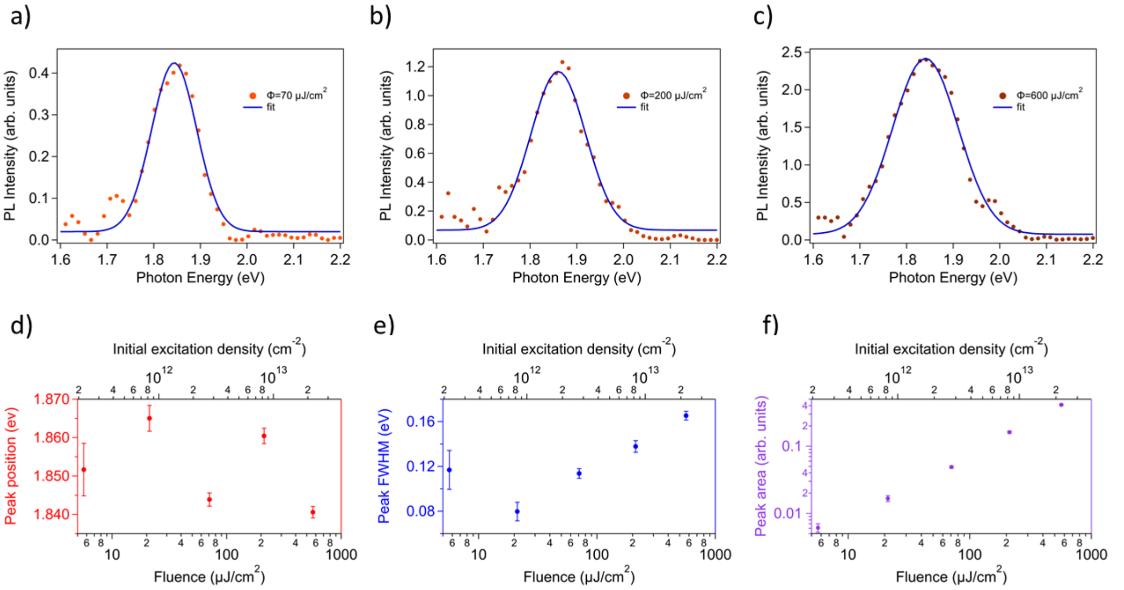

**Figure 4.35:** *a,b,c) PL spectra of monolayer* $MoS_2$ *at the time t=0 ps, at three excitation fluences, along with the fits with a Gaussian. d,e,f) Parameters of the Gaussian fit: peak position, peak FWHM and peak area, plotted versus the excitation fluence.*

### 4.6.5 Bulk $MoS_2$, time resolved photoluminescence

We performed TR-PL measurements on bulk $MoS_2$, at two fluences: 4.2 $mJ/cm^2$ and 11 $mJ/cm^2$. Figure 4.36 a) and b) report respectively the TR- interferogram map and the corresponding TR-spectra map, at the lowest fluence. Figure 4.36 c) and d) shows the TR- spectra maps at the two fluences, deconvoluted by the time IRF. At the highest fluence, the spectrum is ultra-broadband around the time zero, with a short lifetime. A long lived PL emission is detectable at low photon

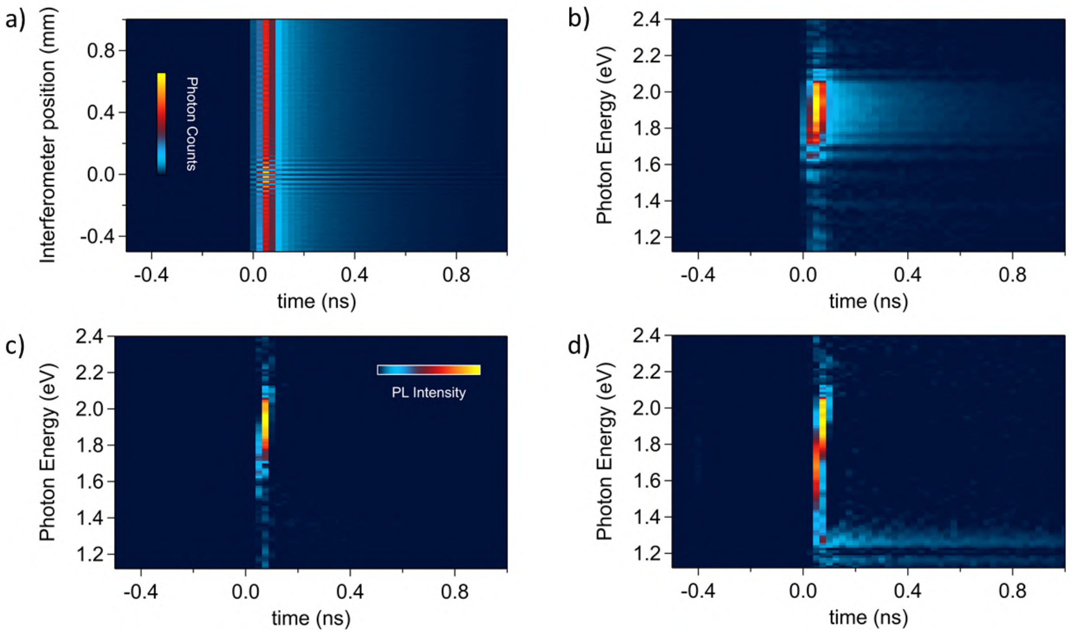

**Figure 4.36:** *Bulk* $MoS_2$*. a) TR- interferogram map and related TR- spectra map, at a fluence of 4* $mJ/cm^2$*. c) TR- spectra map, obtained by the map reported in panel b, by the deconvolution by the time IRF. d) TR- spectra map, deconvoluted, for another value of fluence, 11* $mJ/cm^2$*.*

energy, in the range [1.1, 1.4] eV.
In this section we report TR-PL experimental data for bulk $MoS_2$ at an extremely high excitation fluence, 4 $mJ/cm^2$, corresponding to an initial excitation density, in 3D, of $\approx 10^{21} cm^{-3}$. Figure 4.37 a) shows the TR-PL map for bulk $MoS_2$. An intense and broadband initial emission is detectable in the in the range [1.6, 2.2] eV. Figure 4.37 c) shows a zoom in the TR-PL map around the time zero, and in the energy range [1.15, 2.0] eV. This map is represented with a different contrast for the color scale, to highlight the presence of a long-lived signal in the spectral range [1.2, 1.4] eV. Figure 4.37 b) reports TR- spectra extracted from the TR-PL map, at the time t=0

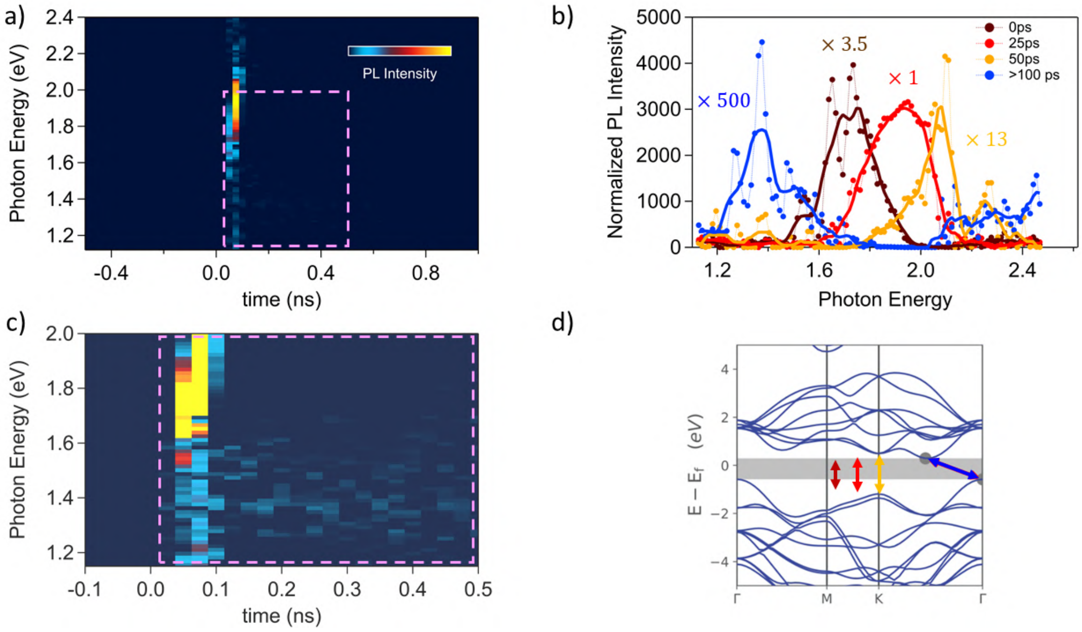

**Figure 4.37:** *a) TR-PL map for bulk $MoS_2$. b) TR- spectra at t=0 ps, 25 ps, 50 ps, and for t>100 ps, extracted from the map shown in panel a). c) Zoom of the TR-PL map, with enhanced color scale, to highlight the weaker and long lived emission in the spectral range [1.2, 1.5] eV. d) Calculated electronic band structure for bulk $MoS_2$ [90], with a scheme of the optical transitions corresponding to the TR- spectra shown in panel b.*

ps, t=25 ps, t=50 ps, and integrated for t>100 ps. The experimental data are represented along with the smoothing, to help the visualization of the PL spectra. The first spectrum (0 ps) is centered at 1.7 eV (lower than the A exciton emission in the monolayer, by $\approx$ 200 meV), with a FWHM of $\approx$ 230 meV. The spectrum at t=25 ps shows a peak at $\approx$ 1.92 eV with a FWHM of around 300 meV. At t=50 ps, the PL spectrum exhibits a main peak at $\approx$ 2.1 eV, and a lower intensity peak at 2.25 eV. We associate this spectrum to the direct A and B free exciton emissions. The relative spectral positions of these two peaks, with an energy difference around $\approx$ 150 meV suggest that they can arise from the spin-orbit splitting of the valence band of bulk $MoS_2$. The tail towards lower photon energy can be related to a contribution of the EHP, arising from the first part of the 25 ps-wide time interval where the PL spectrum is integrated. At times t>100 ps, the spectrum is completely different, with emission peak around 1.4 eV. We associate this emission to the indirect exciton transitions $K - \Gamma$ and $K - \Sigma$.
The bulk $MoS_2$ is an indirect bandgap semiconductor: after a pulsed photo-excitation at 2.4 eV (excitation at the K point in the first Brillouin zone) we first observe a dense and hot electron-hole plasma generated by the light pulse. The huge band gap renormalization shifts the emission line, reducing the free carrier band gap from >2 eV to 1.6 eV. As the electrons and holes in the EHP recombines and cool down, the BGR effect is reverted, and the emission spectrum shifts towards higher photon energy. The spectrum at t=25 ps is broader with respect to the spectrum at the time t=0 ps, while we would expect the opposite behavior. This can be explained as follows: each PL spectra is an average of a continuum of PL spectra emitted within 25 ps, by an EHP that is decreases its density, due to recombination. Since the decreasing of the EHP density results in a

reduction of the BGR, which induces a shift, this effect results in an apparent broadening of the observed PL spectrum at the "fixed time". Unlike the second spectrum (t=25 ps), the first one is averaged on a time interval where the PL signal may present only in the second part, and low or absent in the first part (the PL photons haven't been detected), resulting in an apparent lower width of the emission line.

At long delay, the density of the EHP drops down below the Mott density, and direct A and B excitons form. Finally indirect excitons forms (the lowest energy states in bulk $MoS_2$), resulting an emission at 1.4 eV with a long lifetime. Figure 4.37 d) shows a scheme of the band structure of the bulk $MoS_2$, where the optical transitions corresponding to the TR-PL spectra at t=0 ps, 25 ps, 50 ps and >100 ps are shown with the same color code of the spectra reported in panel b).

We fitted the high energy tail at t=0 ps and t=25 ps with a decreasing exponential, corresponding to the Maxwell-Boltzmann distribution, to extract the EHP temperature. The fit function is

$$F(E) = I_0 + A \cdot e^{-\frac{E}{k_B T}} \tag{4.37}$$

Figure 4.38 a) and b) shows the TR-PL spectra at 0 ps and 25 ps, along with the fits. We obtained $850 \pm 50$ K and $520 \pm 60$ K respectively, allowing to associate these spectra to hot EHP emissions, at different temperatures and densities. Figure 4.39 a) reports the PL time dynamics, extracted as horizontal profiles by the TR-PL map shown in figure 4.37 a), at fixed emission photon energy. The PL dynamics at 1.65 eV and 1.95 eV exhibit a fast raise and a fast decrease, on less than 50 ps. The dynamics at 1.95 eV is delayed by one experimental point with respect to the dynamics at 1.65 eV, as can be also seen by looking at the TR- spectra in figure 4.37 b).

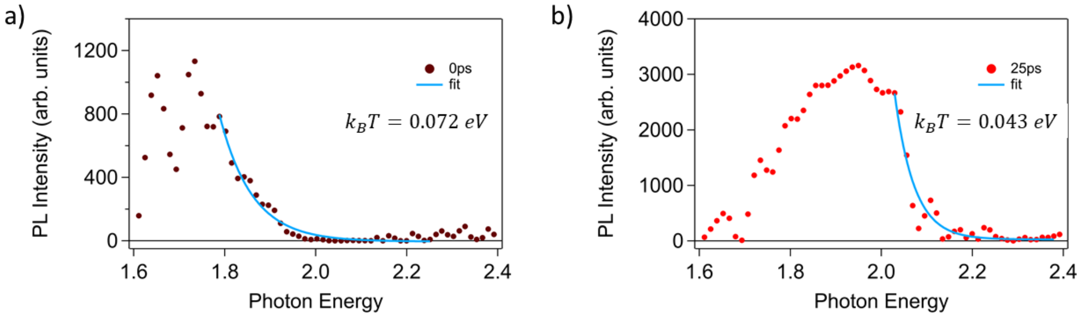

**Figure 4.38:** *TR- spectra for bulk $MoS_2$, at t=0 ps and t=25 ps. Fit of the high energy tail with an exponential function, corresponding to the Maxwell-Boltzmann distribution. The values of $k_B T$ extracted by the fit are shown.*

The time dynamics integrated in [1.2, 1.5] eV, shows a slower decay. We fitted this data with a single exponential (see figure 4.39 c), obtaining a lifetime of $0.264 \pm 0.126$ ns, that we associate to the non-radiative recombination of free excitons.

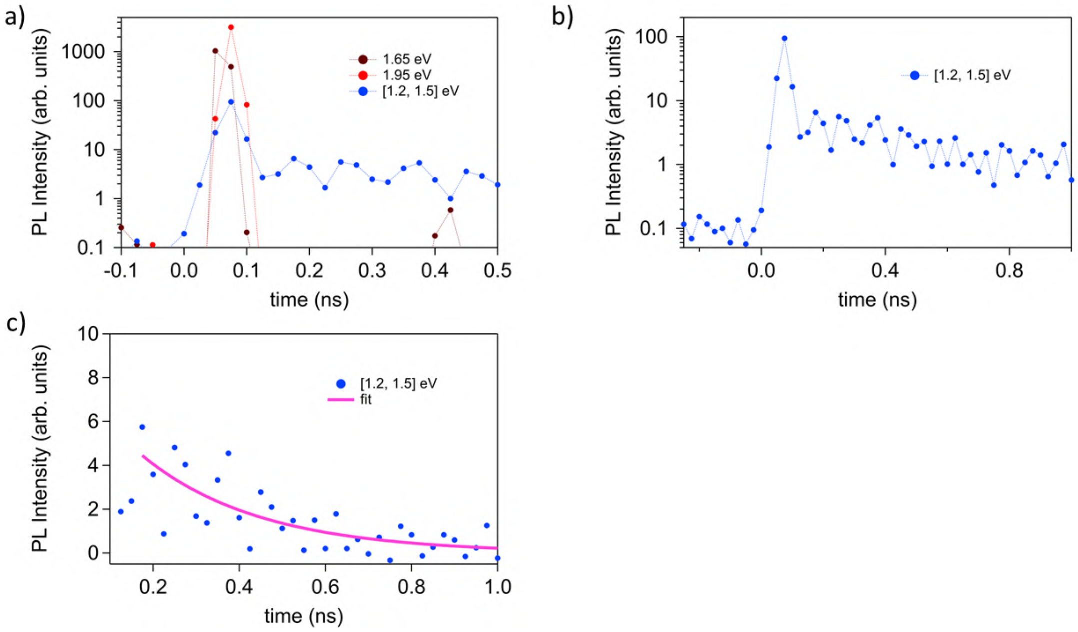

**Figure 4.39:** *a) PL time dynamics, at fixed emission photon energy: 1.65 eV, 1.95 eV and integrated in [1.2,1.5] eV. b) PL time dynamics integrated in [1.2,1.5] eV, shown in a larger time interval. c) PL time dynamics integrated in [1.2,1.5] eV, shown for t>0.15 ns and with intensity in linear scale, along with the fit, performed with a single exponential function.*

## 4.7 Conclusions

In this chapter we analyzed the photoluminescence (PL) experimental data for exfoliated monolayers $WS_2$ and $MoS_2$ on $SiO_2$ substrates. The steady state PL spectra for monolayer $WS_2$ as a function of the excitation intensity (section 4.4) allowed to quantify the shift and the broadening of the A exciton emission peak, that we associate to the lattice heating under CW laser irradiation. The analysis of the PL images for monolayer $WS_2$ (section 4.5) shows that the excitons photo-generated by the CW laser diffuse by about 1 $\mu$m from the photo-excited area. Beside this, the spatially-resolved steady state PL spectra for monolayer $WS_2$, allows to access the PL spectra arising from different regions of the photo-excited area, where the exciton density vary following the intensity profile of the excitation laser. In particular, at the center of the photo-excited area, the spectrum is broader with respect to the outer region, and it exhibit a second peak about 30 meV below the A exciton, which we associate to the trions.

The analysis of the TR-PL spectra for monolayer $WS_2$ as a function of the excitation fluence (section 4.6) allows to identify a threshold fluence for the density-induced ionization of FE in an electron hole plasma (EHP), between $\approx 7\ \mu J/cm^2$ and $20\ \mu J/cm^2$. At the highest excitation fluence, $\approx 70\ \mu J/cm^2$, the features of the EHP emission, i.e. the presence of a broad emission peak at a photon energy lower than the A exciton peak, are clearly detectable at the time t=0 ps and t=25 ps, showing that the dynamics of the EHP is too fast to be fully recorded with our experimental system, and accordingly with previous time resolved experiments [75, 63]. We report the analysis of the energy integrated TR-PL time dynamics for monolayer $WS_2$, by using a custom dynamic model which takes into account the radiative recombination of free excitons, the exciton-exciton annihilation, the trapping and de-trapping of free excitons in defect states. By this analysis we obtained a radiative lifetime in the range 0.8 - 1.8 ns, a time constant for the exciton trapping in the range 65 - 200 ps, and an exciton-exciton annihilation rate between 1.4 and 2.4 $cm^2 s^{-1}$. We take into account the fast non-radiative recombination by considering an initial excitation density lower than the one that can be calculated by the excitation fluence.

The analysis of the TR-PL spectra for monolayer $WS_2$ as a function of the excitation fluence (section 4.6.4) allows to disentangle an EHP emission, at the time t=0 ps, hot excitons emission at t=25 ps, where both A and B exciton emissions strongly contribute to the PL spectrum, and cold excitons emission, for t>50 ps where only the A exciton peak is detectable. The EHP emission (t=0 ps), detectable at each excitation fluence (>7 $\mu J/cm^2$), is red shifted and broad with respect to the A exciton emission line. At the maximum fluence, $\approx$ 600 $\mu J/cm^2$, corresponding to an initial excitation density of $\approx 2 \cdot 10^{13}$ $cm^{-2}$, the EHP line exhibits a red-shift of $\approx$ 60 meV and a FWHM of $\approx$ 170 meV, in good agreement with theoretical calculations for monolayers $MoS_2$ [69]. We were not able to observe the PL emission of denser EHPs and of the EHL, since our try to measure at twice the maximum excitation fluence (i.e. 1.2 $mJ/cm^2$) resulted in the irreversible damaging of the monolayer.

The TR-PL spectra for bulk $MoS_2$, at high excitation fluence, $\approx$ 4 $\mu J/cm^2$, show a fast evolution from a broadband emission centered at 1.7 eV (t=0 ps), to a broadband emission centered at 1.95 eV (t=25 ps), to a sharper emission at 2.05 eV (t=50 ps), that we associate to the direct optical transitions of hot carriers at the K point in the first Brillouin zone, arising from the recombination of an EHP which decreases its temperature and density. Finally we detect a long lived PL peak at 1.4 eV, that we associate to the indirect $\Gamma - \Sigma$ exciton emission (at t>100 ps).

The TR-PL spectra reported and analyzed in this chapter constitute new data for the TMD literature, since the fast evolution of the PL spectrum on a broadband range has never been reported in before.

# Chapter 5

# Photoelectron spectroscopy data analysis

In this chapter we report and analyze the photoelectron spectroscopy experimental data of bulk $MoS_2$. We performed TR- angle resolved photoelectron spectroscopy (TR-ARPES) experiments at the Sprint laboratory, to access the electronic and excitonic excited states, induced by a pulsed optical excitation, on the 100 fs - 100 ps time-scale. These data can provide complementary information with respect to the TR-PL measurements.

## 5.1 Experimental methods

A $MoS_2$ single crystal (HQ-graphene [30]) was cleaved in situ UHV ($P \approx 10^{-10}$ mbar), to expose a clean surface to measure. We aligned the sample to probe the angular dispersion along the high symmetry direction $\Gamma - K$, in the horizontal direction (laboratory reference system). We performed low energy electron diffraction (LEED) measurement, to check the alignment of the sample. Figure 5.1 reports the LEED images, acquired at 112 eV and 198 eV (energy of the electron beam).

A light pulse at 26.5 eV (high harmonic generation), polarized along the vertical direction (s-polarization) and with a pulse duration of ≈100 fs is focused on a spot of ≈100 $\mu m$ on the sample, and used as probe. The pump is a pulsed laser at 1.95 eV, collinear with the probe pulse, almost resonant with the A exciton transition, linearly polarized along the vertical direction (s-polarization), and with a pump fluence of ≈50 $\mu J/cm^2$. However, it's important to note that the pump fluence scales with the beam incidence angle, which changed for the measurements in different parts of the Brillouin zone (which is 34°, 50° and 65° respectively for the $K, \Gamma, \Sigma$ points). The time resolution is given by the cross correlation of the pump and probe pulses, resulting in a gaussian profile with a FWHM of ≈110 fs [16]. In the present experiment, the energy resolution is ≈ 100 meV, mostly determined by the width of the analyzer's slit, which is kept open to 4 mm to increase the pump-probe signal-to-noise ratio.

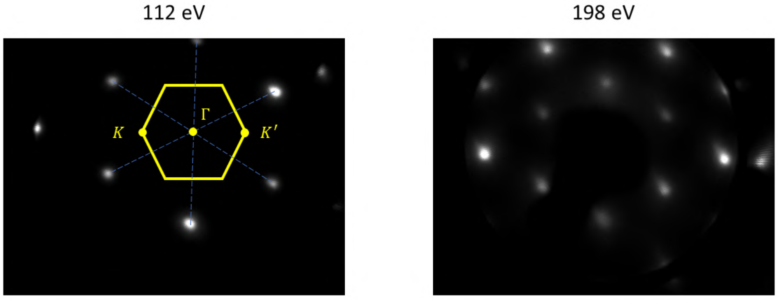

**Figure 5.1:** *LEED images of the bulk $MoS_2$ sample, at 112 eV and 198 eV. The first Brillouin zone is drawn, along with the points K, Γ, K'.*

## 5.2 Static ARPES

Figure 5.2 reports the measured (E,k) photoemission map obtained by composing different measurements, acquired by rotating the polar angle to access the different wave-vector intervals in the first Brillouin zone. The valence band exhibit a local maximum at $k \approx -1.2$ Å$^{-1}$, corresponding to the K point. The absolute maximum of the valence band is located at $k \approx 0$ ($\Gamma$ point), and it is not clearly visible in this data, while lower energy bands are detectable. The low photoemission intensity at the $\Gamma$-point has already been observed in previous measurements, and it is associated to a matrix element effect [81, 43] (indeed the band is visible in synchrotron measurements with circularly polarized light). These experimental data are in good agreement with the calculated band structure for bulk $MoS_2$ (see figure 5.2 b), and with high-resolution ARPES measurements that we performed at the APE beamline on the same sample (see figure 5.2 c). However, the position of the local maximum at the K point differs by $\approx$0.1 Å$^{-1}$. This difference can be explain in the following way. At the APE beamline, the electron analyzer is equipped with an automatic deflector for electrons, which allows to obtain the band structure both along the direction of the analyzer slit (polar angle) and along the orthogonal direction (tilt angle). Moreover, at the APE beamline, the high photon energy (60 eV to 90 eV) of the probe allows to explore almost all the first Brillouin zone, without rotating the sample. Hence, it is easy to precisely identify the $\Gamma - K$ direction. At the Sprint laboratory, the tilt angle is fixed, while we probe the polar angle: although we have the possibility to tilt the sample, this angle remains fixed during the ARPES measurements. Since the surface of a cleaved sample is not smooth, and it is constitute by several domains whose dimension compared to the probe spot size depends on the particular cleave, it is difficult identify exactly the $\Gamma - K$ direction, and to probe the system along it. Moreover, with our "low" photon energy (26.5 eV) we need to rotate the sample to explore the band dispersion from $K$ to $\Gamma$, and this adds an uncertainty on the azimuth angle, since by rotating, the position of the probe beam on the sample is modified.

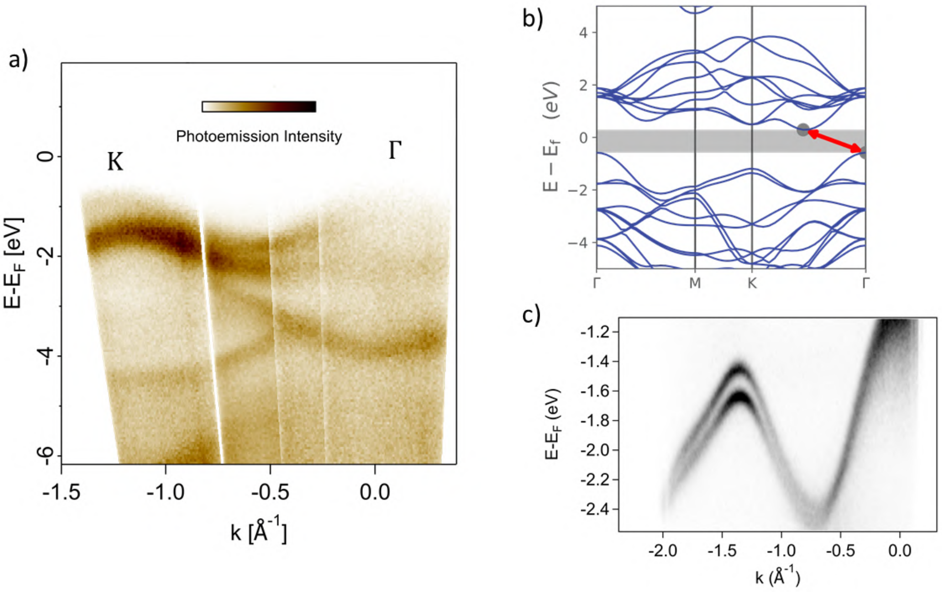

**Figure 5.2:** *a) (E,k) photoemission map: static ARPES data for bulk $MoS_2$, acquired at the Sprint laboratory, with pulsed source (HHG) at 26.5 eV, s-polarized. b) Calculated band structure for $MoS_2$. Figure from [90]. c) High energy resolution static ARPES data, acquired at the APE beamline with Synchrotron light, left circularly polarized with a photon energy 60 eV. With high energy resolution, the spin-orbit splitting ($\approx$ 170 meV) of the valence band can be clearly resolved.*

The fine structure of the energy bands is not resolved because we completely opened the slit of the electron analyzer, to maximize the signal, especially for the pump-probe measurements. In high resolution measurements, we were able to detect the spin-orbit splitting of the valence band at K (not shown here).

### 5.2.1 Surface photovoltage (SPV)

Even high quality semiconductors are always characterized by a residual, unintentional doping, which can be predominantly n-type or p-type. Moreover, the surface of semiconductors are depletion regions due to the presence of surface defect states, with energy levels in the electronic bandgap. If the doping of the semiconductor is predominantly p-type (n-type), holes (electrons) from the bulk are captured in these surface states, giving rise to a thin depletion region near the surface. The diffusion and capture of holes (electrons) near the surface continues until a sufficiently strong built-in electric field is set. The Fermi level raises (lowers) in this depletion region, with respect to the bulk of the semiconductor, moving away from the top of the valence (conduction) band. Since the Fermi level is pinned to a fixed value, the valence (conduction) band experiments a shift, which is called *band bending* [73]. When the semiconductor is photo-excited, electrons and holes are generated at the surface and separated by the built-in electric field. The drift of these free carriers reduces or even deletes the surface band bending. Since this effect induces a modification of the built-in electric field and of the band bending, which are dependent on the photo-excited carrier density at the surface, it is called *surface photo voltage* (SPV). After a pulsed photo-excitation, the SPV results in a continuous modification of band bending, as the photo-excited carriers recombine. In a photoemission experiment, the SPV effect induces a voltage in the sample area illuminated by the radiation, causing a shift of the electronic band structure, resulting in a shift of the measured kinetic energy of photo-electrons.

In a pump-probe photoemission experiment, what we observe is a continuous shift of the valence band as a function of the pump-probe delay. The shift with respect to the equilibrium condition is maximum within few ps with respect to time zero. At positive pump-probe delay, the shift slowly recovers towards the equilibrium condition, giving access to the dynamics of the SPV in the material. The relaxation of the SPV is quite slow in most of the materials (hundreds of ps) and hence can be easily compensated by measuring the shift of valence band or core level peaks. At negative pump-probe delays, the modification of the electric field at the surface, induced by the delayed absorption of the pump pulse, results in an electrostatic contribution in the modification of the final kinetic energy for photo-electrons.

The decay time of this effect at negative delays is generally longer than the pump and probe pulses cross correlation, since it is related to the kinetic energy of photoemitted electrons, i.e. the speed at which they escape from the surface of the sample, and to the spot size of the pump pulse [35]. Figure 5.3 reports the pump-probe photoemission map, acquired on the bulk $MoS_2$, which reports the photoemission intensity versus electron kinetic energy and pump-probe delay, in the range [-200,200] ps, k-integrated at the $\Gamma$ point, in the range [-0.25, 0,25] $\text{Å}^{-1}$. This map allows to detect the shift of the valence band, both at negative and positive pump-probe delays. The kinetic energy corresponding to the high-energy edge of the valence band, as a function of the pump-probe dealy, is represented in figure 5.3 b).

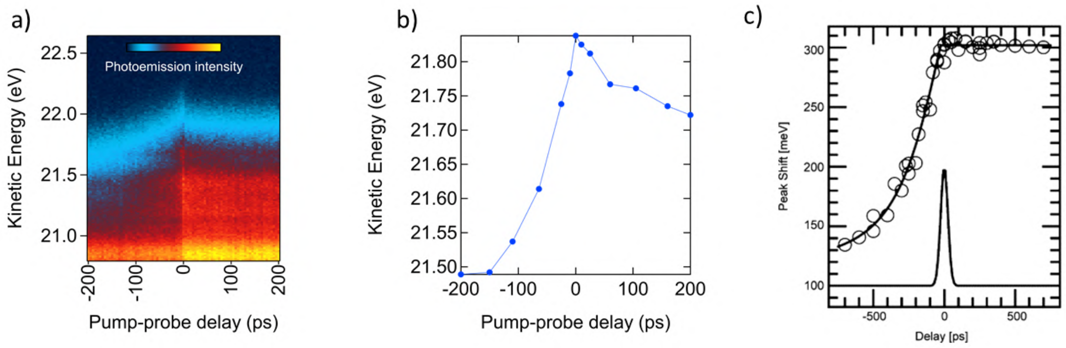

**Figure 5.3:** *a) Pump-probe photoemission map for bulk* $MoS_2$*, reporting the photoemission intensity (k-integrated around* $\Gamma$*, in the range [-0.25, 0,25]* $\text{Å}^{-1}$*), as a function of electron kinetic energy and pump-probe delay. b) Kinetic energy of the high energy edge of the valence band, versus the pump-probe delay. c) Experimental shift of the Si 2p core level, as a function of the pump-probe delay. Figure from [88].*

In our experimental conditions the shift persists for hundreds of ps, with a faster time constant than positive side, but is almost constant in the few-ps range, before time-zero, allowing a careful analysis of the pump-probe signal. A similar behavior for the SPV have already been observed, for example for the Si 2p core level [88].

### 5.2.2 Data processing

The efficiency of the micro channel plate (MCP) detector, that amplifies the signal of photoemitted electrons, is not spatially uniform. Hence, before the analysis, the raw photoemission data must be corrected by considering the MCP detector's efficiency, both along the energy and polar angle directions. Figure 5.4 a) shows the efficiency of the MCP detector, as a function of the energy channel. When working in fixed mode (fixed window for the kinetic energy of photoelectrons), we normalized the raw data by dividing the acquired spectra by this curve, while for swept scans the detector efficiency is automatically averaged. Also the angular dispersion of the photoemitted electrons must be normalized by the angular efficiency of the MCP detector (not reported here).

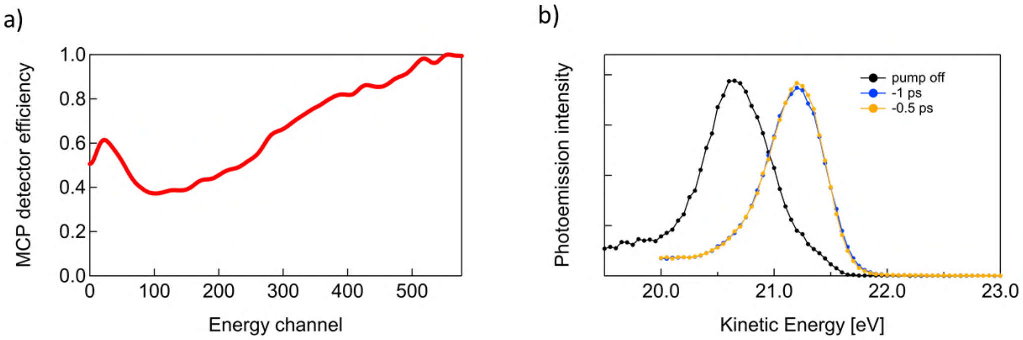

**Figure 5.4:** *a) Efficiency of the MCP detector, versus the number of the energy channel. b) Photoemission spectrum, k-integrated around the K point, in the first Brillouin zone. The static spectrum, with pump-off is compared with the spectrum with pump-on, and negative pump-probe delay.*

The kinetic energy was converted in energy of electrons with respect to the Fermi level. The latter was obtained by measuring a polycristalline gold sample, and its value in kinetic energy, 22.15 eV, was subtracted to the measured kinetic energy of electrons in our data. In pump-probe data, we evaluate the shift of the Fermi level, due to the pump-induced SPV, by comparing a photoemission spectrum with pump off, and a photoemission spectrum at negative delay. The new Fermi level, obtained by considering this additional shift, is located at a kinetic energy of 22.50 eV. Figure 5.4 b) reports the photoemission spectrum k-integrated around the the K point, in the range [-1.35, -0.85] $\text{Å}^{-1}$, with pump off, and with pump on and negative pump-probe delay (- 3 ps). It's important to note that the contribution of the SPV is almost constant in a range of few tens of picoseconds around $t_0$. For this reason we kept fixed the Fermi level in our analysis, except in some cases (explicitly noted) where we added the time-dependent shift retrieved in section 6.3.

## 5.3 Analysis of the valence band

The conduction band of $MoS_2$ is characterized by local minima at the $K$ point and along the $\Sigma$ line. An optical excitation with an ultrashort pulse induces an almost istantaneous population of the conduction band, proportional to the fluence of the light pulse. After photo-excitation, electron-electron scattering, electron-phonon scattering, carrier trapping in defect states and exciton formation are the processes that lead the system in a thermalized excited state, where free electrons in the conduction band and excitons occupy the lowest available excited states, accordingly to their quasi- temperature and quasi- chemical potential, "waiting" for radiative or non-radiative recombinations. The pump-induced photo-excitation at 1.95 eV is below the free particle band-gap, and it is almost resonant with the A exciton transition in $MoS_2$ [66, 58], leading to the generation of direct free excitons (exciton with wavevector $|\vec{k}_{EX}| \approx 0$). Depending on the fluence, photo-excitation induces a band gap renormalization. Moreover, if the initial carrier density is high, above the Mott density, free excitons can ionize and give rise to an electron hole plasma (see chapter 1, 2 and 5). In bulk $MoS_2$, the carrier's temperature plays an important role in the ionization of excitons, since thier binding energy is of about 0.1 eV, much lower than in the monolayer [37, 70, 13].
In our experiment, bulk $MoS_2$ is predominantly p-type,as inferred by the positive SPV-induced shift of the valence band due to the photo-excitation. To evaluate the relaxation of this effect at

positive delays we acquired pump-probe angle resolved photoemission data, around the K point in the first Brillouin zone, at several fixed pump-probe delay, in the range [-1,+200] ps. Figure 5.5 reports the (E,k) photoemission maps, around the K point, at four selected time delays. The difference with respect to the first negative delay are also shown, in the low part of the figure. The shift of the valence band towards lower energy $(E - E_F)$ is clearly visible, especially by comparing the photoemission maps at +0.1 ps and +100 ps. Although the valence band has shifted back towards lower kinetic energy already at 0.1 ps. This effect could be due not only to SPV but also to band gap renormalization following the pump excitation. Since it is difficult to disentangle such effects, we must evaluate carefully the shift as a function of the delay in order to reference the conduction band measurements that we are going to present in the following to the top of the valence band.

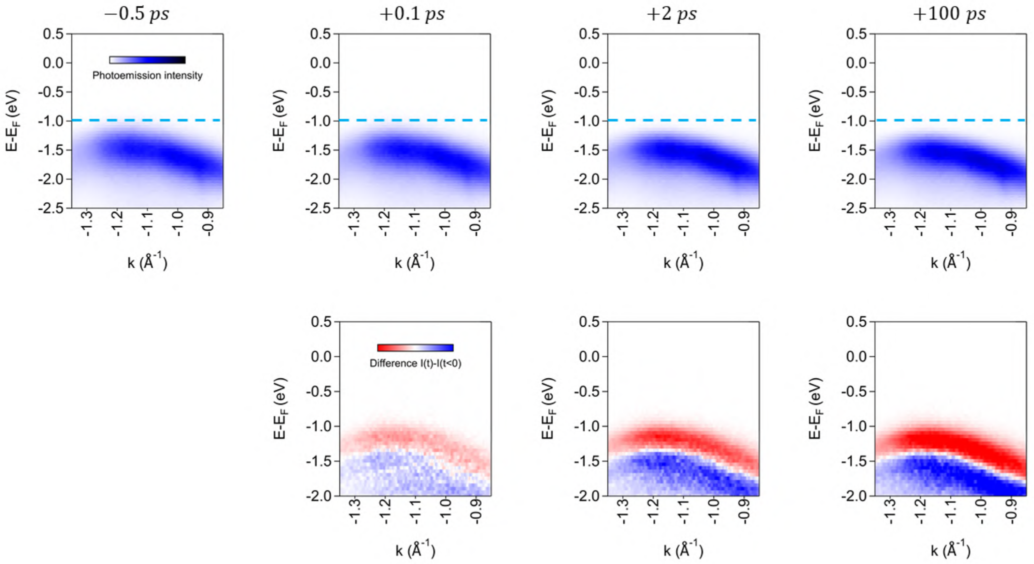

**Figure 5.5:** *(E,k) photoemission maps at fixed pump-probe delays: -0.5 ps, +0.1 ps, +2 ps and +100 ps. A fixed line, highlighting the maximum of the valence band, is drawn to allow to see the shift of the valence band, induced by the SPV effect and by the band gap renormalization. The maps below reports the difference of photoemission maps at the fixed delays with respect to the map at -0.5 ps.*

Figure 5.6 a) and b) reports the photoemission spectra at fixed wave vectors 1.0 Å$^{-1}$ and 1.2 Å$^{-1}$ and at several pump-probe delays. We calculated the shift, by matching the peak and the low energy tail of the photoemission spectra.

Figure 5.6 c) reports the shift of the photoemission spectra at 1.0 Å$^{-1}$ and 1.2 Å$^{-1}$, versus the pump-probe delay. We attribute the shift at short delays to the band-gap renormalization, while the slow progressive rigid shift of the valence band at long delays can be associated to the reversion of the SPV effect. We compute an average of the value obtained by the shift at the two wavevector points, we interpolate the resulting point series, an use the latter to correct any other experimental spectra.

It is interesting to note that also the shape of the valence band spectrum changes with time delay. Figure 5.6 d) reports the photoemission spectra, at 1.2 Å$^{-1}$, at -1 ps, +0.1 ps, +0.8 ps, +5 ps and +200 ps, corrected by the rigid shift of the valence band (BGR and SPV). The spectrum at +0.1 ps exhibit an higher intensity, with respect to the spectrum at negative time delays, for energy $E - E_F < -1.1eV$, and a lower intensity for energies above this value. At +0.8 ps, this effect increases, and it is saturated, showing no further variation at the subsequent time delays.

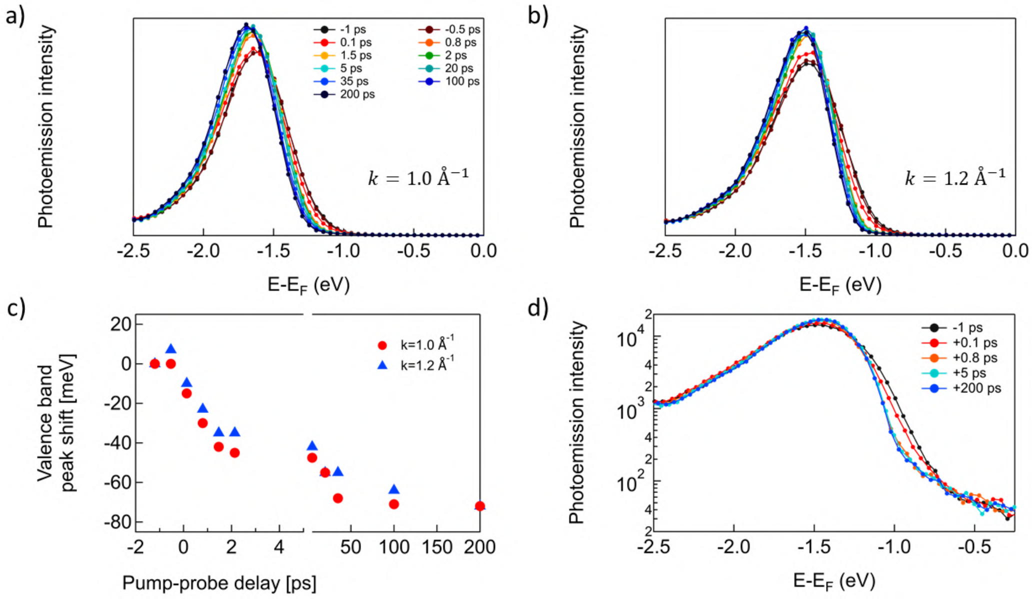

**Figure 5.6:** *a,b) photoemission spectra at k=1.0 Å$^{-1}$ and k=1.2 Å$^{-1}$ at fixed pump probe delays. c) Shift of the photoemission peak, with respect to the spectrum at negative delays, calculated from the photoemission spectra reported in panels b) and c). d) Photoemission spectra at 1.2 Å$^{-1}$, at five time delays, corrected by the shift calculated in panel c. The photoemission intensity is represented in log scale, allowing to notice the modification of the shape of the valence band, as a function of the pump-probe delay.*

## 5.4 Analysis of the conduction band

We investigated the dynamics of photo-excited carriers in the conduction band, around the high symmetry points $K, \Sigma, \Gamma$. First, we present the data around the K point in the first Brillouin zone, since the absorption of the pump pulse (at 1.95 eV) occurs around this point [66]. Figure 5.7 a) shows pump-probe photoemission spectra, angle integrated around K, in the range [-1.35, -0.85] Å$^{-1}$, at -1 ps, +0.1 ps, +5 ps and +100 ps, corrected by the shift of the valence band. We computed the difference between the spectra at positive time delay and the spectrum at -1 ps, to highlight the pump-induced modifications of the photoemission spectrum (figure 5.7 b). At +0.1 ps, an intense peak is detectable at about +0.8 eV with respect to the Fermi level, with a width of $\approx$ 0.4 eV. We associate this peak to a transient population of the bottom of the conduction band by non-thermal free electrons and excitons at the K point, due to the photo-excitation with a photon energy close to the A and B exciton transitions, and to the free particle band-gap. The tail at lower energy, is associated to the transient population of defect states. At +5 ps, the difference spectrum is less intense and shifted to lower energy, by $\approx$ 250 meV. This peak may be associated to the formation of direct free excitons, which follows the thermalization and relaxation of free carriers. At +100 ps, the difference spectrum exhibits small changes with respect to the spectrum at +5 ps, signalling that direct free excitons persist at long time delays, after photo-excitation. The intensity of the difference spectrum at the low energy tail is significantly reduced with respect to +5 ps, signalling a decrease in the population of defect states, that may be due both to the recombination and de-trapping of carriers, leading to the formation of new direct free excitons.

Figure 5.7 c) reports the (E,k) photoemission map in the conduction band, around the K point, in the range [-1.35,-0.85] Å$^{-1}$, at +0.1 ps pump-probe delay. A high photoemission intensity by transiently occupied defect states is detectable above the Fermi level, showing no appreciable dispersion in k. Another intensity spot about 0.8 eV above the Fermi level is clearly detectable, showing a dependence on the wavevector. Spectra integrated in selected momentum regions, indicated by the colored rectangles in figure 5.7 c), were extracted from this map, and reported in a separate plot, shown in figure 5.7 d). These data confirms that the peak appearing in the spectrum is dependent on the wavevector, showing a dispersion in k around the K point, and signalling a transient population of the conduction band by free carriers, or the presence of direct free excitons.

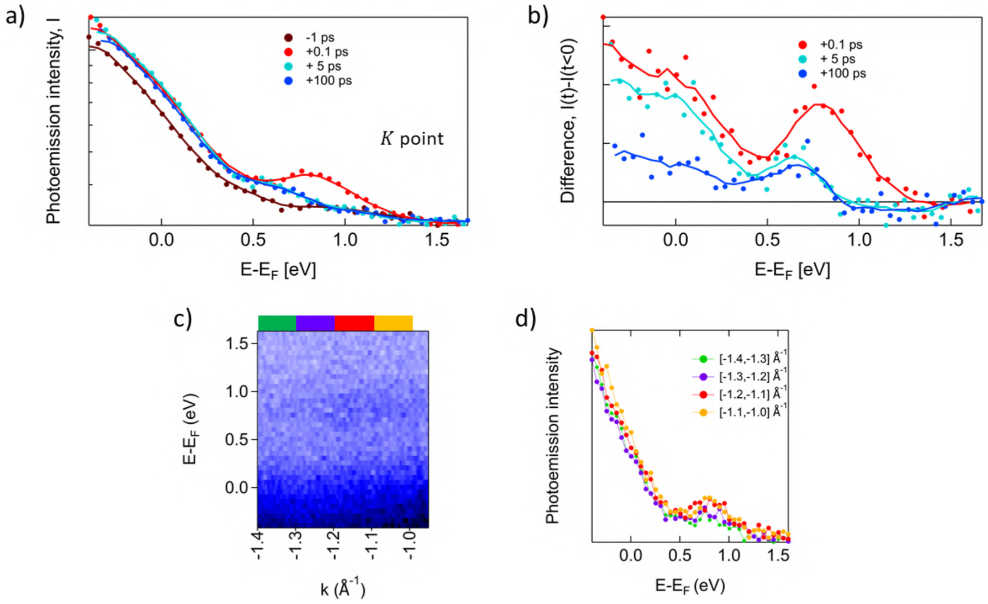

**Figure 5.7:** *a) Photoemission spectra, integrated around the K point, at four selected pump-probe delays: -1 ps, +0.1 ps, +5 ps and +100 ps. b) Difference between the spectra at positive time delays and the spectrum at -1 ps. c) (E,k) photoemission map for the conduction band at +0.1 ps. A non-dispersive intensity just above the Fermi level is associated to defects. A dispersive intensity $\approx$ 0.8 eV above the Fermi level is associated to a transient population of free carriers in the conduction band. d) spectral profiles extracted from the (E,K) photoemission map in panel c). The colors of the spectra match with the colors of the rectangles drawn above the map, to show the wavevector intervals where the photoemission map is k-integrated.*

Theoretical calculations [90] have shown that the absolute minimum of the conduction band in bulk MoS$_2$ is located between $K$ and $\Gamma$, along the $\Sigma$ line. Since we espect that the scattering of electrons towards this absolute conduction band minimum is favored, we acquired pump-probe photoemission spectra, angle integrated around this point, in the range [-0.8,-0.3] Å$^{-1}$, at fixed pump-probe delays. Figure 5.8 a) reports these spectra, at -1 ps, +0.1 ps, +0.8 ps, +5 ps and +100 ps, corrected by the valence band. The difference spectra are shown in figure 5.8 b). At +0.1 ps the difference spectrum exhibit a decreasing tail above the Fermi level (defects), and a peak at 0.8 eV above the Fermi level, corresponding to a transient population of free electrons. This peak undergoes a shift towards lower energy (see spectrum at +0.8 ps), that is almost completed in less than 1 ps. These data suggest that there is a transient population of the $\Sigma$ valley, due to the scattering of free electrons from the K valley towards the $\Sigma$, with a subsequent formation of

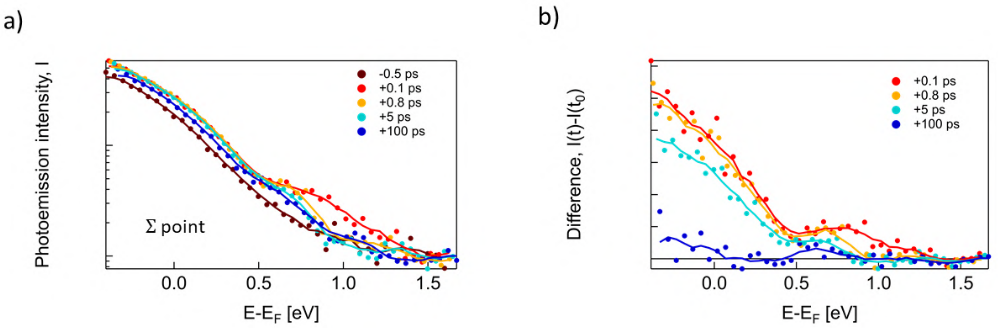

**Figure 5.8:** *a) Photoemission spectra, integrated around the $\Sigma$ point (in the range [-0.8,-0.3] Å$^{-1}$), at four selected pump-probe delays: -1 ps, +0.1 ps, +0.8, +5 ps and +100 ps. b) Difference between the spectra positive time delays and the spectrum at -1 ps.*

indirect excitons, i.e. excitons with momentum $|\vec{k}_{EX}| \neq 0$ (see section 1.5 for furhter analysis). The defect tail exhibits a slower dynamics, resulting almost unchanged after 1 ps. At +100 ps, there is a small residual difference intensity, both from excitons and from defects.
Since the time evolution of the peak corresponding to the photo-excited free carriers is ultrafast, both at the $K$ and $\Sigma$ points, we acquired pump-probe maps in a short time range around the time zero (in the range [-1,+1.5 ps]), and with a short step (33 fs). The top panel of figure 5.9 reports the *pump-probe photoemission maps* where the photoemission intensity (k-integrated in the selected momentum range) is represented in color-scale versus the pump-probe delay and versus the electron energy with respect to the Fermi level.

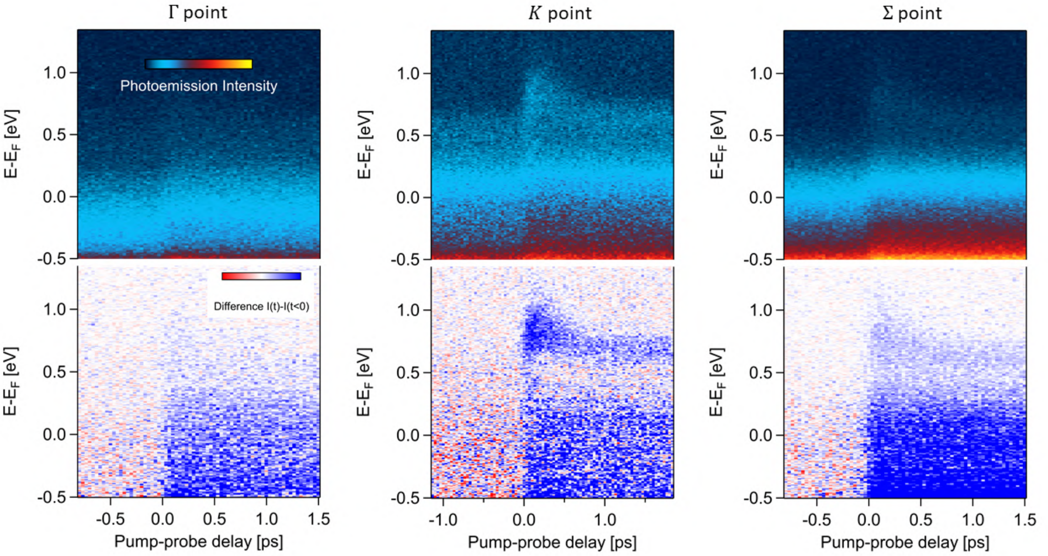

**Figure 5.9:** *Top panel) Pump-probe photoemission maps, reporting the TR- photoemission spectra k-integrated around the points* $\Gamma, K, \Sigma$*. The photoemission intensity is represented in colorscale versus the pump-probe delay and the electron's energy with respect to the Fermi level. Bottom panel) Pump-probe difference maps, obtained by subtracting to each spectrum the average of 15 spectra before the time zero, and allowing to easily access the effects induced by the pump.*

The low panel of figure 5.9 shows the *pump-probe difference maps*, where the average of the spectra at negative delays is subtracted to each spectrum. A positive difference is represented by the blue color, a negative difference is represented by the red color.
From these data we can identify an intense positive signal in the broadband range [-0.4,+0.3] eV, that we already associated to a transient population of defect states. At the K and $\Sigma$ points, a positive signal is visible more than 0.8 eV above the Fermi level. At the K point, this positive signal appears in the range 0.6-1.1 eV around the time zero, while this spectral range tightens and shift towards lower energy, as the pump-probe delay increases, leading to a persistent positive signal in the range 0.6-0.8 eV for t>1 ps. At the $\Sigma$ point the pump-probe map is similar, while at $\Gamma$ the signal above 0.6 eV is barely detectable.

## 5.5 Ultrafast dynamics in conduction band around the K and $\Sigma$ points

Figure 5.10 a) reports the difference pump-probe map k-integrated around the K point (same as figure 5.9). We extracted horizontal profiles in this map (see figure 5.10 b) ), representing the time dynamics of the difference photoemission spectrum, at selected energies. At energy above 0.8 eV, the time dynamics exhibit a fast raise, within the experimental resolution ($\approx$ 110 fs), and a fast decay to zero on the ps time-scale. The dynamics at 0.65 eV and 0.7 eV are characterized by a fast dynamics and a slow dynamics, resulting in a difference intensity signal that decays from its maximum value to a nearly constant intensity value.

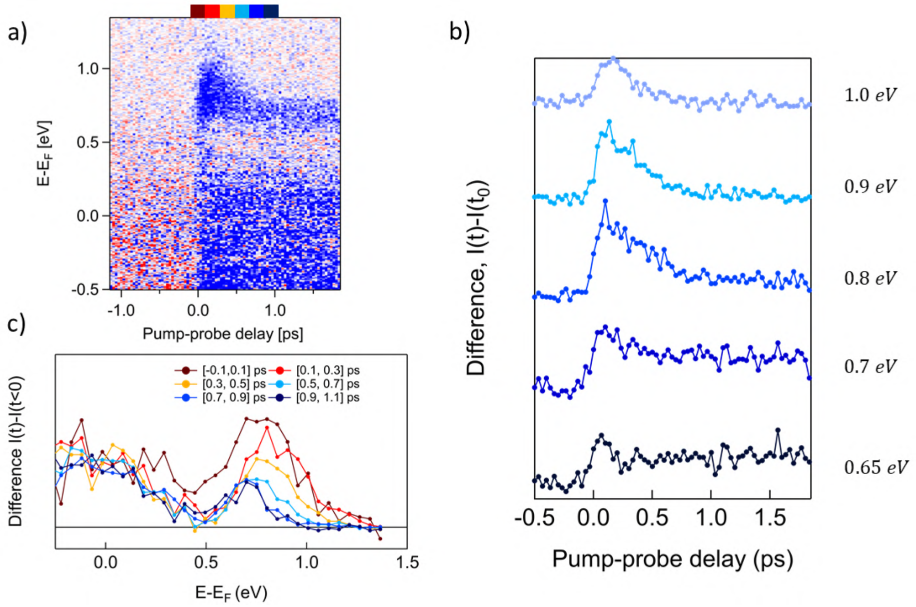

**Figure 5.10:** *a) Pump-probe difference map, k-integrated around the K point. b) Horizontal profiles extracted from the pump-probe difference map, representing time dynamics at fixed electron's energy. c) Vertical profiles extracted from the pump-probe difference map, representing difference photoemission spectra, integrated in selected pump-probe delay ranges. We corrected these data by the rigid shift of the valence band (BGR and SPV), shown in figure 5.6 c).*

Figure 5.10 c) shows difference photoemission spectra integrated in selected time intervals, corrected by the shift of the valence band, calculated in the previous section. At t=0 ps the spectrum is peaked at $\approx$ 0.8 eV and with a broadeing around 400 meV at FWHM. At 0.2 ps the peak appears sligthly shifted towards higher energy and it exhibit a FWHM of $\approx$ 350 meV. At subsequent delays the peak tightens and shifts toward lower energy.

We compared these data with the pump-probe difference photoemission spectra shown in figure 5.7 b), to unveil the dynamics of the difference photoemission spectrum between 0.1 ps and 5 ps. Figure 5.11 a) reports the difference spectra at +0.1 ps and +5 ps, together with the difference spectra in the range 0-1 ps, with 0.2 ps step.

At the time zero the difference photoemission spectrum has a peak at $\approx$ 0.8 eV. In the range 0-0.2 ps this peak shifts towards higher energy, while at subsequent pump-probe delay, it shifts towards lower energy as the FWHM decreases. The position and the FWHM of the peak are represented in figure 5.11 b) and c) respectively. We associate the initial blue-shift to an ultrafast inversion of the bandgap renormalization, due to the decrease of the electron density. We associate the subsequent red-shift to thermalization of free carriers and to the formation of free excitons [11].

Figure 5.12 a) reports the difference pump-probe map k-integrated around the $\Sigma$ point ((same as figure 5.9)).

The horizontal profiles extracted from this pump-probe photoemission map, at selected energies, are reported in figure 5.12 b). These dynamics exhibit a fast raise and a single component in the

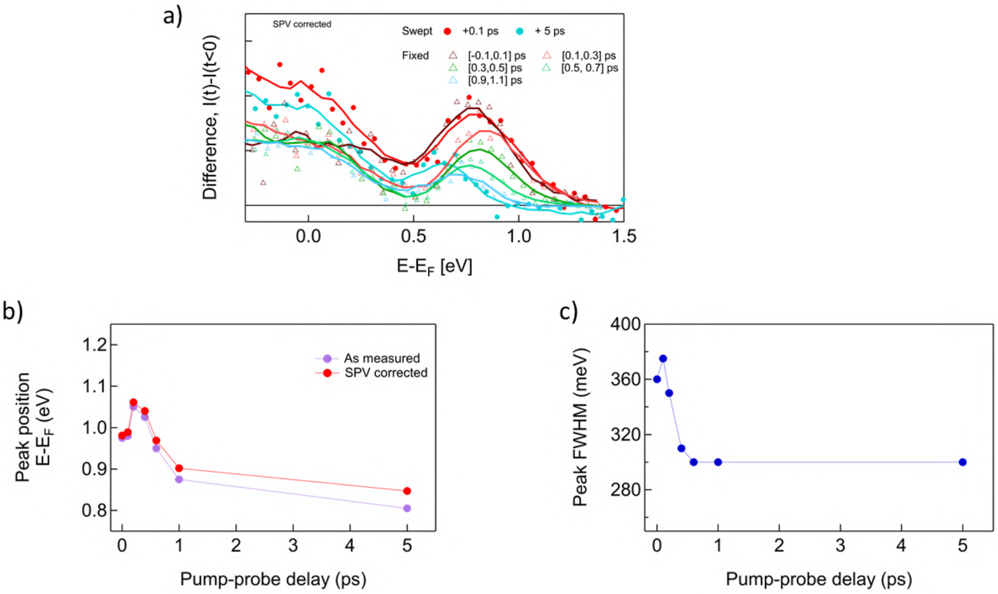

**Figure 5.11:** *a) Difference photoemission spectra integrated around the K point in the first Brillouin zone, at +0.1 ps, +5 ps and + 100 ps (experimental points and smoothing on 5 experimental points). Same as figure 5.7 b). The difference photoemission spectrum exhibits a fast evolution between 0.1 ps and 5 ps. b) The difference photoemission spectra at +0.1 ps and +5 ps, together with the difference photoemission spectra at 0 ps, 0.2 ps, 0.4 ps, 0.6 ps and 1.0 ps, extracted from the difference photoemission map reported in figure 5.11 a). c,d) Position and FWHM of the preak of the difference spectrum, versus the pump-probe delay. The position of the peak is represented "as measured" (violet), and after the correction by the valence band shift (red). The latter were obtained by using the data in figure 5.6 c), linearly interpolated between 0 and 2 ps.*

decay of the difference signal, at each energy. This behavior is different from what we observe at K, where the time dynamics of the difference spectrum at E<1 eV exhibit a fast decreasing component and a slow decreasing component.

Figure 5.12 c) shows the difference photoemission spectra integrated in selected time intervals (shown in the figure). At t=0 ps the spectrum is peaked at ≈ 0.8 eV, while at subsequent delays the peak undergoes a continuous shift toward lower energy. We associate this behavior of the pump-probe difference spectrum to thermalization of free carriers at the Σ valley, and to the formation of indirect free excitons.

We fitted the difference spectra time dynamics, extracted at fixed values of the electron energy, with respect to the Fermi level, at the $K$ and Σ points (same dynamics of figures 5.10 b) and 5.12 b) ). As a fit function we used the sum of two decreasing exponentials, multiplied by an exponential function to consider the raise time, and convoluted with a Gaussian G(t), representing the time resolution. The explicit expression for the fit function is the following:

$$I(t) = (f * G)(t) = \int_{-R}^{R} \left(1 - e^{-\frac{t'-t_0}{\tau_{raise}}}\right)\left(I_1 \cdot e^{-\frac{t'-t_0}{\tau_1}} + \kappa I_1 \cdot e^{-\frac{t'-t_0}{\tau_1}}\right) \cdot G(t-t')dt' \qquad (5.1)$$

where $t_0$ is the time zero, $\tau_{raise}$ is the raise time of the difference signal, $I_1$ is the intensity of the first component in the decay, $I_2 = \kappa \cdot I_1$ is the intensity of the second component in the decay, and $\tau_1, \tau_2$ are the time constant for the two exponential decays. Figure 5.13 reports the horizontal profiles of the pump-probe difference maps at the five fixed electron's energy, at K (left column) and Σ (right column) along with the fits, obtained using the function 5.1.

In the fitting procedure, we keep the raise time $\tau_{raise}$ fixed at 10 fs (the fit is scarcely dependent on this variable since it results much shorter than the experimental resolution). We used a FWHM for the experimental resolution Gaussian of 110 fs. We also fixed the slow decay constant at 100 ps for the data at the K point, since the decay time is much larger than the range of the experimental data. To fix the value of this slow decay constant, we considered the difference spectra reported

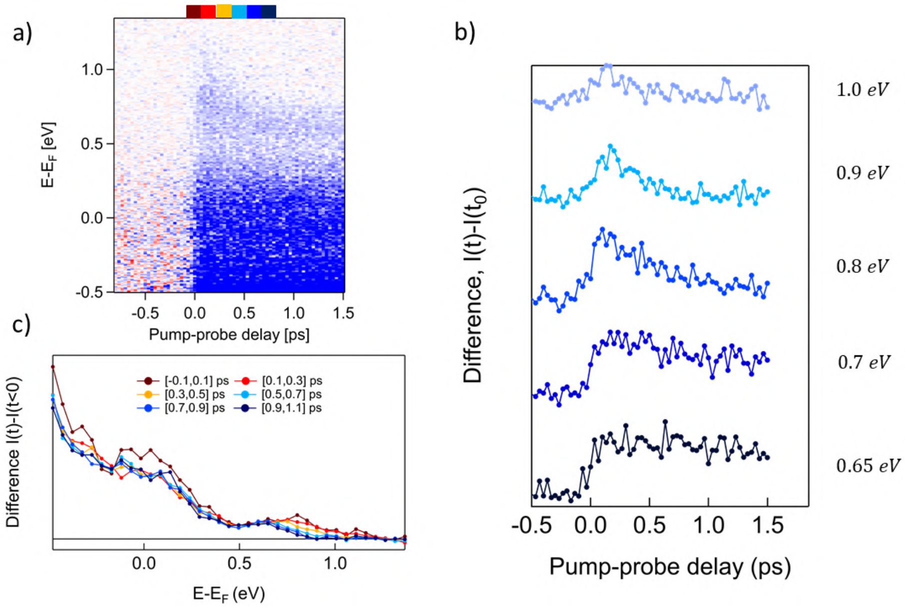

**Figure 5.12:** *a) Pump-probe difference map, k-integrated around the $\Sigma$ point. b) Horizontal profiles extracted from the pump-probe difference map, representing time dynamics at fixed electron's energy. c) Vertical profiles extracted from the pump-probe difference map, representing difference photoemission spectra, integrated in selected pump-probe delay ranges.*

in figure 5.7 b), and integrated in the range [0.85,0.95] eV, at the three positive time delays: +0.1 ps, +5 ps and +100 ps. The value of this integral decreases by a factor 4 in +100 ps, suggesting an exponential decreasing with time constant ≈100 ps.
At the $\sigma$ valley, we set $\kappa$ to zero, to consider a single exponential decay in the dynamics.
The interest parameters of the fits are the fast time constant $\tau_1$, the time zero $t_0$ and the ratio between the intensity of the two decay dynamics, $\kappa$. Figure 5.14 reports these fit parameters with the related error bars, for the dynamics at both $K$ and $\Sigma$ points, versus the energy of the electrons with respect to the Fermi level.
At the K point, the fast decay time ranges from 100-400 fs. For energies E≥0.8 eV, we associate this time constant to the lifetime of hot free electrons (thermalization and exciton formation). At energies E<0.8 eV, this lifetime is associated to the scattering of carriers from $K$ to $\Sigma$ point. We associate the long time constant to the recombination of direct free excitons.
At the $\Sigma$ point, the decay time decreases as the electron energy increases. At high energies, we associate this decay time to the thermalization of free carriers and to the exciton formation at the $\Sigma$ point. At low energies, we associate this decay time to the recombination of indirect free excitons. The intensity ratio parameter $\kappa$, at the K point, is ≈0 at high electron energy, signalling the presence of a single component in the decay, supporting the interpretation as due to the thermalization and exciton formation. At low electron energy, the slower component in the decay (recombination of direct free excitons), becomes relevant.
The time zero contains information on the onset of the electron and/or exciton population. Even with a cross-correlation of the pump and probe pulses of 110 fs, we are able to appreciate some differences in this parameter. At both K and $\Sigma$ points it seems to move towars positive value, as the energy increases. At the K point this effect may be related to the initial blue-shift of the spectrum. Figure 5.15 reports the direct comparison between the time dynamics at $K$ and $\Sigma$, at 1.1 eV, 1.0 eV, 0.9 eV and 0.85 eV of electron's energy. The intensity is normalized to the maximum value at 0.9 eV, by multiplying the signal at $\Sigma$ by a factor ≈2.5. This is the ratio between the intensity of the signal at the two points, due to both the physics of the system, and to the different pump fluence (different incident angle for the pump beam). We used the same normalization factor for the other energies. By this direct comparison, we observe that at high energies, the normalized signal is higher at $K$ while at lower energies, the normalized signal is higher at $\Sigma$. Moreover, at 0.9 eV and 0.85 eV, the signal at K exhibits a fast decay, while the raise of the signal at $\Sigma$ appears

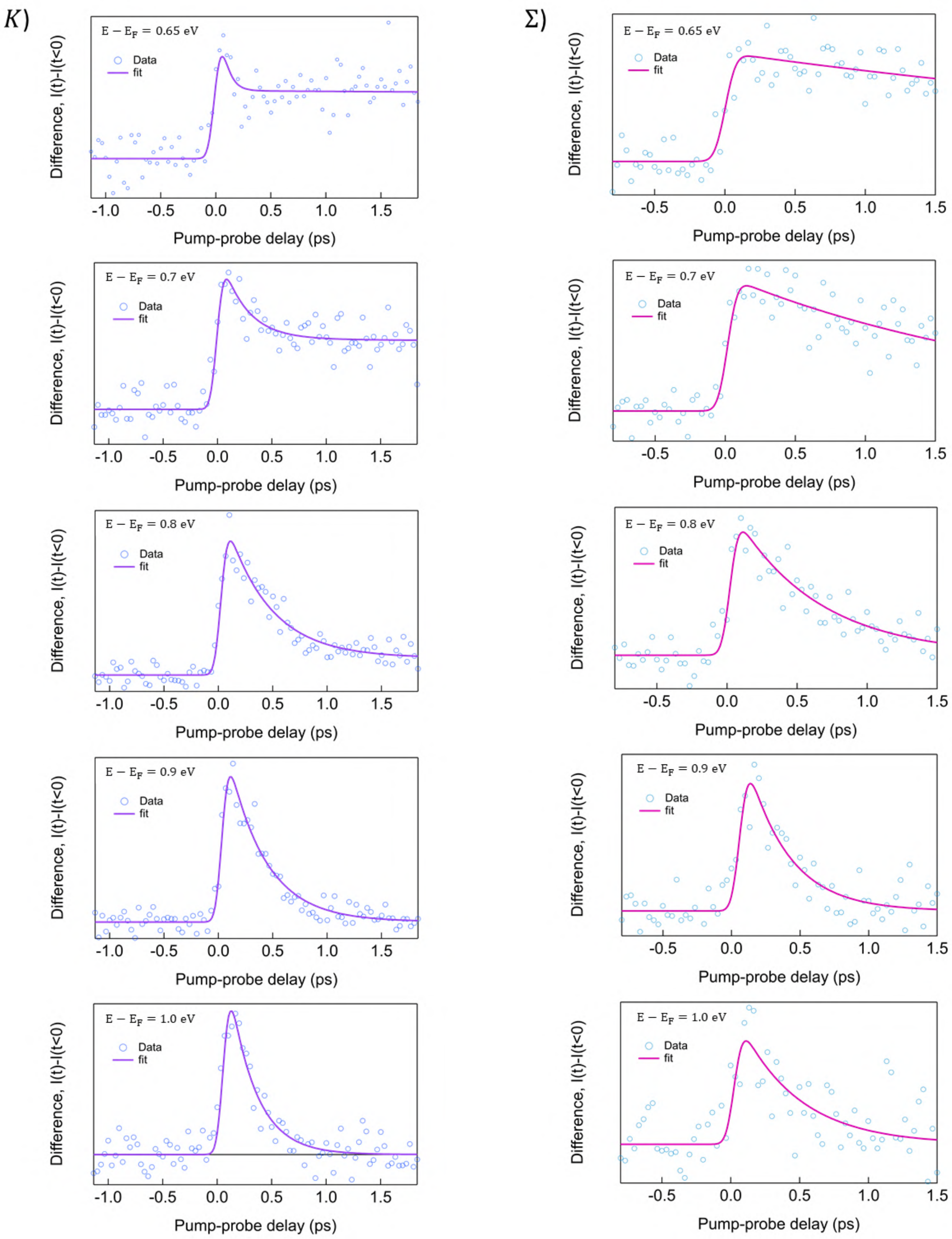

**Figure 5.13:** *Time dynamics, horizontal profiles extracted from the pump-probe difference maps, k-integrated around $K$ and $\Sigma$, at fixed electron's energies: 0.85 eV, 0.9 eV, 1.0 eV, 1.1 eV, 1.2 eV (same time dynamics of the figures 5.10 b) and 5.12 b) ). The experimental data (dots) and the fits (continuous lines) are represented.*

delayed, reaching its maximum at about 200 fs. After this time, the dynamics at both points show a slow decrease. We associate the behavior to the fast scattering of excitons and from $K$ to $\Sigma$. This have already been observed in previous works [81, 18].

## 5.6 Conclusions

In this chapter we reported and analyzed the TR-ARPES experimental data for bulk $MoS_2$, cleaved in UHV.

We observed a positive pump-probe signal for the conduction band, in the range [0.6, 1.0] eV

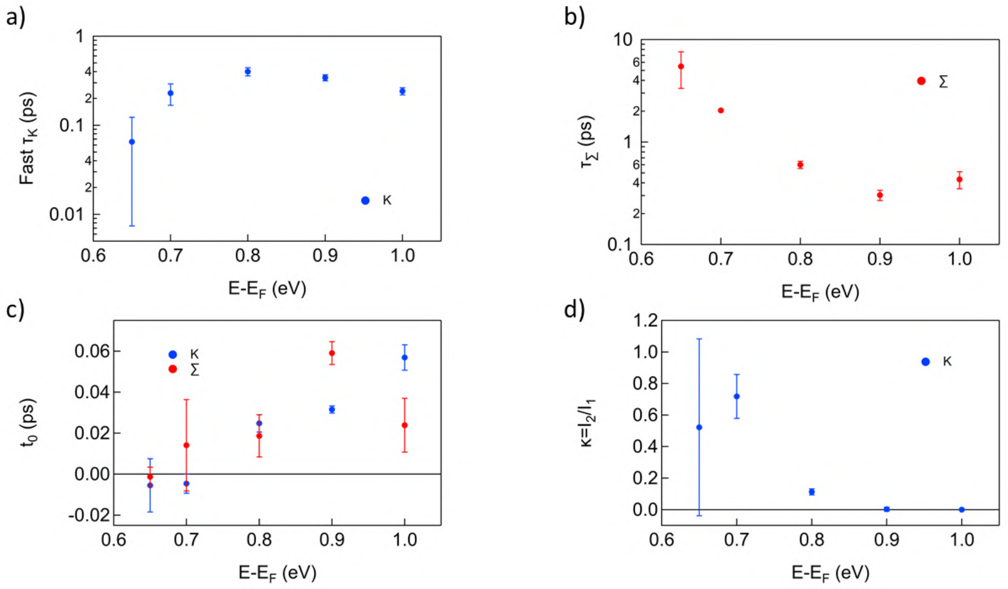

**Figure 5.14:** *Fit parameters versus the energy of electrons with respect to the Fermi level. a) Fast decay time at the K point: $\tau_K$ (the long decay time is kept fixed to 100 ps) b) Decay time at $\Sigma$: $\tau_\Sigma$. c) Time zero $t_0$. d) Intensity ratio between the slow and the fast dynamics $\kappa = I_2/I_1$ (at $\Sigma$, $\kappa$ is kept fixed to zero).*

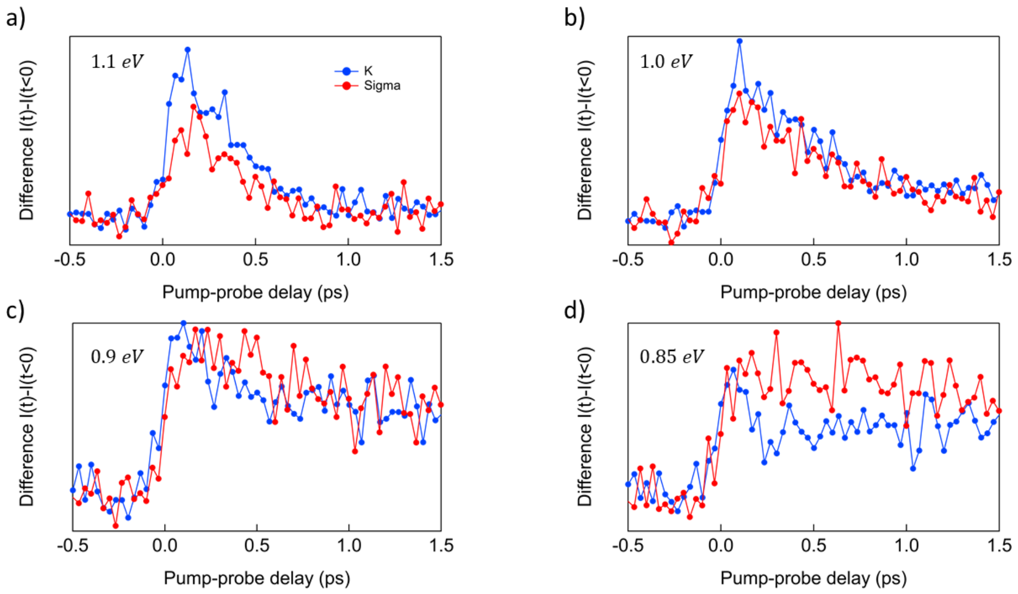

**Figure 5.15:** *Direct comparison between the time dynamics at K and $\Sigma$, at four energies. The intensity is normalized at the maximum value at 0.9 eV.*

(above the Fermi Energy), at the K point and at the $\Sigma$ valley in the first Brillouin zone, which we associate to a transient population of photo-excited electrons, arising from either an electron hole plasma (EHP) or bound in free exciton (FE) states. We observe a long-lived positive pump-probe signal at energies $<$0.6 eV above the Fermi level, associated to the transient population of defect states.

For energies $>$0.8 eV, the pump probe signal decays on the sub picosecond to picosecond time scale at both K and $\Sigma$ points. We associate this fast dynamics to the cooling of the EHP, the fast non-radiative recombination and the exciton formation. For energies in the range [0.6, 0.7] eV, at the K point, the pump-probe signal shows a fast dynamics with a time constant of on the sub ps

time scale, which we associate to fast non-radiative recombination of excitons and to the scattering from $K-K$ to $K-\Sigma$ and $\Gamma-\Sigma$ excitons. We observe a slower additional component in the decay that we associate to the formation of indirect excitons.
The pump-probe difference spectra in conduction band show an initial blue-shift and decrease of the FWHM, for a delay $<$300 fs. We associate this behaviour to an ultrafast reduction of the excitation density, due to non-radiative recombination of electrons and holes, resulting in the inversion of the bandgap renormalization. For t$>$300 fs, the peak exhibits a red-shift, that we associate to the thermalization of free carriers and to the formation of free excitons.

# Conclusions

In this thesis we reported novel time resolved photoluminescence (TR-PL) data for monolayers $WS_2$ and $MoS_2$ on $SiO_2$ substrate and for bulk $MoS_2$, and time resolved angle resolved photoelectron spectroscopy (TR-ARPES) data for bulk $MoS_2$.

The aim of the TR-PL measurement is to study the time evolution of the PL spectrum (25 ps time resolution), especially at high excitation densities, where the strong exchange and correlation terms induces the ionization of free excitons (FE) in an electron-hole plasma (EHP). This transition both pose operational limitations for excitonic light-emitting devices and opens the possibility for the development of ultra-high-power LEDs with broadband emission.

For both $MoS_2$ and $WS_2$ we observed an EHP emission up to 25 ps after the pulsed excitation, with a threshold fluence of $\approx 70\ \mu J/cm^2$.

In monolayer $WS_2$, at this fluence, the fit of the PL spectra at the time zero with two Gaussian peaks reveals the presence of two emissions, with spectral position 1.96 eV and 2.01 eV and FWHM 100 meV and 60 meV, that we associate to the EHP and FE emissions, respectively. At the time zero, the EHP emission is dominant. At t=25 ps we still observe both emission peaks, with inverted intensity ratio with respect to the spectrum at the time zero, showing that the lifetime of the EHP emission is on the timescale of tens of picoseconds.

In monolayer $MoS_2$, at the highest excitation fluence, $\approx 0.6\ mJ/cm^2$, the TR- spectrum at the time zero exhibits a red-shift of $\approx 60$ meV and a broadening $\approx 100$ meV with respect to the free exciton emission line, that we associate respectively to the band gap renormalization (BGR) and to the high occupation of the renormalized conduction and valence band by free electrons and holes. We evaluated the effects of the lattice heating due to the absorption of the excitation pulse and of the exciton-exciton interaction, showing that these contributions are not sufficient to explain the shift and broadening.

We fit the TR-PL time dynamics of $WS_2$ monolayer at four fluences below $2\ \mu J/cm^2$, where excitons dominate the PL emission, by using a dynamic model which takes into account the exciton radiative and non-radiative decay, the exciton-exciton annihilation (EEA), the trapping and de-trapping of excitons in "slow" defect states. We found an exciton radiative lifetime ranging from 0.8 ns to 1.7 ns, a time constant of 0.05-0.2 ns for the trapping of free excitons in defect states, and an EEA coefficient in the range 1.4-2.4 $cm^2s^{-1}$.

For the bulk $MoS_2$, at very high excitation fluence, $4\ mJ/cm^2$, we observe a fast evolution of the PL spectrum, from a broadband emission with peak at 1.7 eV and a FWHM of $\approx 250$ meV at t=0 ps, to a sharp emission with peak at 2.1 eV, at t=50 ps. We associate the first spectrum to a huge BGR induced by the high EHP density after the high-fluence photo-excitation, resulting in the red-shift of the PL spectrum of $\approx 0.4$ eV. The subsequent fast decrease of the EHP density induces a reversion of the BGR and the formation of FEs. At t>100 ps, the emission peak at 2.1 eV vanishes as a peak at $\approx 1.4$ eV appears, signalling the formation of indirect excitons, energetically favored in the indirect band gap bulk $MoS_2$, which PL emission persists for hundreds of picoseconds.

The TR-ARPES data provide complementary information, giving direct access to the electronic excited states along the first Brillouin zone after a pulsed excitation, and to their time evolution on the ultrafast time scale. We observe a transient population of the conduction band at the K point and at the $\Sigma$ valley in the first Brillouin zone. At the K point, the pump-probe signal from electrons shows a fast dynamics on the ps time scale, that we associate to fast non-radiative recombination of excitons and to the scattering from $K-K$ to $K-\Sigma$ and $\Gamma-\Sigma$ excitons. Beside the fast dynamics, we observe a second slow dynamics at the K point, with time constant >100 ps, that we associate to the formation of indirect excitons. The experimental data shown in this

thesis constitute the final result of the experimental work that I performed at the Sprint and TReX laboratory (Elettra Sinctrotrone Trieste). I implemented many upgrades on this apparatus, among which the micro-PL configuration, the possibility to quickly switch from the TR-PL to steady state PL configuration, the spatially resolved PL, and the PL imaging, making this setup efficient and very versatile. The fine improvement of the optical alignment in order to maximize the collected PL signal at the detector, made this setup capable to detect even the weaker PL signal emitted by indirect band gap semiconductors, such as Silicon or bulk $MoS_2$, at room temperature.
Another important part of my PhD work consisted of learning the exfoliation technique and how to use a transfer system for exfoliated flakes. This important skill allows to fabricate custom samples in situ, and to obtain many samples starting for a single high-quality crystal. The possibility to measure custom samples is a big advantage, since it allows to control an important step of the experiment. Master the exfoliation and transfer is challenging but useful since it implies the possibility to fabricate samples with a selected number of layer, on selected substrates, and even to assembly hetero-structures. The ability to exfoliate TMD monolayers in UHV would constitute an important step in this direction, allowing to investigate TMD monolayers by means of TR-ARPES.
The wealth of information and the expertise acquired during this thesis constitute the first milestone to go further in the study of the ultrafast electron and exciton dynamics TMDs monolayers. The goal for the near future would be to exploit the potentialities of the Sprint laboratory to perform this investigation with a powerful multi-technique approach, combining complementary experiments of TR-PL, TR-ARPES, TR-RAMAN, transient absorption (TA) and transient grating (TG).

# Chapter 6

# Appendix

## 6.1 Derivation of the explicit expression for the imaginarty part of the dielectric function $\varepsilon_2(\hbar\omega)$

The following introduction of optical properties in solids is taken from [6, 62], and summarized, taking only the fundamental elements needed to understand the basics of optical transition in solids. In this approach we define the electronic ground state of the crystal, we define the simplest single-particle excited states, and finally we show how the electromagnetic radiation field interacts with these states.

We start from the electronic Hamiltonian.

$$H_e = \sum_i h_i + \frac{1}{2}\sum_{i\neq j}\frac{e^2}{|\vec{r}_i - \vec{r}_j|} \text{ ; where } h_i = -\frac{\hbar^2}{2m_e}\vec{\nabla}_i^2 - \sum_I \frac{Z_I e^2}{|\vec{R}_I - \vec{r}_i|} \tag{6.1}$$

The ground state in a solid, in first approximation, can be written as a single Slater determinant,

$$< \vec{r}|0 >= \Psi_0 \approx A_N \prod_{n,\vec{k};E_n(\vec{k})<E_F} \varphi_{n,\vec{k}}(\vec{r})\gamma(\sigma_{n,\vec{k}}) \tag{6.2}$$

where $\varphi_{n,\vec{k}}(\vec{r}) =< \vec{r}|n,\vec{k} >$ are the Bloch functions [4], the quantum numbers n and $\vec{k}$ are the band index and the crystal momentum in the first Brillouin zone, $E_F$ is the Fermi energy for the electrons, and $\gamma(\sigma_{n,\vec{k}})$ are the wave functions for the spin of the electrons [4, 6, 62]. The energy of the electronic ground state is given by the average value of the total Hamiltonian on the state $|0>$:

$$E_0 =< 0|H_0|0 > \tag{6.3}$$

The simplest excited state of this system is a *single-particle excited state*, where an electron in the valence band (band index n=v) with crystal momentum $\vec{k}$ is destroyed (leaving a hole in the valence band and at that $\vec{k}$), and an electron in the conduction band (band index n=c) with crystal momentum $\vec{k}'$ is created:

$$|1 >= a^+_{c,\vec{k}'}a_{v,\vec{k}}|0 > \tag{6.4}$$

The energy of this excited state is given by

$$E_1 = E_0 + E_c(\vec{k}') - E_v(\vec{k}) + \delta_{cv}(\vec{k},\vec{k}') \tag{6.5}$$

where $E_c(\vec{k}')$ is the energy of the new electron in the conduction band, $E_v(\vec{k})$ is the energy of the destroyed electron in the valence band, and $\delta_{cv}(\vec{k},\vec{k}')$ is a corrective term due to the Coulomb attraction between the new electron in the conduction band and the hole in the valence band, to the band gap renormalization effect [4, 6], and to other correlation effects. In the first approximation, we neglect this term.

The wave function of the excited state is a Slater determinant where the wave function $\varphi_{v,\vec{k}}(\vec{r})\gamma(\sigma_{v,\vec{k}})$ is replaced by $\varphi_{c,\vec{k}'}(\vec{r})\gamma(\sigma_{c,\vec{k}'})$. However, we should point out that this is an approximated approach, where we neglect the fact that also the wave functions of the other electrons vary as a consequence of the single-particle excitation.

The Hamiltonian of the system interacting with an electromagnetic field is $H_0 + \Delta H_{eR}$, where $\Delta H_{eR}$ is the interaction Hamiltonian of the electromagnetic field of radiation [6], produced by the vector potential $\vec{A}(\vec{r}, t) = A_0 \hat{\eta} e^{i(\vec{q}\cdot\vec{r} - \omega t)} + cc$:

$$\Delta H_{eR} = \frac{|e|}{m_e c} \sum_{i=1}^{N} \vec{A}(\vec{r}_i, t) \cdot \vec{p}_i = \sum_{i=1}^{N} \frac{|e| A_0}{m_e c} \hat{\eta} \cdot \vec{p}_i e^{i\vec{q}\cdot\vec{r}_i} e^{-i\omega t} + H.C. = F^{(ch)} e^{-i\omega t} + H.C. \tag{6.6}$$

Here $\vec{p}_i$ is the momentum operator of the electron, $\hat{\eta}$, $\vec{q}$ and $\omega$ are the polarization, the wavevector and the angular frequency of the electro-magnetic field of radiation, respectively. $F^{(ch)}$ is the static part (independent on time) of the interaction Hamiltonian.

The probability to have a transition from the initial state $|0>$ (ground state) to the final state $|1>$ (single particle excited state) per unit time is given by the *Fermi Golden rule*:

$$\pi_{|0> \to |1>} = \frac{2\pi}{\hbar} | < 1 | F^{(ch)} | 0 > |^2 \delta(E_c(\vec{k}') - E_v(\vec{k}) - \hbar\omega) \tag{6.7}$$

Since $F^{(ch)}$ is a single particle operator, the element matrix, calculated on Slater determinants, simplifies to transition rate from single particle states: $|v, \vec{k}>$ to $|c, \vec{k}'>$ (see appendix 5A in [6]). By writing explicitly the part of the operator $F^{(ch)}$ which act on the excited electron, the transition rate for a single electronic excitation becomes:

$$\pi_{|v,\vec{k}> \to |c,\vec{k}'>} = \frac{2\pi}{\hbar} \left( \frac{|e| A_0}{m_e c} \right)^2 |\hat{\eta} \cdot < c, \vec{k}' | \vec{p} e^{i\vec{q}\cdot\vec{r}} | v, \vec{k} > |^2 \delta(E_c(\vec{k}') - E_v(\vec{k}) - \hbar\omega) \tag{6.8}$$

By analyzing the matrix element

$$M_{vc}(\vec{k}) = < c, \vec{k}' | \vec{p} e^{i\vec{q}\cdot\vec{r}} | v, \vec{k} > \tag{6.9}$$

and using the fact that the wave vector of a photon in the IR-visible-UV range is much less than the size of the first Brillouin zone (i.e. $q = \frac{\omega}{c} << \frac{\pi}{a}$), it is possible to obtain the selection rules for optical transitions:

1. Single particle excitations.
2. $\Delta n_{band} \neq 0$: only inter-band transitions are allowed.
3. $\Delta \vec{k} = \vec{q} \approx \vec{0} \implies \vec{k}' \approx \vec{k}$. Early "vertical" transitions in the $(\vec{k}, E_n(\vec{k}))$ space.

Optical transitions in $\vec{k}$ points where the matrix element is non zero are called *first class optical transitions.* In the $\vec{k}_0$ points where the matrix element vanishes because of symmetry, the latter is proportional to $\vec{k}$ as going far from $\vec{k}_0$, giving rise to the *second class optical transitions.*

Equation 6.8 gives the transition rate for a single excitation, with a specific $\vec{k}$ which verifies the energy conservation Dirac delta. However, in a solid there may be many other transitions which verify this condition, at different $\vec{k}$ points in the first Brillouin zone. Hence, to obtain the total probability of absorption per unit time (and per unit volume) $W(\hbar\omega)$, it is necessary to consider the two spin projections for electrons, to sum on each couple of valence and conduction bands and to integrate equation 6.8 in $d^3k$ in the first Brillouin zone [6, 62].

$$W(\hbar\omega) = \frac{2}{V} \sum_{v,c} \int_{1ZB} d^3k \pi_{v,\vec{k} \to c,\vec{k}}(\hbar\omega) d^3k \tag{6.10}$$

This quantity can be related to the absorption coefficient $\alpha(\hbar\omega)$ and to the imaginary part of the dielectric function $\varepsilon_2(\hbar\omega)$, allowing to calculate its analytical expression, in the approximation of homogeneous, isotropic and non-magnetic crystal [6, 52, 62]:

$$\varepsilon_2(\hbar\omega) = \frac{4\pi e^2}{\omega^2 m_e^2} \frac{2}{(2\pi)^3} \sum_{v,c} \int_{1ZB} d\vec{k} |\hat{\eta} \cdot M_{c,v}(\vec{k})|^2 \delta(E_c(\vec{k}) - E_v(\vec{k}) - \hbar\omega)) \tag{6.11}$$

## 6.2 Second order optical transitions in solids

In the this appendix we introduce the two possible second order optical transitions in solids, involving the simultaneous absorption of two photons and the simultaneous absorption of a photon and absorption/emission of a phonon [6, 62]. The first process enables absorption of light with photon energy below the band gap, the second process enables absorption of light with a photon energy close to that of the indirect band gap.

The transition rate for the second order absorption for a *two-photon* optical transition (same photon energy and same polarization) can be written as [6]:

$$\pi_{|v,\vec{k}>\rightarrow|c,\vec{k}>} = \frac{2\pi}{\hbar}\left(\frac{|e|A_0}{m_e c}\right)^4 \left|2\frac{\hat{\eta}\cdot <c,\vec{k}|\vec{p}|\beta,\vec{k}> \hat{\eta}\cdot <\beta,\vec{k}|\vec{p}|c,\vec{k}>}{E_\beta(\vec{k})-E_v(\vec{k})-\hbar\omega}\right|^2 \delta(E_c(\vec{k})-E_v(\vec{k})-2\hbar\omega) \quad (6.12)$$

where $|\beta,\vec{k}>$ is an intermediate *virtual state* at the same $\vec{k}$ and with energy $E_\beta(\vec{k})$. It's important to note that this transition rate is much lower than the transition rate for a first order transition rate with a single photon of energy $2\hbar\omega$ (and with the same polarization). However, since the rate in equation 6.12 scales with the square of the intensity of the electric field of radiation (i.e. with $A_0^4$), the two-photon absorption becomes more and more relevant as the intensity of the electromagnetic field of radiation increases.

In a second order optical transition with a photon and a phonon, the interaction can significantly change the wave vector of the excited electron, along the first Brillouin zone. A photon in the visible range has a photon energy in the range 1-3 eV, with a wavevector much smaller than the size of the first Brillouin zone ($q << \frac{\pi}{a}$). On the other side, a phonon has an energy $\hbar\Omega << 1$ eV, and a wavevector which spans all over the first Brillouin zone. Thus, a second order optical transition with a photon and a phonon enables the absorption in indirect band gap semiconductors, for photon energies between the energy gap $E_g$ and the *effective energy gap*, $E_g^{eff}$ (energy gap for direct, vertical optical transitions). The transition rate for the second order absorption for a photon+phonon optical transition is the following [6]:

$$\begin{aligned}\pi_{|v,\vec{k}_1>\rightarrow|c,\vec{k}_2>} = \frac{2\pi}{\hbar}\left(\frac{|e|A_0}{m_e c}\right)^2 &\left|\frac{<c,\vec{k}_2|V_p(\vec{q},\vec{r})|\beta,\vec{k}_1> \hat{\eta}\cdot <\beta,\vec{k}_1|\vec{p}|c,\vec{k}_1>}{E_\beta(\vec{k})-E_v(\vec{k})-\hbar\omega}\right|^2 n_q \quad (6.13)\\ &\cdot\,\delta(E_c(\vec{k})-E_v(\vec{k})-\hbar\omega\pm\hbar\Omega)\end{aligned}$$

where $V_p(\vec{q},\vec{r})$ is the operator for electron-phonon interaction, which connects an electronic state in the conduction band (c) with wavevector $\vec{k}_2$ and a virtual electronic state ($\beta$) with wavevector $\vec{k}_1$. The effect of the temperature is taken into account, by considering the occupation number for the phonons, $n_q$, which obey to the Bose-Einstein distribution.

As for the first order optical transitions, the transition rate between single states is only an ingredient to the second-order absorption coefficient. To obtain the latter we need to sum on each spin projection, on each couple of valence and conduction bands, each possible virtual state, and to integrate in the first Brillouin zone (for other details see [6], chapter 5, section 5-4).

## 6.3 The NIREOS GEMINI Interferometer

The Gemini Interferometer is an ultra-stable interferometer opearating in a braodband spectral range. The incoming light is divided in two orthogonally polarized replicas with a tunable time delay which can be controlled by software, with high reproducibility. Thanks to the common path geometry for the two replicas, the Gemini interferometer is insensitive to external noise and vibrations, ensuring an excellent interferometric stability. The working princile of the Gemini Interferometer is sketched in figure 6.1.

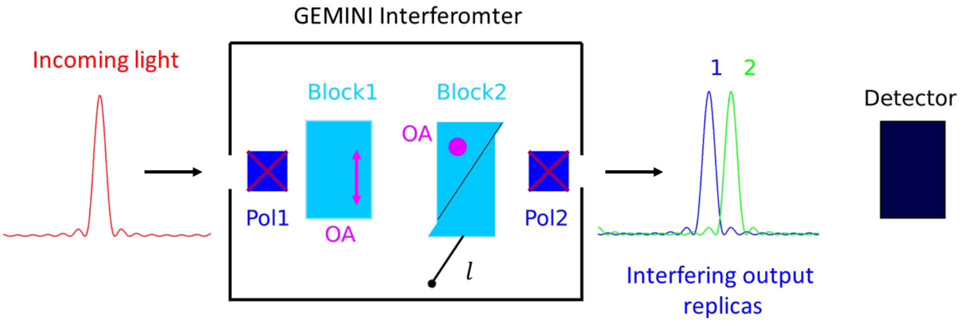

**Figure 6.1:** *Scheme of the Gemini interferometer. This device is constituted by two linear polarizers, and two birefringent blocks, with mutually orthogonal optical axis. The second block is divided into two triangular wedges which can translate along the hypotenuse, in the l direction. The incoming light pulse hits the first polarized at 45° and it is divided into two orthogonal replicas. Block 1 introduce a relative time delay between the replicas, block 2 reverts this time delay, when l=0. By moving the block 2 along the l coordinate, a time delay is introduced. The two replicas hit a second polarizer which projects them on the same direction to make them interfere at the detector.*

After the incoming light hits a linear polarizer (Pol1) at 45°, its electric field can be decomposed into two orthogonal components (replicas), horizontal and vertical, with the same amplitude and relative zero time delay. A birefringent plate (Block1), with optical axis aligned in the horizontal direction, introduces a time delay between the two replicas, given by;

$$\tau_1 = \frac{\Delta n(\nu) h}{c} \tag{6.14}$$

where h is the thickness of the plate, c is the speed of light and $\Delta n(\nu) = n_e(\nu) - n_o(\nu)$ is the birefringence of the plate, i.e. the difference between the extraordinary refraction index and the ordinary refraction index. A second birefringent plate (Block2), with optical axis alighed along the vertical direction, allows to revert the time delay introduced in Block1. This second plate is divided into two triangular wedges with apex angle $\alpha$. One wedge is mounted on a precision piezo manipulator that allows to translate it along the direction if its hypotenuse ($\hat{l}$), resulting in a plate with tunable thickness. When the wedge is moved by $l\hat{l}$, the thickness of BP2 becomes: $h' = h + lsin(\alpha)$. The time delay between the two replicas is then reverted by a time

$$\tau_2 = \frac{\Delta n(\nu)(h + lsin(\alpha))}{c} \tag{6.15}$$

After crossing BP1 and BP2, the relative time delay between the two replicas is then given by:

$$\tau(l,\nu) = \tau_2 - \tau_1 = \frac{\Delta n(\nu) lsin(\alpha)}{c} \tag{6.16}$$

When the wedge position is $l = 0$, there is no time delay between the two replicas. Finally, the light hits a linear polarizer (Pol2) at -45°, which projects the two orthogonal replicas on the same direction, to make them interfere. Since the linear polarization P1 and P2 are mutually orthogonal, the interference is destructive when l=0.

The intensity of the light at the detector versus the wedge position $l$ of the interferometer, is named *interferogram*, and its analytical expression is given by the integral over all frequencies of the superposition of the two replicas:

$$I(l) = \int |\tilde{E}(\nu) - \tilde{E}(\nu)e^{-i2\pi\tau(l,\nu)\nu}|^2 d\nu = \int |\tilde{E}(\nu) - \tilde{E}(\nu)e^{-i2\pi\frac{\Delta n(\nu)\cdot l\cdot sin\alpha}{c}\nu}|^2 d\nu \tag{6.17}$$

where $\tilde{E}(\nu)$ is the amplitude of the electric field along both the horizontal and vertical directions. The Fourier Transform of the interferogram gives the spectrum of the light, as a function of the *pseudo-frequency* $f_l$:

$$\tilde{S}(f_l) = \frac{1}{\sqrt{2\pi}} \int I(l)e^{i2\pi f_l l} dl \tag{6.18}$$

The experimental interferogram is not a continuous function of the wedge position $l$, define on all $\mathbb{R}$, but it is given by a finite series of N points $(l_i, I(l_i))$, in a finite wedge position range. Hence we need to perform a discrete Fourier transform. We need to discretise equation 6.18, and to calculate the transform by using only the N experimental points (a finite number and in a finite range) to calculate a finite number M of spectrum points $(f_l^{(j)}, \tilde{S}(f_l^{(j)}))$.

$$\tilde{S}(f_x^{(j)}) = \frac{1}{\sqrt{2\pi}} \sum_{i=i}^{N} I(l_i)e^{-if_x^{(j)}l_i}\Delta l_i \tag{6.19}$$

Finally, to get the spectrum of the light versus the optical frequency, $S(\nu)$ (or photon energy $(h\nu)$), it is necessary to convert the pseudo-frequencies into optical frequencies, i.e. to obtain the relation $f_l \to \nu$. The calibration procedure is the following procedure:

1. Send a monocromatic wave with known optical frequency $\bar{\nu}$, such as a laser line, through the Gemini Interferometer, and acquire an interferogram $I(x)$. The latter is given by a sinusoidal wave with spatial period $\Lambda = \frac{c}{\Delta n(\bar{\nu})\cdot sin\alpha\cdot\bar{\nu}}$.
2. The Fourier Transform of the interferogram gives the spectrum $\tilde{S}(f_x)$, with a peak at the pseudofrequency $\bar{f}_x = \frac{1}{\Lambda} = \frac{\Delta n(\bar{\nu})\cdot sin\alpha\cdot\bar{\nu}}{c}$.
3. Repeat the procedure by using several monocromatic sources with different known optical frequencies. We get a point series $(\nu, f_x)$.
4. Interpolate the point series with a polinomial function: $\nu = \sum_{i=1}^{n} P_i {f_x}^i$. The coefficients of the polinomial fit depends on $\alpha$, and on $\Delta n(\nu)$.

Beside the frequency calibration, an intensity calibration is required, in order to have $\tilde{S}(f_x)df_x = \tilde{S}(\nu)d\nu$. This condition leads to:

$$\tilde{S}(\nu) = \tilde{S}(f_x)\left[\frac{d\Delta n(\nu)}{d\nu}\frac{\nu sin\alpha}{c} + \frac{\Delta n(\nu)sin\alpha}{c}\right] \tag{6.20}$$

The intensity calibration is not necessary when considering the ratio between physical quantities, such as the differential reflectivity. More details are provided in the Gemini Interferometer user manual[29].

The spectral resolution of the interferometer is related to the scan range along the wedge position $l$, for positive values of $l$. If the spectrum of the light to measure is broad-band, a high resolution is not required, hence it is sufficient to scan near the zero position of the interferometer. On the other hand, when measuring a very sharp peak, it is necessary to scan the wedge position of the interferometer on a large range. The spectral resolution of the Gemini Interfeometer is given by

$$\Delta\lambda(l,\lambda)[nm] = \frac{\lambda^2[nm^2]}{l[mm]|\Delta n(\lambda)|\sin\alpha 10^6} \tag{6.21}$$

where $\lambda$ is the wavelength of the light. This relation allows to obtain the resolution in photon energy, by using the $E = \frac{hc}{\lambda}$, and the formula for the propagation of absolute uncertainty. We get:

$$\Delta E(l,E)[meV] = 10^3\frac{hc\cdot 6.242\cdot 10^{18}[eV\cdot m]}{10^9}\frac{\Delta\lambda(l,(\frac{1239.6}{E[eV]}))}{(\frac{1239.6}{E[eV]})^2} \tag{6.22}$$

Another important parameter to consider is the scan step $\delta l$, which is the displacement between one position of the interferometer and the subsequent position in a scan: the sampling must be sufficient to capture all the intensity oscillations in the interferogram. The condition to determine an adequate scan step is the following:

$$\delta l[mm] = \frac{\lambda_{min}[nm]}{n_s \sin\alpha |\Delta n(\lambda)| 10^6} \tag{6.23}$$

where $\lambda_{min}$ is the minimum wavelength contained in the spectrum of the light that we want to measure, and $n_s$ is the so called *sampling factor*, the number of experimental points required to capture a complete oscillation of $\lambda_{min}$. This number should be greater or equal than 4.

## 6.4 The Discrete Fourier Transform (D-FT)

The discrete Fourier transform (D-FT) is a mathematic operation that converts a finite sequence of N complex numbers $x_n$ into another finite sequence of N complex numbers $Y_k$:

$$Y_k = \sum_{n=0}^{N-1} x_n e^{-i2\pi \frac{k}{N} n} \tag{6.24}$$

In the analysis of periodic signals, the D-FT is used to obtain the frequency contained in a spatial or time periodic signal. If we consider a periodic function $f(l)$ defined in a close and limited interval $[a, b] \in \mathbb{C}$, and we calculate this function in a finite sequence of N finite values, we obtain the point series $(l_n, f(l_n))$. Its discrete Fourier transform gives the point series $(p_j, \tilde{f}(p_j)$, where $p_j$ are the frequency values for the new function, and $\tilde{f}(p_j)$ is the new function calculated in $p_j$. This D-FT is given by

$$\tilde{f}(p_j) = \frac{1}{\sqrt{2\pi}} \sum_{n=0}^{N-1} f(l_n) e^{-i2\pi p_j l_n} \Delta l_n \tag{6.25}$$

where $\Delta l_n = \frac{b-a}{N}$. The frequency $p_j$ are equally spaced, in the interval $[0, p_j^{MAX}]$ where $p_j^{MAX} = \frac{\pi}{\Delta l_n}$.

## 6.5 Access to the Time domain: The Time Correlated Single Photon Counting system

When a sample is photoexcited by a ultra-short light pulse, the intensity of the PL light emitted by the sample suddenly grows up and then it decreases in time. The intensity of the PL light in a selected time interval, after the excitation time $t_0$, is proportional to the probability of detecting a photon in the same time interval. The access to the time domain is obtained with the "Time Correlated Single Photon Counting" (TCSPC) approach.

In the TCSPC approach, a high repetition rate (usually 1 MHz) pulsed light source is used to excite the sample, while single PL photons are detected by the SPAD in many excitation cycles, and correletad to a reference time, corresponding to the photo-excitation. A fast acquisition board, TimeHarp260P (PicoQuant), is used to record the arrival time of two electric signals: the first (*sync*) is produced by a photo-diode which measures a small fraction of the excitation laser light. This signal is related to the photo-excitation time. The second (*input*) is generated by the SPAD detector, when a single PL photon is detected. The TimeHarp260P allows to perform the difference between the arrival time of the input and the sync signals, and after many excitation cycles it builds up an histogram of Photon Counts versus time after photo-excitation. Figure 6.2 summarizes the acquisition of time histograms with the TCSPC system.

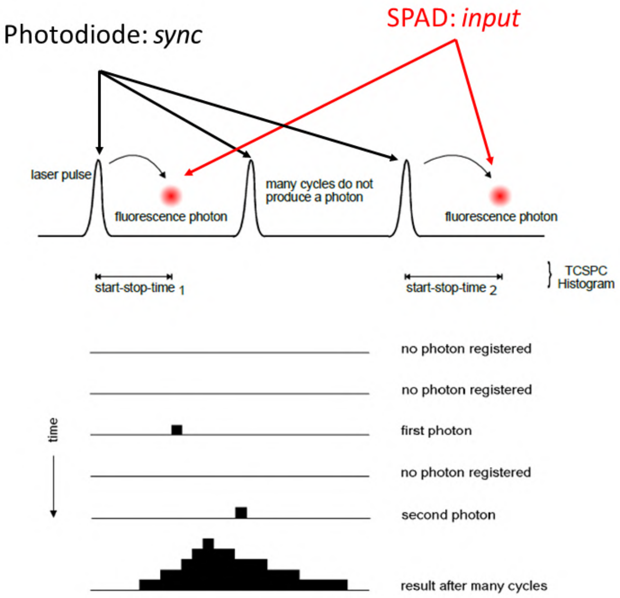

**Figure 6.2:** *Scheme of the TCSPC approach. At each excitation cycle, when a single photon is detected by the SPAD, the fast acquisition board performs the difference $\Delta t = t_{input} - t_{sync}$, where $t_{input}$ is the the detection time for the single photon, and $t_{sync}$ is the reference time related to pulsed laser photo-excitation. After many excitation cycle, the system builds up and histogram representing the photon counts Vs $\Delta t$. The ratio between the number of detected photons and excitation cycle should be <5 %, to avoid the 'pile up' effect (see main text).*

In the TimeHarp260P board, histograms have a maximum number of intervals (*bins*) of $2^{15}$, and a minimum interval width of 25 ps. The time resolution is determined by the Instrument Response Function (IRF) of the system, corresponding to the time histogram that we obtain when we measure a ligth pulse with duration $t_p << 25$ ps. The measured time dynamics is given by the convolution between the "real time dynamics" and the instrument response function:

$$I_{meas}(t) = I_{real}(t) * IRF(t) \tag{6.26}$$

Hence, to obtain the real time dynamics, it is necessary yo deconvolve the measured dynamics by the instrument response function. We will explain this in detail in subsection 3.1.5.

### The Single Photon Avalanche Diode (SPAD)

The detector we use is a Single Photon Avalanche Diode (SPAD), PDM series from Micro Photon Devices[34]. A SPAD consist in a reversed biased p-n junction with an applied voltage higher than the breakdown voltage, $V_A > V_{BD}$, and it is able to detect single photons. The working principle of a SPAD is the following. Since the p-n junction is reversed biased, only a small inverse saturation current flows, and there are not free carriers in the depletion region. If a single photon is absorbed, a single e-h pair is generated and the high electric field accelerate the electron and the hole in opposite directions. The electron acquires a kinetic energy which is high enough to produce a secondary e-h pair in an *impact ionization*, giving rise to a so called *avalanche*, where the number of the free carriers increase exponentially in the depletion region. The current exponentially rises to a value in the mA range, which is easy to discriminate. The leading edge of the current pulse is correlated to the generation of an e-h pair in the active region of the detector, due to the absorption of a single photon (signal) or to a thermal generation (noise). A *quenching* circuit is used to stop the avalanche, by lowering the applied voltage (quenching) below the breakdown voltage. After the avalanche is over, the current drops down to the inverse saturation value, and the value of the applied voltage is restored to $V_A$ (charging), getting the detector ready to detect another photon. Due to the quenching and the charging, the detector is not able to detect photons for a time $t_{dead-time}$. Hence, the measured photon count rate differs from the actual one, especially for high count rates. The correction factor can be calculated from the deadtime, and is given by:

$$\frac{CR_{actual}}{CR_{meas}} = \frac{1}{1 - CR_{meas} t_{dead-time}} \tag{6.27}$$

In the TCSPC approach, because of the dead time, it is necessary to maintain a low probability of registering more than one photon per cycle: if the number of photons occurring in one excitation cycle would be >1, the system would register the first photon but miss the second and the subsequent ones. This would lead to the so called ‘pile–up’ effect, i.e. an over–representation of early photons in the histogram, resulting in a apparently shorter PL lifetime. To avoid this problem we should work in a “safe” condition, where the average count rate at the detector (input) should be at most the 5 % of the excitation rate (sync).

The PDM series SPAD main features are reported in the table 6.1. The figure 6.3 b) reports the Photon Detection Efficiency (PDE) versus wavelength, showing a maximum of 50% at 550 nm, and a decreasing of the PDE towards the near infrared and towards the near ultraviolet. The figure 6.3 c) shows the correction factor for the count rate as a function of the measured count rate. This value is close to one for a measured count rate $CR_{meas} < 2$ Mcps (million counts per second). In all the measurement that we performed in our experimental work, the measured count rate was $CR_{meas} < 1$ Mcps.

| | |
|---|---|
| Time resolution | 50 ps |
| Spectral range | [375, 1000] nm |
| Photon detection efficiency | 50% at 550 nm (max) |
| Sensible area dimensions | 20 $\mu$m diameter |
| Dark counts rate | <35 cps |
| Afterpulsing | <3% |
| Cooling | Peltier |
| Standard | NIM, -800 mV |
| Dead time | 77 ns (max 13 Mcps) |

**Table 6.1:** *Features of the PDM series SPAD*

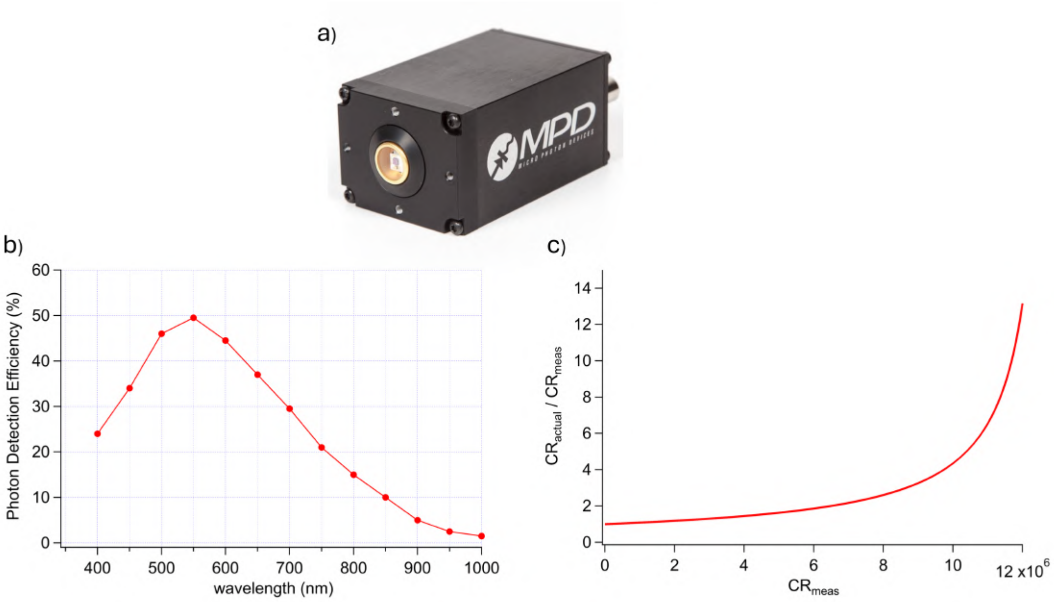

**Figure 6.3:** *a) PDM series single photon avalanche diode (SPAD). b) Photon Detection efficiency versus wavelength of the light. The maximum is at 550 nm, with a value of* $\approx 50\%$. *c) Correction factor for the measured count rates. For* $CR_{meas} < 2$ *Mcps, the correction factor is close to 1. As the measured count rate increases, the correction factor increases, diverging for* $CR_{meas} \to 13$ *Mcps (the maximum count rate for this SPAD). [34]*

## 6.6 List of abbreviations and simbols used in the thesis

**List of the main abbreviations**

- PL = Photoluminescence
- ARPES = angle resolved photoelectron spectroscopy
- TR- = Time-resolved
- TMDs = Transition metal dichalcogenides
- TCSPS = Time correlated single photon counting
- SPAD = Single photon avalanche photodiode
- FT = Fourier transform
- D-FT = Discrete Fourier transform
- IRF = Instrument response function of the time correlated single photon counting system
- FE = Free excitons
- EHP = Electron hole plasma
- EHL = Electron hole liquid
- EEA = Exciton-exciton annihilation
- BGR = Bandgap renormalization
- JDOS = Joint density of states
- FWHM = full width at half maximum

**List of the main simbols used in equations/formulas and in the main test**

- $e$ = electron charge
- $m_e$ = electron mass
- c = speed of light
- a = lattice constant
- $E_g$ = energy bandgap
- h = Planck constant
- $\hbar$ = Planck constant divided by $2\pi$
- $\nu$ = Frequency of the electromagnetic field of radiation
- $\omega$ = Angular frequency of the electromagnetic field of radiation
- $\lambda$ = wavelength of the electromagnetic field of radiation
- $\vec{k}$ = wave vector for electrons in crystals
- $\vec{q}$ = wave vector for the electromagnetic field of radiation
- $\alpha(\hbar\omega)$ = absorption coefficient
- $\varepsilon_2(\hbar\omega)$ = imaginary part of the dielectric function
- $Ry$ = Rydberg constant
- $Ry^*$ = effective Rydberg constant
- n = principal quantum number for hydrogen-like states
- $n$ = used also for the number density, electron-hole pairs in a photo-excited system
- $E_F$ = Fermi energy
- $\mu$ = chemical potential
- $k_B$ = Boltzmann constant
- T = temperature
- QY = quantum yield
- l = interferometer position
- P = excitation power
- $\phi$ = fluence of the excitation laser in TR- experiments

# Acknowledgements

I thank Riccardo Cucini (IOM-CNR) for the supervision of my PhD project along these three years, and Giancarlo Panaccione (IOM-CNR) for the planning and organization of the scientific activities.

I acknowledge the helpful discussions with prof. Silvio Modesti (University of Trieste) and Gian Marco Pierantozzi (IOM-CNR) for the data analysis and interpretation.

I acknowledge the experimental support of Riccardo Cucini, Andrea Fondacaro (IOM-CNR), and Federico Cilento (Elettra Sincrotrone Trieste).

I thank Paul Sanders (university student, Telecom physique Strasbourg) and Edvard Dobovicnik (third year PhD student, University of Trieste) for the realization of part of the LabView softwares for the experimental apparatus, and Simone Dal Zilio (IOM-CNR) for the fabrication of custom substrates for the samples.

I thank Alice Margherita Finardi (second year PhD student, University of Milan), for the support in the exfoliation, for the fruitful discussions and for the study together.

I thank Elena Stellino (post-doc, University of Rome) and Paolo Postorino (University of Rome), Fausto Sirotti (CNRS) and Fabian Cadiz (CNRS), for the training experiences at the University la Sapienza (Roma) and at the PMC institute Polytechnique (Paris), and for the experimental and scientific hints for my research work.

# Bibliography

[1] Obafunso A Ajayi, Jenny V Ardelean, Gabriella D Shepard, Jue Wang, Abhinandan Antony, Takeshi Taniguchi, Kenji Watanabe, Tony F Heinz, Stefan Strauf, X-Y Zhu, and James C Hone. Approaching the intrinsic photoluminescence linewidth in transition metal dichalcogenide monolayers. *2D Materials*, 4(3):031011, jul 2017.

[2] Matin Amani, Der-Hsien Lien, Daisuke Kiriya, Jun Xiao, Angelica Azcatl, Jiyoung Noh, Surabhi R. Madhvapathy, Rafik Addou, Santosh KC, Madan Dubey, Kyeongjae Cho, Robert M. Wallace, Si-Chen Lee, Jr-Hau He, Joel W. Ager, Xiang Zhang, Eli Yablonovitch, and Ali Javey. Near-unity photoluminescence quantum yield in mos<sub>2</sub>. *Science*, 350(6264):1065–1068, 2015.

[3] Ashish Arora, Thorsten Deilmann, Till Reichenauer, Johannes Kern, Steffen Michaelis de Vasconcellos, Michael Rohlfing, and Rudolf Bratschitsch. Excited-state trions in monolayer ws 2. *Physical Review Letters*, 123, 10 2019.

[4] N. W. Ashcroft and N. D. Mermin. *Solid State Physics.* Holt-Saunders, 1976.

[5] M. Baranowski, A. Surrente, L. Klopotowski, J. M. Urban, N. Zhang, D. K. Maude, K. Wiwatowski, S. Mackowski, Y. C. Kung, D. Dumcenco, A. Kis, and P. Plochocka. Probing the interlayer exciton physics in a mos2/mose2/mos2 van der waals heterostructure. *Nano Letters*, 17(10):6360–6365, Oct 2017.

[6] Bassani and Pastori Parravicini, Electronic States and Optical Transitions in Solids, 1975.

[7] Alexander W. Bataller, Robert A. Younts, Avinash Rustagi, Yiling Yu, Hossein Ardekani, Alexander Kemper, Linyou Cao, and Kenan Gundogdu. Dense electron–hole plasma formation and ultralong charge lifetime in monolayer mos2 via material tuning. *Nano Letters*, 19(2):1104–1111, Feb 2019.

[8] Gunnar Berghäuser, Ivan Bernal-Villamil, Robert Schmidt, Robert Schneider, Iris Niehues, Paul Erhart, Steffen Michaelis de Vasconcellos, Rudolf Bratschitsch, Andreas Knorr, and Ermin Malic. Inverted valley polarization in optically excited transition metal dichalcogenides. *Nature Communications*, 9(1):971, Mar 2018.

[9] F. Cadiz, E. Courtade, C. Robert, G. Wang, Y. Shen, H. Cai, T. Taniguchi, K. Watanabe, H. Carrere, D. Lagarde, M. Manca, T. Amand, P. Renucci, S. Tongay, X. Marie, and B. Urbaszek. Excitonic linewidth approaching the homogeneous limit in $\mathrm{mos}_2$-based van der waals heterostructures. *Phys. Rev. X*, 7:021026, May 2017.

[10] Fabian Cadiz, E. Courtade, Cédric Robert, Gang Wang, Yuxia Shen, Hui Cai, T. Taniguchi, K. Watanabe, H. Carrère, D. Lagarde, Marco Manca, Thierry Amand, P. Renucci, Sefaattin Tongay, Xavier Marie, and Bernhard Urbaszek. Excitonic linewidth approaching the homogeneous limit in mos2 based van der waals heterostructures : accessing spin-valley dynamics. *PRX*, 2017.

[11] Stefano Calati, Qiuyang Li, Xiaoyang Zhu, and Julia Stähler. Dynamic screening of quasiparticles in $\mathrm{ws}_2$ monolayers. *Phys. Rev. B*, 107:115404, Mar 2023.

[12] Y. Chan, Jonah Haber, Mit Naik, J. Neaton, Diana Qiu, Felipe Da Jornada, and Steven Louie. Exciton lifetime and optical linewidth profile via exciton-phonon interactions: Theory and first-principles calculations for monolayer mos$_2$. *Physical Review Letters*, 123, 12 2022.

[13] Alexey Chernikov, Timothy C. Berkelbach, Heather M. Hill, Albert Rigosi, Yilei Li, Burak Aslan, David R. Reichman, Mark S. Hybertsen, and Tony F. Heinz. Exciton binding energy and nonhydrogenic rydberg series in monolayer ws$_2$. *Phys. Rev. Lett.*, 113:076802, Aug 2014.

[14] Alexey Chernikov, Claudia Ruppert, Heather M. Hill, Albert F. Rigosi, and Tony F. Heinz. Population inversion and giant bandgap renormalization in atomically thin ws2 layers. *Nature Photonics*, 9(7):466–470, Jul 2015.

[15] Junho Choi, Jacob Embley, Daria D. Blach, Raül Perea-Causín, Daniel Erkensten, Dong Seob Kim, Long Yuan, Woo Young Yoon, Takashi Taniguchi, Kenji Watanabe, Keiji Ueno, Emanuel Tutuc, Samuel Brem, Ermin Malic, Xiaoqin Li, and Libai Huang. Fermi pressure and coulomb repulsion driven rapid hot plasma expansion in a van der waals heterostructure. *Nano Letters*, 23(10):4399–4405, May 2023.

[16] Riccardo Cucini, Tommaso Pincelli, Giancarlo Panaccione, Damir Kopic, Fabio Frassetto, Paolo Miotti, Gian Marco Pierantozzi, Simone Peli, Andrea Fondacaro, Aleksander De Luisa, Alessandro De Vita, Pietro Carrara, Damjan Krizmancic, Daniel T. Payne, Federico Salvador, Andrea Sterzi, Luca Poletto, Fulvio Parmigiani, Giorgio Rossi, and Federico Cilento. Coherent narrowband light source for ultrafast photoelectron spectroscopy in the 17–31 eV photon energy range. *Structural Dynamics*, 7(1):014303, 01 2020.

[17] Zhongwei Dai, Wencan Jin, Maxwell Grady, Jerzy T. Sadowski, Jerry I. Dadap, Richard M. Osgood, and Karsten Pohl. Surface structure of bulk 2h-mos2(0001) and exfoliated suspended monolayer mos2: A selected area low energy electron diffraction study. *Surface Science*, 660:16–21, 2017.

[18] Shuo Dong, Michele Puppin, Tommaso Pincelli, Samuel Beaulieu, Dominik Christiansen, Hannes Hübener, Christopher W. Nicholson, Rui Patrick Xian, Maciej Dendzik, Yunpei Deng, Yoav William Windsor, Malte Selig, Ermin Malic, Angel Rubio, Andreas Knorr, Martin Wolf, Laurenz Rettig, and Ralph Ernstorfer. Direct measurement of key exciton properties: Energy, dynamics, and spatial distribution of the wave function. *Natural Sciences*, 1(1):e10010, 2021.

[19] Maja Feierabend, Gunnar Berghäuser, Andreas Knorr, and Ermin Malic. Proposal for dark exciton based chemical sensors. *Nature Communications*, 8(1):14776, Mar 2017.

[20] E. Fortin and W.M. Sears. Photovoltaic effect and optical absorption in mos2. *Journal of Physics and Chemistry of Solids*, 43(9):881–884, 1982.

[21] Minglang Gao, Lingxiao Yu, Qian Lv, Feiyu Kang, Zheng-Hong Huang, and Ruitao Lv. Photoluminescence manipulation in two-dimensional transition metal dichalcogenides. *Journal of Materiomics*, 9(4):768–786, 2023.

[22] Roland Gillen and Janina Maultzsch. Light-matter interactions in two-dimensional transition metal dichalcogenides: Dominant excitonic transitions in mono- and few-layer mox-2 and band nesting. *IEEE Journal of Selected Topics in Quantum Electronics*, PP:1–1, 08 2016.

[23] G.D. Gilliland. Photoluminescence spectroscopy of crystalline semiconductors. *Materials Science and Engineering: R: Reports*, 18(3):99–399, 1997.

[24] A. J. Goodman, A. P. Willard, and W. A. Tisdale. Exciton trapping is responsible for the long apparent lifetime in acid-treated mos$_2$. *Phys. Rev. B*, 96:121404, Sep 2017.

[25] Sang Han, Ravi Bhatia, and Sang-Woo Kim. Synthesis, properties and potential applications of two-dimensional transition metal dichalcogenides. *Nano Convergence*, 2, 12 2015.

[26] Aubrey T. Hanbicki, Marc Currie, George Kioseoglou, Adam L. Friedman, and Berend T. Jonker. Measurement of high exciton binding energy in the monolayer transition-metal dichalcogenides ws2 and wse2. *Solid State Communications*, 203:16–20, 2014.

[27] Keliang He, Charles Poole, Kin Fai Mak, and Jie Shan. Experimental demonstration of continuous electronic structure tuning via strain in atomically thin mos2. *Nano Letters*, 13(6):2931–2936, Jun 2013.

[28] Jinhua Hong, Zhixin Hu, Matt Probert, Kun Li, Danhui Lv, Xinan Yang, Lin Gu, Nannan Mao, Qingliang Feng, Liming Xie, Jin Zhang, Dianzhong Wu, Zhiyong Zhang, Chuanhong Jin, Wei Ji, Xixiang Zhang, Jun Yuan, and Ze Zhang. Exploring atomic defects in molybdenum disulphide monolayers. *Nature Communications*, 6(1):6293, Feb 2015.

[29] official website of the Gemini Nireos.

[30] https://www.hqgraphene.com/.

[31] https://www.ioffe.ru/.

[32] official website of PI.

[33] https://www.testo-unico-sicurezza.com/database-delle-proprieta-termiche-dei-materiali.html.

[34] official website of the Micro Photon Devices.

[35] Shin ichiro Tanaka. Utility and constraint on the use of pump-probe photoelectron spectroscopy for detecting time-resolved surface photovoltage. *Journal of Electron Spectroscopy and Related Phenomena*, 185(5):152–158, 2012.

[36] Joshua O. Island, Agnieszka Kuc, Erik H. Diependaal, Rudolf Bratschitsch, Herre S. J. van der Zant, Thomas Heine, and Andres Castellanos-Gomez. Precise and reversible band gap tuning in single-layer mose2 by uniaxial strain. *Nanoscale*, 8:2589–2593, 2016.

[37] Vishwas Jindal, Dipankar Jana, and Sandip Ghosh. Electroreflectance spectroscopy of few-layer MoS2 : Issues related to A1s exciton subspecies, exciton binding energy, and inter-layer exciton. *Journal of Applied Physics*, 132(21):214303, 12 2022.

[38] Manobina Karmakar, Subhrajit Mukherjee, Samit K. Ray, and Prasanta Kumar Datta. Electron-hole plasma formation dynamics observed through exciton-plasma interactions in transition metal dichalcogenides. *Phys. Rev. B*, 104:075446, Aug 2021.

[39] Reelika Kaupmees, Hannu-Pekka Komsa, and Jüri Krustok. Photoluminescence study of b-trions in mos 2 monolayers with high density of defects. *physica status solidi (b)*, 256:1800384, 03 2019.

[40] Zahra Khatibi, Maja Feierabend, Malte Selig, Samuel Brem, Christopher Linderälv, Paul Erhart, and Ermin Malic. Impact of strain on the excitonic linewidth in transition metal dichalcogenides. *2D Materials*, 6(1):015015, nov 2018.

[41] Hyungjin Kim, Der-Hsien Lien, Matin Amani, Joel W. Ager, and Ali Javey. Highly stable near-unity photoluminescence yield in monolayer mos2 by fluoropolymer encapsulation and superacid treatment. *ACS Nano*, 11(5):5179–5185, May 2017.

[42] Hannu-Pekka Komsa and Arkady Krasheninnikov. Effects of confinement and environment on the electronic structure and exciton binding energy of mos2 from first principles. *Phys. Rev. B*, 86, 12 2012.

[43] Drew W. Latzke, Wentao Zhang, Aslihan Suslu, Tay-Rong Chang, Hsin Lin, Horng-Tay Jeng, Sefaattin Tongay, Junqiao Wu, Arun Bansil, and Alessandra Lanzara. Electronic structure, spin-orbit coupling, and interlayer interaction in bulk $\text{mos}_2$ and $\text{ws}_2$. *Phys. Rev. B*, 91:235202, Jun 2015.

[44] Ming-Fu Lin, Vidya Kochat, Aravind Krishnamoorthy, Lindsay Bassman Oftelie, Clemens Weninger, Qiang Zheng, Xiang Zhang, Amey Apte, Chandra Sekhar Tiwary, Xiaozhe Shen, Renkai Li, Rajiv Kalia, Pulickel Ajayan, Aiichiro Nakano, Priya Vashishta, Fuyuki Shimojo, Xijie Wang, David M. Fritz, and Uwe Bergmann. Ultrafast non-radiative dynamics of atomically thin mose2. *Nature Communications*, 8(1):1745, Nov 2017.

[45] Yung-Chang Lin, Dumitru O. Dumcenco, Hannu-Pekka Komsa, Yoshiko Niimi, Arkady V. Krasheninnikov, Ying-Sheng Huang, and Kazu Suenaga. Properties of individual dopant atoms in single-layer mos2: Atomic structure, migration, and enhanced reactivity. *Advanced Materials*, 26(18):2857–2861, 2014.

[46] Yuanshuang Liu, Huan Liu, Jiangcai Wang, and Dameng Liu. Defect-type-dependent carrier lifetimes in monolayer ws2 films. *The Journal of Physical Chemistry C*, 126(10):4929–4938, Mar 2022.

[47] Dongxiao Lu, Qiang Zhou, Fangfei Li, Xiaowei Li, and Geyu Lu. Influence of interlayer interactions on the relaxation dynamics of excitons in ultrathin mos2. *Nanoscale Adv.*, 1:1186–1192, 2019.

[48] Ivan Pelant, Jan Valenta, Luminescence spectroscopy of semiconductors, 2012.

[49] Supplementary information for: Phase Diagram of High-Temperature Electron–Hole Quantum Droplet in Two-Dimensional Semiconductors. Yu et al, ACS Nano, 17, 16, 15474-15481, 2023.

[50] Xavier Marie and Bernhard Urbaszek. Ultrafast exciton dynamics. *Nature Materials*, 14(9):860–861, Sep 2015.

[51] Stephen McDonnell, Rafik Addou, Creighton Buie, Robert M. Wallace, and Christopher L. Hinkle. Defect-dominated doping and contact resistance in mos2. *ACS Nano*, 8(3):2880–2888, Mar 2014.

[52] Tesi magistrale in fisica della materia, 2021.

[53] M R Molas, C Faugeras, A O Slobodeniuk, K Nogajewski, M Bartos, D M Basko, and M Potemski. Brightening of dark excitons in monolayers of semiconducting transition metal dichalcogenides. *2D Materials*, 4(2):021003, jan 2017.

[54] Thomas Mueller and Ermin Malic. Exciton physics and device application of two-dimensional transition metal dichalcogenide semiconductors. *npj 2D Materials and Applications*, 2(1):29, Sep 2018.

[55] Sina Najmaei, Zheng Liu, Wu Zhou, Xiaolong Zou, Gang Shi, Sidong Lei, Boris I. Yakobson, Juan-Carlos Idrobo, Pulickel M. Ajayan, and Jun Lou. Vapour phase growth and grain boundary structure of molybdenum disulphide atomic layers. *Nature Materials*, 12(8):754–759, Aug 2013.

[56] Hoang Tung Nguyen, Tae Jung Kim, Han Gyeol Park, Van Long Le, Xuan Au Nguyen, Dohyoung Koo, Chul-Ho Lee, Do Duc Cuong, Soon Cheol Hong, and Young Dong Kim. Temperature dependence of optical properties of monolayer ws2 by spectroscopic ellipsometry. *Applied Surface Science*, 511:145503, 2020.

[57] Maurizia Palummo, Marco Bernardi, and Jeffrey C. Grossman. Exciton radiative lifetimes in two-dimensional transition metal dichalcogenides. *Nano Letters*, 15(5):2794–2800, May 2015.

[58] Soohyung Park, Niklas Mutz, Thorsten Schultz, Sylke Blumstengel, Ali Han, Areej Aljarb, Lain-Jong Li, Emil J W List-Kratochvil, Patrick Amsalem, and Norbert Koch. Direct determination of monolayer mos2 and wse2 exciton binding energies on insulating and metallic substrates. *2D Materials*, 5(2):025003, jan 2018.

[59] M. Perlangeli, F. Proietto, Fulvio Parmigiani, and F. Cilento. Sub-nanosecond free carrier recombination in an indirectly excited quantum-well heterostructure. *Journal of the Optical Society of America B*, 41, 12 2023.

[60] Antonio Perri, John H. Gaida, Andrea Farina, Fabrizio Preda, Daniele Viola, Matteo Ballottari, Jürgen Hauer, Sandro De Silvestri, Cosimo D'Andrea, Giulio Cerullo, and Dario Polli. Time- and frequency-resolved fluorescence with a single tcspc detector via a fourier-transform approach. *Opt. Express*, 26(3):2270–2279, Feb 2018.

[61] Antonio Perri, Fabrizio Preda, Cosimo D'Andrea, Erling Thyrhaug, Giulio Cerullo, Dario Polli, and Jürgen Hauer. Excitation-emission fourier-transform spectroscopy based on a birefringent interferometer. *Opt. Express*, 25(12):A483–A490, Jun 2017.

[62] Personale notes of the university course: 'Dinamica di sistemi quantistici, di Alfonso Baldereschi.

[63] Eva A. A. Pogna, Margherita Marsili, Domenico De Fazio, Stefano Dal Conte, Cristian Manzoni, Davide Sangalli, Duhee Yoon, Antonio Lombardo, Andrea C. Ferrari, Andrea Marini, Giulio Cerullo, and Deborah Prezzi. Photo-induced bandgap renormalization governs the ultrafast response of single-layer mos2. *ACS Nano*, 10(1):1182–1188, Jan 2016.

[64] Ya. Pokrovskii. *Condensation of Non-Equilibrium Charge Carriers in Semiconductors*, pages 385–410. De Gruyter, Berlin, Boston, 1972.

[65] Hao Qiu, Tao Xu, Zilu Wang, Wei Ren, Haiyan Nan, Zhenhua Ni, Qian Chen, Shijun Yuan, Feng Miao, Fengqi Song, Gen Long, Yi Shi, Litao Sun, Jinlan Wang, and Xinran Wang. Hopping transport through defect-induced localized states in molybdenum disulphide. *Nature Communications*, 4(1):2642, Oct 2013.

[66] refractiveindex.info.

[67] Pasqual Rivera, John R. Schaibley, Aaron M. Jones, Jason S. Ross, Sanfeng Wu, Grant Aivazian, Philip Klement, Kyle Seyler, Genevieve Clark, Nirmal J. Ghimire, Jiaqiang Yan, D. G. Mandrus, Wang Yao, and Xiaodong Xu. Observation of long-lived interlayer excitons in monolayer mose2–wse2 heterostructures. *Nature Communications*, 6(1):6242, Feb 2015.

[68] C. Robert, D. Lagarde, F. Cadiz, G. Wang, B. Lassagne, T. Amand, A. Balocchi, P. Renucci, S. Tongay, B. Urbaszek, and X. Marie. Exciton radiative lifetime in transition metal dichalcogenide monolayers. *Phys. Rev. B*, 93:205423, May 2016.

[69] Avinash Rustagi and Alexander F. Kemper. Theoretical phase diagram for the room-temperature electron–hole liquid in photoexcited quasi-two-dimensional monolayer mos2. *Nano Letters*, 18(1):455–459, Jan 2018.

[70] Nihit Saigal, Vasam Sugunakar, and Sandip Ghosh. Exciton binding energy in bulk MoS2: A reassessment. *Applied Physics Letters*, 108(13):132105, 04 2016.

[71] Bei Shi, Lei Wang, Aidan Taylor, Simone Brunelli, Hongwei Zhao, Song Bowen, and Jonathan Klamkin. Mocvd grown low dislocation density gaas-on-v-groove patterned (001) si for 1.3 $\mu$m quantum dot laser applications. *Applied Physics Letters*, 114:172102, 04 2019.

[72] Hongyan Shi, Rusen Yan, Simone Bertolazzi, Jacopo Brivio, Bo Gao, Andras Kis, Debdeep Jena, Huili Grace Xing, and Libai Huang. Exciton dynamics in suspended monolayer and few-layer mos2 2d crystals. *ACS Nano*, 7(2):1072–1080, Feb 2013.

[73] P. Siffalovic, M. Drescher, and U. Heinzmann. Femtosecond time-resolved core-level photoelectron spectroscopy tracking surface photovoltage transients on p–gaas. *Europhysics Letters*, 60(6):924, dec 2002.

[74] Ashish Soni, Dushyant Kushavah, Li-Syuan Lu, Wen-Hao Chang, and Suman Kalyan Pal. Ultrafast exciton trapping and exciton–exciton annihilation in large-area cvd-grown monolayer ws2. *The Journal of Physical Chemistry C*, 125(43):23880–23888, Nov 2021.

[75] Frederico B Sousa, Raül Perea-Causin, Sean Hartmann, Lucas Lafetá, Bárbara Rosa, Samuel Brem, Chirag Palekar, Stephan Reitzenstein, Achim Hartschuh, Ermin Malic, and Leandro M Malard. Ultrafast hot electron-hole plasma photoluminescence in two-dimensional semiconductors. *Nanoscale*, 15(15):7154–7163, April 2023.

[76] A. Steinhoff, J.-H. Kim, F. Jahnke, M. Rösner, D.-S. Kim, C. Lee, G. H. Han, M. S. Jeong, T. O. Wehling, and C. Gies. Efficient excitonic photoluminescence in direct and indirect band gap monolayer mos2. *Nano Letters*, 15(10):6841–6847, Oct 2015.

[77] Philipp Tonndorf, Robert Schmidt, Philipp Böttger, Xiao Zhang, Janna Börner, Andreas Liebig, Manfred Albrecht, Christian Kloc, Ovidiu Gordan, Dietrich R. T. Zahn, Steffen Michaelis de Vasconcellos, and Rudolf Bratschitsch. Photoluminescence emission and raman response of monolayer mos2, mose2, and wse2. *Opt. Express*, 21(4):4908–4916, Feb 2013.

[78] Philipp Tonndorf, Robert Schmidt, Robert Schneider, Johannes Kern, Michele Buscema, Gary A. Steele, Andres Castellanos-Gomez, Herre S. J. van der Zant, Steffen Michaelis de Vasconcellos, and Rudolf Bratschitsch. Single-photon emission from localized excitons in an atomically thin semiconductor. *Optica*, 2(4):347–352, Apr 2015.

[79] Arend M. van der Zande, Pinshane Y. Huang, Daniel A. Chenet, Timothy C. Berkelbach, YuMeng You, Gwan-Hyoung Lee, Tony F. Heinz, David R. Reichman, David A. Muller, and James C. Hone. Grains and grain boundaries in highly crystalline monolayer molybdenum disulphide. *Nature Materials*, 12(6):554–561, Jun 2013.

[80] Péter Vancsó, Gábor Zsolt Magda, János Pető, Ji-Young Noh, Yong-Sung Kim, Chanyong Hwang, László P. Biró, and Levente Tapasztó. The intrinsic defect structure of exfoliated $mos_2$ single layers revealed by scanning tunneling microscopy. *Scientific Reports*, 6(1):29726, Jul 2016.

[81] R. Wallauer, J. Reimann, N. Armbrust, J. Güdde, and U. Höfer. Intervalley scattering in MoS2 imaged by two-photon photoemission with a high-harmonic probe. *Applied Physics Letters*, 109(16):162102, 10 2016.

[82] Haining Wang, Jared H. Strait, Changjian Zhang, Weimin Chan, Christina Manolatou, Sandip Tiwari, and Farhan Rana. Fast exciton annihilation by capture of electrons or holes by defects via auger scattering in monolayer metal dichalcogenides. *Phys. Rev. B*, 91:165411, Apr 2015.

[83] Haining Wang, Changjian Zhang, Weimin Chan, Christina Manolatou, Sandip Tiwari, and Farhan Rana. Radiative lifetimes of excitons and trions in monolayers of the metal dichalcogenide $mos_2$. *Phys. Rev. B*, 93:045407, Jan 2016.

[84] Haining Wang, Changjian Zhang, and Farhan Rana. Ultrafast dynamics of defect-assisted electron–hole recombination in monolayer mos2. *Nano Letters*, 15(1):339–345, Jan 2015.

[85] Qing Hua Wang, Kourosh Kalantar-Zadeh, Andras Kis, Jonathan N. Coleman, and Michael S. Strano. Electronics and optoelectronics of two-dimensional transition metal dichalcogenides. *Nature Nanotechnology*, 7(11):699–712, Nov 2012.

[86] https://physicsofsemiconductors.myblog.it/media/01/00/723380648.pdf.

[87] Ke Wei, Yu Liu, Hang Yang, Xiangai Cheng, and Tian Jiang. Large range manipulation of exciton species in monolayer ws2. 06 2016.

[88] W Widdra, D Bröcker, T Gießel, I.V Hertel, W Krüger, A Liero, F Noack, V Petrov, D Pop, P.M Schmidt, R Weber, I Will, and B Winter. Time-resolved core level photoemission: surface photovoltage dynamics of the sio2/si(100) interface. *Surface Science*, 543(1):87–94, 2003.

[89] Fengcheng Wu, Fanyao Qu, and A. Macdonald. Exciton band structure of monolayer $mos_2$. *Physical Review B*, 91, 01 2015.

[90] www.ossila.com, website which reports properties of materials.

[91] Yiling Yu, Alexander W. Bataller, Robert Younts, Yifei Yu, Guoqing Li, Alexander A. Puretzky, David B. Geohegan, Kenan Gundogdu, and Linyou Cao. Room-temperature electron–hole liquid in monolayer mos2. *ACS Nano*, 13(9):10351–10358, Sep 2019.

[92] Yiling Yu, Guoqing Li, Yan Xu, Chong Hu, Xiaoze Liu, and Linyou Cao. Phase diagram of high-temperature electron–hole quantum droplet in two-dimensional semiconductors. *ACS Nano*, 17(16):15474–15481, Aug 2023.

[93] Long Yuan and Libai Huang. Exciton dynamics and annihilation in ws2 2d semiconductors. *Nanoscale*, 7, 03 2015.

[94] Chendong Zhang, Yuxuan Chen, Amber Johnson, Ming-Yang Li, Lain-Jong Li, Patrick C. Mende, Randall M. Feenstra, and Chih-Kang Shih. Probing critical point energies of transition metal dichalcogenides: Surprising indirect gap of single layer wse2. *Nano Letters*, 15(10):6494–6500, Oct 2015.

[95] Wu Zhou, Xiaolong Zou, Sina Najmaei, Zheng Liu, Yumeng Shi, Jing Kong, Jun Lou, Pulickel M. Ajayan, Boris I. Yakobson, and Juan-Carlos Idrobo. Intrinsic structural defects in monolayer molybdenum disulfide. *Nano Letters*, 13(6):2615–2622, Jun 2013.

[96] Bairen Zhu, Xi Chen, and Xiaodong Cui. Exciton binding energy of monolayer ws2. *Scientific Reports*, 5(1):9218, Mar 2015.

[97] Xiaolong Zou, Yuanyue Liu, and Boris I. Yakobson. Predicting dislocations and grain boundaries in two-dimensional metal-disulfides from the first principles. *Nano Letters*, 13(1):253–258, Jan 2013.